

IRON-BASED MATERIALS FOR THE REMEDIATION OF CHLORINATED
ETHENES

by

YANLAI HAN, B.S., M.S.,

A Dissertation

In

Civil Engineering

Submitted to the Graduate Faculty
of Texas Tech University in
Partial Fulfillment of
the Requirements for
the Degree of

DOCTOR OF PHILOSOPHY

Approved

Weile Yan, Ph.D.
Chair of Committee

Andrew Jackson, Ph.D., P.E.

Juske Horita, Ph.D

Ken Rainwater, Ph.D., P.E.

Mark Sheridan, Ph.D.
Dean of the Graduate School

August 2016

Copyright 2016, Yanlai Han

ACKNOWLEDGEMENTS

Now when writing this section at this moment and looking back the past five years, I am emotional. I would like to sincerely express my huge gratitude to my Doctoral advisor, Dr Weile Yan. I really cannot pull this dissertation off without her support. To be honest, I was not a no-brainer for this Ph.D. project, but she could always find the right direction for me and gave me invaluable suggestions when I felt frustrated and lost. She also gradually walked me through how to critically think and conduct deep analysis of experimental data and eventually found what these data really mean, which I believe is the critical ability for a researcher. No matter how busy she was, she always reserved time available for me. Besides all this science and research support, Dr. Yan also gave me support when my family undergone the big accident in 2014. I am indebted to her.

I want to extend my gratitude to my doctoral committee members, Dr Horita, Dr Jackson and Dr Rainwater. Working with Dr Horita together on the interdisciplinary research programs was an excellent and unforgettable experience for me. Dr Rainwater is the first professor who brought me to the fantastic environmental modeling area, and I was motivated to learn Matlab, R, and Python programming because of him. Dr Jackson is an interesting professor and “office happy events” organizer, and I had loads of happy memories with him and my officemates.

I also would like to say thank you to my family, to my parents, to my sister, and to special Cathy for their love and listening to my boring research stories. I also want express my great gratitude to my awesome friends that I made at TTU, Matt, Elliott, Jasmine, Whitney, Preston, Nubia, Spencer, and Siva, your guys are awesome and makes my life at TTU credible exciting.

TABLE OF CONTENTS

ACKNOWLEDGEMENTS	ii
ABSTRACT.....	viii
LIST OF TABLES.....	x
LIST OF FIGURES.....	xi
CHAPTER ONE Introduction	1
1.1 Overview of Zero-valent Iron Technology Development.....	1
1.2 Synthesis or Production Methods of ZVI Materials.....	2
1.3 Characterization of ZVI	4
1.4 Reaction Mechanisms of ZVI with Common Contaminants	5
1.4.1 Reductive Dehalogenation by ZVI.....	5
1.4.2 Reductive Dehalogenation by Bimetallic ZVI	9
1.4.3 Sequestration of Inorganic Contaminants.....	10
1.4.3.1 Metals Ions.....	10
1.4.3.2 Arsenite and Arsenate	11
1.4.3.3 Hexavalent Chromium.....	11
1.4.3.4 Nitrate	12
1.5 Limitations of ZVI technology.....	12
1.5.1 Passivation of ZVI.....	12
1.5.2 Passivation and Deactivation of Iron-based Bimetallic Materials.....	13
1.5.3 Effective Delivery of nZVI to Contaminant Sources	15
1.6 Reductive Dechlorination of Chlorinated Ethenes by Iron Sulfide Materials	16
1.6.1 Iron Sulfides Minerals Formation in the Natural Systems	16
1.6.2 Remediation of Chlorinated Ethenes by Iron Sulfides or Sulfide-modified Iron	17
1.7 Stable Isotope Fractionation Analysis for Environmental Monitoring	18
1.8 Research Objectives	20
References	1
CHAPTER TWO Optimizing Synthesis Conditions of Nanoscale Zero-Valent Iron (nZVI) through Aqueous Reactivity Assessment	35
2.1 Introduction	35

2.2 Materials and Methods	37
2.2.1 Materials	37
2.2.2 Synthesis of nZVI.....	38
2.2.3 Solid Phase Characterization.....	39
2.2.4 nZVI Reactivity Assessment	39
2.3 Results and Discussion.....	40
2.3.1 Characterization of nZVI.....	40
2.3.2 nZVI Reactivity Assessment using Cu(II) as a Probe Reagent.....	41
2.3.3 nZVI Reactivity Assessment using Nitrate as a Probe Reagent.....	45
2.4 Conclusion.....	46
Reference.....	47
CHAPTER THREE Bimetallic Nickel-Iron Nanoparticles for Groundwater Decontamination: Effect of Groundwater Constituents on Surface Deactivation....	63
3.1. Introduction	63
3.2. Materials and Methods	65
3.2.1. Preparation of Nanoparticles	65
3.2.2. Aging Experiments	66
3.2.3. TCE Experiments	67
3.2.4. Material Characterization	67
3.3. Results and Discussion.....	68
3.3.1. Reactivity of Fresh Ni-Fe BNPs	68
3.3.2. Mildly Deactivating Groundwater Solutes	69
3.3.3. Solutes with Strong Deactivation Effects	70
3.3.4. Deactivation of SDP-Ni-Fe BNPs	71
3.3.5. Surface Chemistry Analysis with XPS.....	72
3.3.6. Reaction Pathway and Deactivation Mechanisms.....	74
3.4. Conclusions and Environmental Implications.....	75
References	76
3.5. Supporting Information	93
CHAPTER FOUR Trichloroethene Hydrodechlorination by Ni-Fe Bimetallic Nanoparticles: Reaction Pathways and Catalytic Surface Reaction Mechanisms Analyzed by Carbon Isotope Fractionation	98

4.1. Introduction	98
4.2. Materials and methods	100
4.2.1. Preparation of nanoparticles	100
4.2.2. Aging Experiments	101
4.2.3. TCE Experiments	102
4.2.4. Evaluation of Isotope Fractionation	103
4.3. Results and Discussion.....	103
4.3.1. Carbon Isotope Fractionation during TCE Hydrodechlorination	103
4.2. Kinetic Modeling Results.....	107
4.4. Conclusion.....	110
References	111
CHAPTER FIVE Trichloroethene Hydrodechlorination by Pd-Fe Bimetallic Nanoparticles: Solute-Induced Catalyst Deactivation Analyzed by Carbon Isotope Fractionation	127
5.1. Introduction	127
5.2. Materials and Methods.....	130
5.2.1. Preparation of Nanoparticles	130
5.2.2. Aging Experiments	130
5.2.3. TCE Experiments and Analytical Method.....	131
5.2.4. Evaluation of Isotope Fractionation	132
5.3. Results	133
5.3.1. TCE Dechlorination by Fresh Fe and Pd-Fe NPs.....	133
5.3.2. TCE Dechlorination by Aged Pd-Fe NPs.....	135
5.4. Discussion	138
5.4.1. Solute-induced Deactivation Mechanisms	138
5.5. Environmental Significance	142
References	143
CHAPTER SIX Surface Sulfided Nanoscale Zero-Valent Iron (nZVI) for Reductive Dechlorination of Trichloroethene	162
6.1. INTRODUCTION.....	162
6.2. MATERIALS AND METHODS	164
6.2.1 Chemicals	164

6.2.2 Preparation of Sulfided nZVI (S-nZVI)	164
6.2.3 Commercial Iron Sulfidation Treatment.....	165
6.2.4. TCE Dechlorination Experiments	165
6.2.5. Analytical methods	165
6.2.6. Material Characterization	166
6.3. Results and Discussion.....	167
6.3.1. Effect of Different Sulfur Precursors.....	167
6.3.2 Effect of Sulfidation Procedure: Initial Sulfidation vs. Post-synthesis Sulfidation	169
6.3.3 The Effect of S/Fe Mole Ratio	170
6.3.4 Sulfidation Treatment Process for Peerless TM Iron Filings	171
6.4. Discussion	172
6.4.1 S-nZVI.....	172
6.4.2 S-Peerless filings	175
6.5. Conclusions	175
Reference.....	176
CHAPTER SEVEN Reductive Dechlorination of Chlorinated Ethenes by Sulfided Zero-Valent Iron Materials: Kinetic, Pathways, Aqueous Stability and Reaction Mechanism.....	197
7.1. Introduction	197
7.2. Materials and Methods	199
7.2.1 Chemicals	199
7.2.2 Sulfided nZVI Preparation Method	200
7.2.3 Commercial Iron Sulfidation Treatment.....	200
7.2.4. Reduction of Chlorinated Ethenes Experiments.....	201
7.2.5 Aging Experiments	201
7.2.6. Analytical Methods.....	202
7.3. Results and Discussion.....	202
7.3.1 Reduction of Chlorinated Ethenes by nZVI and S-nZVI	202
7.3.1.1 Ethene and Acetylene	202
7.3.1.2 Tetrachloroethene (PCE)	204
7.3.1.3 <i>trans</i> -dichloroethene (<i>trans</i> -DCE)	206

7.3.1.4 <i>cis</i> -dichloroethene (<i>cis</i> -DCE).....	207
7.3.1.5 1,1-dichloroethene (1,1-DCE)	207
7.3.1.6 Discussion	209
7.3.2 Reduction of Chlorinated Ethenes by Peerless TM Fe and S-Peerless TM Fe	211
7.3.3 Reduction of Chlorinated Ethenes by BASF TM Fe and S- BASF TM Fe.....	213
7.3.4 Reactivity of Particles Aged in Groundwater Media and Air	213
7.4. Implications for Subsurface Remediation	214
Reference.....	215
7.5 Supporting information	238
CHAPTER EIGHT Conclusions and Future Research Recommendations.....	248
8.1 Conclusions	248
8.2 Future Research Recommendations	251
8.2.1 Interactions of nZVI with Microorganisms in the Subsurface Environment .	251
8.2.2 Target Delivery Study of S-nZVI.....	253
References	253

ABSTRACT

Zero-valent iron (ZVI) is one of the most widely used engineered materials for the remediation of chlorinated ethenes in the subsurface environment. The material has been widely used in various *in situ* remediation technologies including Fe-permeable reactive barriers (Fe-PRB) and subsurface injection of nanoscale zero-valent iron (nZVI) for contaminant plume attenuation and source zone remediation. However, there are two serious drawbacks when ZVI is used for the remediation of chlorinated ethenes: (i) ZVI tends to undergo rapid passivation which undermines its longevity for remediation applications, and (ii) ZVI has low dechlorination reactivity in the absence of catalyst additives. Bimetallic nanoparticles (BNPs), prepared by doping a small amount of catalytic metals (e.g., Pd or Ni), can significantly enhance the particles' dechlorination reactivity. However, BNPs suffer rapid deactivation when exposed to groundwater media, and the BNPs deactivation mechanisms are still poorly understood.

The first part of this dissertation aims to investigate Ni-Fe BNPs and Pd-Fe BNPs deactivation mechanisms when exposing them to common groundwater solutes. Aging experiments were conducted by pre-immersing fresh prepared BNPs in solutions containing different groundwater solutes for 24 h prior to reacting the particles with trichloroethene (TCE) to assess their dechlorination reactivity. Analyses of reaction kinetics and product distribution and stable carbon isotope fractionation measurements suggest that Pd-Fe BNPs were sensitive to solute-induced deactivation, particularly in solutions containing chloride, bicarbonate, nitrate or sulfite ions. Although Ni-Fe BNPs possess higher electrochemical stability than Pd-Fe BNPs in the aqueous media, strong deactivation was observed in sulfate, nitrate, and phosphate solutions. Multiple modes of BNP deactivation were proposed for the two types of BNPs.

To overcome the intrinsic limitations of conventional and bimetallic ZVI materials, the second part of this dissertation aims to develop a new form of ZVI with higher dechlorination reactivity without the use of catalyst additives and a greater resistance to environmental passivation. A surface sulfidation treatment was designed and optimized for laboratory-made nZVI and commercial ZVI. The sulfided nZVI

demonstrates remarkable improvements in dechlorination rates for chlorinated ethenes. Aging experiments indicated that sulfided nZVI possesses greater stability and maintains its dechlorination reactivity over long-term aging processes. Applying sulfidation treatment to commercial iron results in more efficient tetrachloroethene (PCE) and TCE degradation. Sulfidation treatment therefore represents a simple yet promising approach to increase the reactivity of ZVI using earth-abundant reagents in place of precious catalyst metals.

LIST OF TABLES

1.1. Commonly used commercial mZVI and nZVI size and surface area	4
2.1 Experimental conditions used to prepare nZVI evaluated in this study	52
2.2 Pseudo-first-order reaction rate constants (k_R) and first-order deactivation rate constants (k_D) of nitrate reduction	53
3.1. Mass-normalized reaction rate constants (k_m) and product yields of fresh and aged Ni-Fe BNPs	91
3.2. Surface composition of freshly made and aged Ni-Fe nanoparticles measured by XPS analysis.....	92
S3.1. Solution pH before and after TCE dechlorination and loss of nickel and iron due to dissolution into the reaction media	96
4.1. Reaction rate constants obtained from model fitting, carbon mass recovery, production distribution, and bulk enrichment factor of TCE dechlorination reactions with fresh and aged Ni-Fe BNPs.....	125
4.2. Bulk ^{13}C enrichment factor (ε_{bulk}) reported in the literature for TCE dechlorination by different types of iron.....	126
5.1. Pertinent kinetic, isotopic, and production distribution parameters of TCE hydrodechlorination reactions with fresh and aged Pd-Fe BNPs	148
6.1. Pseudo-first-order rate constants, product yields, and carbon mass recovery for TCE dechlorination by nZVI and S-nZVI synthesized under different conditions.....	190
6.2. Effects of sulfidation conditions on pseudo-first-order rate constants, product yields, and carbon mass recovery for TCE dechlorination by different S-Peerless TM iron filings	191
7.1. Pseudo-first-order rate constants, products yield, and C2 mass recoveries for chlorinated ethenes by nZVI and S-nZVI (S/Fe mole ratio at 0.05).....	235
7.2. Pseudo-first-order rate constants, products yields, and C2 mass recoveries for chlorinated ethenes by S-nZVI sulfidated at different S/Fe mole ratios.....	236
7.3. Pseudo-first-order rate constants, products yield, and C2 mass recoveries for chlorinated ethenes by Peerless TM iron and S-Peerless TM iron	237
S7.1. Elemental composition of BASF TM iron powder ^a	246
S7.2. Pseudo-first-order rate constants of TCE degradation by S-nZVI (S/Fe mole ratio at 0.05) aged in aqueous solutions for 1 day and for 1 month, respectively.....	247

LIST OF FIGURES

1.1. Transmission electron microscopy (TEM) images of nZVI synthesized in our lab. The operational voltage of TEM is 300 kV, and magnification is 200,000 times.....	5
1.2. Chlorinated ethenes dechlorination pathway ²	7
1.3. The mechanisms of TCE dechlorination by nZVI and Pd-Fe BNPs.	10
2.1. Morphology characterization of nZVI particles synthesized using the baseline conditions. (a) and (b) are TEM and SEM images of as-synthesized nZVI. (c) and (d) are secondary electron and back-scattered electron images of nZVI reacted with Cu(II) for 10 min.	54
2.2 (a). Removal of aqueous Cu(II) by nZVI in N ₂ -sparged solutions and (b) release of dissolved iron into solutions after Cu(II) reaction. (c) Cu(II) removal in a solution open to atmosphere. (d) Cu(II) removal capacity at varying Cu(II)/nZVI loading ratios in deoxygenated solutions. Initial Cu(II) concentration was 200 mg/L in (a) and (c) and varied in the range of 50 - 1200 mg/L in (b) and (d). Dose of nZVI was 0.75 g/L in (d). 55	
2.3. Identification of Cu(II) reduction products with X-ray diffraction analysis.....	56
2.4. Cu(II) reduction by nZVI prepared under different synthesis conditions. (a) Effect of solution agitation speed, (b) effect of reductant feed rate, (c) effect of initial Fe(III) concentration, and (d) effect of reductant to iron molar ratio. For each nZVI, the initial slope at low Cu/nZVI loading ratio was fitted to a straight line, and the maximum Cu(II) removal per unit mass of nZVI was denoted by a dashed line.	59
2.5. Nitrate reduction by nZVI of different synthesis batches. Initial nitrate concentration was 50 mg/L and 150 mg/L, respectively. Dose of nZVI was 2 g/L. Solid lines are model fit to experimental data using the pseudo-first-order reaction and first-order deactivation model.....	69
2.6 Correlation of the initial slope of Cu(II) reduction data with kinetics of nitrate reduction experiments.	70
3.1. TEM micrographs of (a) fresh <i>CR</i> -Ni-Fe, (b) fresh <i>SDP</i> -Ni-Fe, and (c) <i>CR</i> -Ni-Fe aged in 5 mM phosphate solution for 24 h.	81
3.2. TCE degradation by fresh Ni-Fe BNPs prepared from various nickel precursors and synthesis routes. Inset shows TCE degradation by monometallic Fe nanoparticles. Initial TCE concentration was 50 mg/L. Nanoparticle dose was 2 g/L.....	82
3.3. Effect of aging of Ni-Fe in solutions with (a) non or mildly-deactivating solutes and (b) strongly deactivating solutes on TCE degradation. Particles were prepared using co-reduction method (i.e., <i>CR</i> -Ni-Fe). Initial TCE concentration was 50 mg/L. Nanoparticle dose was 3.3 g/L. Initial pH was in the range of 8.1-8.3.	83
3.4. Products of TCE degradation by (a) fresh <i>CR</i> -Ni-Fe, (b) <i>CR</i> -Ni-Fe aged in 5 mM chloride, and (c) <i>CR</i> -Ni-Fe aged in 5 mM phosphate solutions. Nanoparticle dose was 2 g/L for (a) and 3.3 g/L for (b) and (c). Initial pH was 8.1 – 8.3.	85

3.5. Effect of sulfate concentration on TCE dechlorination by aged <i>CR-Ni-Fe</i> BNPs. Initial TCE concentration was 50 mg/L. Nanoparticle dose was 3.3 g/L. Initial pH was in the range of 8.1 -8.3.....	86
3.6. Effect of phosphate concentration on TCE dechlorination by <i>CR-Ni-Fe</i> BNPs. Solid lines denote particles that had aged in phosphate solutions prior to reacting with TCE. Dash line represents fresh Ni-Fe particles reacting in a solution containing both phosphate and TCE. Initial TCE concentration was 50 mg/L. Nanoparticle dose was 3.3 g/L. Initial pH was in the range of 8.1 -8.3.....	87
3.7. TCE degradation by fresh and aged Ni-Fe BNPs prepared via solution deposition method. The concentrations of background anions in the aging media were 5 mM. Initial TCE concentration was 50 mg/L. Nanoparticle dose was 3.3 g/L. Initial pH was in the range of 8.1 -8.3.....	88
3.8. XPS Ni 2p _{3/2} spectra of Ni-Fe BNPs prepared via co-reduction method. (a) As- synthesized particles, (b) as-synthesized particles after sputtering in XPS chamber with argon for 2.5 min, and (c) particles aged in DDI for 24 h.....	89
3.9. XPS Ni 2p _{3/2} spectra of Ni-Fe BNPs prepared via solution-deposition method. (a) As- synthesized particles, (b) as-synthesized particles after sputtering in XPS chamber with argon for 2.5 min, and (c) particles aged in a phosphate solution for 24 h.....	90
S3.1. Comparison of TCE degradation by monometallic iron nanoparticles in DDI and in 5 mM phosphate solution. Initial TCE concentration was 50 mg/L. Nanoparticle dose was 5 g/L.....	94
S3.2. TCE degradation by Ni-Fe BNPs prepared from various nickel precursors and aged in 1 mM NaCl solutions for 24 hours. Initial TCE concentration was 50 mg/L. Nanoparticle dose was 3.3 g/L. Initial pH was in the range of 8.1 -8.3.....	95
4.1. TCE dechlorination by fresh Ni-Fe BNPs ((a)-(b)) and those aged in different groundwater solutions for 24 h ((c)-(h)) and carbon isotope fractionation during TCE degradation. The dose of fresh CR-Ni-Fe BNPs and fresh SDP-Ni-Fe BNPs was 2 g/L. CR-Ni-Fe BNPs were used in all aqueous aging experiments. The dose of aged Ni-Fe BNPs was 3.3 g/L. The initial pH values of aging experiments and TCE dechlorination experiments were between 7.8-8.1.....	116
4.2. Rayleigh plot of different types of Ni-Fe BNPs. Experimental conditions were the same as those described in Figure 4.1. $f = [TCE]/[TCE_0]$ and $Q=R/R_0$ refer to Rayleigh model equation.....	118
4.3. TCE degradation by (a) fresh CR-Ni-Fe BNPs in D ₂ O or in H ₂ O, and by (b) nZVI in D ₂ O or in H ₂ O. Dose of Ni-Fe BNPs was 1 g/L, and dose of nZVI was 5 g/L. Initial pH was between 7.8-8.3 for each reactor batch.....	119
4.4. Fitting results of TCE dechlorination by Ni-Fe BNPs based on the kinetic model that TCE completely transforms to ethane via ethene as the only intermediate.....	120
4.5. Fitting results of TCE dechlorination by Ni-Fe BNPs based on the “dual pathways” model.....	121

4.6. TCE dechlorination by Ni-Fe BNPs aged in solutions with different concentrations of humic acid. The particle dose was 3.3 g/L. Initial pH was between 7.8-8.1.....	122
4.7. TCE dechlorination by Ni-Fe BNPs aged in dilute phosphate solutions (0.01 – 0.3 mM).....	123
4.8. TCE dechlorination by aged Ni-Fe BNPs aged in 1 mM and 5 mM phosphate solutions. Initial concentration of TCE was 50 mg/L. The particle dose was 3.3 g/L. Initial pH was between 7.8-8.1.....	124
5.1. (a) Reductive dechlorination of TCE by fresh Pd-Fe nanoparticles and (b) changes in $\delta^{13}\text{C}$ values of TCE and reaction products during the experiment. Nanoparticle dose was 1 g/L.....	149
5.2. (a) Reductive dechlorination of TCE by fresh Fe nanoparticles and (b) changes in $\delta^{13}\text{C}$ values of TCE and reaction products during the experiment. Nanoparticle dose was 4 g/L.....	150
5.3. TCE degradation by (a) fresh and moderately deactivated and (b) severely deactivated Pd-Fe nanoparticles. Aging was conducted by immersing freshly made Pd-Fe in various aqueous solutions for 24 h prior to TCE experiments. Initial TCE concentration was 50 mg/L. Dose of Pd-Fe was 1 g/L and 2 g/L for fresh and aged particles, respectively.....	151
5.4. Product distribution and carbon isotope fractionation during TCE degradation by Pd-Fe aged in the presence of (a) 20 mg/L humic acid, (b) 5 mM sulfite, (c) 5 mM phosphate, and (d) 5 mM sulfate. The initial pH of the aging solutions was in the range of 7.4 - 8.2.....	153
5.5. Product distribution and carbon isotope fractionation during TCE degradation by Pd-Fe aged in the presence of (a) distilled deionized water (DDI), (b) 5 mM chloride, (c) 1 mM carbonate, and (d) 1 mM nitrate. The initial pH of the aging solutions was in the range of 7.4 - 8.2.....	154
5.6. Proposed mechanisms for Pd-Fe BNP deactivation in different groundwater media. (i) Surface accumulation of iron oxidation products, (ii) direct poisoning of Pd catalyst, (iii) interaction of Fe surface with passivating anions inhibiting Fe corrosion and H ₂ production; and (iv) selective deactivation of hydrogenation sites.....	156
5.7. Isotope fractionation during TCE hydrodechlorination by freshly made monometallic Fe and Pd-Fe nanoparticles and fitting of the experiment data to the Raleigh model....	157
5.8. TCE degradation by Pd-Fe bimetallic nanoparticles aged in 5 mM Cl ⁻ solutions for 24 hours. Solid symbol: aged Pd-Fe without surface cleaning. Hollow symbol: aged Pd-Fe cleaned by sonicating in deionized water for 3 minutes before collection by vacuum filtration and subsequent use in TCE hydrodechlorination experiments. The results suggest that the initial degradation of TCE by the aged Pd-Fe without the ultrasound cleaning procedure was due to a limited amount of reactive hydrogen species accumulated on the Pd-Fe surface during aqueous aging. Removing the reactive hydrogen species by sonication renders the particles to be completely unreactive towards TCE..	158

5.9. Raleigh plots of isotope fractionation during TCE degradation by fresh and aged Fe or Pd-Fe bimetallic nanoparticles. To account for TCE adsorption to the solid phase, the first data point was not included and the fitted line was not forced to pass through zero. $f = [TCE]/[TCE_0]$, and $Q=R/R_0$	160
5.10. TCE degradation by Al_2O_3 -supported Pd. The particles were prepared by mixing a palladium acetate solution with α - Al_2O_3 particles for 30 min followed by H_2 purging for 30 min. Particles were immersed in various solutions for 24 h and were collected by filtration after aging. TCE experiment was performed by adding aged particles (dose of Pd at 14 mg/L) into a TCE solution ($C_0 = 50$ mg/L) amended with 2.5 g/L fresh iron nanoparticles as a hydrogen source.....	161
6.1. TCE dechlorination by sulfided nZVI (s-nZVI) prepared using different sulfur precursors. All particles were prepared using the “20-min post-synthesis sulfidation” method. The mole ratio of sulfur precursor to iron (S/Fe mole ratio) was fixed at 0.05. Initial TCE concentration was approximately 25 mg/L. Solid dose was at 5 g/L. Initial pH was between 7.8-8.1.....	180
6.2. Pathways for TCE reductive dechlorination by nZVI and S-nZVI.	181
6.3. TCE dechlorination by (a) nZVI, (b) S-nZVI prepared with sodium sulfide, (c) sodium dithionite, and (d) sodium thiosulfate, respectively. The “20-min post-synthesis sulfidation” method was used for (b) – (d). S/Fe mole ratio was fixed at 0.05. Initial TCE concentration was approximately 25 mg/L. Nanoparticles dose was at 5 g/L. Initial pH was between 7.8-8.1.....	182
6.4. Product formation during TCE dechlorination by S-nZVI prepared using the (a) “initial sulfidation” method (b) and “10-min post-synthesis sulfidation” method, respectively. All particles used sodium thiosulfate as the sulfur precursor. S/Fe mole ratio was fixed at 0.05. Nanoparticles dose was at 5 g/L. Initial pH was between 7.8-8.1....	200
6.5. TEM micrographs of S-nZVI prepared using the “initial sulfidation” method (labeled with “0 min”) and “20-min post-synthesis sulfidation” method (labeled with “20 min”), respectively. S/Fe mole ratio was at 0.05.	184
6.6. XPS S 2p _{3/2} spectra of S-nZVI prepared using (a) the “initial sulfidation” method and (b) “20-min post-synthesis sulfidation” method. Sodium thiosulfate was used as sulfur precursor, and S/Fe mole ratio was at 0.05	185
6.7. Impact of varying S/Fe mole ratio on TCE pseudo-first-order dechlorination rate constants. Nanoparticles were prepared using the “20-min post-synthesis sulfidation” method. Nanoparticles dose was at 5 g/L. Initial pH was between 7.8-8.1.....	186
6.8. Product formation during TCE dechlorination by S-nZVI prepared at an S/Fe mole ratio of (a) 0.5, (b) 0.0025, and (c) 0.00125, respectively. Nanoparticles dose was at 5 g/L. Initial pH was between 7.8-8.1	187
6.9. Total yield of C ₂ products (i.e., acetylene, ethene, and ethane) by S-nZVI prepared at different S/Fe mole ratios. Product yield was measured when approximately 90% of TCE was degraded. Nanoparticles dose was at 5 g/L. Initial pH was between 7.8-8.1.....	188

6.10. Acetylene hydrogenation by S-nZVI prepared at different S/Fe mole ratios. Initial acetylene concentration was 13 μ M. Nanoparticles dose was at 5 g/L. Initial pH was between 7.8-8.1.....	189
S6.1. X-ray diffraction patterns of S-nZVI (0 min), S-nZVI (20 min), S-nZVI (20 min) exposed to air for 1 week, and S-nZVI (20 min) aged in DDI water for 1 week. Sodium thiosulfate was used as sulfur precursor. S/Fe mole ratio was at 0.05. “Mag” refers to magnetite, and “ISH” refers to hydrous iron sulfate.....	193
S6.2. TCE dechlorination by Peerless TM iron filings prepared under different sulfidation conditions. TCE concentration was 25 mg/L. Particles dose was 10 g/L. Initial pH was between 7.8-8.1.....	194
S6.3. TCE dechlorination and major daughter product formation by S-Peerless TM iron filings. TCE concentration was 25 mg/L. Particles dose was 10 g/L. Initial pH was between 7.8-8.1.....	195
S6.4. TCE dechlorination and major daughter product formation by a physical mixture of amorphous iron sulfide and nZVI. TCE concentration was 25 mg/L. Dose of amorphous iron sulfide was 1 g/L, and dose of nZVI was 5 g/L. Initial pH was between 7.8-8.1...	196
7.1. Acetylene hydrogenation by (a) nZVI, and (b) S-nZVI. Sulfidation was conducted at an S/Fe ratio of 0.05. Insert shows the formation of longer hydrocarbons (sum of mole of C3, C4, C5 and C6 species detected in the reactor in terms of C2 mass balance). Initial mass of acetylene was 14 μ mol. Nanoparticles dose was at 5 g/L for two batches. Initial pH was between 7.8-8.1.....	221
7.2. Proposed acetylene hydrogenation pathways mediated by nZVI and S-nZVI. Longer hydrocarbons represent the sum of mole of C3, C4, C5 and C6 species detected in the reactor in terms of C2 mass balance.	222
7.3. PCE dechlorination by (a) nZVI, and (b) S-nZVI (S/Fe mole ratio at 0.05). Nanoparticles dose was at 5 g/L for each reaction batch. Initial pH was between 7.8-8.1.	223
7.4. PCE dechlorination by S-nZVI synthesized at different S/Fe mole ratios. Initial PCE mass was around 6 μ mol for each batch. Nanoparticles dose was 5 g/L. Initial pH was between 7.8-8.1.....	224
7.5. Yields of ethene and ethane upon dechlorination of different chlorinated ethenes by S-nZVI prepared at varied S/Fe mole ratios. Product yields were determined when 90% of parent compounds were consumed in the reaction system. Dose of particles was 5 g/L for each reaction batch. Initial pH was between 7.8-8.1.....	225
7.6. <i>trans</i> -DCE dechlorination by (a) nZVI, and (b) S-nZVI (S/Fe mole ratio at 0.05). Initial <i>trans</i> -DCE mass was 6 μ mol. Dose of particles was at 5 g/L. Initial pH was between 7.8-8.1.....	226
7.7. <i>cis</i> -DCE dechlorination by (a) nZVI, and (b) S-nZVI (S/Fe mole ratio at 0.05). Dose of particles was at 5 g/L. Initial pH was between 7.8-8.1.....	227

7.8. <i>cis</i> -DCE by S-nZVI synthesized at different S/Fe mole ratios. Initial <i>cis</i> -DCE mass was 6 μmol . Dose of particles was at 5 g/L. Initial pH was between 7.8-8.1.....	228
7.9. 1,1-DCE dechlorination by (a) nZVI, and (b) S-nZVI (S/Fe mole ratio at 0.05). Dose of particles was at 5 g/L. Initial pH was between 7.8-8.1.....	229
7.10. 1,1-DCE by S-nZVI synthesized at different S/Fe mole ratios. Dose of particles was at 5 g/L for each batch. Initial pH was between 7.8-8.1.....	230
7.11. Proposed reduction pathways of chlorinated ethene by nZVI and S-nZVI. For PCE reduction, because only minor quantity of TCE was formed, so a dash arrow was used to indicate TCE formation was only a minor pathway.....	231
7.12. Reduction of chlorinated ethenes by S-Peerless TM iron and Peerless TM iron after acid-wash treatment. (a) PCE, (b) TCE, (c) <i>cis</i> -DCE and (d) 1,1-DCE. Iron dose was 10 g/L for all batches. Initial pH was between 7.8-8.1.....	232
7.13. PCE, TCE and <i>cis</i> -DCE dechlorination rate constants by S-BASF TM iron and BASF TM iron pre-washed by HCl. The rate constant was calculated based on a pseudo-first-order kinetic model. Mass of initial PCE, TCE and <i>cis</i> -DCE was 6 μmol . Iron dose was 10 g/L. Initial pH was between 7.8-8.1.....	233
7.14. (a) TCE dechlorination rate constants by S-nZVI aged for 1 day and 1 month in aqueous solutions containing different groundwater solutes. (b) Comparison of aqueous aging effect on nZVI, S-nZVI and Pd-Fe BNPs. The pH of aging solutions and TCE solutions was between 7.8-8.1. nZVI and S-nZVI particles were dosed at 5 g/L, whereas Pd-Fe BNPs were used at 2 g/L.....	234
S7.1. PCE dechlorination by S-nZVI prepared at an S/Fe ratio of (a) 0.5 and (b) 0.00125, respectively. Nanoparticle dose was 5 g/L for each batch. Initial pH was between 7.8-8.1. For (b), PCE dechlorination and major products formation could not be fitted well with the kinetic model.....	239
S7.2. <i>trans</i> -DCE dechlorination by S-nZVI prepared at an S/Fe ratio at (a) 0.5, and (b) 0.00125, respectively. Nanoparticle dose was 5 g/L. Initial pH was between 7.8-8.1...	240
S7.3. <i>cis</i> -DCE dechlorination by S-nZVI prepared at an S/Fe ratio at (a) 0.5, and (b) 0.00125, respectively. Nanoparticle dose was 5 g/L. Initial pH was between 7.8-8.1...	241
S7.4. 1,1-DCE dechlorination by S-nZVI prepared at an S/Fe ratio at (a) 0.5, and (b) 0.00125, respectively. Nanoparticle dose was 5 g/L. Initial pH was between 7.8-8.1...	242
S7.5. XPS survey spectrum of as-received Peerless TM Fe.....	243
S7.6. (a) Reduction of <i>cis</i> -DCE by Cu-nZVI, S-nZVI and S-Cu-nZVI, and (b) products formation of <i>cis</i> -DCE dechlorination by Cu-nZVI. Mass of <i>cis</i> -DCE was 6 μmol . Nanoparticles dose was at 5 g/L. Initial pH was between 7.8-8.....	244
S7.7. TCE dechlorination by S-Peerless TM iron exposed to air for different amount of time. Particles dose was at 10 g/L. Initial pH was between 7.8-8.1.....	245

CHAPTER ONE

Introduction

1.1 Overview of Zero-valent Iron Technology Development

Zero-valent iron (ZVI) is one of the most prevalently used engineered materials for groundwater and soil remediation in the past three decades. Based on the particle size, ZVI materials are commonly divided into two categories, namely conventional ZVI (with particle size being tens of microns or larger), such as granular iron or iron filings, and nanoscale ZVI (nZVI, with particle size in the sub-100 nm range). In 1994, a study by Gillham and O'Hannesin first demonstrated that ZVI particles were able to degrade a variety of chlorinated alkanes and alkenes, and the degradation rates were three orders of magnitude higher than those of biotic degradation, indicating the potential application of ZVI for groundwater remediation ¹. In the following years, iron-based materials have been studied for treating different groundwater and wastewater contaminants, including chlorinated ethenes ^{2,3}, organophosphates ⁴, nitroamines ⁵, nitroaromatics ⁶, polybrominated diphenyl ethers ^{7,8}, chromium (VI) ⁹, arsenic (III) and (V) ^{10,11}, and nitrate ^{12,13}. The first field application of ZVI for treating trichloroethene (TCE) and perchloroethene (PCE) in the subsurface environment was reported in 1991 at Canadian Forces Base, Borden, Ontario, Canada ¹. Subsequently, the design of permeable reactive barriers (PRB) by filling a underground trench installed in the flow path of a contaminant plume with granular ZVI or a mixture of ZVI and aquifer material has been proposed based on the property of iron that can treat various groundwater contaminants, and the implementation of ZVI-PRB has been successful at many sites in the U.S. and Canada ¹⁴⁻¹⁶. In 2002, ZVI-PRB was designated as the standard plume treatment method by the US Environmental Protection Agency (US EPA), and more than 200 PRB treatment systems have been installed in US.

In 1997, Wang and Zhang first reported that nZVI could degrade trichloroethene (TCE) and polychlorinated biphenyls (PCBs) with significantly higher degradation rates than conventional ZVI ¹⁷. The contaminant removal mechanisms by nZVI are considered

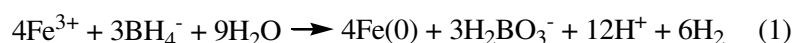
by many to be the same as with the conventional ZVI, while nZVI usually exhibits higher reaction rates due to size and surface area effects. It is generally accepted that because nZVI has a higher surface area compared to bulk ZVI, nZVI has higher adsorption capacities and reactivity^{15, 18}. Another advantage of nZVI is that nZVI can be used for remediation of a contamination source by directly injecting the particles in the form of aqueous colloidal suspension to a contamination zone. Although the use of ZVI particles in PRB has been proven as an effective technology for near surface plume treatment, conventional ZVI cannot be applied to direct injection in source zones, which means that it is not an option for targeted containment or destruction of contaminant source zones. Another critical limitation undermines the long-term effectiveness of ZVI-PRB technology is the high cost of installation of PRB and decreased permeability due to the formation of iron oxidation products and biofilm growth. nZVI, owing to the diminutive size, has been successfully applied for direct injection into subsurface to capture the contaminant source, rendering it a highly flexible remediation technology for treating contaminated sites with complicated hydro-geological characteristics^{14, 19}. Over the course of past 20 years, nZVI-based remediation technology has been developed into a widely used nanotechnology for environmental remediation. More than 50 pilot and full-scale implementations are deployed worldwide, and a considerable amount of research manuscripts have published^{14, 20}. To date, the vast majority of the pioneering nZVI field work was deployed in the U.S., and European countries, such as Czech Republic, Germany, Italy, and Slovakia, are also conducting 15 field work demonstrations that are either full-scale implementations completed or in process^{20, 21}. A pilot nZVI field test has been completed in Taiwan²², and there are several nZVI field projects being planned in China and other Asian countries.

1.2 Synthesis or Production Methods of ZVI Materials

Generally, commercial iron is placed in rotary kilns to burn off other non-metallic materials under a high temperature (700 - 1200°C), during which granular ZVI is produced²³. nZVI can be synthesized by either “bottom-up” or “top-down” approaches. The “bottom-up” approach refers to the physical or chemical methods to produce the

nanomaterial from basic building blocks¹⁷. The “top-down” indicates physical or chemical methods to breakdown or restructure a bulk material to nanoscale level particle²⁸.

The “bottom-up” approach usually involves the use of a strong reducing agent. The reduction of ferric or ferrous salt by sodium borohydride is the most widely studied method within academia^{17, 24, 25}. This method can produce highly reactive nZVI, and nZVI and nZVI-based materials used in this dissertation were synthesized following this method (Equation(1)):



However, this method is difficult to scale up to industrial scale production for two reasons: (1) the method is expensive due to the high cost of sodium borohydride, and (2) it involves several separation steps and produces a considerable amount of wastewater. In 2006, Toda Kogyo Ltd. developed a method of reducing iron oxides with hydrogen gas under a high temperature (between 350 - 600 °C)²⁶. In addition, carbothermal reduction of ferrous iron has recently been investigated as a potential low-cost alternative to prepare reactive nZVI. This method involves the use of the thermal energy and reducing gas formed (e.g., H₂) during the thermal decomposition of carbon-based materials (e.g., black carbon, hollow carbon, carbon nanoparticles) to drive the reduction of iron oxide nanoparticles²⁷. Because carbon-based materials have high surface area and are inexpensive, this technology represents a cost-effective method for nZVI production.

For the “top-down” approach, a precision ball-milling technique has been used to break down bulk iron materials into nanoscale particles. The ball-milling system usually uses stainless steel balls to grind the bulk iron materials. A previous study demonstrated that ball-milling technique is able to produce highly reactive nanoparticles²⁸. A leading nZVI supplier, Golder Associates Inc., has used this ball-milling method to produce nZVI in large quantities. The ball-milling technique takes less time and consumes less energy compared to the hydrogen reduction method, but this technique has less control of the particle size.

1.3 Characterization of ZVI

One noticeable difference between conventional ZVI and nZVI is the size of particles. Based on the previously published studies, the typical size of nZVI is much smaller than the size of commercial ZVI powder (e.g., PeerlessTM iron, FisherTM iron), but nZVI has a higher surface area. Table 1.1 summarizes the sizes and surface areas of some widely used ZVI and nZVI.

X-ray powder diffraction (XRD) and X-ray photoelectron spectroscopy (XPS) analyses have been extensively used to characterize the surface compositions of ZVI materials. Studies indicated that the as-purchased commercial ZVI contains Fe(0) covered with a discontinuous and highly disordered passivation layer of iron oxides. The formation of iron oxides layer is related to the ZVI manufacturing process. As indicated in Section 1.2, commercial granular ZVI is prepared in rotary kilns. After exposing to these gradually elevated temperatures, the iron is oxidized. Besides formation during the manufacturing process, iron oxides can also be formed due to spontaneous iron corrosion when ZVI is exposed to water (or moisture), or during the handling and storing processes. Therefore, the formation of iron oxide layer is an intrinsic property of iron materials.

Table 1.1. Commonly used commercial mZVI and nZVI size and surface area

Commercial microscale zero-valent iron			
Supplier	Size	Surface area	References
Ada Iron & Metal	1-10 mm	1.4 m ² /g	²⁹
Connelly GPM	0.25 - 2 mm	1.2 – 2.5 m ² /g	³⁰⁻³⁴
Master Builder	0.25 - 2 mm	1.1 - 1.5 m ² /g	^{29, 35, 36}
Peerless Iron	0.77 mm	0.87 m ² /g	³⁷
Fisher Scientific	0.15 mm	2.3 m ² /g	³⁸
BASF	< 10 mm	N.A.	
Nanoscale zero-valent iron			
Supplier	Size	Surface area	References
Toda Kogyo Corporation	70 nm	29 m ² /g	³⁸
Laboratory synthesized nZVI	10 – 100 nm	33.5 m ² /g	¹⁷

For nZVI, the structure of particles features an Fe(0) core covered with a surface layer of iron oxides, which is shown in Figure 1.1. This distinct structure of nZVI is commonly referred to as the *core-shell structure*. It has been demonstrated that nZVI synthesized using the laboratory borohydride method has a smooth amorphous oxide skin³⁹, whereas the nZVI prepared by the H₂ thermal reduction method is covered with crystalline oxide structures³⁸. The average thickness of the iron oxide layer on the freshly prepared nZVI is around 3 nm. The formation of iron oxide layer is a complicated process, and the structure, morphology and compositions of iron oxide layer are influenced by synthesis process and storage conditions, which will be introduced in Section 1.5.1. In addition, the core-shell structure of nZVI has a profound impact on contaminant removal mechanism and removal performance, which is discussed in Section 1.4.

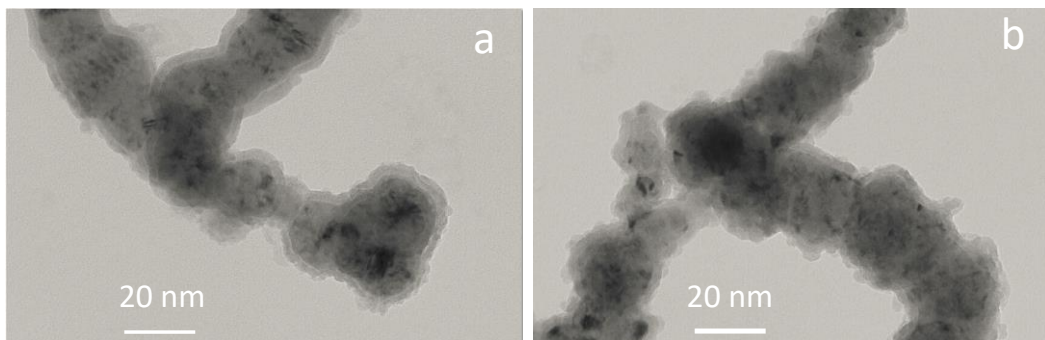


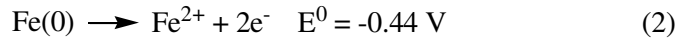
Figure 1.1. Transmission electron microscopy (TEM) images of nZVI synthesized in our lab. The operational voltage of TEM is 300 kV, and magnification is 200,000 times.

1.4 Reaction Mechanisms of ZVI with Common Contaminants

1.4.1 Reductive Dehalogenation by ZVI

One of the most successful engineering applications of ZVI materials is dehalogenation of aliphatic chlorinated contaminants in subsurface environments. Aqueous Fe(0) corrosion occurs spontaneously in water through an electrochemical mechanism, and this corrosion process involves Fe(0) dissolution owing to the corrosion of Fe(0) with the release of Fe²⁺ and electrons as shown in Equation (2) in the absence of dissolved oxygen⁴⁰. The half-reaction of dehalogenation of chlorinated contaminants is

shown in Equation (3), which has a standard reduction potential ranging from +0.5 V to +1.5 V in the neutral pH range⁴¹. Accordingly, a strong thermodynamic driving force can initiate the dehalogenation reaction by ZVI materials.



The mechanisms of iron-mediated dehalogenation reactions have been well studied. It is generally accepted that the reaction is heterogeneous in nature, involving adsorption of contaminants at the iron surface before the carbon-halogen bonds breakage⁴².

Specifically, this dissertation primarily focused on the reductive dechlorination of chlorinated ethenes by iron-based materials. Chlorinated ethenes, such as tetrachloroethene (PCE) and trichloroethene (TCE), are widespread groundwater and soil contaminants at US Superfund sites due to their extensive use as industrial solvents for extraction, spraying, cleaning, and degreasing⁴³⁻⁴⁵. PCE and TCE are reported to be toxic, carcinogenic, and mutagenic to human beings and animals⁴⁶, and they are also very recalcitrant to the natural attenuation process⁴⁷, therefore, removing PCE and TCE from subsurface has been a primary environmental challenge for decades. Besides PCE and TCE, *trans*-dichloroethene (*trans*-DCE), *cis*-dichloroethene (*cis*-DCE), 1,1-dichloroethene (1,1-DCE) and vinyl chloride (VC) are other common chlorinated contaminants detected in the subsurface environment⁴⁷⁻⁴⁹, and their accumulation is due to the incomplete degradation of parent compounds^{50, 51} or as intermediates during the abiotic remediation⁵²⁻⁵⁴. Furthermore, *cis*-DCE, 1,1-DCE and VC are more toxic, volatile, and difficult to remove^{48, 55} than the parent compounds PCE and TCE. Therefore, the development of effective remediation technologies to remove chlorinated ethenes from subsurface has been an active research field for decades.

The reductive dechlorination of chlorinated ethenes by ZVI has been extensively studied, and the dechlorination rates of chlorinated ethenes by nZVI were reported to be higher than that by conventional iron materials owing to the fact that nZVI has larger

specific surface areas¹⁷. The typical pathways of reduction of chlorinated ethenes are summarized in Figure 1.2 based on previous studies^{2, 56}.

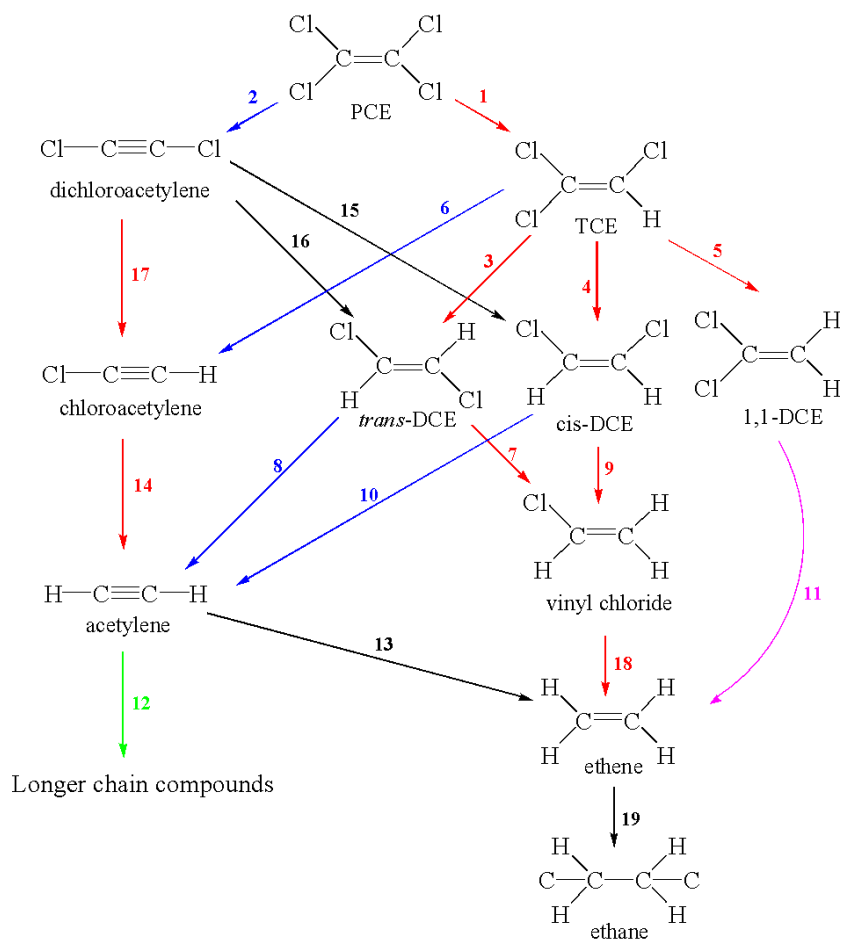


Figure 1.2. Chlorinated ethenes dechlorination pathway adapted from Arnold and Roberts².

The reactions 1, 3, 4, 5, 7, 9, 14, 17, and 18 correspond to hydrogenolysis reactions (that is, successive replacement of the chlorine substituents, one at a time, by hydrogen), while reactions 2, 6, 8, and 10 are reductive β-elimination reactions. Reductive elimination reaction is one form of dichlo-elimination, in which two chlorine substituents are lost simultaneously from one (α-elimination) or two adjacent (β-elimination) carbons. Reaction 11 proceeds via reductive α-elimination, with reactions 13, 15, 16, and 19 being hydrogenation reactions. As indicated in Figure 1.2, the dechlorination scheme includes hydrogenolysis, reductive elimination, and hydrogenation.

Previous studies have demonstrated that reductive β -elimination is the primary reductive pathway for PCE, TCE, *cis*-DCE, and *trans*-DCE^{2, 56}. Hydrogenolysis products were observed during the reduction of chlorinated ethenes (e.g., the formation of TCE during PCE reduction, and *cis*-DCE during TCE reduction) by ZVI materials, but studies have shown that the products of hydrogenolysis in general constitute a minor quantity compared to β -elimination products, suggesting that the β -elimination pathway is the primary reductive pathway for the reduction of PCE, TCE, *cis*-DCE, and *trans*-DCE by ZVI materials^{2, 57}. Degradation of chlorinated ethenes by other types of abiotic materials has been studied as well, and the results also indicated that the primary dechlorination route mainly follows the β -elimination pathway⁵⁸⁻⁶¹. Even though acetylene or chlorinated acetylenes are expected to be the intermediates of β -elimination, the accumulation of these two intermediates was rarely observed during the dechlorination processes^{2, 56}. Chlorinated acetylenes are extremely reactive and quickly decompose to acetylene, and acetylene can undergo coupling reactions on the metal surface⁶², therefore chlorinated acetylenes are usually below detection limits and are rarely reported to be accumulated and observed in PCE or TCE reduction reactions. Importantly, previous studies suggested that, ethane is produced from ethene during the hydrogenation process on iron materials^{2, 56}. However, as is discussed in Chapter 6 and 7 of this dissertation, we confirm that acetylene is the precursor of ethene, ethane, and other longer-chain hydrocarbon species (e.g., C3, C4, C5 and C6 species), while ethene is not an important precursor of ethane due to the very slow kinetics of ethene hydrogenation.

Compared to *trans*-DCE and *cis*-DCE, 1,1-DCE reduction by different types of ZVI materials shows different reductive elimination pathways. Besides the reported β -elimination pathway, Arnold and Roberts showed that the reduction of 1,1-DCE followed α -elimination based on the analysis of distribution of products when electrolytic iron was used, which involves alkylidene carbene or carbeniod as the intermediates².

The mechanisms of reductive dechlorination of chlorinated ethenes are different if different types of iron materials are used as the reducing agent. Johnson et al⁵⁷ has summarized the dechlorination rates of chlorinated ethenes by common commercial ZVI

and suggested that the reduction of chlorinated ethenes were under a thermodynamic control, meaning the dechlorination rates increase with an increasing degree of halogenation because chlorinated ethenes with more halogen substituents have higher reduction potentials⁵⁸. However, in a study by Arnold and Roberts, the reduction rates of chlorinated ethenes decreased remarkably with increasing halogenation, suggesting that the formation of di- σ -bonded surface intermediate is the rate-limiting step instead of thermodynamic control². Song and Carraway used laboratory synthesized nZVI to conduct the reduction of chlorinated ethenes and observed a similar trend as that by Arnold and Roberts, yet the reduction mechanism was attributed to the catalytic hydrogenation involving the activation of hydrogen on the surface⁶³. Another important point is that the reduction of chlorinated ethenes by ZVI materials is a slow process.

1.4.2 Reductive Dehalogenation by Bimetallic ZVI

Iron-based bimetallic nanoparticles (BNPs), prepared by doping a small amount of catalytic metals (e.g., Ni or Pd) on the nZVI surface, can significantly enhance chlorinated ethenes degradation rates compared to the unamended nZVI. Previous studies showed that fresh prepared Ni-Fe BNPs can increase the TCE degradation rate constant by up to three orders of magnitude⁶⁴, and Pd-Fe can enhance the degradation rate by a factor of 640 compared to the unamended nZVI⁶⁵. The addition of catalytic metal on nZVI can adsorb the hydrogen and generate active hydrogen species^{66, 67}. The detailed dehalogenation reactions by bimetallic iron-based nanoparticles can be summarized into three steps: (i) Fe(0) reacts with water to produce H₂, (ii) H₂ is adsorbed on the catalytic metal and active hydrogen species (atomic hydrogen or hydride) is formed from surface-catalyzed dissociation of H₂, and (iii) active hydrogen species initiate hydrodehalogenation of surface adsorbed halogenated contaminants. The reaction mechanisms for TCE hydrodechlorination by Pd-Fe are illustrated in Figure 1.3. In addition to increases in dehalogenation rates, another evident advantage of iron-based BNPs is their propensity to form more completely dehalogenated hydrocarbons, which greatly circumvents the accumulation of toxic intermediates (e.g., VC)⁶⁷⁻⁶⁹. However, iron-based BNPs usually exhibit rapid reactivity decline in the aqueous environment due

to the higher rates of iron oxidation⁷⁰ and solute-induced catalyst deactivation^{64, 65}, which are two serious drawbacks limiting the application of iron-based BNPs for groundwater remediation.

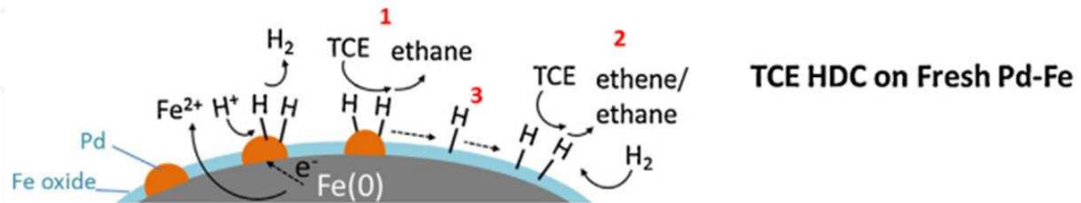


Figure 1.3. The mechanisms of TCE dechlorination by nZVI and Pd-Fe BNPs.

1.4.3 Sequestration of Inorganic Contaminants

In addition to halogenated hydrocarbons, ZVI has been applied to treating a variety of inorganic contaminants in groundwater, including heavy metals^{71, 72}, As(III)⁷³ and As(V)⁷³, Cr(VI)⁷⁴, and nitrate⁷⁵.

1.4.3.1 Metal Ions

ZVI can effectively remove a variety of metal ions in the aqueous environment, in which both Fe(0) core and the iron oxides on ZVI materials are involved in sequestering different types of metal ions. For the metal ions with more positive reduction potentials than Fe(0) (e.g., Cu(II)⁷⁶, and Hg(II)⁷⁷), the removal of metal ions by ZVI generally relies on the redox principle, in which species with more positive reduction potential than Fe(0) ($E_H^{\circ} = -0.41$ V) would be sequestered in their reduced states. Metal ions with reduction potentials similar to or more negative than that of Fe(0) (such as Zn(II) and Cd(II)⁷⁷) are retained by adsorption onto the iron oxide shell. Metal ions with E_H° slightly more positive than that of Fe(0) (e.g., Ni(II) and Pd(II)⁷⁷) could be immobilized at the nZVI surface by both sorption and reduction. Additionally, the release of hydroxyl ions due to iron corrosion also favors the formation of metal-Fe hydroxide (co)-precipitates. Therefore, the unique structure of ZVI materials enables the ZVI to be a multi-functional remediation agent for heavy metals' removal.

1.4.3.2 Arsenite and Arsenate

Arsenic (As) exists in groundwater predominantly as inorganic arsenite (As(III), mainly as H_3AsO_3) and arsenate (As (V), mainly as H_2AsO_4^- or HAsO_4^{2-} at an environmentally relevant pH)⁷⁸. The existence of As(III) in groundwater is a serious threat for safe drinking water supply due to its higher toxicity⁷⁹ and higher mobility⁸⁰ in aquifers than As(V) species. It is important to develop effective treatment methods to remove As(III) from subsurface environments. ZVI technology has been demonstrated as an effective treatment process, which can rapidly achieve the removal of As(III) and As(V) in the subsurface⁸¹⁻⁸⁴. The As(III) removal mechanisms are related to iron the oxide layer on the ZVI surface. Previous research has demonstrated that As(III) could spontaneously adsorb and co-precipitate on the iron oxide layer of ZVI because iron oxides have a high affinity for As(III) in the neutral pH range⁷³. The sequestration of As(III) on nZVI is more complicated compared to the process on bulk ZVI, and the core-shell structure of nZVI plays a key role for As(III) removal, which involves adsorption, simultaneous oxidation and reduction, and intra-particle translocation. In general, oxidation of As(III) occurs at the iron oxide shell, while the reduction of As(III) takes place within the solid matrix of the particles close to the Fe(0) core of nZVI, entailing the diffusion of As(III) through the iron oxide layer to form an As-Fe intermetallic phase adjacent to Fe(0)^{11, 85}. Accordingly, arsenic has been observed to exist in a multi-layered fashion within nZVI⁸⁶.

1.4.3.3 Hexavalent Chromium

Hexavalent chromium (Cr(VI)) is another common groundwater contaminant due to its widespread use in metallurgy, chemical synthesis, and wood preserving industries⁸⁷. Cr(VI) is extremely toxic to human beings⁸⁸, and is highly mobile in groundwater because it does not sorb appreciably to soil minerals⁸⁹. Cr(III) is relatively nontoxic and is sparingly soluble at neutral pH. The removal of Cr(VI) by ZVI mainly involves the reduction of Cr(VI) to Cr(III) as Cr(III) hydroxide or mixed Cr(III)-Fe(III) hydroxides on Fe(0) surface^{37, 74}.

1.4.3.4 Nitrate

Nitrate is a common contaminant detected in surface water, groundwater, and industrial and agricultural wastewater. Nitrate can transform to nitrite, and nitrite may hinder oxygen from combining with hemoglobin resulting in serious toxicity⁹⁰, and nitrate can also cause eutrophication when exposed to an ecosystem⁹¹. Fe(0) is an electron donor that can initiate the nitrate reduction based on the redox reaction principle¹². Several published studies outlined some promising applications of nZVI for nitrate reduction in groundwater⁹²⁻⁹⁴, yet nitrate is a strong passivating agent, and the reaction of ZVI with nitrate at a high concentration can result in diminished reactivity of ZVI, which limits the application of iron materials for nitrate removal^{24, 95}.

1.5 Limitations of ZVI technology

1.5.1 Passivation of ZVI

One serious technical limitation of ZVI technology is formation of a passivation layer on the ZVI surface, which is inevitable for both bulk ZVI and nZVI. The formation of iron oxide could occur during iron manufacturing, handling, and storage, and the application of ZVI in aqueous environment inevitably leads to the formation of iron oxides. Many factors may influence the morphology, structure, and composition of iron corrosion products. As indicated in a Section 1.4.1, the removal of contaminants by ZVI involves the transfer of electrons and Fe(0) corrosion. It is generally acknowledged that the corrosion of Fe(0) leads to the release of Fe²⁺^{1, 41, 96}. Fe²⁺ may hydrolyze to form Fe(OH)₂ on the Fe(0) surface under anaerobic conditions⁴⁰. Magnetite (Fe₃O₄) may then be formed due to the oxidation of Fe(OH)₂. Mixed Fe(II)/Fe(III) oxides (*e.g.*, green rusts), as the intermediate to the formation of magnetite, may form under neutral pH conditions⁴⁰. Green rusts are stable under low redox potentials only, and their oxidation commonly can lead to the formation of maghemite (γ -Fe₂O₃) or lepidocrocite. Maghemite formation over lepidocrocite occurs due to dihydroxylation of the green rusts phase under slow oxidation condition. Maghemite has the same inverse spinel structure as magnetite but contains only Fe(III)⁴⁰. Besides the formation of iron oxides on the ZVI surface during ZVI corrosion in the water, commercial ZVI is usually covered with a discontinuous

passivation layer, the formation of which might be owing to the manufacturing, handling, or storing process^{14, 28, 39, 76}. The existence of a passivation layer on ZVI surface has a large influence on the extent and mechanisms of contaminant removal and the reaction rates. Batch reactions, column tests, and field studies have confirmed that the reactivity of ZVI decreased over time due to formation of iron oxide layers on the nZVI surface caused by the corrosion products^{22, 54, 95}.

Also, interactions of ZVI materials with common groundwater constituents may affect the longevity of ZVI for groundwater remediation. Common inorganic anions in groundwater including Cl⁻, SO₄²⁻, HCO₃⁻, phosphate, and NO₃⁻, silica and natural organic matters (NOM) can affect the reactivity of iron particles. Phosphate and NO₃⁻ are particularly important because they can significantly undermine iron longevity and reactivity⁷⁵. Even if generally low concentration in pristine groundwater, phosphate species may exist in a contaminated aquifer because of their functions to enhance bioremediation⁹⁷. Noticeable changes in the reactivity of ZVI have been reported when exposing these groundwater solutes^{54, 98, 99}. Possible mechanisms for solute effects on the reactivity of ZVI can be attributed to the following reasons: (i) competition for reactive sites by Fe(0)-reducible solutes that leads to the exhaustion of available reactive sites on Fe(0) surface (e.g., NO₃⁻)^{54, 100}, (ii) formation of oxide layer that covers on the ZVI surface and thereby blocks access to reactive sites available Fe(0) sites on ZVI surface (e.g., HCO₃⁻, SO₄²⁻, phosphate, silica, NOM^{75, 98, 99, 101}), or (iii) dissolution of the iron oxide layer that results in increased reactivity (e.g., Cl⁻, HCO₃⁻, SO₄²⁻^{98, 101, 102}). Reported by Liu ang Lowry⁹⁵, common groundwater anions (5mN) had a minor effect on H₂ evolution but inhibited TCE reduction up to 7-fold in increasing order of Cl⁻ < SO₄²⁻ < HCO₃⁻ < phosphate. With nitrate at less than 1mM, a significant negative effect on H₂ evolution was noticed, but did not affect TCE dechlorination rate. While in the presence of 5 mM of NO₃⁻, TCE dechlorination and H₂ evolution ceased to occur⁹⁵.

1.5.2 Passivation and Deactivation of Iron-based Bimetallic Materials

Iron-based BNPs showed great degradation reactivity towards halogenated contaminants as introduced in Section 1.4.2. However, chemical stability of BNPs in

complex groundwater media is a crucial consideration in assessing the feasibility of this remediation technology in actual field applications. While most of the prior studies employed freshly synthesized Ni-Fe and Pd-Fe nanoparticles, a clear understanding of the effect of background constituents in groundwater on particle reactivity is not available thus far. An interesting contrast among different iron-based BNPs is that the deactivation behavior of Pd-amended iron nanoparticles (Pd-Fe BNPs) is expected to differ significantly from that of Ni-Fe BNPs due to the intrinsic differences in their electrochemical properties and in the chemical speciation of the additive metals in the presence of the iron material. Previous studies have observed rapid deactivation of Pd-amended BNPs in simple aqueous media without salt amendment^{70, 95}. With aberration-corrected analytical electron microscopic characterizations, it was reported that the Pd-Fe particles experienced pronounced oxidation of the zerovalent iron, and the Pd(0) sites originally present on the outer surface of the nanoparticles were engulfed by an extensive matrix of iron oxide after 24 h of immersion in an aqueous solution⁷⁰. In comparison, monometallic iron nanoparticles were able to retain a significant fraction of the Fe(0) component for over a month in deoxygenated waters¹⁰³. The excessively fast corrosion occurring in the case of Pd-Fe can cause loss of Fe(0) to unproductive reaction with water, leaving no stable form of reductant in the soil media for sustained contaminant reduction. Pd is also known to be strongly deactivated by groundwater constituents such as dissolved organic matter and reduced sulfur ligands¹⁰⁴. Although the rapid deactivation of Pd-Fe BNPs observed in simple laboratory reaction media may be alleviated to some degree in real groundwater media owing to background solutes serving as corrosion inhibitors (e.g. dissolved silica), the intrinsic material instability of Pd-Fe in aqueous solutions will remain a significant barrier when promulgating the BNP technology to large-scale field applications. Compared to palladium ($E_{H,Pd(II)/Pd(0)}^{\circ} = 0.92$ V), the standard reduction potential of nickel ($E_{H,Ni(II)/Ni(0)}^{\circ} = -0.28$ V) is close to that of iron ($E_{H,Fe(II)/Fe(0)}^{\circ} = -0.44$ V) (Bard et al. 1985), and one would expect that galvanic effect would play a less important role in the deactivation of Ni-Fe BNPs. Furthermore, in solutions where a strongly reducing environment cannot be established (e.g. when Fe(0)

is limiting or in the presence of background oxidants), a sizable fraction of nickel may present as Ni(II) on the particle surface. This suggests that the chemical stability of surface nickel sites would be markedly different from those of Pd material. Prior studies have noted that Ni-Fe BNPs endured repeated cycles of reactions without significant loss of reactivity⁶⁸. However, as these studies were conducted in simple solutions without electrolytes, a detailed investigation to look at the effect of common background solutes on the deactivation of Ni-Fe nanoparticles is warranted.

1.5.3 Effective Delivery of nZVI to Contaminant Sources

As indicated in Section 1.1, nZVI can be directly injected into the subsurface to treat contaminant source zones. However, unmodified nZVI is inclined to undergo self-aggregation due to the high surface energy and strong magnetic properties¹⁰⁵, which limits the mobility of nZVI in the subsurface. This is another serious technical limitation of nZVI for subsurface remediation. Elliott and Zhang demonstrated that most nZVI injected into the subsurface would rapidly deposit on the well screen and the remaining nZVI would only move a few feet before they become completely immobilized^{106, 107}. Another field study also demonstrated that nZVI particles tend to agglomerate rapidly after injection, clogging pores, and limiting migration. This agglomeration, along with the rapid corrosion of nZVI, can lead to contaminant flow bypassing the iron material resulting in limited contaminant degradation¹⁰⁸. Strategies to overcome the agglomeration of nZVI have been developed, including coating nZVI surface with polymers, and dispersing the particles in oil-water emulsions to prepare emulsified nZVI.

Coating of nZVI with polymers can prevent nZVI agglomeration¹⁰⁹, enhance transport in porous media¹¹⁰⁻¹¹², and facilitate targeted delivery to contaminants¹¹³. Adsorbed polymers can produce electrosteric repulsions and mitigate the magnetic and van der Waals attractions between nanoparticles, thereby providing the driving forces to counter agglomeration and facilitating the mobility of nanoparticles in the porous media¹¹⁴. Among different types of polymers, carboxymethylcellulose (CMC) and polyacrylic acid (PAA) have been extensively studied, because studies have shown that these two polymers could enhance the transport of nanoparticles to the contaminant zones

based on the results of field tests. Bennett et al.¹¹⁵ conducted field test by injecting CMC-nZVI into the aquifer contaminated with TCE and proved that nZVI coated with CMC were more mobile in the aquifer. He et al.¹¹⁶⁻¹¹⁸ conducted a pilot-test using Pd-Fe BNPs coated with CMC and showed that the delivery of nanoparticles to the source zones could be enhanced, which resulted in increased PCE and TCE dechlorination. A field study demonstrated a successful application of nZVI coated with PAA to treat VC²². One important finding based on the field tests indicated that reactivity of polymer-coated-nZVI decreased over time, yet the biotic process was boosted over the long run because the polymer could serve as an electron donor¹¹⁸. Besides CMC and PAA, several other types of polymers were studied, such as natural organic matter (NOM)¹¹⁹, polystyrene sulfonate (PSS)^{114, 120}, polyaspartate (PAP)^{120, 125}, and laboratory column tests showed that these polymers all could enhance the particles delivery.

Emulsified nZVI is another method to enhance the target nZVI delivery to contaminant source zones. Emulsified nZVI is prepared by dispensing the nZVI in the emulsified suspensions, which are composed of food-grade surfactant, biodegradable vegetable oil, and water¹²¹. Field tests have shown enhanced delivery effects of emulsified nZVI¹²¹⁻¹²³. Similar field results were obtained compared to those from polymer coated nZVI¹²⁴. The emulsified nZVI could somehow enhance the bioremediation process in the subsurface based on long term monitoring, suggesting that the oil and surfactant served as the electron donors for the bacteria in the subsurface.

1.6 Reductive Dechlorination of Chlorinated Ethenes by Iron Sulfide Materials

1.6.1 Iron Sulfide Minerals Formation in the Natural Systems

Iron sulfides are ubiquitous in the subsurface environments, and they are redox-active minerals that can be formed under anaerobic conditions in natural environments and engineered systems for groundwater remediation⁶⁰. Iron sulfides species found in natural environments are generally amorphous Fe(II) monosulfide (FeS_{am}), mackinawite (tetragonal FeS), greigite (Fe_3S_4), and pyrite (FeS_2)⁶⁰. Disordered mackinawite (or FeS_{am}) is usually the first iron sulfide phase generated during reaction between aqueous Fe^{2+} and S^{2-} under ambient conditions¹²⁵. Pyrite is widely found in natural environments, such as

coastal sediments¹²⁶, wetlands¹²⁷, aquifers¹²⁸, and soils¹²⁹. The transformation kinetics of mackinawite to pyrite relies on different factors, such as the rate of hydrogen sulfide formation, availability of reactive iron, metabolizable organic matter, and oxidants¹³⁰. Research has suggested that the sulfate-reducing microorganisms play an important role for the mackinawite-to-pyrite transformation compared to other factors^{131, 132}. Besides mackinawite and pyrite, the formation mechanisms of other iron sulfide minerals were widely studied as well. FeS can transform to Fe₃S₄ and FeS₂ through either biotic or abiotic pathways¹³⁰. Greigite is the sulfur analogue of magnetite, which has a similar structure as inverse spinel. The greigite structure can be considered as a cubic, close-packed array of S atoms connected by smaller Fe atoms¹²⁵. The transformation from mackinawite to greigite happens during an oxidation process¹³³. Studies also have shown that some bacteria form intracellular nanoscale level crystals of greigite (Fe₃S₄), and the precursors could be nonmagnetic mackinawite (tetragonal FeS) or cubic FeS^{134, 135}.

1.6.2 Remediation of Chlorinated Ethenes by Iron Sulfides or Sulfide-modified Iron

Iron sulfides draw attention as reducing agents for chlorinated ethenes, and extensive studies have been conducted. Abiotic transformation of TCE and PCE by iron sulfides has been evaluated using pyrite (FeS₂)¹³⁶⁻¹⁴⁰ and mackinawite (FeS)^{59, 140-142}. These studies have shown that iron sulfide materials are able to degrade TCE and PCE, but dechlorination rates by various iron sulfides are exceedingly slow compared to ZVI materials. The major product is acetylene instead of the more saturated hydrocarbons such as ethene and ethane produced in ZVI systems^{59, 141-144}.

In addition to their occurrence in natural environments, iron sulfides can be synthesized in the laboratory. The most common approach to synthesize iron sulfides is via the co-precipitation of Fe(II) and sulfide ions to form FeS in the aqueous phase under an anoxic condition. Different types of ferrous (FeSO₄, FeCl₂) and sulfide salts (Na₂S, NaHS) have been used to prepare laboratory-synthesized iron sulfide^{30, 59, 60}.

In recent years, a new biphasic structure of “Fe/FeS” nanoparticle showed great reactivity on TCE dechlorination compared to unamended nZVI. Kim et al¹⁴⁵ synthesized “Fe/FeS” nanoparticles by adapting the common borohydride reduction

method with the co-addition of sodium dithionite, a reducing agent used widely in research and industrial applications¹⁴⁶. TCE dechlorination experiments with this biphasic “Fe/FeS” nanoparticles indicated that “Fe/FeS” nanoparticles have good electrical conductivity and better magnetic properties compared to unamend nZVI, which might be the possible reasons for enhanced TCE reductive dechlorination. This argument is consistent with the fact that iron sulfide is a good semi-conductor¹⁴⁷⁻¹⁵¹, which might facilitate electron transfer to the nZVI surface. A recent published paper presented that sodium sulfide can also be used as a sulfidation agent to prepare highly reactive sulfided nZVI to enhance TCE dechlorination¹⁵². The author proposed that electrons are effectively conducted through an iron sulfide layer from Fe(0) core, the latter serving as the electron source, to TCE. However, no other explanations have been made to account for the enhanced dechlorination effects of sulfided iron, and the details concerning reaction pathways and product distribution have not been systematically examined so far.

1.7 Stable Isotope Fractionation Analysis for Environmental Monitoring

Monitoring stable isotope fractionation of contaminants is a new tool for assessing contaminant attenuation in natural environments. Stable isotope fractionations of contaminants are mainly determined by compound specific stable isotope analysis (CSIA), which is measured with a gas chromatography isotope ratio mass spectrometer (GC-IRMS). This new analytical method has been used to gain direct evidences of *in situ* biochemical/chemical degradation, including quantifying the extent of different types of remediation process and diagnosing the nature of degradation process (e.g., biotic or abiotic). The isotope signatures of common groundwater contaminants during the biotic or abiotic remediation process have been studied, such as tetrachloroethene¹⁵³⁻¹⁵⁵, trichloroethene^{153, 156-158}, 1,1,2,2-tetrachloroethane¹⁵⁹, MTBE^{160, 161}, carbon tetrachloride¹⁶², chloroform¹⁶³, monochlorobenzene and 1,2,4-trichlorobenzene¹⁶⁴.

The kinetic isotope effect associated with chemical and biochemical reactions is the key principle to monitor organic contaminant degradation. In general, chemical bonds are broken more easily if they contain a light isotope. In other words, molecules with

heavy isotopes experience slower bond breakage, and thus the heavy isotope tends to accumulate in the remaining parent compounds while the daughter products are more enriched with the lighter isotope. However, if the degradation of contaminants is caused by physical processes (e.g., sorption, volatilization, diffusion), the isotope effect is associated with negligible isotope fractionation^{165, 166}.

In CSIA, the carbon isotope signature is determined by measuring two stable isotopes of ¹²C and ¹³C, which yield a $\delta^{13}\text{C}$ value as expressed in Equation (4):

$$\delta^{13}\text{C} \text{ (unit of ‰)} = \left(\frac{R_{\text{sample}}}{R_{\text{standard}}} - 1 \right) \times 1000 \quad (4)$$

where R_{sample} is the ¹³C/¹²C ratio in a given sample and R_{standard} is the ¹³C/¹²C ratio in the international standard reference material-Vienna Pee Dee Belemnite (VPDB). For many organic contaminants, the relationship between isotopic fractionation and the extent of degradation can be modeled by the Rayleigh model¹⁶⁷. The Rayleigh model assumes constant isotope fractionation during degradation that is represented by the fractionation factor α . α relates the isotopic composition of a substrate at a given time, R , to the initial isotopic composition, R_0 , and to the fraction of substrate remaining, f , through Equation (5):

$$\frac{R}{R_0} = f^{(\alpha-1)} \quad (5)$$

The α value is directly equivalent to the inverse kinetic isotope effect at the reactive site (Equation (6)), and can also be expressed as an enrichment factor, ϵ , as in Equation (7):

$$\alpha = \frac{h_k}{l_k} \quad (6)$$

$$\epsilon = 1000 \times (\alpha - 1) \quad (7)$$

where ^lk and ^hk refer to the rate constants for bond cleavage involving the bond containing the lighter and heavier isotopes, respectively, and ^hk/k defines the kinetic isotope effect (KIE). Isotope enrichment factor (ϵ) is a function of the bonds broken during degradation and has been shown to be a powerful tool for diagnosing reaction

mechanisms¹⁵³, pathways¹⁶⁸, and enzyme kinetics¹⁶⁹ in biochemical reactions. However, in the consideration that Rayleigh model represents the overall isotope fractionation for the whole reaction and assumes the reaction itself as the rate-limiting step, it may not reflect the intrinsic isotope effect of a reaction which involves multiple steps where previous steps before the chemical reaction such as adsorption of a substrate to a reactive site are rate-limiting step. Therefore, for the chemical reactions on BNP surfaces, the combination of CSIA analysis and distribution of products results would gain profound insight on the catalytic reaction mechanisms as well as the deactivation mechanisms when are exposed the BNPs to the aquifer media.

1.8 Research Objectives

As mentioned in the previous sections, two major concerns have emerged from laboratory and field studies regarding the application of ZVI technology: (1) The reduction rates for chlorinated ethenes by ZVI materials in the absence of catalyst metals are relatively slow, and (2) ZVI materials tend to experience rapid reactivity loss due to the formation of passivation layers, which is an intrinsic property of ZVI materials. Iron-based BNPs, such as Ni-Fe BNPs or Pd-Fe BNPs, are highly reactive when they are freshly made and are used in simple aqueous solutions. Few studies have been conducted to investigate the deactivation mechanisms of groundwater constituents on the BNPs. The thorough understanding on the particles deactivation mechanisms by different groundwater constituents can help predict the potential influences of different groundwater solutes in the subsurface environments when BNPs are used for remediation. Accordingly, new surface treatment methods to minimize the negative influence of the passivation layers can lead to the effective application of ZVI materials to in situ groundwater remediation.

The overarching objectives of this dissertation are to understand the deactivation of BNPs in different groundwater matrices and to develop a class of iron-based materials with improved reactivity and longevity for remediation of chlorinated ethenes to address the problems mentioned above. The main body of this dissertation is composed of a series of studies focusing on the following specific research objectives.

- Optimize laboratory synthesis protocol to obtain reactive nZVI and develop facile methods to evaluate its reactivity (Chapter II, and this paper has been published in *Frontiers of Environmental Science and Technology*).
- Investigate the deactivation behavior of Ni-Fe BNPs in groundwater matrices through a combination of aqueous experiments and material and surface characterizations (Chapter III, published in *Water Research*) and examine the deactivation mechanisms of Ni-Fe BNPs through kinetic modeling and stable isotope fractionation analyses (Chapter IV, about to be submitted to *Chemosphere*).
- Investigate the deactivation mechanisms of Pd-Fe BNPs in groundwater matrices based on kinetics, production distribution, and stable isotope fractionation analyses (Chapter V, Published in *Applied Catalysis B: Environmental*).
- Develop a facile surface sulfidation method to prepare ZVI with enhanced reactivity for TCE dechlorination and investigate the mechanisms of sulfur-enhanced dechlorination on TCE reduction (Chapter VI, to be submitted to *Environmental Science and Technology*).
- Evaluate the applicability and stability of surface sulfidation treatment for different forms of ZVI (including both laboratory prepared nZVI and commercial ZVI products) in degrading various chlorinated ethenes in ambient and groundwater environments (Chapter VII, to be submitted to *Environmental Science and Technology*).

References

1. Gillham, R. W.; Ohannesian, S. F., ENHANCED DEGRADATION OF HALOGENATED ALIPHATICS BY ZERO-VALENT IRON. *Ground Water* **1994**, *32*, (6), 958-967.
2. Arnold, W. A.; Roberts, A. L., Pathways and kinetics of chlorinated ethylene and chlorinated acetylene reaction with Fe(O) particles. *Environmental Science & Technology* **2000**, *34*, (9), 1794-1805.
3. Comba, S.; Di Molfetta, A.; Sethi, R., A Comparison Between Field Applications of Nano-, Micro-, and Millimetric Zero-Valent Iron for the Remediation of Contaminated Aquifers. *Water Air and Soil Pollution* **2011**, *215*, (1-4), 595-607.

4. Ambashta, R. D.; Repo, E.; Sillanpaa, M., Degradation of Tributyl Phosphate Using Nanopowders of Iron and Iron-Nickel under the Influence of a Static Magnetic Field. *Industrial & Engineering Chemistry Research* **2011**, *50*, (21), 11771-11777.
5. Naja, G.; Halasz, A.; Thiboutot, S.; Ampleman, G.; Hawari, J., Degradation of hexahydro-1,3,5-trinitro-1,15-triazine (RDX) using zerovalent iron nanoparticles. *Environmental Science & Technology* **2008**, *42*, (12), 4364-4370.
6. Zhang, X.; Lin, Y.-M.; Chen, Z.-l., 2,4,6-Trinitrotoluene reduction kinetics in aqueous solution using nanoscale zero-valent iron. *Journal of Hazardous Materials* **2009**, *165*, (1-3), 923-927.
7. Kim, Y.-M.; Murugesan, K.; Chang, Y.-Y.; Kim, E.-J.; Chang, Y.-S., Degradation of polybrominated diphenyl ethers by a sequential treatment with nanoscale zero valent iron and aerobic biodegradation. *Journal of Chemical Technology and Biotechnology* **2012**, *87*, (2), 216-224.
8. Li, A.; Tai, C.; Zhao, Z.; Wang, Y.; Zhang, Q.; Jiang, G.; Hu, J., Debromination of decabrominated diphenyl ether by resin-bound iron nanoparticles. *Environmental Science & Technology* **2007**, *41*, (19), 6841-6846.
9. Wilkin, R. T.; Su, C.; Ford, R. G.; Paul, C. J., Chromium-Removal Processes during Groundwater Remediation by a Zerovalent Iron Permeable Reactive Barrier. *Environmental Science & Technology* **2005**, *39*, (12), 4599-4605.
10. Rahmani, A. R.; Ghaffari, H. R.; Samadi, M. T., A COMPARATIVE STUDY ON ARSENIC (III) REMOVAL FROM AQUEOUS SOLUTION USING NANO AND MICRO SIZED ZERO-VALENT IRON. *Iranian Journal of Environmental Health Science & Engineering* **2011**, *8*, (2), 175-180.
11. Ramos, M. A. V.; Yan, W.; Li, X.-q.; Koel, B. E.; Zhang, W.-x., Simultaneous Oxidation and Reduction of Arsenic by Zero-Valent Iron Nanoparticles: Understanding the Significance of the Core-Shell Structure. *Journal of Physical Chemistry C* **2009**, *113*, (33), 14591-14594.
12. Huang, Y. H.; Zhang, T. C., Kinetics of nitrate reduction by iron at near neutral pH. *Journal of Environmental Engineering* **2002**, *128*, (7), 604-611.
13. Chen, Y.-M.; Li, C.-W.; Chen, S.-S., Fluidized zero valent iron bed reactor for nitrate removal. *Chemosphere* **2005**, *59*, (6), 753-759.
14. Li, X.-q.; Elliott, D. W.; Zhang, W.-x., Zero-valent iron nanoparticles for abatement of environmental pollutants: Materials and engineering aspects. *Critical Reviews in Solid State and Materials Sciences* **2006**, *31*, (4), 111-122.
15. Wadley, S. L. S.; Gillham, R. W.; Gui, L., Remediation of DNAPL source zones with granular iron: Laboratory and field tests. *Ground Water* **2005**, *43*, (1), 9-18.
16. Gillham, R. W.; Vogan, J.; Gui, L.; Duchene, M.; Son, J., Iron barrier walls for chlorinated solvent remediation. In *In situ remediation of chlorinated solvent plumes*, Springer: 2010; pp 537-571.

17. Wang, C.-B.; Zhang, W.-x., Synthesizing Nanoscale Iron Particles for Rapid and Complete Dechlorination of TCE and PCBs. *Environmental Science & Technology* **1997**, *31*, (7), 2154-2156.
18. Choe, S.; Lee, S. H.; Chang, Y. Y.; Hwang, K. Y.; Khim, J., Rapid reductive destruction of hazardous organic compounds by nanoscale Fe-0. *Chemosphere* **2001**, *42*, (4), 367-372.
19. Tratnyek, P. G.; Johnson, R. L., Nanotechnologies for environmental cleanup. *Nano Today* **2006**, *1*, (2), 44-48.
20. Mueller, N. C.; Braun, J.; Bruns, J.; Cernik, M.; Rissing, P.; Rickerby, D.; Nowack, B., Application of nanoscale zero valent iron (NZVI) for groundwater remediation in Europe. *Environmental Science and Pollution Research International* **2012**, *19*, (2), 550-558.
21. Theron, J.; Walker, J. A.; Cloete, T. E., Nanotechnology and water treatment: Applications and emerging opportunities. *Critical Reviews in Microbiology* **2008**, *34*, (1), 43-69.
22. Wei, Y.-T.; Wu, S.-C.; Chou, C.-M.; Che, C.-H.; Tsai, S.-M.; Lien, H.-L., Influence of nanoscale zero-valent iron on geochemical properties of groundwater and vinyl chloride degradation: A field case study. *Water Research* **2010**, *44*, (1), 131-140.
23. Ritter, K.; Odziemkowski, M. S.; Gillham, R. W., An in situ study of the role of surface films on granular iron in the permeable iron wall technology. *Journal of Contaminant Hydrology* **2002**, *55*, (1-2), 87-111.
24. Han, Y.; Yang, M. D. Y.; Zhang, W.; Yan, W., Optimizing synthesis conditions of nanoscale zero-valent iron (nZVI) through aqueous reactivity assessment. *Frontiers of Environmental Science & Engineering* **2015**, *9*, (5), 813-822.
25. Hwang, Y.-H.; Kim, D.-G.; Shin, H.-S., Effects of synthesis conditions on the characteristics and reactivity of nano scale zero valent iron. *Applied Catalysis B: Environmental* **2011**, *105*, (1-2), 144-150.
26. Uegami, M.; Kawano, J.; Okita, T.; Fujii, Y.; Okinaka, K.; Kakuya, K.; Yatagi, S., Iron particles for purifying contaminated soil or ground water. In Google Patents: 2006.
27. Bystrzejewski, M., Synthesis of carbon-encapsulated iron nanoparticles via solid state reduction of iron oxide nanoparticles. *Journal of Solid State Chemistry* **2011**, *184*, (6), 1492-1498.
28. Li, S.; Yan, W.; Zhang, W.-x., Solvent-free production of nanoscale zero-valent iron (nZVI) with precision milling. *Green Chemistry* **2009**, *11*, (10), 1618-1626.
29. Puls, R. W.; Paul, C. J.; Powell, R. M., The application of in situ permeable reactive (zero-valent iron) barrier technology for the remediation of chromate-contaminated groundwater: a field test. *Applied Geochemistry* **1999**, *14*, (8), 989-1000.

30. Liu, T.; Tsang, D. C. W.; Lo, I. M. C., Chromium(VI) Reduction Kinetics by Zero-Valent Iron in Moderately Hard Water with Humic Acid: Iron Dissolution and Humic Acid Adsorption. *Environmental Science & Technology* **2008**, *42*, (6), 2092-2098.
31. Liu, T.; Rao, P.; Mak, M. S. H.; Wang, P.; Lo, I. M. C., Removal of co-present chromate and arsenate by zero-valent iron in groundwater with humic acid and bicarbonate. *Water Research* **2009**, *43*, (9), 2540-2548.
32. Jeen, S.-W.; Blowes, D. W.; Gillham, R. W., Performance evaluation of granular iron for removing hexavalent chromium under different geochemical conditions. *Journal of Contaminant Hydrology* **2008**, *95*, (1–2), 76-91.
33. Jeen, S.-W.; Jambor, J. L.; Blowes, D. W.; Gillham, R. W., Precipitates on Granular Iron in Solutions Containing Calcium Carbonate with Trichloroethene and Hexavalent Chromium. *Environmental Science & Technology* **2007**, *41*, (6), 1989-1994.
34. Lai, K. C. K.; Lo, I. M. C., Removal of Chromium (VI) by Acid-Washed Zero-Valent Iron under Various Groundwater Geochemistry Conditions. *Environmental Science & Technology* **2008**, *42*, (4), 1238-1244.
35. Gandhi, S.; Oh, B.-T.; Schnoor, J. L.; Alvarez, P. J. J., Degradation of TCE, Cr(VI), sulfate, and nitrate mixtures by granular iron in flow-through columns under different microbial conditions. *Water Research* **2002**, *36*, (8), 1973-1982.
36. Blowes, D. W.; Ptacek, C. J.; Benner, S. G.; McRae, C. W. T.; Bennett, T. A.; Puls, R. W., Treatment of inorganic contaminants using permeable reactive barriers1. *Journal of Contaminant Hydrology* **2000**, *45*, (1–2), 123-137.
37. Lee, T.; Lim, H.; Lee, Y.; Park, J.-W., Use of waste iron metal for removal of Cr(VI) from water. *Chemosphere* **2003**, *53*, (5), 479-485.
38. Nurmi, J. T.; Tratnyek, P. G.; Sarathy, V.; Baer, D. R.; Amonette, J. E.; Pecher, K.; Wang, C.; Linehan, J. C.; Matson, D. W.; Penn, R. L.; Driessen, M. D., Characterization and Properties of Metallic Iron Nanoparticles: Spectroscopy, Electrochemistry, and Kinetics. *Environmental Science & Technology* **2005**, *39*, (5), 1221-1230.
39. Yan, W.; Vasic, R.; Frenkel, A. I.; Koel, B. E., Intraparticle reduction of arsenite (As (III)) by nanoscale zerovalent iron (nZVI) investigated with in situ X-ray absorption spectroscopy. *Environmental science & technology* **2012**, *46*, (13), 7018-7026.
40. Cornell, R. M.; Schwertmann, U., *The iron oxides: structure, properties, reactions, occurrences and uses*. John Wiley & Sons: 2003.
41. Matheson, L. J.; Tratnyek, P. G., Reductive Dehalogenation of Chlorinated Methanes by Iron Metal. *Environmental Science & Technology* **1994**, *28*, (12), 2045-2053.
42. Weber, E. J., Iron-Mediated Reductive Transformations: Investigation of Reaction Mechanism. *Environmental Science & Technology* **1996**, *30*, (2), 716-719.
43. Norris, R. D., *Handbook of bioremediation*. CRC press: 1993.

44. McCarty, P. L., GROUNDWATER CONTAMINATION BY CHLORINATED SOLVENTS: HISTORY, REMEDIATION TECHNOLOGIES AND STRATEGIES. *In Situ Remediation of Chlorinated Solvent Plumes* **2010**, 1-28.
45. Moran, M. J.; Zogorski, J. S.; Squillace, P. J., Chlorinated solvents in groundwater of the United States. *Environmental Science & Technology* **2007**, *41*, (1), 74-81.
46. Hileman, B., Concerns broaden over chlorine and chlorinated hydrocarbons. *Chemical and Engineering News(USA)* **1993**, *71*, (16), 11-20.
47. McCarty, P. L., In situ bioremediation of chlorinated solvents. *Current opinion in biotechnology* **1993**, *4*, (3), 323-330.
48. Kielhorn, J.; Melber, C.; Wahnschaffe, U.; Aitio, A.; Mangelsdorf, I., Vinyl chloride: still a cause for concern. *Environmental Health Perspectives* **2000**, *108*, (7), 579.
49. Chen, K. F.; Kao, C. M.; Sung, W. P.; Lin, C. C.; Yeh, T. Y., Enhanced In Situ Anaerobic Bioremediation of TCE-contaminated Groundwater Using Nanoscale Zero-valent Iron (nZVI). *Frontier of Nanoscience and Technology* **2011**, *694*, 3-7.
50. Kao, C. M.; Chen, Y. L.; Chen, S. C.; Yeh, T. Y.; Wu, W. S., Enhanced PCE dechlorination by biobarrier systems under different redox conditions. *Water research* **2003**, *37*, (20), 4885-4894.
51. Pant, P.; Pant, S., A review: Advances in microbial remediation of trichloroethylene (TCE). *Journal of Environmental Sciences* **2010**, *22*, (1), 116-126.
52. Arnold, W. A.; Roberts, A. L., Pathways of Chlorinated Ethylene and Chlorinated Acetylene Reaction with Zn(0). *Environmental Science & Technology* **1998**, *32*, (19), 3017-3025.
53. Su, C.; Puls, R. W., Kinetics of Trichloroethene Reduction by Zerovalent Iron and Tin: Pretreatment Effect, Apparent Activation Energy, and Intermediate Products. *Environmental Science & Technology* **1999**, *33*, (1), 163-168.
54. Farrell, J.; Kason, M.; Melitas, N.; Li, T., Investigation of the long-term performance of zero-valent iron for reductive dechlorination of trichloroethylene. *Environmental Science & Technology* **2000**, *34*, (3), 514-521.
55. Weaver, J. W.; Wilson, J. T.; Kampbell, D. H. In *Case study of natural attenuation of trichloroethene at St. Joseph, Michigan*, 1997, p 67.
56. Liu, Y. Q.; Majetich, S. A.; Tilton, R. D.; Sholl, D. S.; Lowry, G. V., TCE dechlorination rates, pathways, and efficiency of nanoscale iron particles with different properties. *Environmental Science & Technology* **2005**, *39*, (5), 1338-1345.
57. Johnson, T. L.; Scherer, M. M.; Tratnyek, P. G., Kinetics of Halogenated Organic Compound Degradation by Iron Metal. *Environmental Science & Technology* **1996**, *30*, (8), 2634-2640.

58. Roberts, A. L.; Totten, L. A.; Arnold, W. A.; Burris, D. R.; Campbell, T. J., Reductive elimination of chlorinated ethylenes by zero valent metals. *Environmental Science & Technology* **1996**, *30*, (8), 2654-2659.
59. Butler, E. C.; Hayes, K. F., Kinetics of the transformation of trichloroethylene and tetrachloroethylene by iron sulfide. *Environmental Science & Technology* **1999**, *33*, (12), 2021-2027.
60. He, Y. T.; Wilson, J. T.; Wilkin, R. T., Impact of iron sulfide transformation on trichloroethylene degradation. *Geochimica et Cosmochimica Acta* **2010**, *74*, (7), 2025-2039.
61. Lesage, S.; Brown, S.; Millar, K., A Different Mechanism for the Reductive Dechlorination of Chlorinated Ethenes: Kinetic and Spectroscopic Evidence. *Environmental Science & Technology* **1998**, *32*, (15), 2264-2272.
62. Ponec, V.; Bond, G. C., Studies in Surface Science and Catalysis. In *Catalysis by Metals and Alloys*, Elsevier Science BV Amsterdam: 1995.
63. Song, H.; Carraway, E. R., Catalytic hydrodechlorination of chlorinated ethenes by nanoscale zero-valent iron. *Applied Catalysis B-Environmental* **2008**, *78*, (1-2), 53-60.
64. Han, Y.; Yan, W., Bimetallic nickel–iron nanoparticles for groundwater decontamination: Effect of groundwater constituents on surface deactivation. *Water Research* **2014**, *66*, (0), 149-159.
65. Han, Y.; Liu, C.; Horita, J.; Yan, W., Trichloroethene hydrodechlorination by Pd-Fe bimetallic nanoparticles: Solute-induced catalyst deactivation analyzed by carbon isotope fractionation. *Applied Catalysis B: Environmental* **2016**, *188*, 77-86.
66. Lien, H.-L.; Zhang, W.-X., Nanoscale Pd/Fe bimetallic particles: Catalytic effects of palladium on hydrodechlorination. *Applied Catalysis B-Environmental* **2007**, *77*, (1-2), 110-116.
67. Cwiertny, D. M.; Bransfield, S. J.; Livi, K. J. T.; Fairbrother, D. H.; Roberts, A. L., Exploring the Influence of Granular Iron Additives on 1,1,1-Trichloroethane Reduction. *Environmental Science & Technology* **2006**, *40*, (21), 6837-6843.
68. Schrick, B.; Blough, J. L.; Jones, A. D.; Mallouk, T. E., Hydrodechlorination of trichloroethylene to hydrocarbons using bimetallic nickel-iron nanoparticles. *Chemistry of Materials* **2002**, *14*, (12), 5140-5147.
69. Urbano, F. J.; Marinas, J. M., Hydrogenolysis of organohalogen compounds over palladium supported catalysts. *Journal of Molecular Catalysis A: Chemical* **2001**, *173*, (1-2), 329-345.
70. Yan, W.; Herzing, A. A.; Li, X.-Q.; Kiely, C. J.; Zhang, W.-X., Structural Evolution of Pd-Doped Nanoscale Zero-Valent Iron (nZVI) in Aqueous Media and Implications for Particle Aging and Reactivity. *Environmental Science & Technology* **2010**, *44*, (11), 4288-4294.

71. Liendo, M. A.; Navarro, G. E.; Sampaio, C. H., Nano and micro ZVI in aqueous media: copper uptake and solution behavior. *Water, Air, & Soil Pollution* **2013**, *224*, (5), 1-8.
72. Su, Y.; Adeleye, A. S.; Keller, A. A.; Huang, Y.; Dai, C.; Zhou, X.; Zhang, Y., Magnetic sulfide-modified nanoscale zerovalent iron (S-nZVI) for dissolved metal ion removal. *Water Research* **2015**, *74*, 47-57.
73. Jang, M.; Min, S.-H.; Kim, T.-H.; Park, J. K., Removal of arsenite and arsenate using hydrous ferric oxide incorporated into naturally occurring porous diatomite. *Environmental science & technology* **2006**, *40*, (5), 1636-1643.
74. Shi, L.-n.; Zhang, X.; Chen, Z.-l., Removal of chromium (VI) from wastewater using bentonite-supported nanoscale zero-valent iron. *Water research* **2011**, *45*, (2), 886-892.
75. Su, C. M.; Puls, R. W., Nitrate reduction by zerovalent iron: Effects of formate, oxalate, citrate, chloride, sulfate, borate, and phosphate. *Environmental Science & Technology* **2004**, *38*, (9), 2715-2720.
76. Martin, J. E.; Herzing, A. A.; Yan, W.; Li, X.-q.; Koel, B. E.; Kiely, C. J.; Zhang, W.-x., Determination of the oxide layer thickness in core-shell zerovalent iron nanoparticles. *Langmuir* **2008**, *24*, (8), 4329-4334.
77. Li, X.-q.; Zhang, W.-x., Sequestration of Metal Cations with Zerovalent Iron NanoparticlesA Study with High Resolution X-ray Photoelectron Spectroscopy (HR-XPS). *The Journal of Physical Chemistry C* **2007**, *111*, (19), 6939-6946.
78. Ferguson, J. F.; Gavis, J., A review of the arsenic cycle in natural waters. *Water Research* **1972**, *6*, (11), 1259-1274.
79. Hughes, M. F., Arsenic toxicity and potential mechanisms of action. *Toxicology letters* **2002**, *133*, (1), 1-16.
80. Dixit, S.; Hering, J. G., Comparison of Arsenic(V) and Arsenic(III) Sorption onto Iron Oxide Minerals: Implications for Arsenic Mobility. *Environmental Science & Technology* **2003**, *37*, (18), 4182-4189.
81. Kanel, S. R.; Manning, B.; Charlet, L.; Choi, H., Removal of Arsenic(III) from Groundwater by Nanoscale Zero-Valent Iron. *Environmental Science & Technology* **2005**, *39*, (5), 1291-1298.
82. Kanel, S. R.; Greneche, J.-M.; Choi, H., Arsenic (V) removal from groundwater using nano scale zero-valent iron as a colloidal reactive barrier material. *Environmental science & technology* **2006**, *40*, (6), 2045-2050.
83. Leupin, O. X.; Hug, S. J., Oxidation and removal of arsenic (III) from aerated groundwater by filtration through sand and zero-valent iron. *Water Research* **2005**, *39*, (9), 1729-1740.
84. Nikolaidis, N. P.; Dobbs, G. M.; Lackovic, J. A., Arsenic removal by zero-valent iron: field, laboratory and modeling studies. *Water research* **2003**, *37*, (6), 1417-1425.

85. Yan, W.; Vasic, R.; Frenkel, A. I.; Koel, B. E., Intraparticle Reduction of Arsenite (As(III)) by Nanoscale Zerovalent Iron (nZVI) Investigated with In Situ X-ray Absorption Spectroscopy. *Environmental Science & Technology* **2012**, *46*, (13), 7018-7026.
86. Yan, W.; Ramos, M. A. V.; Koel, B. E.; Zhang, W.-x., As (III) sequestration by iron nanoparticles: study of solid-phase redox transformations with X-ray photoelectron spectroscopy. *The Journal of Physical Chemistry C* **2012**, *116*, (9), 5303-5311.
87. Palmer, C. D.; Wittbrodt, P. R., Processes affecting the remediation of chromium-contaminated sites. *Environmental Health Perspectives* **1991**, *92*, 25-40.
88. Cieślak-Golonka, M., Toxic and mutagenic effects of chromium (VI). A review. *Polyhedron* **1996**, *15*, (21), 3667-3689.
89. Richard, F. C.; Bourg, A. C. M., Aqueous geochemistry of chromium: a review. *Water Research* **1991**, *25*, (7), 807-816.
90. Soares, O. S. G. P.; Órfão, J. J. M.; Pereira, M. F. R., Bimetallic catalysts supported on activated carbon for the nitrate reduction in water: Optimization of catalysts composition. *Applied Catalysis B: Environmental* **2009**, *91*, (1-2), 441-448.
91. Ghafari, S.; Hasan, M.; Aroua, M. K., Bio-electrochemical removal of nitrate from water and wastewater-A review. *Bioresource Technology* **2008**, *99*, (10), 3965-3974.
92. Yang, G. C. C.; Lee, H. L., Chemical reduction of nitrate by nanosized iron: Kinetics and pathways. *Water Research* **2005**, *39*, (5), 884-894.
93. Sohn, K.; Kang, S. W.; Ahn, S.; Woo, M.; Yang, S. K., Fe(0) nanoparticles for nitrate reduction: Stability, reactivity, and transformation. *Environmental Science and Technology* **2006**, *40*, (17), 5514-5519.
94. Choe, S.; Chang, Y. Y.; Hwang, K. Y.; Khim, J., Kinetics of reductive denitrification by nanoscale zero-valent iron. *Chemosphere* **2000**, *41*, (8), 1307-1311.
95. Liu, Y.; Phenrat, T.; Lowry, G. V., Effect of TCE concentration and dissolved groundwater solutes on NZVI-Promoted TCE dechlorination and H-2 evolution. *Environmental Science & Technology* **2007**, *41*, (22), 7881-7887.
96. Liu, Y.; Choi, H.; Dionysiou, D.; Lowry, G. V., Trichloroethene Hydrodechlorination in Water by Highly Disordered Monometallic Nanoiron. *Chemistry of Materials* **2005**, *17*, (21), 5315-5322.
97. Duba, A. G.; Jackson, K. J.; Jovanovich, M. C.; Knapp, R. B.; Taylor, R. T., TCE remediation using in situ, resting-state bioaugmentation. *Environmental Science & Technology* **1996**, *30*, (6), 1982-1989.
98. Agrawal, A.; Ferguson, W. J.; Gardner, B. O.; Christ, J. A.; Bandstra, J. Z.; Tratnyek, P. G., Effects of carbonate species on the kinetics of dechlorination of 1,1,1-trichloroethane by zero-valent iron. *Environmental Science & Technology* **2002**, *36*, (20), 4326-4333.

99. Klausen, J.; Vikesland, P. J.; Kohn, T.; Burris, D. R.; Ball, W. P.; Roberts, A. L., Longevity of granular iron in groundwater treatment processes: Solution composition effects on reduction of organohalides and nitroaromatic compounds. *Environmental Science & Technology* **2003**, 37, (6), 1208-1218.
100. Schlicker, O.; Ebert, M.; Fruth, M.; Weidner, M.; Wust, W.; Dahmke, A., Degradation of TCE with iron: The role of competing chromate and nitrate reduction. *Ground Water* **2000**, 38, (3), 403-409.
101. Devlin, J. F.; Allin, K. O., Major anion effects on the kinetics and reactivity of granular iron in glass-encased magnet batch reactor experiments. *Environmental Science & Technology* **2005**, 39, (6), 1868-1874.
102. Johnson, T. L.; Fish, W.; Gorby, Y. A.; Tratnyek, P. G., Degradation of carbon tetrachloride by iron metal: Complexation effects on the oxide surface. *Journal of Contaminant Hydrology* **1998**, 29, (4), 379-398.
103. Sarathy, V.; Tratnyek, P. G.; Nurmi, J. T.; Baer, D. R.; Amonette, J. E.; Chun, C. L.; Penn, R. L.; Reardon, E. J., Aging of iron nanoparticles in aqueous solution: Effects on structure and reactivity. *Journal of Physical Chemistry C* **2008**, 112, (7), 2286-2293.
104. Hildebrand, H.; Mackenzie, K.; Kopinke, F.-D., Pd/Fe₃O₄ nano-catalysts for selective dehalogenation in wastewater treatment processes-Influence of water constituents. *Applied Catalysis B-Environmental* **2009**, 91, (1-2), 389-396.
105. Phenrat, T.; Saleh, N.; Sirk, K.; Tilton, R. D.; Lowry, G. V., Aggregation and Sedimentation of Aqueous Nanoscale Zerovalent Iron Dispersions. *Environmental Science & Technology* **2007**, 41, (1), 284-290.
106. Zhang, W.-x., Nanoscale Iron Particles for Environmental Remediation: An Overview. *Journal of Nanoparticle Research* **2003**, 5, (3), 323-332.
107. Elliott, D. W.; Zhang, W.-x., Field Assessment of Nanoscale Bimetallic Particles for Groundwater Treatment. *Environmental Science & Technology* **2001**, 35, (24), 4922-4926.
108. Grieger, K. D.; Fjordbøge, A.; Hartmann, N. B.; Eriksson, E.; Bjerg, P. L.; Baun, A., Environmental benefits and risks of zero-valent iron nanoparticles (nZVI) for in situ remediation: Risk mitigation or trade-off? *Journal of Contaminant Hydrology* **2010**, 118, (3-4), 165-183.
109. Phenrat, T.; Kim, H.-J.; Fagerlund, F.; Illangasekare, T.; Tilton, R. D.; Lowry, G. V., Particle Size Distribution, Concentration, and Magnetic Attraction Affect Transport of Polymer-Modified Fe₀ Nanoparticles in Sand Columns. *Environmental Science & Technology* **2009**, 43, (13), 5079-5085.
110. Zhan, J.; Zheng, T.; Piringer, G.; Day, C.; McPherson, G. L.; Lu, Y.; Papadopoulos, K.; John, V. T., Transport Characteristics of Nanoscale Functional Zerovalent Iron/Silica Composites for in Situ Remediation of Trichloroethylene. *Environmental Science & Technology* **2008**, 42, (23), 8871-8876.

111. Kanel, S. R.; Goswami, R. R.; Clement, T. P.; Barnett, M. O.; Zhao, D., Two Dimensional Transport Characteristics of Surface Stabilized Zero-valent Iron Nanoparticles in Porous Media. *Environmental Science & Technology* **2008**, *42*, (3), 896-900.
112. Vecchia, E. D.; Luna, M.; Sethi, R., Transport in Porous Media of Highly Concentrated Iron Micro- and Nanoparticles in the Presence of Xanthan Gum. *Environmental Science & Technology* **2009**, *43*, (23), 8942-8947.
113. Saleh, N.; Phenrat, T.; Sirk, K.; Dufour, B.; Ok, J.; Sarbu, T.; Matyjaszewski, K.; Tilton, R. D.; Lowry, G. V., Adsorbed Triblock Copolymers Deliver Reactive Iron Nanoparticles to the Oil/Water Interface. *Nano Letters* **2005**, *5*, (12), 2489-2494.
114. Phenrat, T.; Saleh, N.; Sirk, K.; Kim, H.-J.; Tilton, R. D.; Lowry, G. V., Stabilization of aqueous nanoscale zerovalent iron dispersions by anionic polyelectrolytes: adsorbed anionic polyelectrolyte layer properties and their effect on aggregation and sedimentation. *Journal of Nanoparticle Research* **2008**, *10*, (5), 795-814.
115. Bennett, P.; He, F.; Zhao, D.; Aiken, B.; Feldman, L., In situ testing of metallic iron nanoparticle mobility and reactivity in a shallow granular aquifer. *Journal of Contaminant Hydrology* **2010**, *116*, (1), 35-46.
116. He, F.; Zhao, D., Preparation and Characterization of a New Class of Starch-Stabilized Bimetallic Nanoparticles for Degradation of Chlorinated Hydrocarbons in Water. *Environmental Science & Technology* **2005**, *39*, (9), 3314-3320.
117. He, F.; Zhao, D.; Liu, J.; Roberts, C. B., Stabilization of Fe–Pd Nanoparticles with Sodium Carboxymethyl Cellulose for Enhanced Transport and Dechlorination of Trichloroethylene in Soil and Groundwater. *Industrial & Engineering Chemistry Research* **2007**, *46*, (1), 29-34.
118. He, F.; Zhao, D.; Paul, C., Field assessment of carboxymethyl cellulose stabilized iron nanoparticles for in situ destruction of chlorinated solvents in source zones. *Water Research* **2010**, *44*, (7), 2360-2370.
119. Johnson, R. L.; Johnson, G. O. B.; Nurmi, J. T.; Tratnyek, P. G., Natural Organic Matter Enhanced Mobility of Nano Zerovalent Iron. *Environmental Science & Technology* **2009**, *43*, (14), 5455-5460.
120. Saleh, N.; Sirk, K.; Liu, Y.; Phenrat, T.; Dufour, B.; Matyjaszewski, K.; Tilton, R. D.; Lowry, G. V., Surface modifications enhance nanoiron transport and NAPL targeting in saturated porous media. *Environmental Engineering Science* **2007**, *24*, (1), 45-57.
121. Quinn, J.; Geiger, C.; Clausen, C.; Brooks, K.; Coon, C.; O'Hara, S.; Krug, T.; Major, D.; Yoon, W.-S.; Gavaskar, A.; Holdsworth, T., Field Demonstration of DNAPL Dehalogenation Using Emulsified Zero-Valent Iron. *Environmental Science & Technology* **2005**, *39*, (5), 1309-1318.
122. Geiger, C. L.; Clausen, C. A.; Brooks, K.; Coon, C.; Huntley, C.; Filipek, L.; DeVor, R.; Krug, T.; O'Hara, S.; Majors, D.; Quinn, J. In *Remediation of dnapls using*

- emulsified zero-valent iron: Laboratory and field results*, ACS, Division of Environmental Chemistry - Preprints of Extended Abstracts, 2003; 2003; pp 939-944.
123. Berge, N. D.; Ramsburg, C. A., Iron-mediated trichloroethene reduction within nonaqueous phase liquid. *Journal of contaminant hydrology* **2010**, *118*, (3), 105-116.
124. Quinn, J.; Geiger, C.; Clausen, C.; Brooks, K.; Coon, C.; O'Hara, S.; Krug, T.; Major, D.; Yoon, W. S.; Gavaskar, A.; Holdsworth, T., Field demonstration of DNAPL dehalogenation using emulsified zero-valent iron. *Environmental Science & Technology* **2005**, *39*, (5), 1309-1318.
125. Rickard, D.; Luther, G. W., Chemistry of Iron Sulfides. *Chemical Reviews* **2007**, *107*, (2), 514-562.
126. Gagnon, C.; Mucci, A.; Pelletier, É., Anomalous accumulation of acid-volatile sulphides (AVS) in a coastal marine sediment, Saguenay Fjord, Canada. *Geochimica et Cosmochimica Acta* **1995**, *59*, (13), 2663-2675.
127. Fortin, D.; Goulet, R.; Roy, M., Seasonal cycling of Fe and S in a constructed wetland: The role of sulfate-reducing bacteria. *Geomicrobiology Journal* **2000**, *17*, (3), 221-235.
128. Kimblin, R. T.; Johnson, A. C., Recent localised sulphate reduction and pyrite formation in a fissured Chalk aquifer. *Chemical Geology* **1992**, *100*, (1-2), 119-127.
129. Brennan, E. W.; Lindsay, W. L., The role of pyrite in controlling metal ion activities in highly reduced soils. *Geochimica et Cosmochimica Acta* **1996**, *60*, (19), 3609-3618.
130. Schoonen, M. A. A., Mechanisms of sedimentary pyrite formation. *Geological Society of America Special Papers* **2004**, *379*, 117-134.
131. Canfield, D. E.; Thamdrup, B.; Fleischer, S., Isotope fractionation and sulfur metabolism by pure and enrichment cultures of elemental sulfur-disproportionating bacteria. *Limnology and Oceanography* **1998**, *43*, (2), 253-264.
132. Donald, R.; Southam, G., Low temperature anaerobic bacterial diagenesis of ferrous monosulfide to pyrite. *Geochimica et Cosmochimica Acta* **1999**, *63*, (13-14), 2019-2023.
133. Boursiquot, S.; Mullet, M.; Abdelmoula, M.; Génin, J. M.; Ehrhardt, J. J., The dry oxidation of tetragonal FeS_{1-x} mackinawite. *Physics and Chemistry of Minerals* **2001**, *28*, (9), 600-611.
134. Posfai, M.; Buseck, P. R.; Bazylinski, D. A.; Franke, R. B., Iron sulfides from magnetotactic bacteria: structure, composition, and phase transitions. *American Mineralogist* **1998**, *83*, (11), 1469-1481.
135. Pósfai, M.; Buseck, P. R.; Bazylinski, D. A.; Frankel, R. B., Reaction sequence of iron sulfide minerals in bacteria and their use as biomarkers. *Science* **1998**, *280*, (5365), 880-883.

136. Cipollone, M. G.; Wolfe, N. L.; Anderson, J. L., Long-term kinetic column studies on the iron and iron-pyrite for remediating TCE in water. *Abstracts of Papers American Chemical Society* **1997**, 213, (1-3), 172-ENVR 172.
137. Lee, W.; Batchelor, B., Abiotic reductive dechlorination of chlorinated ethylenes by iron-bearing soil minerals. 1. Pyrite and magnetite. *Environmental Science & Technology* **2002**, 36, (23), 5147-5154.
138. Pham, H. T.; Kitsuneduka, M.; Hara, J.; Suto, K.; Inoue, C., Trichloroethylene transformation by natural mineral pyrite: The deciding role of oxygen. *Environmental Science & Technology* **2008**, 42, (19), 7470-7475.
139. Weerasooriya, R.; Dharmasena, B., Pyrite-assisted degradation of trichloroethene (TCE). *Chemosphere* **2001**, 42, (4), 389-396.
140. Elsner, M.; Schwarzenbach, R. P.; Haderlein, S. B., Reactivity of Fe(II)-bearing minerals toward reductive transformation of organic contaminants. *Environmental Science & Technology* **2004**, 38, (3), 799-807.
141. Butler, E. C.; Hayes, K. F., Factors influencing rates and products in the transformation of trichloroethylene by iron sulfide and iron metal. *Environmental Science & Technology* **2001**, 35, (19), 3884-3891.
142. Kyung, D.; Amir, A.; Choi, K.; Lee, W., Reductive Transformation of Tetrachloroethene Catalyzed by Sulfide-Cobalamin in Nano-Mackinawite Suspension. *Industrial & Engineering Chemistry Research* **2015**, 54, (5), 1439-1446.
143. Butler, E. C.; Hayes, K. F., Effects of Solution Composition and pH on the Reductive Dechlorination of Hexachloroethane by Iron Sulfide. *Environmental Science & Technology* **1998**, 32, (9), 1276-1284.
144. Jeong, H. Y.; Kim, H.; Hayes, K. F., Reductive dechlorination pathways of tetrachloroethylene and trichloroethylene and subsequent transformation of their dechlorination products by mackinawite (FeS) in the presence of metals. *Environmental Science & Technology* **2007**, 41, (22), 7736-7743.
145. Kim, E.-J.; Kim, J.-H.; Azad, A.-M.; Chang, Y.-S., Facile Synthesis and Characterization of Fe/FeS Nanoparticles for Environmental Applications. *Acs Applied Materials & Interfaces* **2011**, 3, (5), 1457-1462.
146. Sun, Q.; Feitz, A. J.; Guan, J.; Waite, T. D., COMPARISON OF THE REACTIVITY OF NANOSIZED ZERO-VALENT IRON (nZVI) PARTICLES PRODUCED BY BOROHYDRIDE AND DITHIONITE REDUCTION OF IRON SALTS. *Nano* **2008**, 3, (5), 341-349.
147. Karguppikar, A. M.; Vedeshwar, A. G., ELECTRICAL AND OPTICAL-PROPERTIES OF NATURAL IRON PYRITE (FES₂). *Physica Status Solidi a-Applied Research* **1988**, 109, (2), 549-558.
148. Tributsch, H.; Rojas-Chapana, J. A., Metal sulfide semiconductor electrochemical mechanisms induced by bacterial activity. *Electrochimica Acta* **2000**, 45, (28), 4705-4716.

149. Puthussery, J.; Seefeld, S.; Berry, N.; Gibbs, M.; Law, M., Colloidal Iron Pyrite (FeS_2) Nanocrystal Inks for Thin-Film Photovoltaics. *Journal of the American Chemical Society* **2011**, *133*, (4), 716-719.
150. Caban-Acevedo, M.; Faber, M. S.; Tan, Y.; Hamers, R. J.; Jin, S., Synthesis and Properties of Semiconducting Iron Pyrite (FeS_2) Nanowires. *Nano Letters* **2012**, *12*, (4), 1977-1982.
151. Lai, C.-H.; Lu, M.-Y.; Chen, L.-J., Metal sulfide nanostructures: synthesis, properties and applications in energy conversion and storage. *Journal of Materials Chemistry* **2012**, *22*, (1), 19-30.
152. Rajajayavel, S. R. C.; Ghoshal, S., Enhanced reductive dechlorination of trichloroethylene by sulfidated nanoscale zerovalent iron. *Water Research* **2015**, *78*, 144-153.
153. Liang, X.; Dong, Y.; Kuder, T.; Krumholz, L. R.; Philp, R. P.; Butler, E. C., Distinguishing abiotic and biotic transformation of tetrachloroethylene and trichloroethylene by stable carbon isotope fractionation. *Environmental Science & Technology* **2007**, *41*, (20), 7094-7100.
154. Hunkeler, D.; Aravena, R.; Butler, B. J., Monitoring Microbial Dechlorination of Tetrachloroethene (PCE) in Groundwater Using Compound-Specific Stable Carbon Isotope Ratios: Microcosm and Field Studies. *Environmental Science & Technology* **1999**, *33*, (16), 2733-2738.
155. Morrill, P. L.; Sleep, B. E.; Seepersad, D. J.; McMaster, M. L.; Hood, E. D.; LeBron, C.; Major, D. W.; Edwards, E. A.; Sherwood Lollar, B., Variations in expression of carbon isotope fractionation of chlorinated ethenes during biologically enhanced PCE dissolution close to a source zone. *Journal of Contaminant Hydrology* **2009**, *110*, (1–2), 60-71.
156. Liang, X.; Philp, R. P.; Butler, E. C., Kinetic and isotope analyses of tetrachloroethylene and trichloroethylene degradation by model Fe(II)-bearing minerals. *Chemosphere* **2009**, *75*, (1), 63-69.
157. Elsner, M.; Chartrand, M.; Vanstone, N.; Couloume, G. L.; Lollar, B. S., Identifying abiotic chlorinated ethene degradation: Characteristic isotope patterns in reaction products with nanoscale zero-valent iron. *Environmental Science & Technology* **2008**, *42*, (16), 5963-5970.
158. Aepli, C.; Hofstetter, T. B.; Amaral, H. I. F.; Kipfer, R.; Schwarzenbach, R. P.; Berg, M., Quantifying In Situ Transformation Rates of Chlorinated Ethenes by Combining Compound-Specific Stable Isotope Analysis, Groundwater Dating, And Carbon Isotope Mass Balances. *Environmental Science & Technology* **2010**, *44*, (10), 3705-3711.
159. Elsner, M.; Cwiertny, D. M.; Roberts, A. L.; Sherwood Lollar, B., 1,1,2,2-tetrachloroethane reactions with OH-, Cr(II), granular iron, and a copper-iron bimetal:

- Insights from product formation and associated carbon isotope fractionation. *Environmental Science & Technology* **2007**, *41*, (11), 4111-4117.
160. Hunkeler, D.; Butler, B. J.; Aravena, R.; Barker, J. F., Monitoring biodegradation of methyl tert-butyl ether (MTBE) using compound-specific carbon isotope analysis. *Environmental Science & Technology* **2001**, *35*, (4), 676-681.
161. Elsner, M.; McKelvie, J.; Couloume, G. L.; Lollar, B. S., Insight into methyl tert-butyl ether (MTBE) stable isotope Fractionation from abiotic reference experiments. *Environmental Science & Technology* **2007**, *41*, (16), 5693-5700.
162. Zwank, L.; Elsner, M.; Aeberhard, A.; Schwarzenbach, R. P.; Haderlein, S. B., Carbon isotope fractionation in the reductive dehalogenation of carbon tetrachloride at iron (hydr)oxide and iron sulfide minerals. *Environmental Science & Technology* **2005**, *39*, (15), 5634-5641.
163. Chan, C. C. H.; Mundle, S. O. C.; Eckert, T.; Liang, X.; Tang, S.; Lacrampe-Couloume, G.; Edwards, E. A.; Lollar, B. S., Large Carbon Isotope Fractionation during Biodegradation of Chloroform by Dehalobacter Cultures. *Environmental Science & Technology* **2012**, *46*, (18), 10154-10160.
164. Liang, X.; Howlett, M. R.; Nelson, J. L.; Grant, G.; Dworatzek, S.; Lacrampe-Couloume, G.; Zinder, S. H.; Edwards, E. A.; Lollar, B. S., Pathway-Dependent Isotope Fractionation during Aerobic and Anaerobic Degradation of Monochlorobenzene and 1,2,4-Trichlorobenzene. *Environmental Science & Technology* **2011**, *45*, (19), 8321-8327.
165. Bouchard, D.; Hunkeler, D.; Gaganis, P.; Aravena, R.; Hohener, P.; Broholm, M. M.; Kjeldsen, P., Carbon isotope fractionation during diffusion and biodegradation of petroleum hydrocarbons in the unsaturated zone: Field experiment at Vaerlose airbase, Denmark, and modeling. *Environmental Science & Technology* **2008**, *42*, (2), 596-601.
166. Kuder, T.; Philp, P.; Allen, J., Effects of Volatilization on Carbon and Hydrogen Isotope Ratios of MTBE. *Environmental Science & Technology* **2009**, *43*, (6), 1763-1768.
167. Slater, G. F.; Lollar, B. S.; Sleep, B. E.; Edwards, E. A., Variability in carbon isotopic fractionation during biodegradation of chlorinated ethenes: Implications for field applications. *Environmental Science & Technology* **2001**, *35*, (5), 901-907.
168. Hirschorn, S. K.; Dinglasan, M. J.; Elsner, M.; Mancini, S. A.; Lacrampe-Couloume, G.; Edwards, E. A.; Lollar, B. S., Pathway dependent isotopic fractionation during aerobic biodegradation of 1,2-dichloroethane. *Environmental Science & Technology* **2004**, *38*, (18), 4775-4781.
169. Lollar, B. S.; Hirschorn, S.; Mundle, S. O. C.; Grostern, A.; Edwards, E. A.; Lacrampe-Couloume, G., Insights into Enzyme Kinetics of Chloroethane Biodegradation Using Compound Specific Stable Isotopes. *Environmental Science & Technology* **2010**, *44*, (19), 7498-7503.

CHAPTER TWO

Optimizing Synthesis Conditions of Nanoscale Zero-Valent Iron (nZVI) through Aqueous Reactivity Assessment¹

2.1 Introduction

Nanoscale zero-valent iron (nZVI) is one of the most prevalently used engineered nanoparticles for groundwater and soil remediation ¹⁻⁴. Over the past two decades, nZVI and its variations, the latter including bimetallic nZVI and surfactant-stabilized nZVI, have been deployed at more than 50 pilot or full-scale remediation sites in the U.S. and other countries for treating underground soil and water tarnished by halogenated solvents and a variety of inorganic contaminants ⁵⁻⁸. The most widely reported preparation method for nZVI is chemical synthesis via reduction of ferrous or ferric salts by strong reducing agents such as sodium borohydride ^{9,10}. At a larger scale, production of nZVI with thermal reduction of iron oxides ^{11,5} and precision ball-milling ¹² have been reported. In many cases of field remediation, nZVI particles are stabilized with surfactants or encapsulated in silica or carbon matrices to improve dispersion of particles in the aqueous media and impart longer service-lives ^{13,14}.

A practical question arising from the availability of nZVI in various forms and from different sources is whether there exist facile tests to probe the chemical functionality of nZVI. Material-focused characterization techniques, such as electron microscopy, diffraction analyses, and X-ray absorption spectroscopy have been used to examine the morphology, chemical composition, and internal structure of fresh or environmentally-aged iron nanoparticles ¹⁵⁻¹⁷. However, limited access to many of these advanced characterization instruments prohibits their general use as a screening tool for selecting nZVI or optimizing its production conditions. And material characteristics cannot be quantitatively translated to particles' chemical reactivity. Other methods, such

¹ This chapter is published as: Yanlai Han, Michael Yang, Weixian Zhang, Weile Yan. Optimizing synthesis conditions of nanoscale zero-valent iron (nZVI) through aqueous reactivity assessment. *Frontiers of Environmental Science and Engineering*, 2015. Springer Nature Publishing Company.

as the measurement of oxidation-reduction potential (ORP) and electrochemical evaluations, have been used to probe the reductive property of nZVI^{18,19}. However, these methods are not contaminant-specific and are subject to interference from side reactions or secondary processes²⁰. In this context, the use of model contaminants to assay the reactivity of nZVI is a desired option. An ideal probe should be able to react rapidly and specifically with nZVI, capable of discriminating surface passivation state, and requiring relatively simple analyses instrumentation. Using nitrate as a probe reactant, Liou *et al.* studied the effect of initial iron precursor concentration on the nZVI reactivity²¹. Hwang *et al.* also compared the effect of different synthesis conditions by measuring the nitrate reduction rates²². However, owing to the complex reaction mechanisms and a difficulty in assessing the distribution of nitrate reduction products, the reaction stoichiometry is not well defined. Furthermore, nitrate at elevated concentrations impairs the surface reactivity of iron by forming an oxide phase of lower electron conductivity²³⁻²⁶. This inherent deactivating effect complicates kinetic analysis and limits detailed chemical and structural information that can be gleaned from nitrate tests. In a prior study, we used Cu (II) ion to evaluate the thickness of the oxide layer present on the nZVI surface²⁷. This test is based on the premise that, in an anoxic solution, copper reduction by nZVI is the dominant reaction, and coincidentally, the reaction is auto-catalyzed because metal copper deposited on the nZVI surface is able to serve as additional cathode sites²⁸. Therefore, the reaction is rapid and its simple stoichiometry can be exploited to reveal structural properties.

Solution-phase syntheses of metal nanoparticles using borohydride reduction reactions have been extensively studied^{9,10}. The emergence of metal nanoparticles via reductive precipitation consists of three steps: (1) homogeneous nucleation, (2) growth of particle nuclei, and (3) ripening or agglomeration^{10,29}. Many synthesis parameters can influence the particle yield, size, morphology as well as chemical reactivity. The ratio of the reducing agent to the iron precursor is crucial to nuclei formation and growth. Excessive agglomeration of nuclei or primary particles can lead to oversized particles, which may undermine their reactivity, yet this can be alleviated by controlling the stirring speed of the precursor solution during the borohydride feeding process¹⁰. Upon

formation of nascent metal nuclei, an oxide layer develops spontaneously in the presence of air or water, giving rise to the frequently observed core-shell structure of nZVI^{27,30,31}. Furthermore, the oxidation rate of the metal iron core is size-dependent, implying that particles smaller than a critical diameter (typically on the order of single nanometers) can be completely oxidized within the synthesis time scale^{16,32}. For this reason, the contact time between nZVI and water during the synthesis process and the reductant feed rate are relevant parameters to optimize. Lastly, the yield of particles per synthesis batch depends on the initial concentration of iron precursor as well as the concentration of the reducing agent. Many of these variables are interrelated and their optimization is essential to obtaining highly reactive nZVI.

The objective of this chapter is to assess the effects of synthesis conditions on the reactivity of nZVI prepared from the borohydride reduction method. We examined four pertinent experiment parameters, namely, solution stirring speed, feed rate of sodium borohydride, concentration ratio of borohydride to ferric ion, and initial concentration of ferric ion in the synthesis solutions, by adjusting them independently at multiple levels. The nZVI prepared under varying conditions were characterized by their reactions with Cu(II) and nitrate in aqueous solutions to reveal the state of particle surface passivation and the total reduction capacity. The synthesis conditions exerting a critical influence on particle reactivity are identified and their roles in nanoparticle nucleation, growth, and stabilization are discussed. In addition, we seek to compare the nZVI reactivity characteristics revealed through the nitrate and Cu(II) reduction tests and infer the usefulness or drawbacks of these two evaluation methods.

2.2 Materials and Methods

2.2.1 Materials

Sodium borohydride (98%, Acros Organics), ferric chloride (Fisher Chemical), and ethanol (95%, Sigma Aldrich) are used for nZVI synthesis. Sodium nitrate and cupric sulfate, both of A.C.S reagent grade, were purchased from Acros Organics and MCB Reagents, respectively. Dilute sodium hydroxide and hydrochloric acid solutions were used for pH adjustment. All solutions were prepared with distilled deionized (DDI) water,

and the DDI water was purged with N₂ for 30 min to eliminate dissolved oxygen prior to its use.

2.2.2 Synthesis of nZVI

nZVI particles used in this study were synthesized via reduction of a dilute Fe (III) solution by sodium borohydride (NaBH₄). The synthesis procedure follows those of the previous studies ^{27,33} except that several key synthesis variables were varied in appropriate ranges in order to assess their effects on the morphology and chemical reactivity of the resultant particles. In brief terms, a 500-ml of ferric chloride solution (FeCl₃) of varying concentration was intensely agitated with a mechanical rotary mixer (Cole Parmer, Model 50007-20), during which 500 ml of sodium borohydride solution was introduced into the ferric chloride solution at a constant feed rate using a peristaltic pump (Masterflex Model 07524-40). After the feeding was completed, the slurry was left to settle for 5 minutes. The particles were then collected by vacuum filtration and rinsed two times with 95% ethanol. The as-synthesized particles were stored in 95% ethanol in a closed HDPE container at 4°C prior to use. The dry weight of nZVI was determined using a halogen-lamp moisture analyzer (Ohaus MB45) and the dry solid content was found to remain constant during a storage period of up to four weeks. Microscopic characterization and reactivity assessment confirmed that the quality of the nanoparticles did not deteriorate during the storage period.

To evaluate the effects of synthesis conditions on nanoparticle structure and chemical reactivity, we systematically adjusted four important synthesis parameters, namely, the stirring speed of the rotary mixer, the feed rate of borohydride solution, initial FeCl₃ concentration, and the molar ratio of borohydride concentration in the feed solution to the initial concentration of ferric ions. A total of nine batches of nZVI particles were prepared and Table 1 displays the detailed settings used to prepare each batch of nZVI. Batch No. 1 represents a standard preparation protocol used in the authors' former lab. The nZVI prepared under such conditions was used as a benchmark to compare with the other eight batches.

2.2.3 Solid Phase Characterization

Fresh or reacted particles were rinsed with ethanol and dried in a N₂ glove box for up to 48 h before solid phase characterization. X-Ray diffractogram was obtained with a Bruker diffractometer (Bruker D5005) with a Cu K α radiation source at a step size of 0.02° and a scan rate of 15 second/step. Samples for electron microscope analysis were prepared by dispersing a small amount of particles in ethanol, depositing 1-2 drops of ethanol suspension on SEM sample studs covered with conductive carbon tape or TEM copper grids, and allowing to dry. The morphology of fresh nZVI and those reacted with Cu(II) was characterized with a field emission scanning electron microscope (SEM, Hitachi S-4300) at a beam acceleration voltage of 3 – 20 kV. Additional characterization was made on the fresh nZVI using transmission electron microscopy (TEM) (JOEL 2000FX) at a beam energy of 200 kV.

2.2.4 nZVI Reactivity Assessment

In this research, Cu(II) and nitrate were selected as two model contaminants to diagnose the reactivity and composition of nZVI. Both reactants undergo facile reduction in the presence of zero-valent iron material ³⁴⁻³⁸ and their analyses are relatively simple compared to those for halogenated hydrocarbons. These considerations make Cu(II) and nitrate expedient candidates for assessing the reductive properties of nZVI prepared through different synthesis routes or under various sets of preparation conditions. Cu(II) reduction experiments were conducted in 45-ml EPA glass vials containing 40 ml of Cu(II) solutions of varying concentrations (50 – 1200 mg/L). Upon addition of fresh prepared nZVI at 0.75 g/L (dry weight), the reaction vials were closed and placed on a wrist-action shaker at 150 rpm at room temperature for 30 minutes. Our kinetic assessment suggests Cu(II) reduction was completed well within this time period. After reaction, samples were withdrawn and filtered through 0.2- μ m PTFE syringe filters (SLLG025SS, Millipore). Aqueous copper or iron concentrations were determined using an Atomic Absorption Spectrometer (AAnalyst800, Perkin-Elmer).

In nitrate reduction experiments, 100 ml of nitrate solution at an initial concentration of 50 mg/L or 150 mg/L was amended with 2 g/L of fresh made nZVI (dry

weight). The solutions were mixed on a shaker at 150 rpm for 3 hours. Since nitrate reduction was considerably slower than Cu(II) reduction by nZVI, small aliquots of samples were taken at suitable intervals to assess the rates of nitrate removal. All samples were filtered using 0.2- μ m PTFE syringe filters before determination of nitrate concentrations using a UV-Vis spectrophotometric method at 220 nm with background correction at 275 nm as per the established nitrate analysis method³⁹.

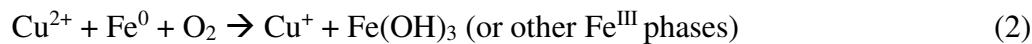
2.3 Results and Discussion

2.3.1 Characterization of nZVI

The size and structure of nZVI prepared using the baseline conditions (Batch No. 1 in Table 2.1) were shown in Figures 2.1(a) and 2.1(b). The fresh made particles appear smooth and round-shaped with well-resolved metal-core-oxide-shell structure under TEM analysis. The average size of the primary particles was approximately 50 nm, although size distribution in the range of 20 -100 nm was observed based on inspection of a few dozens of particles under the microscope. SEM image reveals clustering of particles into micron-scale aggregates. These aggregates were not densely packed; instead, they assembled into an open and highly fractal structure giving rise to a large surface area accessible to aqueous reactions. These structural features are in agreement with similarly prepared nZVI reported in the literature^{27,40,31}. After reaction with Cu(II), the iron nanoparticles display a considerably different appearance as shown in Figure 2.1(c). Notably, cylindrical stalks with length spanning on the order of a micron were observed. Under the back scattered electron (BSE) mode (Figure 2.1(d)), which is an SEM imaging technique sensitive to atomic number contrast⁴¹, the chunky rod formation stands out as a brighter phase (indicated by arrows) compared to the more faint background particles, suggesting the former is a more electron-dense phase that can be identified as Cu(0). This attribution is supported by solution analysis and X-ray diffraction characterization as mentioned below.

2.3.2 nZVI Reactivity Assessment using Cu(II) as a Probe Reagent

Figure 2.2(a) shows the trend of aqueous Cu(II) concentration in the presence of various doses of nZVI. In all experiments, Cu(II) concentration decreased to a stable level in less than 10 min. Tests conducted at higher nZVI doses attained equilibria in even shorter time periods (not shown in the figure). As is evident in Figure 2.2(a), Cu(II) concentrations in the final solutions are strongly dependent on the dose of nZVI. Specifically, 48% of Cu(II) was removed in the presence of 0.1 g/L of nZVI, whereas more than 96% and 99% uptake was observed when the iron loading was increased to 0.25 g/L and 0.4 g/L, respectively. Solution analysis indicates that the total Fe dissolved into the aqueous phase correlates linearly with the amount of Cu(II) being removed (Figure 2.2(b)). The slope is 0.93, which is close to the stoichiometry of 1:1 in the classic metal displacement reaction as in Eq. (1)²⁸:



It has been reported in earlier studies that the reaction of zero-valent iron with aqueous Cu(II) solutions can produce metallic Cu or cuprous oxide (Cu₂O). Based on XPS Cu 2p3/2 spectra and Cu auger lines, Shahwan *et al.* identified the primary products of Cu(II) reduction by nZVI or clay-supported nZVI to be cuprous oxide^{42,43}. Using similar XPS analysis, Li *et al.* showed that the product formed with nZVI was chiefly Cu(0)⁴⁴. Other studies have detected the presence of both Cu(0) and Cu(I) on the surface of reacted iron materials⁴⁵. Comparative experiments conducted in different aqueous environment using the same iron material demonstrate that the speciation of copper is sensitive to dissolved oxygen and the solution pH⁴⁶. Specifically, in anoxic and weakly acidic aqueous solutions (pH 4), only metal copper was identified with X-ray diffraction analysis, whereas in oxygenated water at neutral pH, Cu₂O was the dominant product. The reactions in the presence of dissolved oxygen are described in Eq. (2).

In this study, X-ray diffraction pattern of the solid residues, shown in Figure 2.3, indicates highly crystalline *fcc* Cu(0) was formed, which is consistent with the findings of

⁴⁶ considering that the solutions in our experiments were deoxygenated and the final pH was below 5. Collectively, the kinetics of Cu(II) reduction as well as the morphological and crystallographic characteristics of the products point to an autocatalytic nature of the reaction, *i.e.*, the presence of initially formed Cu(0) forms a galvanic couple with Fe(0), leading to accelerated reduction of Cu(II) at Cu(0) cathode sites and oriented growth of Cu(0) crystallites.

In comparison to the above, we conducted Cu(II) removal in a solution that was open to air (thus having a substantial amount of dissolved oxygen) and the kinetics are depicted in Figure 2.2(c). It was noticed that the amount of Cu(II) sequestered from this solution was approximately 60% of the Cu(II) removal in an equivalent experiment in N₂-purged solution (Figure 2.2(a)). The aqueous Cu(II) concentration, reaching a minimum at around 10 min, rebounded after 40 min, indicating re-oxidation of the reduced copper by dissolved oxygen and dissolution of the oxidized copper into the aqueous phase. To avoid complication caused by dissolved oxygen, all subsequent experiments were conducted in deoxygenated solutions.

Figure 2.2 (d) shows the removal of Cu(II) by a batch of nZVI at varying ratios of initial Cu(II) concentration and nZVI loading. The trend resembles the results we reported in an early study ²⁷ and reveals two distinct reaction regimes. Specifically, at lower Cu(II)/nZVI ratios (*i.e.*, when the iron is in excess of Cu(II) ions), uptake of Cu(II) from the aqueous phase correlates linearly with an increase in Cu(II) concentration. Since the reaction is self-catalyzed, all Cu(0) would be removed by reductive precipitation in the presence of excess iron, and therefore the initial data points should fall on a straight line with a slope of unity. This is indeed the case found for the particular batch of nZVI used in Figure 2.2(d), for which a line with a slope of 0.97 fits the data well. However, in many cases, we observed that the slopes of various batches of nZVI were smaller than one, suggesting not all Fe(0) was accessible to the probe reactant even though iron was present at sufficient quantities. It is recognized that the nature of the oxide shell on nZVI imparts a large influence on the reductive properties of the particles. Iron nanoparticles prepared by borohydride reduction tend to form more disordered oxide

shell compared to particles made through mechanical means or thermal reduction^{40,31,47}. The amorphous oxide is thought to enable enhanced electron transfer and a higher reductive reactivity. On the other hand, exposure to aqueous media, particularly those with elevated concentrations of background salts such as nitrate^{48,23}, dissolved silica⁴⁹, and phosphate²⁴ are known to decrease the reactivity of iron by forming passivating oxides that are less amenable to electron passage. The outcome of such effect is a decrease in the chemically accessible Fe(0) phase and lower contaminant degradation rates. In this context, the slope of the line in the first regime of Cu(II) reduction test can be used as an indicator of the nanoparticle surface reactivity.

As the Cu(II)/nZVI ratio increases, Cu(II) removal (normalized by the dose of nZVI) approaches a limiting value. The maximum Cu(II) uptake is represented by a dashed horizontal line in Figure 2.2(d). Because Fe(0) is consumed by copper reduction (Eq. 1), the limiting value of Cu(II) sequestration per unit mass of nZVI is a measure of the content of Fe(0) in nZVI. We have shown earlier that, while the mass fraction of iron oxides is negligible in bulk ZVI materials, oxides can account for more than 10% the mass of iron nanoparticles²⁷. The exact makeup of the metal phase and the oxide skin is a function of the particle size, synthesis procedure, and aging history. For instance, a decrease in the primary particle diameter is expected to lead to more oxidized iron being present in the nanoparticles due to the core-shell geometry and the fact that smaller particles oxidize at higher rates. Considering the above, the limiting value of Cu(II) removal per unit mass of nZVI reveals the chemical composition of iron nanoparticles, which also correlates to the total reductive capacity of the nanoparticles at the point of use.

Figure 2.4 shows the Cu(II) reduction performance of nZVI prepared under different synthesis conditions. In reference to the classical nucleation theory, researchers consider that the formation of nanoparticles consists of three main phases: initial burst of solid seeds (also known as burst nucleation), growth, and ripening or stabilization^{10,29}. In the case of preparation of metal nanoparticles using borohydride with no addition of surface-stabilizing surfactants, very fast formation of particle nuclei is expected²⁹. This is

followed by increases in nuclei diameters or coalescence of multiple nuclei to form primary particles. As iron has a more negative reduction potential than water, the ripening phase involves stabilization of the freshly minted particles via growth of a layer of passivating oxide on the particle surface. Meanwhile, aggregation of passivated primary particles occurs and may continue beyond the ripening phase. As with other solution synthesis methods, the outcome of each step is affected by the reagent concentrations as well as the mixing conditions. Figure 2.4(a) shows the effect of solution agitation speed on nZVI reactivity as probed with Cu(II). Compared to the baseline synthesis protocol (nZVI Batch No. 1), increasing the mixer rotation speed from 650 to 900 rpm poses no significant impact on the particle reactivity and its core-shell composition. In contrast, more gentle mixing markedly decreases the relative content of Fe(0) in the nanoparticles, suggesting this batch of nZVI contains a significant share of iron oxides. Figure 2.4(b) investigates the effect of borohydride feed rate. Increasing the pumping rate of the reductant into the synthesis solution by two folds (from a baseline of 17 ml/min to 35 ml/min) resulted in a drastic decrease in the particle reactivity as well as the content of the metal core. Since fast delivery of borohydride favors nucleation over particle growth, very fine particles are likely produced in the reactor with a high reductant flow rate, and the particles thus formed are susceptible to rapid oxidation during synthesis or particle harvesting steps. In comparison, lowering the pump rate from 17 ml/min to 6.8 ml/min did not cause significant deterioration of particle reactivity and its Cu(II) removal capacity. In Figure 2.4(c), the effect of concentration ratio of borohydride to ferric ion was evaluated. It can be seen that the baseline ratio ($[NaBH_4]/[Fe^{3+}] = 5$) is the optimal setting. Decreasing the ratio to 2 has a detrimental effect on the total amount of Fe(0) present in the resultant particles, a result to be expected because the system may not have sufficient NaBH₄ to reduce Fe³⁺ to Fe(0), taking into account that a fraction of the borohydride is lost to aqueous decomposition. On the other hand, increasing the concentration ratio of borohydride to Fe³⁺ to 8 is not preferred either, as both particle reactivity and the metal iron content were significantly compromised. The findings are similar to what we observed in the experiment with a higher borohydride feed rate (Figure 2.4(b)), and they can be rationalized based on the

knowledge that exceedingly fast or high dose of borohydride promotes the formation of minuscule particles, which are prone to oxidation during synthesis and particle handling processes. Finally, we assessed the effect of initial ferric ion concentration while keeping the ratio of borohydride to Fe^{3+} constant. The results are exhibited in Figure 2.4(d). For nZVI prepared from a lower initial Fe^{3+} concentration (0.04 M), it possesses comparable Cu(II) reduction capacity as the baseline particles ($[\text{Fe}^{3+}]$ at 0.08 M). At a higher Fe^{3+} concentration (0.2 M), considerable loss of particle reactivity (*i.e.*, characterized by a more slanting slope in the first reaction regime) and a substantial decrease in Cu(II) reduction capacity was observed. A previous study attributed the significant abatement of nZVI reactivity under high iron precursor concentrations to the formation of oversized nZVI particles²¹. This argument is consistent with the particle nucleation theory as higher Fe^{3+} favors nanoparticle growth/agglomeration over nucleation. In all, it can be concluded that the reagent concentrations and the delivery rate of sodium borohydride are the most critical parameters affecting the quality of the nanoparticles made through the borohydride reduction method.

2.3.3 nZVI Reactivity Assessment using Nitrate as a Probe Reagent

Four batches of nZVI (Batch No. 1, 4, 7, and 8) were selected to conduct nitrate reduction experiments based on the knowledge that these materials have shown large differences in Cu(II) removal behavior compared to the reference nZVI (Batch no. 1). Each nZVI material was reacted with nitrate at an initial concentration of 50 mg/L and 150 mg/L, respectively. The kinetic results are shown in Figure 2.5. In fitting the experimental data, it was observed that the rate of nitrate disappearance was faster than the classical first-order decay at the beginning of the reaction. However, close to the completion of these experiments, nitrate reactions nearly grounded to a halt, as is evident in the figures for experiments conducted at the higher nitrate concentration (150 mg/L). The kinetic characteristics resemble the first-order-reaction and first-order deactivation model reported for many heterogeneous catalysis systems⁵⁰. This model considers that the main reaction (*i.e.*, nitrate reduction) follows pseudo-first-order kinetics (Eq. (3)), and it is coupled to a first-order deactivation term as in Eq. (4). k_R and k_D are first-order

reaction and deactivation constants, respectively, and a is a dimensionless parameter reflecting surface activity at different time.

$$d[NO_3^-]/dt = -k_R[NO_3^-]a \quad (3)$$

$$da/dt = -k_D a \quad (4)$$

The experimental data were fitted to the above-mentioned model and the fitting parameters for different iron materials are summarized in Table 2.2. At the low nitrate starting concentration (50 mg/L), k_R is greater than k_D for all batches of nZVI. The baseline particles (Batch No. 1) delivered the highest nitrate reduction rate, having a k_R value more than two folds those of the other batches. Based on the initial slopes of the Cu(II) reduction data, the surface reactivity of nZVI can be listed in the order of (B stands for Batch no.): B1 > B7 > B8 > B4. The nitrate reduction rate constant, k_R , follows the same sequence (Table 2.2). More importantly, plotting the reactivity data of the two types of experiments reveal a strong positive correlation (Figure 2.6). These results confirm that both nitrate and Cu(II) assays are capable of measuring the surface reactivity of iron nanoparticles in a consistent way. At the higher nitrate concentration (150 mg/L), the reaction kinetics is dominated by the deactivation effect of nitrate ($k_D > k_R$ for all particles), as a result, information related to the intrinsic reactivity of nZVI cannot be extracted from the experimental data. Finally, owing to the quantitative reaction of nZVI with Cu(II), Cu(II) reaction is able to assess the core-shell composition of nZVI. Such capability is not available in nitrate assessments.

2.4 Conclusion

In this study, the effects of synthesis parameters on the reactivity of borohydride-reduced iron nanoparticles were investigated. In an effort to establish a facile test protocol for rapid screening of many candidate nZVI materials, two model contaminants, Cu(II) and nitrate, were used as potential nZVI reactivity assays. The findings confirm that the concentration of iron precursor, borohydride feed rate, and the ratio of reductant to iron impose significant influences on the nature of the particles formed. Solution

mixing speed in the range of 280 to 900 rpm has a relatively smaller impact on nZVI reactivity. Furthermore, comparison between the two probe reactions suggests that the two systems can generate consistent inference about the surface reductive activity of different nZVI materials, however, nitrate tests are valid within a small concentration range and are not capable of interrogating the chemical composition of nZVI due to its deactivating effect on the iron surface.

Reference

1. O'Carroll, D.; Sleep, B.; Krol, M.; Boparai, H.; Kocur, C., Nanoscale zero valent iron and bimetallic particles for contaminated site remediation. *Advances in Water Resources* **2013**, *51*, 104-122.
2. Crane, R. A.; Scott, T. B., Nanoscale zero-valent iron: Future prospects for an emerging water treatment technology. *Journal of Hazardous Materials* **2012**, *211*, 112-125.
3. Wilkin, R. T.; Su, C.; Ford, R. G.; Paul, C. J., Chromium-Removal Processes during Groundwater Remediation by a Zerovalent Iron Permeable Reactive Barrier. *Environmental Science & Technology* **2005**, *39*, (12), 4599-4605.
4. Chen, K. F.; Kao, C. M.; Sung, W. P.; Lin, C. C.; Yeh, T. Y., Enhanced In Situ Anaerobic Bioremediation of TCE-contaminated Groundwater Using Nanoscale Zero-valent Iron (nZVI). *Frontier of Nanoscience and Technology* **2011**, *694*, 3-7.
5. Mueller, N. C.; Braun, J.; Bruns, J.; Cernik, M.; Rissing, P.; Rickerby, D.; Nowack, B., Application of nanoscale zero valent iron (NZVI) for groundwater remediation in Europe. *Environmental Science and Pollution Research* **2012**, *19*, (2).
6. Theron, J.; Walker, J. A.; Cloete, T. E., Nanotechnology and water treatment: Applications and emerging opportunities. *Crit. Rev. Microbiol.* **2008**, *34*, (1), 43-69.
7. Li, X. Q.; Elliott, D. W.; Zhang, W. X., Zero-valent iron nanoparticles for abatement of environmental pollutants: Materials and engineering aspects. *Critical Reviews in Solid State and Materials Sciences* **2006**, *31*, (4), 111-122.
8. Karn, B.; Kuiken, T.; Otto, M., Nanotechnology and in Situ Remediation: A Review of the Benefits and Potential Risks. *Environmental Health Perspectives* **2009**, *117*, (12), 1823-1831.
9. Glavee, G. N.; Klabunde, K. J.; Sorensen, C. M.; Hadjipanayis, G. C., Chemistry of borohydride reduction of iron(II) and iron(III) ions in aqueous and nonaqueous media - Formation of nanoscale Fe, FeB, and Fe₂B powders *Inorg. Chem.* **1995**, *34*, (1), 28-35.
10. Cushing, B. L.; Kolesnichenko, V. L.; O'Connor, C. J., Recent advances in the liquid-phase syntheses of inorganic nanoparticles. *Chemical Reviews* **2004**, *104*, (9), 3893-3946.

11. Liu, H. B.; Chen, T. H.; Chang, D. Y.; Chen, D.; Liu, Y.; He, H. P.; Yuan, P.; Frost, R., Nitrate reduction over nanoscale zero-valent iron prepared by hydrogen reduction of goethite. *Mater. Chem. Phys.* **2012**, *133*, (1), 205-211.
12. Li, S.; Yan, W.; Zhang, W.-x., Solvent-free production of nanoscale zero-valent iron (nZVI) with precision milling. *Green Chemistry* **2009**, *11*, (10), 1618-1626.
13. He, F.; Zhao, D. Y.; Paul, C., Field assessment of carboxymethyl cellulose stabilized iron nanoparticles for in situ destruction of chlorinated solvents in source zones. *Water Research* **2010**, *44*, (7), 2360-2370.
14. Zhan, J. J.; Sunkara, B.; Le, L.; John, V. T.; He, J. B.; McPherson, G. L.; Piringer, G.; Lu, Y. F., Multifunctional Colloidal Particles for in Situ Remediation of Chlorinated Hydrocarbons. *Environmental Science & Technology* **2009**, *43*, (22), 8616-8621.
15. Wang, Q.; Kanel, S. R.; Park, H.; Ryu, A.; Choi, H., Controllable synthesis, characterization, and magnetic properties of nanoscale zerovalent iron with specific high Brunauer-Emmett-Teller surface area. *Journal of Nanoparticle Research* **2009**, *11*, (3), 749-755.
16. Signorini, L.; Pasquini, L.; Savini, L.; Carboni, R.; Boscherini, F.; Bonetti, E.; Giglia, A.; Pedio, M.; Mahne, N.; Nannarone, S., Size-dependent oxidation in iron/iron oxide core-shell nanoparticles. *Physical Review B* **2003**, *68*, (19).
17. Wang, C. M.; Baer, D. R.; Amonette, J. E.; Engelhard, M. H.; Antony, J.; Qiang, Y., Morphology and Electronic Structure of the Oxide Shell on the Surface of Iron Nanoparticles. *Journal of the American Chemical Society* **2009**, *131*, (25), 8824-8832.
18. Ponder, S. M.; Darab, J. G.; Bucher, J.; Caulder, D.; Craig, I.; Davis, L.; Edelstein, N.; Lukens, W.; Nitsche, H.; Rao, L. F.; Shuh, D. K.; Mallouk, T. E., Surface chemistry and electrochemistry of supported zerovalent iron nanoparticles in the remediation of aqueous metal contaminants. *Chemistry of Materials* **2001**, *13*, (2), 479-486.
19. Melitas, N.; Conklin, M.; Farrell, J., Electrochemical study of arsenate and water reduction on iron media used for arsenic removal from potable water. *Environmental Science & Technology* **2002**, *36*, (14), 3188-3193.
20. Shi, Z.; Nurmi, J. T.; Tratnyek, P. G., Effects of Nano Zero-Valent Iron on Oxidation-Reduction Potential. *Environmental Science & Technology* **2011**, *45*, (4), 1586-1592
21. Liou, Y. H.; Lo, S.-L.; Kuan, W. H.; Lin, C.-J.; Weng, S. C., Effect of precursor concentration on the characteristics of nanoscale zerovalent iron and its reactivity of nitrate. *Water Research* **2006**, *40*, (13), 2485-2492.
22. Hwang, Y.-H.; Kim, D.-G.; Shin, H.-S., Effects of synthesis conditions on the characteristics and reactivity of nano scale zero valent iron. *Applied Catalysis B: Environmental* **2011**, *105*, (1-2), 144-150.

23. Farrell, J.; Kason, M.; Melitas, N.; Li, T., Investigation of the long-term performance of zero-valent iron for reductive dechlorination of trichloroethylene. *Environmental Science & Technology* **2000**, *34*, (3).
24. Liu, Y.; Phenrat, T.; Lowry, G. V., Effect of TCE concentration and dissolved groundwater solutes on NUI-Promoted TCE dechlorination and H-2 evolution. *Environmental Science & Technology* **2007**, *41*, (22), 7881-7887.
25. Su, C. M.; Puls, R. W., Nitrate reduction by zerovalent iron: Effects of formate, oxalate, citrate, chloride, sulfate, borate, and phosphate. *Environmental Science & Technology* **2004**, *38*, (9), 2715-2720.
26. Schlicker, O.; Ebert, M.; Fruth, M.; Weidner, M.; Wust, W.; Dahmke, A., Degradation of TCE with iron: The role of competing chromate and nitrate reduction. *Ground Water* **2000**, *38*, (3), 403-409.
27. Martin, J. E.; Herzing, A. A.; Yan, W.; Li, X.-q.; Koel, B. E.; Kiely, C. J.; Zhang, W.-x., Determination of the oxide layer thickness in core-shell zerovalent iron nanoparticles. *Langmuir* **2008**, *24*, (8), 4329-4334.
28. Ku, Y.; Chen, C. H., Kinetic-Study of Copper Deposition on Iron by Cementation Reaction. *Separation Science and Technology* **1992**, *27*, (10), 1259-1275.
29. Thanh, N. T. K.; Maclean, N.; Mahiddine, S., Mechanisms of Nucleation and Growth of Nanoparticles in Solution. *Chemical Reviews* **2014**, *114*, (15), 7610-7630.
30. Carpenter, E. E.; Calvin, S.; Stroud, R. M.; Harris, V. G., Passivated iron as core-shell nanoparticles. *Chemistry of Materials* **2003**, *15*, (17), 3245-3246.
31. Nurmi, J. T.; Tratnyek, P. G.; Sarathy, V.; Baer, D. R.; Amonette, J. E.; Pecher, K.; Wang, C. M.; Linehan, J. C.; Matson, D. W.; Penn, R. L.; Driessens, M. D., Characterization and properties of metallic iron nanoparticles: Spectroscopy, electrochemistry, and kinetics. *Environmental Science & Technology* **2005**, *39*, (5), 1221-1230.
32. Wang, C. M.; Baer, D. R.; Thomas, L. E.; Amonette, J. E.; Antony, J.; Qiang, Y.; Duscher, G., Void formation during early stages of passivation: Initial oxidation of iron nanoparticles at room temperature. *Journal of Applied Physics* **2005**, *98*, (9).
33. Zhang, W. X.; Wang, C. B.; Lien, H. L., Treatment of chlorinated organic contaminants with nanoscale bimetallic particles. *Catalysis Today* **1998**, *40*, (4), 387-395.
34. Alowitz, M. J.; Scherer, M. M., Kinetics of nitrate, nitrite, and Cr(VI) reduction by iron metal. *Environmental Science & Technology* **2002**, *36*, (3), 299-306.
35. Sohn, K.; Kang, S. W.; Ahn, S.; Woo, M.; Yang, S. K., Fe(0) nanoparticles for nitrate reduction: Stability, reactivity, and transformation. *Environmental Science & Technology* **2006**, *40*, (17), 5514-5519.
36. Ryu, A.; Jeong, S.-W.; Jang, A.; Choi, H., Reduction of highly concentrated nitrate using nanoscale zero-valent iron: Effects of aggregation and catalyst on reactivity. *Applied Catalysis B-Environmental* **2011**, *105*, (1-2), 128-135.

37. Miehr, R.; Tratnyek, P. G.; Bandstra, J. Z.; Scherer, M. M.; Alowitz, M. J.; Bylaska, E. J., Diversity of contaminant reduction reactions by zerovalent iron: Role of the reductate. *Environmental Science & Technology* **2004**, *38*, (1), 139-147.
38. Muller, D. B.; Wang, T.; Duval, B.; Graedel, T. E., Exploring the engine of anthropogenic iron cycles. *Proceedings of the National Academy of Sciences of the United States of America* **2006**, *103*, (44), 16111-16116.
39. *Standard methods for the examination of water and wastewater 20th Ed.* American Public Health Association: Washington, DC, 1998.
40. Liu, Y. Q.; Choi, H.; Dionysiou, D.; Lowry, G. V., Trichloroethene hydrodechlorination in water by highly disordered monometallic nanoiron. *Chemistry of Materials* **2005**, *17*, (21), 5315-5322.
41. Goldstein, J.; Newbury, D. E.; Joy, D. C.; Lyman, C. E.; Echlin, P.; Lifshin, E.; Sawyer, L.; Michael, J. R., *Scanning Electron Microscopy and X-ray Microanalysis*. 3rd ed.; Springer: 2003.
42. Karabelli, D.; Uzum, C.; Shahwan, T.; Eroglu, A. E.; Scott, T. B.; Hallam, K. R.; Lieberwirth, I., Batch removal of aqueous Cu²⁺ ions using nanoparticles of zero-valent iron: A study of the capacity and mechanism of uptake. *Industrial & Engineering Chemistry Research* **2008**, *47*, (14), 4758-4764.
43. Uezuem, C.; Shahwan, T.; Eroglu, A. E.; Hallam, K. R.; Scott, T. B.; Lieberwirth, I., Synthesis and characterization of kaolinite-supported zero-valent iron nanoparticles and their application for the removal of aqueous Cu²⁺ and Co²⁺ ions. *Applied Clay Science* **2009**, *43*, (2), 172-181.
44. Li, X. Q.; Zhang, W. X., Sequestration of metal cations with zerovalent iron nanoparticles - A study with high resolution X-ray photoelectron spectroscopy (HR-XPS). *Journal of Physical Chemistry C* **2007**, *111*, (19), 6939-6946.
45. Macdonald, J. E.; Veinot, J. G. C., Removal of residual metal catalysts with iron/iron oxide nanoparticles from coordinating environments. *Langmuir* **2008**, *24*, (14), 7169-7177.
46. Rangseivek, R.; Jekel, M. R., Removal of dissolved metals by zero-valent iron (ZVI): Kinetics, equilibria, processes and implications for stormwater runoff treatment. *Water Research* **2005**, *39*, (17), 4153-4163.
47. Yan, W.; Herzing, A. A.; Kiely, C. J.; Zhang, W.-x., Nanoscale zero-valent iron (nZVI): Aspects of the core-shell structure and reactions with inorganic species in water. *Journal of Contaminant Hydrology* **2010**, *118*, (3-4), 96-104.
48. Liu, Y. Q.; Majetich, S. A.; Tilton, R. D.; Sholl, D. S.; Lowry, G. V., TCE dechlorination rates, pathways, and efficiency of nanoscale iron particles with different properties. *Environmental Science & Technology* **2005**, *39*, (5), 1338-1345.
49. Klausen, J.; Vikesland, P. J.; Kohn, T.; Burris, D. R.; Ball, W. P.; Roberts, A. L., Longevity of granular iron in groundwater treatment processes: Solution composition

effects on reduction of organohalides and nitroaromatic compounds. *Environmental Science & Technology* **2003**, *37*, (6), 1208-1218.

50. Ordonez, S.; Vivas, B. P.; Diez, F. V., Minimization of the deactivation of palladium catalysts in the hydrodechlorination of trichloroethylene in wastewaters. *Applied Catalysis B-Environmental* **2010**, *95*, (3-4), 288-296.

Table 2.1 Experimental conditions used to prepare nZVI evaluated in this study

Batch No.	Synthesis variable adjusted	Initial FeCl ₃ concentration (M)	Molar ratio of NaBH ₄ to FeCl ₃	Stirring speed (rpm)	NaBH ₄ feeding rate (mL•min ⁻¹)
1	Baseline	0.08 M	5 : 1	650	17
2	Stirring speed (low)	0.08 M	5 : 1	280	17
3	Stirring speed (high)	0.08 M	5 : 1	900	17
4	Feeding rate (high)	0.08 M	5 : 1	650	35
5	Feeding rate (low)	0.08 M	5 : 1	650	6.8
6	Ratio of NaBH ₄ to FeCl ₃ (low)	0.08 M	2 : 1	650	17
7	Ratio of NaBH ₄ to FeCl ₃ (high)	0.08 M	8 : 1	650	17
8	Initial FeCl ₃ concentration (high)	0.2 M	5 : 1	650	17
9	Initial FeCl ₃ concentration (low)	0.04 M	5 : 1	650	17

Table 2.2 Pseudo-first-order reaction rate constants (k_R) and first-order deactivation rate constants (k_D) of nitrate reduction

nZVI batch	$C_{0,\text{nitrate}} = 50 \text{ mg/L}$			$C_{0,\text{nitrate}} = 150 \text{ mg/L}$		
	$k_R (\text{min}^{-1})$	$k_D (\text{min}^{-1})$	R^2	$k_R (\text{min}^{-1})$	$k_D (\text{min}^{-1})$	R^2
1	1.5×10^{-1}	2.1×10^{-2}	0.986	8.6×10^{-3}	1.9×10^{-2}	0.783
4	4.8×10^{-2}	9.4×10^{-3}	0.958	1.5×10^{-2}	2.6×10^{-2}	0.989
7	7.3×10^{-2}	1.1×10^{-2}	0.954	1.2×10^{-2}	2.5×10^{-2}	0.993
8	6.9×10^{-2}	1.7×10^{-2}	0.967	2.9×10^{-3}	1.8×10^{-2}	0.766

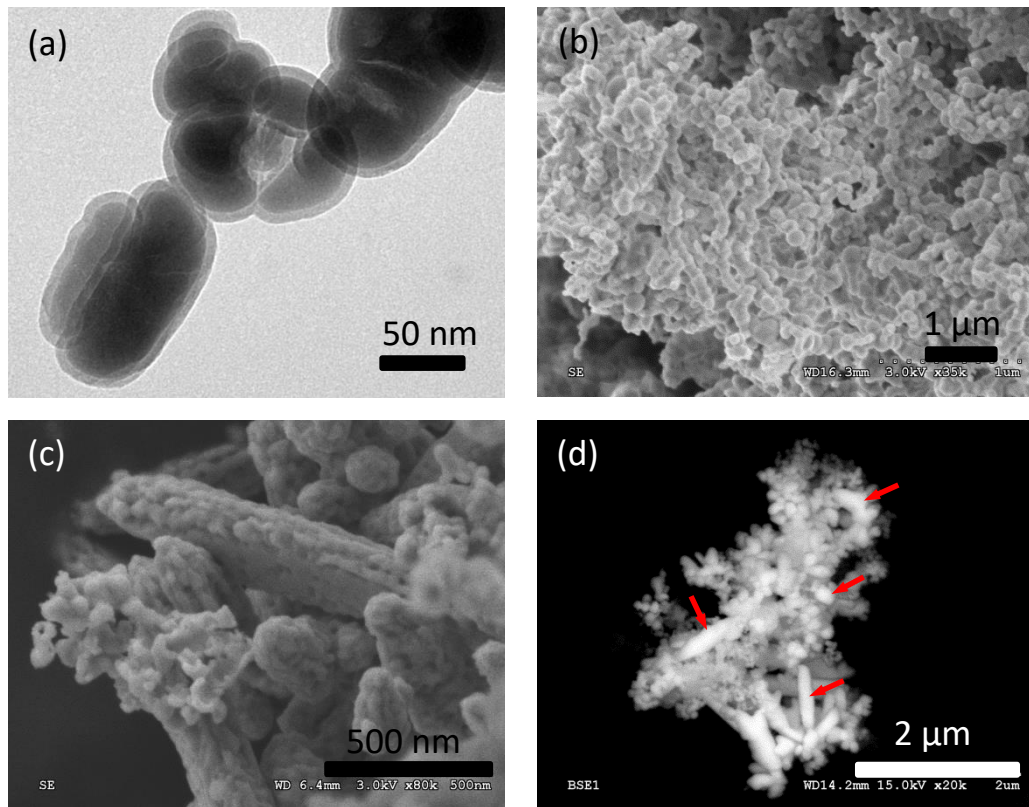


Figure 2.1 Morphology characterization of nZVI particles synthesized using the baseline conditions. (a) and (b) are TEM and SEM images of as-synthesized nZVI. (c) and (d) are secondary electron and back-scattered electron images of nZVI reacted with Cu(II) for 10 min.

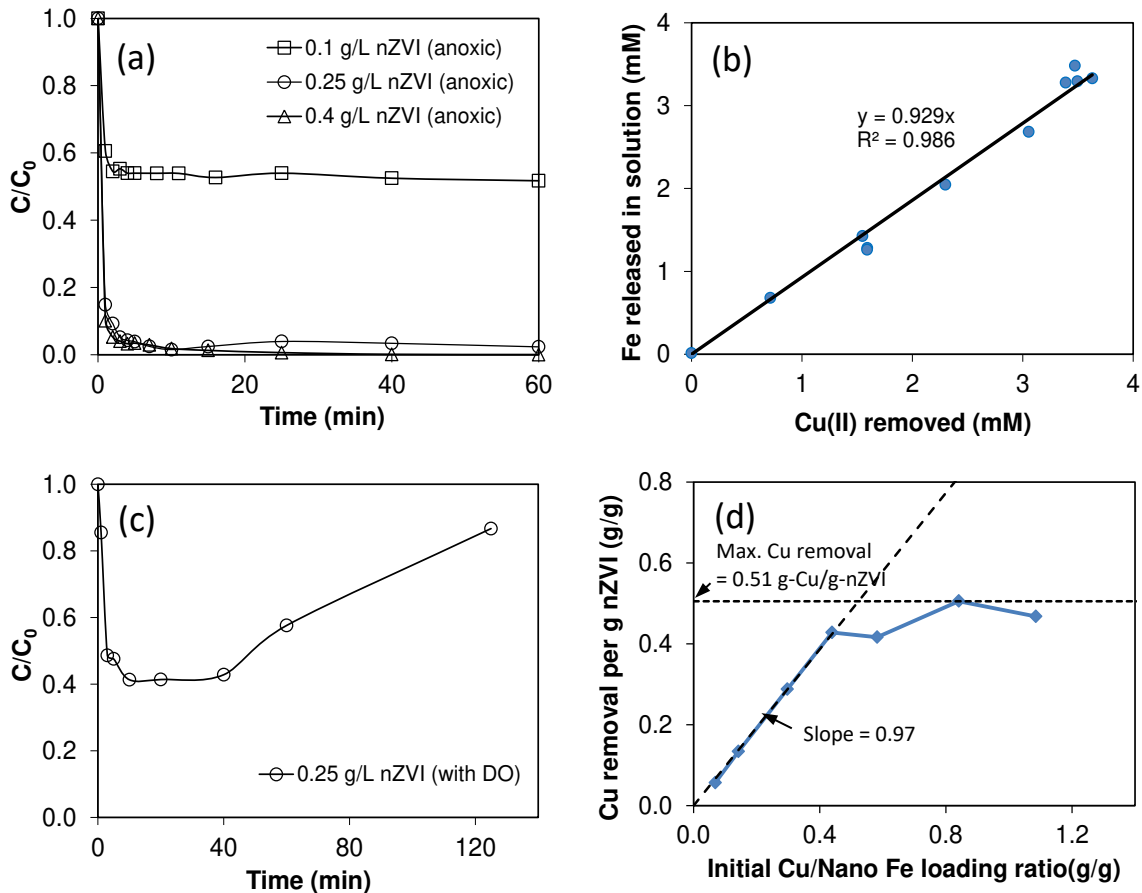


Figure 2.2 (a) Removal of aqueous Cu(II) by nZVI in N_2 -sparged solutions and (b) release of dissolved iron into solutions after Cu(II) reaction. (c) Cu(II) removal in a solution open to atmosphere. (d) Cu(II) removal capacity at varying Cu(II)/nZVI loading ratios in deoxygenated solutions. Initial Cu(II) concentration was 200 mg/L in (a) and (c) and varied in the range of 50 - 1200 mg/L in (b) and (d). Dose of nZVI was 0.75 g/L in (d).

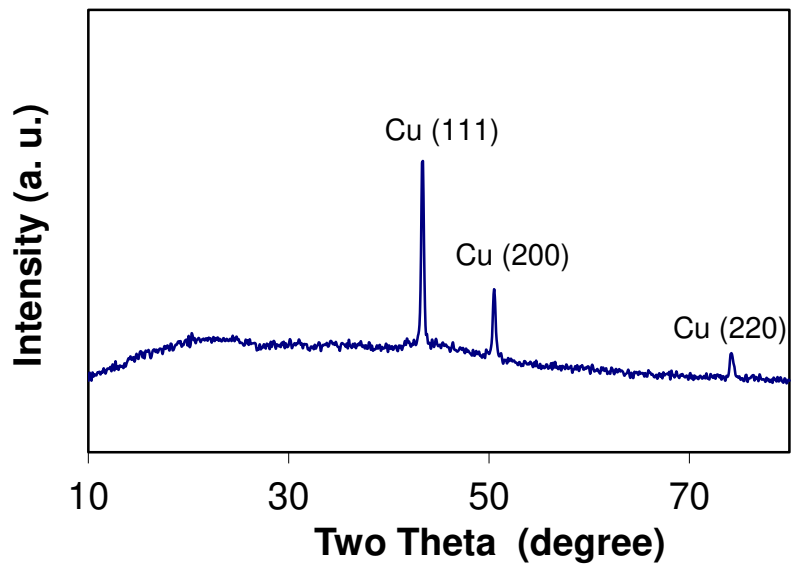
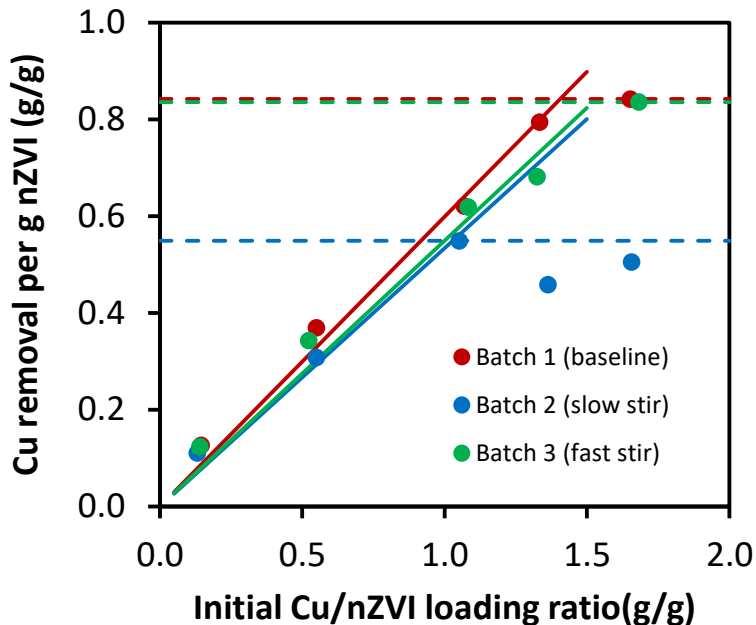
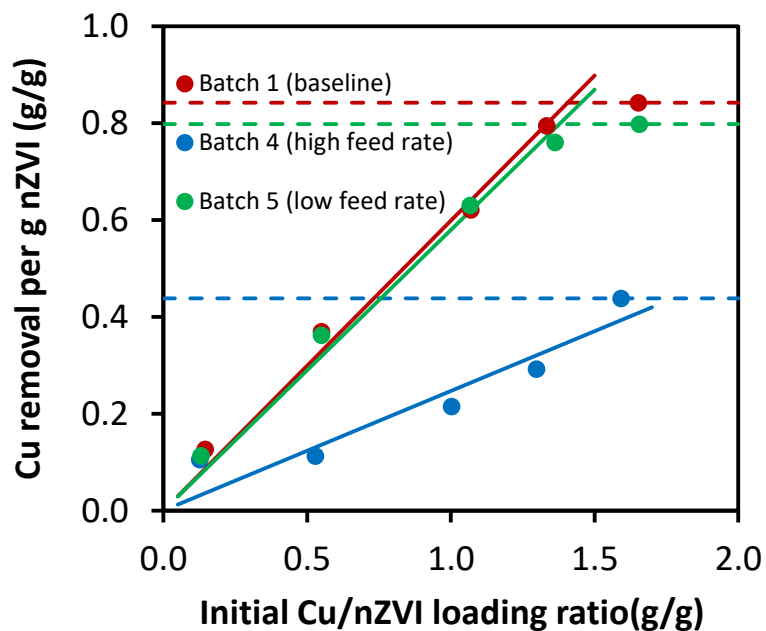


Figure 2.3 Identification of Cu(II) reduction products with X-ray diffraction analysis.

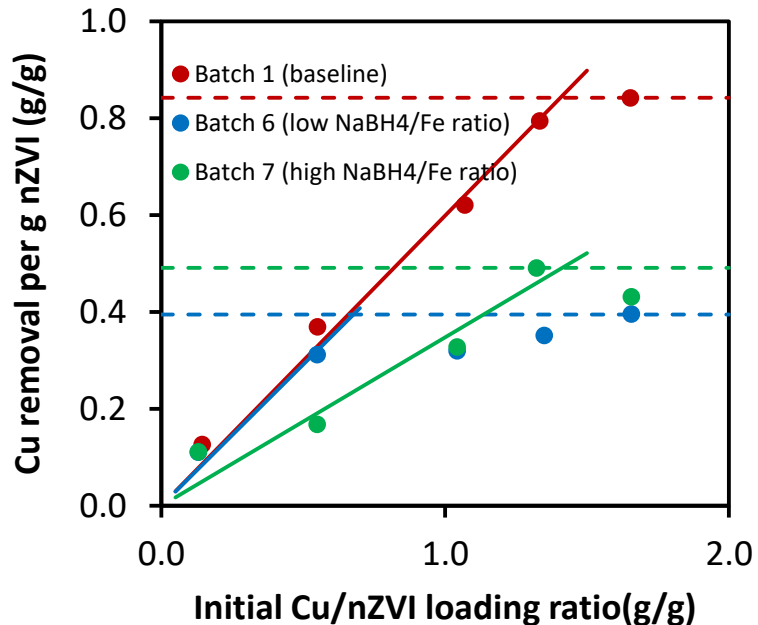
(a)



(b)



(c)



(d)

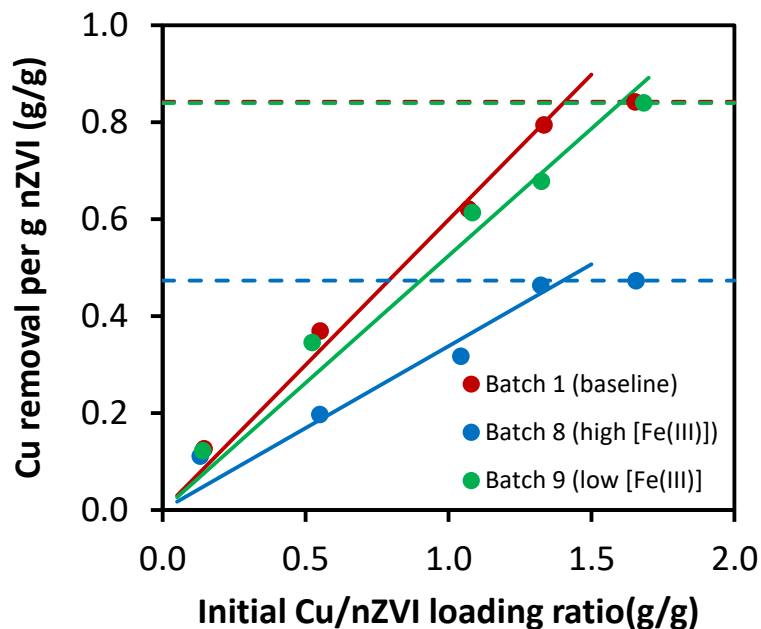
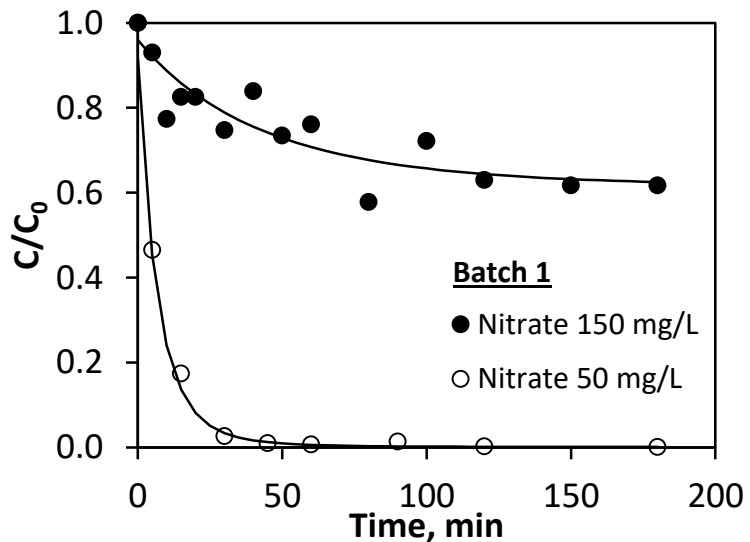
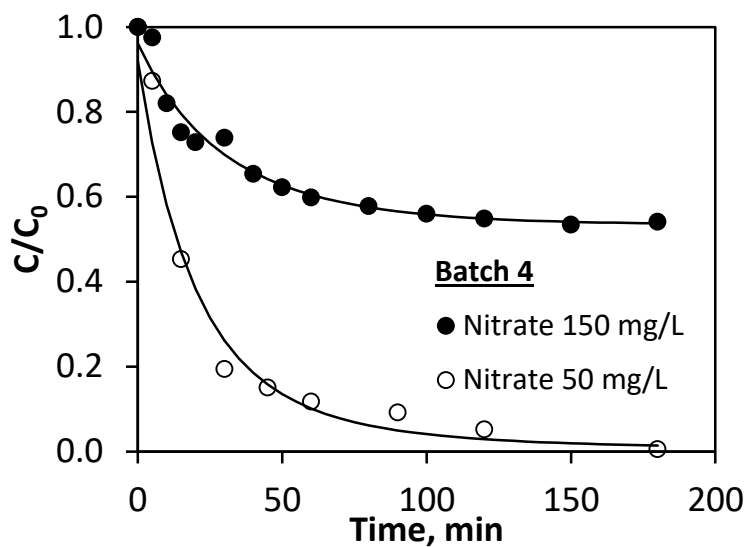


Figure 2.4 Cu(II) reduction by nZVI prepared under different synthesis conditions. (a) Effect of solution agitation speed, (b) effect of reductant feed rate, (c) effect of initial Fe(III) concentration, and (d) effect of reductant to iron molar ratio. For each nZVI, the initial slope at low Cu/nZVI loading ratio was fitted to a straight line, and the maximum Cu(II) removal per unit mass of nZVI was denoted by a dashed line.

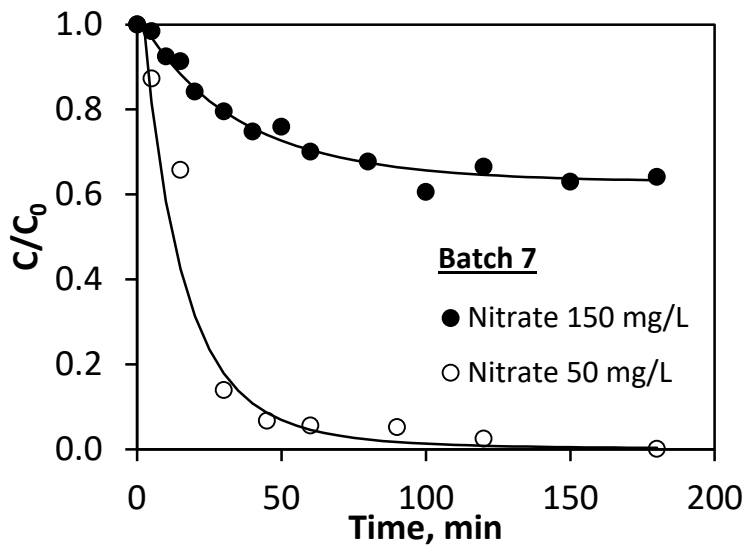
(a)



(b)



(c)



(d)

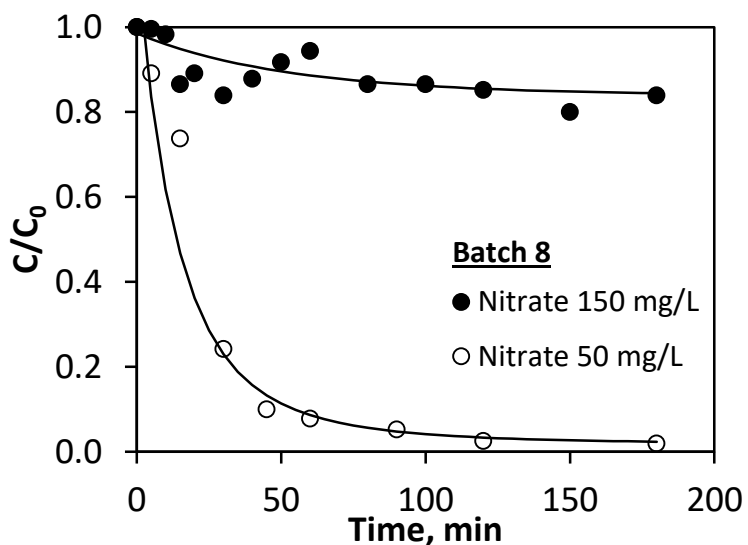


Figure 2.5 Nitrate reduction by nZVI of different synthesis batches. Initial nitrate concentration was 50 mg/L and 150 mg/L, respectively. Dose of nZVI was 2 g/L. Solid lines are model fit to experimental data using the pseudo-first-order reaction and first-order deactivation model.

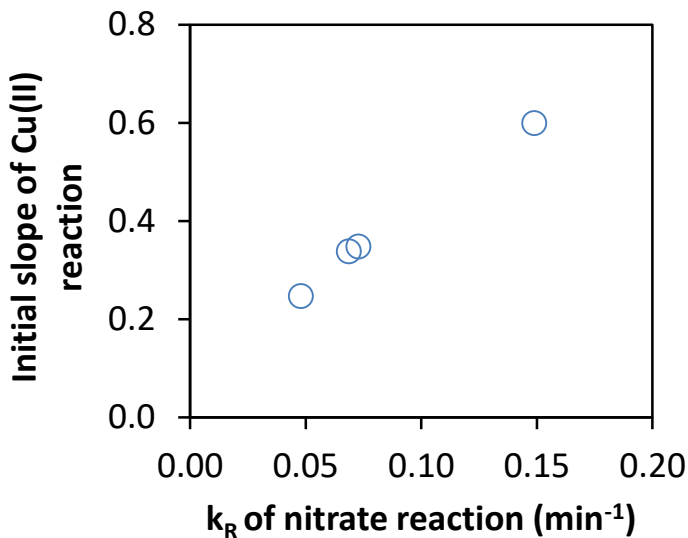


Figure 2.6 Correlation of the initial slope of Cu(II) reduction data with kinetics of nitrate reduction experiments.

CHAPTER THREE

Bimetallic Nickel-Iron Nanoparticles for Groundwater Decontamination: Effect of Groundwater Constituents on Surface Deactivation²

3.1. Introduction

The applications of bimetallic iron nanoparticles (BNPs) to groundwater and soil remediation are prominent examples of recent advancements in environmental nanotechnology ¹. The BNPs are typically comprised of zero-valent iron (Fe(0)) as the base metal and electron source and a small amount of a second metal (*e.g.* palladium and nickel) as catalyst additives ²⁻⁶. Compared to iron alone, the presence of a second metal often brings about enhancement in reaction rates towards organohalides including chlorinated ethenes, chlorobenzenes, and polychlorinated biphenyls (PCBs) ^{2, 7-9}. Another notable advantage of BNPs is their propensity to form more completely dehalogenated hydrocarbons ^{2, 10-12}, which greatly circumvents the accumulation of toxic intermediates (*e.g.*, vinyl chloride). It is conceived that these beneficial effects are resulted from a combination of factors, including higher rates of Fe(0) oxidation and release of electrons¹³, the ability of the metal additives to generate and store active hydrogen species ^{3, 10}, and strong interactions between catalyst sites and contaminants to form surface complexes for more facile dehalogenation transformations ¹⁴⁻¹⁶.

Many structural characteristics of BNPs, including size and morphology of the base metal particles, mass loadings of the catalyst additives, and their chemical states and physical distribution in the particle volume are known to influence the reactivity of BNP particles. Heterogeneous distribution of catalyst metals on BNP surface has been observed in various bimetallic systems ^{10, 17-19}. This is particularly the case for particles prepared via aqueous reductive deposition on pre-formed iron nanoparticles (*i.e.*, the common approach for preparing Pd-Fe particles) as the reduced metal catalyst may serve

² This chapter is published as: Yanlai Han, Weile Yan. Bimetallic nickel–iron nanoparticles for groundwater decontamination: Effect of groundwater constituents on surface deactivation. Water Research, 2014. Elsevier Publishing Company.

as additional cathode sites catalyzing rapid reduction of the catalyst precursors, leading to island-like formations of additive metals instead of a uniform surface layer^{3, 5, 18}. Another common approach to produce BNPs is through simultaneous reduction (co-reduction) of iron and additive metal precursors by sodium borohydride in one reaction pot, which can result in different intra-particle distribution and dispersion of the catalysts from those prepared with the solution deposition method. Curiously, majority of the Ni-Fe materials studied in the past were produced using the co-reduction method^{2, 6}. The hydrodechlorination reactivity and material susceptibility to common solutes in groundwater for Ni-Fe prepared by different methods have not been compared explicitly.

The chemical stability of BNPs in complex groundwater media is a crucial consideration in assessing the feasibility of this remediation technology in actual field applications. While most of the prior studies employed freshly synthesized Ni-Fe nanoparticles, a clear understanding of the effect of background constituents in groundwater on particle reactivity is not available thus far. An interesting contrast among different iron-based BNPs is that the deactivation behavior of Pd-amended iron nanoparticles (Pd-Fe BNPs) is expected to differ significantly from that of Ni-Fe BNPs due to the intrinsic differences in their electrochemical properties and in the chemical speciation of the additive metals in the presence of the iron material. Previous studies have observed rapid deactivation of Pd-amended BNPs in simple aqueous media without salt amendment^{9, 18}. With aberration-corrected analytical electron microscopic characterizations, it was reported that the Pd-Fe particles experienced pronounced oxidation of the zerovalent iron and the Pd(0) sites originally present on the outer surface of the nanoparticles were engulfed by an extensive matrix of iron oxide after 24 h of immersion in an aqueous solution¹⁸. In comparison, monometallic iron nanoparticles were able to retain a significant fraction of the Fe(0) component for over a month in deoxygenated waters^{20, 21}. The excessively fast corrosion occurred in the case of Pd-Fe can cause loss of Fe(0) to unproductive reaction with water, leaving no stable form of reductant in the soil media for sustained contaminant reduction. Pd metal is also known to be strongly deactivated by groundwater constituents such as dissolved organic matter and reduced sulfur ligands²². Although the rapid deactivation of Pd-Fe BNPs observed in

simple laboratory reaction media may be alleviated to some degrees in real groundwater media owing to background solutes serving as corrosion inhibitors (e.g. dissolved silica), the intrinsic material instability in Pd-Fe will remain a significant barrier when promulgating the technology to large-scale field applications. Compared to palladium ($E_H, Pd(II)/Pd(0)^0 = 0.92$ V), the standard reduction potential of nickel ($E_H, Ni(II)/Ni(0)^0 = -0.28$ V) is close to that of iron ($E_H, Fe(II)/Fe(0)^0 = -0.44$ V) (Bard et al. 1985), and one would expect that galvanic effect would play a less important role in the deactivation of Ni-Fe BNPs. Furthermore, in solutions where a strongly reducing environment cannot be established (e.g. when Fe(0) is limiting or in the presence of background oxidants), a sizable fraction of nickel may present as Ni(II) on the particle surface. This suggests that the chemical stability of surface nickel sites would be markedly different from those of Pd material. Prior studies have noted that Ni-Fe BNPs endured repeated cycles of reactions without significant loss of reactivity^{2,5}. However, as these studies were conducted in simple solutions without electrolytes, a detailed investigation to look at the effect of common background solutes on the deactivation of Ni-Fe nanoparticles is warranted.

In this study, we prepared Ni-Fe BNPs via two widely adopted synthesis approaches, namely, (i) co-reduction of Ni(II) and Fe(III) in borohydride solutions, and (ii) deposition of nickel on pre-formed Fe(0) nanoparticles. Three different nickel salts were used in these methods to evaluate their effects on the reactivity of the resultant particles. The as-synthesized particles were immersed in solutions amended with groundwater anions and/or dissolved organic matter for a period of 24 h. We then assessed the reactivity of the particles through batch reactions with trichloroethylene (TCE), a prevalent groundwater contaminant. Analysis of reaction kinetics and product distribution in conjunction with microscopic and surface chemistry characterizations allows us to probe the nature of the catalytic sites and the causes of their deactivation.

3.2. Materials and Methods

3.2.1. Preparation of Nanoparticles

Ni-Fe BNPs were synthesized using two approaches. The first approach involves the reduction of an aqueous solution of Fe(III) ($FeCl_3$, Fisher) and Ni(II) with sodium

borohydride (NaBH_4 , Acros Organics) as described in several previous studies^{5, 24}. Briefly, 6.5 g of FeCl_3 (corresponding to 0.08 M) and an appropriate amount of Ni(II) salt were dissolved in 500 mL of distilled de-ionized (DDI) water and ethanol mixture (1:1, v/v). 500 mL of NaBH_4 solution (0.4 M) was introduced into the metal precursor solution at approximately 17 mL/min under intensive mixing. The particles thus obtained are referred to as co-reduced particles (denoted with a prefix of *CR-*). In the second method, monometallic Fe nanoparticles were synthesized first via reduction of an Fe(III) solution by sodium borohydride, following similar settings as the first method. The freshly prepared Fe nanoparticles were then added into a Ni(II) solution in 30:70 (v/v) ethanol/water mixture and mixed for 30 min. The particles formed are denoted as solution deposited (with a prefix of *SDP-*) bimetallic nanoparticles. In this study, Ni(II) was from one of the three Ni(II) salts (NiSO_4 , Aldrich; $\text{NiCl}_2 \cdot 6\text{H}_2\text{O}$, Alfa Aesar; and $\text{Ni}(\text{CH}_3\text{COO})_2$, Aldrich) and its concentration with respect to Fe(III) was fixed at 2 wt.% in all synthesis batches. DDI water used in all procedures, including particle synthesis, aging and TCE experiments, was deoxygenated by N_2 -purging.

3.2.2. Aging Experiments

Aging experiments were conducted in 45-mL EPA glass vials containing 30 mL of deoxygenated solutions amended with a groundwater solute at 0.1-5 mM. Stock solutions of chloride, bicarbonate, nitrate, phosphate, sulfite, and sulfate were prepared from their sodium salts. Stock solution of humic acid (Sigma-Aldrich, used as received) was prepared at 50 mg/L and was ultrasonicated for 10 min prior to use. The initial pH of the solutions was adjusted with dilute NaOH or HCl to between a range of 8.1-8.3 to simulate the typical pH values encountered in groundwater. An appropriate amount of freshly made BNPs was added into each solution at 1-3.3 g/L (dry weight) and the vial was sealed and agitated on a mechanical shaker for 24 h at room temperature (22 +/- 1 °C). The aged particles were collected by vacuum filtration and were used immediately in TCE degradation experiments. The solutions after aging experiments were analyzed for dissolved metal concentrations using an atomic absorption spectrometer (Perkin Elmer AAnalyst 800).

3.2.3. TCE Experiments

TCE dechlorination experiments were performed to compare the reactivity of fresh and aged BNPs. All batch experiments were conducted in 45-mL EPA vials containing 30 mL of aqueous solution and the balance as headspace. Experiments were performed with fresh or aged nanoparticles added at 1- 3.3 g/L (dry weight) and an initial concentration of TCE at 50 mg/L. Control experiment without nanoparticles was performed in parallel. The vials were capped with Teflon Mininert valves and placed on a mechanical shaker at 250 rpm at room temperature. Periodically, an aliquot (25 - 50 µL) of headspace gas was withdrawn using a gastight syringe and analyzed for TCE concentrations using a GC system (Agilent 6890) equipped with a Supelco SPB 624 capillary column and an electron capture detector (ECD). The amount of TCE in the solution was deduced from its concentration in the headspace using Henry's constant. Reaction intermediates and products were identified using a GC system (Thermo Scientific TRACE GC Ultra) with an Agilent PoraPlot Q column and a flame ionization detector (FID). Direct headspace injections (200 -500 µL) were made and concentrations were calibrated using commercial standards.

3.2.4. Material Characterization

Nanoparticles were dried immediately after synthesis or aging treatments in a glove-box purged with high purity N₂ for up to 48 h. The dried solids were stored in N₂-filled gastight vials prior to analysis. High resolution X-ray photoelectron spectroscopy (HR-XPS) analysis was performed on a PHI 5000 Versa Probe system using a monochromated AlK α radiation. Sample preparation follows the procedure we described previously ²⁵. High-resolution scans were acquired at a 45° takeoff angle and 150 eV pass energy. The software package CasaXPS (Version 2.3.16PR1.6) was used for HR-XPS spectral analysis. The binding energy was referenced to the C1s peak of adventitious carbon at 284.6 eV. Detailed curve-fitting procedure is in the Supporting Information. Morphology of the particles was characterized with a transmission electron microscope (JOEL 1200 EX) using the conventional bright-field imaging mode at 75 – 200 kV.

3.3. Results and Discussion

3.3.1. Reactivity of Fresh Ni-Fe BNPs

Ni-Fe particles were commonly produced in laboratories by co-reduction of aqueous mixture of Fe(II) or Fe(III) and Ni(II)^{2,17} or by reacting pre-formed iron nanoparticles in Ni(II) solutions²⁶. It is difficult to compare the quality of particles reported in those studies because of different synthesis conditions and Ni loadings employed. In the present study, we prepared co-reduced (*CR*-) or solution deposited (*SDP*-) Ni-Fe BNPs at a fixed Ni content (2 wt.%) under similar reaction settings. Figure 3.1 shows TEM images of freshly synthesized *CR*-Ni-Fe and *SDP*-Ni-Fe, respectively. The fresh *CR*-Ni-Fe appears similar to undoped Fe characterized in prior studies in that particles generally assume a spherical shape and are aggregated into small clusters or chains. Each primary particle consists of a well-defined dark phase in the center surrounded by a continuous skin of lighter contrast, corresponding to the metallic iron (Fe(0)) and a passivating layer of iron oxide, respectively. The similarity in electron density of Ni and Fe precludes us from identifying the location of Ni dopants in the nanoparticles and this will be investigated later using HR-XPS analysis. In comparison to co-reduced particles, *SDP*-Ni-Fe contains a significant amount of acicular structures covering the surface of the particles, which resembles solution-formed ferric (oxyhydr)oxides. Their formation can be explained by the particle synthesis method, since solution deposition of Ni involves a metal replacement reaction ($\text{Ni(II)} + \text{Fe(0)} \rightarrow \text{Ni(0)} + \text{Fe(II)}$) that leads to dissolution of Fe(II) and its subsequent oxidation and precipitation as ferric (oxyhydr)oxides. Figure 3.1(c) depicts *CR*-Ni-Fe particles aged in a 5 mM phosphate solution for 24 h. No significant change in morphology with respect to the fresh particles can be discerned, although interestingly these particles were virtually inactive as will be discussed in a later section.

Figure 3.2 shows TCE degradation with different fresh Ni-Fe particles. TCE concentration was reduced to less than 55 µg/L within 90 min in all experiments. Table 3.1 tabulates the mass-normalized pseudo-first-order reaction rate constants²⁷, k_m , which were obtained by normalizing the apparent reaction rate constants by the mass

concentration of the particles. k_m values of fresh Ni-Fe BNPs exceed that of the monometallic iron (inset of Figure 3.2) by more than two orders of magnitude and are comparable to as-synthesized Pd-Fe BNPs at a similar metal additive loading¹⁸, confirming that Ni is an efficient dehalogenation catalysts for chlorinated ethenes.

The concentration of Ni (as atomic percentage) on the surface of particles was analyzed by HR-XPS (Table 3.2). It is noticed that the near-surface Ni content suggested by HR-XPS data is considerably lower than the nominal Ni mass fraction (2 wt.%), which is attributed to the deposition of iron oxides on the particles during the synthesis processes. Fresh *SDP*-Ni-Fe seems to carry higher Ni content on the surface than co-reduced particles. The difference, however, does not translate to obvious difference in reaction rates. Lastly, Ni precursors do not seem to impose a significant effect on the reactivity of the resultant particle, and for this reason nickel acetate was used in all subsequent experiments.

3.3.2. Mildly Deactivating Groundwater Solutes

The reactivity of Ni-Fe BNPs after 24 h of pre-immersion in various groundwater solutes was evaluated with TCE batch experiments. Figure 3.3 shows the decrease in aqueous TCE concentration after addition of aged *CR*-Ni-Fe nanoparticles. Based on the k_m of TCE dechlorination, the groundwater solutes can be classified into two groups: the mildly deactivating solutes (Figure 3.3a) and species that strongly inhibit surface reactivity (Figure 3.3b). Particles aged in DDI water and 5 mM of Cl⁻, HCO₃⁻, and SO₃²⁻ exhibited mild decreases in reactivity ($k_m = 0.62 - 1.6 \times 10^{-2}$ L/g-min) relative to the freshly made *CR*-Ni-Fe particles (Table 3.1). The rate constants of HCO₃⁻ and SO₃²⁻ are essentially equivalent to that of the DDI-aged particles within experimental uncertainty. Cl⁻ has a moderate deactivating effect on Ni-doped iron nanoparticles, resulting in approximately 40% decrease in k_m compared to particles aged in pure water. Stable reactivity in the presence of SO₃²⁻ and Cl⁻ ions is a notable strength of the Ni-Fe material considering their pronounced deactivating effects on Pd-based catalyst materials. The presence of aqueous sulfite and sulfide species is known to lead to pronounced poisoning of Pd catalysts²⁹⁻³¹. Elevated concentrations of halide ions such as Cl⁻ and Br⁻ are able to

form stable complexes with Pd and diminish its reactivity^{11,32}, giving rise to an undesired self-inhibition mechanism when chloride ions are produced as by-products of TCE reduction. Another potent deactivator of Pd catalysts is the ubiquitous dissolved organic carbon (DOC)^{33,34}. In the present study where humic acid (HA) was used as a surrogate of DOC, we did not observe an appreciable inhibitory effect of HA, implying Ni and Pd catalysts are considerably different in terms of material stability in groundwater matrices.

Figure 3.4 shows distribution of reaction products from TCE dechlorination reactions. For fresh *CR*-Ni-Fe, continuous decrease in TCE concentration was accompanied by the formation of predominantly ethane and relatively small quantities of ethene and acetylene. These species plus minor products such as C₄ carbons (e.g. *n*-butane) sum up to a final carbon recovery around 95% (Figure 3.4a). To compare product distribution among different nanoparticles, we determined ethane yield, Y_{ethane}, which is the molar ratio of ethane formed to total products as two-carbon equivalents at 90% removal of TCE. As listed in Table 3.1, Y_{ethane} of the as-synthesized Ni-Fe and monometallic Fe nanoparticles are 0.80 and 0.07, respectively. The large Y_{ethane} attained through the use of fresh Ni-Fe nanoparticles attests to the notion that surface amendment of iron nanoparticles with a small amount of Ni greatly favors the formation of saturated hydrocarbons. We also did not observe noticeable levels of chlorinated intermediates, such as dichloroethylenes (*cis*-, *trans*- and 1,1-DCEs) and vinyl chloride (VC), in the Ni-Fe systems, which are in consistency with other studies employing Ni-Fe bimetallic materials^{2,35}. Aging of *CR*-Ni-Fe in a mild deactivating media (5 mM Cl⁻) gave a similar product distribution (Y_{ethane} = 0.69) as the fresh particles (Figure 3.4b), indicating that the Cl⁻ ions in the background matrix does not impose a strong deactivation effect on the Ni sites.

3.3.3. Solutes with Strong Deactivation Effects

Pre-exposure of *CR*-Ni-Fe to 5 mM of NO₃⁻, SO₄²⁻, and phosphate (predominantly as HPO₄²⁻ under the experimental pH) caused severe loss of reactivity as shown in Figure 3.3b. In the presence of NO₃⁻ and SO₄²⁻, TCE was degraded progressively, although at

considerably slow speeds. The reaction rate constants of particles exposed to the two solutes are approximately an order of magnitude smaller than that of the fresh particles. With particles aged in a 5 mM phosphate solution, a drop in TCE concentration was noticed in the first 1 h, however, no further attenuation in TCE concentration nor product formation could be observed during the remaining experiment period (Figure 3.4c), implying aging in 5 mM of phosphate solution has resulted in near complete surface deactivation. To evaluate the effect of solution concentrations on the extent of particle deactivation, aging was conducted in SO_4^{2-} and HPO_4^{2-} media at lower concentrations. Figure 3.5 shows that the degree of deactivation increases gradually with increasing SO_4^{2-} concentration from 0.1 to 5 mM, whereas there is a more sharp reduction in reactivity with increasing HPO_4^{2-} concentration within the same concentration range (Figure 3.6). Therefore, Ni-Fe particles are most susceptible to phosphate species among the common anions present in the groundwater media. The threshold phosphate concentration before the onset of complete deactivation is between 1 - 3 mM. To understand whether the severe loss of reactivity in phosphate solutions took effect gradually during the exposure period, we spiked 5 mM HPO_4^{2-} into a TCE solution with fresh Ni-Fe particles and observed the reaction rates after phosphate injection. Surprisingly, the results are similar to those of the pre-aged particles (Figure 3.6), confirming that deactivation of Ni-Fe BNPs occurred almost instantaneously after Ni-Fe BNPs were in contact with phosphate ions. Similarly, we observed that the deactivation caused by SO_4^{2-} ions was triggered within the initial stage of contact. NO_3^- , however, requires prolonged exposure before its inhibitory effect was manifested (data not shown).

3.3.4. Deactivation of *SDP*-Ni-Fe BNPs

It is noticeable in Figure 3.7 that some common behaviors are shared by the *SDP*- and *CR*-Ni-Fe BNPs. The particles aged in DDI water for 24 h retain most of the reactivity as the fresh particles. Cl^- , HCO_3^- , and SO_3^{2-} brought about moderate inhibition effects, as they did for the *CR*-Ni-Fe. Particles aged in SO_4^{2-} and HPO_4^{2-} solutions possessed the lowest reactivity. Based on the experimental results, the extent of inhibitory effects of different groundwater solutes on *SDP*-Ni-Fe nanoparticles towards TCE

dechlorination is in the increasing order of: DDI < Cl⁻ < HCO₃⁻ < SO₃²⁻ < SO₄²⁻ ≈ phosphate. In spite of similarity, *SDP*-Ni-Fe and *CR*-Ni-Fe show some noticeable differences in their deactivation behaviors. *SDP*-Ni-Fe particles were more severely impaired than *CR*-Ni-Fe in Cl⁻, HCO₃⁻, SO₃²⁻ and SO₄²⁻ media, although the reactivity of the two types of particles aged in DDI water are similar. Higher susceptibility of solution-deposited particles to groundwater solutes is likely related to more Ni being exposed on the exterior surface of the particles, as discussed in the surface analysis section below. Both types of particles suffered virtually complete deactivation in phosphate media, implying the deactivation mechanism of phosphate ions is independent of the synthesis route and surface distribution of Ni species.

3.3.5. Surface Chemistry Analysis with XPS

Figure 3.8 shows the Ni 2p_{3/2} HR-XPS spectra of *CR*-Ni-Fe materials. The peak at 852.2 eV was assigned to metallic nickel (Ni(0)). The metallic phase also gives a broad satellite at ca. 858.7 eV due to energy loss to surface plasmon ³⁶. The spectra of Ni(II) species contain two broad envelopes at 855.6 eV and 861.8 eV, respectively, corresponding to Ni(II) multiplet structures arising from interactions between unpaired *d* electrons ³⁸. We did not attempt to resolve these component peaks given that the intensities of Ni2p_{3/2} XPS signals are fairly weak. The line shapes and peak positions appear to be similar to the spectra of Ni(II) in a hydroxide environment (Ni(OH)₂) ^{36, 37}. It can be seen in Figure 3.8a that the surface of fresh *CR*-Ni-Fe is predominantly Ni(II). Ni(0) constitutes a minor fraction (ca. 11 at%) of the surface Ni sites. This finding sets up an interesting contrast with Pd-Fe BNPs, where Pd was reported to deposit on the iron surface primarily as Pd(0) ¹⁸. Sputtering the fresh *CR*-Ni-Fe particles with argon plasma for 2.5 min, corresponding to a sputtering depth of *ca.* 4 nm, reveals a large increase in the Ni(0) component (Figure 3.7(b)), which implies Ni(0) is more enriched in the interior structure than being at the surface. Upon aging in a deoxygenated DDI solution, all surface Ni(0) was oxidized to Ni(II) state (Figure 3.7(c)). Since we have deliberately avoided exposing the samples to atmosphere during sample drying and preparation stages (as mentioned in Materials and Methods), the results reflect the chemical states of Ni

formed in the respective solution media. Furthermore, the prevalence of Ni(II) on the external surface of fresh and DDI-aged particles is consistent with theoretical considerations since the redox potential of Ni(II)/Ni(0) favors the formation of Ni(II) at the interface in contact with aqueous solutions.

Figure 3.9 shows the XPS analysis of various types of *SDP*-Ni-Fe particles. The fresh *SDP*-Ni-Fe contains Ni(II) but no Ni(0) on the surface (Figure 3.9a). Upon 2.5 min sputtering treatment, the XPS signals of nickel were greatly attenuated (Figure 3.9b), indicating that Ni was residing predominantly on the surface of the particles. The spatial distribution and speciation of nickel are in line with the particle synthesis history. Li *et al.* have observed that reactions of Ni(II) solutions with iron nanoparticles consist of rapid adsorption of Ni(II) followed by a slow conversion of surface-bound Ni(II) to Ni(0) over a period of 24 h, even though a large stoichiometric excess of Fe(0) was present in the system³⁹. In this study, since we employed a relatively brief mixing time of 30 min during the solution deposition process, the formation of Ni(0) would have occurred to a limited extent. The XPS data is consistent with this prediction. Although only a small amount of Ni(0) was present, the fresh *SDP*-Ni-Fe exhibited excellent reactivity comparable to co-reduced counterparts. This interesting behavior suggests that TCE dechlorination rate is not limited by the amount of nickel catalysts, but likely controlled by other processes such as diffusion of reactants through the surface oxide layer and/or adsorption at active sites. The lack of a strong correlation between particle reactivity and the mass quantity of catalytically active species has been observed in other studies, which reflects complex processes involved in heterogeneous catalysis reactions⁴⁰. Furthermore, in the case of bimetallic iron nanoparticles, an increase in catalyst doping may result in more severe iron oxidation and greater surface passivation and thereby may not translate to more favorable particle reactivity⁴¹.

Lastly, Figure 3.9c presents the spectrum of the *SDP*-Ni-Fe aged in a phosphate solution. No significant attenuation of the Ni 2p_{3/2} photoelectron signals was observed after phosphate treatment, thereby ruling out deposition of iron oxidation products as the main cause of particle deactivation in phosphate solutions. This XPS data also

corroborates with the TEM images of the fresh and phosphate-aged particles (Figure 3.1c) in which the two types of particles were shown to have similar morphology. This insight, in conjunction with the experimentally observed immediate deactivating effect of phosphate, favors a deactivation mechanism involving specific poisoning of the catalyst sites by phosphate ions via formation of strong complexes.

3.3.6. Reaction Pathway and Deactivation Mechanisms

Both metallic nickel or nickel(II) compounds (*e.g.* sulfide or oxide form of Ni(II)) are widely applied in commercial catalysts for hydrodechlorination and hydrotreating applications^{42, 43}. The degradation mechanisms of chlorinated ethylenes on transition metals or metal oxides are generally described as involving the chemical adsorption of the contaminants to form di- σ -bonded surface complexes, breaking of C-Cl bonds via hydrogenolysis or β -elimination, and subsequent hydrogenation of acetylene or ethene to ethane⁴⁴. Comparing the k_m of TCE removal and product distribution for monometallic Fe and Ni-Fe nanoparticles, nickel seems to catalyze both the hydrodechlorination and hydrogenation processes. The absence of lesser chlorinated intermediates and the emergence of C₄ compounds in the product stream indicate that β -elimination is a more important pathway than step-wise hydrogenolysis.

The prevalent speciation of nickel as Ni(II) in Ni-Fe BNPs greatly decreases the galvanic effect between the Fe(0) and the catalyst additive. Therefore, in contrast to palladized iron particles that causes rapid corrosion of Fe(0), Ni-Fe BNPs are expected to be able to sustain reactivity in simple aqueous solutions for longer periods of time. In water with high levels of electrolytes, Ni-Fe BNPs have shown good resistance to species known to deactivate noble metal catalysts, such as Cl⁻, SO₃²⁻, and HA. However, Ni-Fe BNPs are sensitive to high levels of NO₃⁻, SO₄²⁻ and phosphate ions. Earlier studies attribute nitrate-induced deactivation to the formation of less reactive oxide phase^{45, 46}, which is supported by our XPS analysis showing a significant decrease in surface Fe(0) content after aging in a nitrate solution (Table 3.2) and by our observation that deactivation requires extended immersion in nitrate solutions. Both SO₄²⁻ and phosphate may impede the reactions by forming complexes with surface iron and nickel species. In

both cases, deactivation was observed upon immediate contact with the respective ions. The strength of the deactivation agents seem to be in line with the stability constants of the Ni(II) complexes with sulfate or phosphate ligands (Eq. 1-2) ⁴⁷.



Our equilibrium calculation indicates that, at the dose of particles used in this study and assuming all nickel is present at the surface accessible to surface complexation, approximately 90% of nickel sites would be in phosphate complexes if the solute is present at 1 mM, whereas only 67% of the nickel sites would be engaged in complexes at the same concentration of sulfate. This result agrees reasonably well with the experimentally observed declines in particle dechlorination activity in the respective solutions. It is worth noting that palladium catalysts have been reported to be unaffected by phosphate ions ²², which can be rationalized based on the fact that palladium is predominantly in the metallic state. Metallic palladium is a considerably soft Lewis acid and does not interact with phosphate as strongly. Majority of the nickel, on the other hand, is present as Ni(II) on Ni-Fe due to the electrochemical character of the bimetallic material, hence Ni-Fe particles are prone to poisoning by hard ligands such as sulfate and phosphate ions. It should be noted that in actual groundwater systems where the concentrations of both the Ni-Fe particles and the deactivating solutes may be lower, the debilitating actions of solutes may be affected by other dominant surfaces such as silica, iron or manganese oxides and require further investigations.

3.4. Conclusions and Environmental Implications

Results presented in this study show that as-synthesized Ni-amended iron nanoparticles is an efficient material for dechlorination of trichloroethylene and its reactivity is comparable to the palladium-catalyzed iron nanoparticles. A notable strength of Ni-Fe nanoparticles compared to their palladium counterpart is that Ni-Fe is electrochemically stable in the aqueous environment and it possesses good chemical resistance to common solutes in groundwater such as chloride, bicarbonate, and dissolved

organic matter. However, anions such as NO_3^- , SO_4^{2-} and phosphate may cause moderate to severe catalyst deactivation at elevated concentrations (1- 5 mM). Nitrate decreases particle reactivity gradually due to formation of passivating oxides, whereas sulfate and phosphate elicited rapid loss of reactivity as a result of specific poisoning of the active nickel sites. At similar levels, phosphate is the most potent deactivation agent among the solutes examined in this study. Although the concentrations of the anions used in this study are on the high side of their typical environmental occurrence, large spatial variability across different contaminant sites is expected as phosphate, nitrate and sulfate are strongly tied to local hydrogeological formations (e.g. coastal plains subject to estuarine water influence), microbial activities, and anthropogenic inputs. Remediation practitioners may find it of great relevance to assess groundwater characteristics and perform laboratory tests using actual water samples from the contamination sites prior to engaging up-scale studies. One consideration that has hampered the deployment of Ni-Fe BNPs for *in situ* remediation of contaminated groundwater is concerns over potential Ni release. In this study, we analyzed dissolved nickel concentration in the aging media and TCE solutions and found less than 1% of the initial Ni deposited on the particles was released into the aqueous phase after aging and TCE experiments (Table S3.1). Although our experiments were conducted in short periods of time compared to the actual time frames taken to restore a contaminated site, enhanced electrochemical stability and greater material availability with respect to Pd-Fe suggest that Ni-Fe nanoparticles is a viable alternative for hydrodechlorination of chlorinated ethenes in groundwater and other waste streams. The different chemical resistance of Ni and Pd-based bimetallic materials to background solutes suggest that opportunities may exist in material selection and optimization to improve the efficiency of environment clean-up efforts.

References

1. Karn, B.; Kuiken, T.; Otto, M., Nanotechnology and *in situ* remediation: A review of the benefits and potential risks. *Environmental Health Perspectives* **2009**, *117*, (12), 1823-1831.
2. Schrick, B.; Blough, J.L.; Jones, A.D.; Mallouk, T.E., Hydrodechlorination of trichloroethylene to hydrocarbons using bimetallic nickel-iron nanoparticles . *Chemistry of Materials* **2002**, *14*, (12), 5140-5147.

3. Lien, H.L.; Zhang, W.X., Nanoscale Pd/Fe bimetallic particles: Catalytic effects of palladium on hydrodechlorination. *Applied Catalysis B-Environmental* **2007**, 77, (1-2), 110-116.
4. He, F.; Zhao, D.Y., Preparation and characterization of a new class of starch-stabilized bimetallic nanoparticles for degradation of chlorinated hydrocarbons in water. *Environmental Science & Technology* **2005**, 39, (9), 3314-3320.
5. Chun, C.L.; Baer, D.R.; Matson, D.W.; Amonette, J.E.; Penn, R.L., Characterization and Reactivity of Iron Nanoparticles prepared with added Cu, Pd, and Ni. *Environmental Science & Technology* **2010**, 44, (13), 5079-5085.
6. Tee, Y.H.; Bachas, L.; Bhattacharyya, D., Degradation of Trichloroethylene and Dichlorobiphenyls by Iron-Based Bimetallic Nanoparticles. *Journal of Physical Chemistry C* **2009**, 113, (22), 9454-9464.
7. Zhang, W.X.; Wang, C.B.; Lien, H.L., Treatment of chlorinated organic contaminants with nanoscale bimetallic particles. *Catalysis Today* **1998**, 40, (4), 387-395.
8. Choi, H.; Al-Abed, S.R.; Agarwal, S.; Dionysiou, D.D., Synthesis of reactive nano-Fe/Pd bimetallic system-impregnated activated carbon for the simultaneous adsorption and dechlorination of PCBs. *Chemistry of Materials* **2008**, 20, (11), 3649-3655.
9. Zhu, B.W.; Lim, T.T., Catalytic reduction of Chlorobenzenes with Pd/Fe nanoparticles: reactive sites, catalyst stability, particle aging, and regeneration. *Environmental Science & Technology* **2007**, 41, (21), 7523-7529.
10. Cwiertny, D.M.; Bransfield, S.J.; Livi, K.J.T.; Fairbrother, D.H.; Roberts, A.L., Exploring the influence of granular iron additives on 1,1,1-trichloroethane reduction. *Environmental Science & Technology* **2006**, 40, (21), 6837-6843.
11. Urbano, F.J.; Marinas, J.M., Hydrogenolysis of organohalogen compounds over palladium supported catalysts. *Journal of Molecular Catalysis a-Chemical* **2001**, 173, (1-2), 329-345.
12. Lowry, G.V.; Reinhard, M., Hydrodehalogenation of 1-to 3-carbon halogenated organic compounds in water using a palladium catalyst and hydrogen gas. *Environmental Science & Technology* **1999**, 33, (11), 1905-1910.
13. Xu, Y.; Zhang, W.X., Subcolloidal Fe/Ag particles for reductive dehalogenation of chlorinated benzenes. *Industrial & Engineering Chemistry Research* **2000**, 39, (7), 2238-2244.
14. Cheng, I.F.; Fernando, Q.; Korte, N., Electrochemical dechlorination of 4-chlorophenol to phenol. *Environmental Science & Technology* **1997**, 31, (4), 1074-1078.
15. Fennelly, J.P.; Roberts, A.L., Reaction of 1,1,1-trichloroethane with zero-valent metals and bimetallic reductants. *Environmental Science & Technology* **1998**, 32, (13), 1980-1988.

16. Chaplin, B.P.; Reinhard, M.; Schneider, W.F.; Schuth, C.; Shapley, J.R.; Strathmann, T.J.; Werth, C.J., Critical Review of Pd-Based Catalytic Treatment of Priority Contaminants in Water. *Environmental Science & Technology* **2012**, *46*, (7), 3655-3670.
17. Tee, Y.H.; Grulke, E.; Bhattacharyya, D., Role of Ni/Fe nanoparticle composition on the degradation of trichloroethylene from water. *Industrial & Engineering Chemistry Research* **2005**, *44*, (18), 7062-7070.
18. Yan, W.L.; Herzing, A.A.; Li, X.Q.; Kiely, C.J.; Zhang, W.X., Structural Evolution of Pd-Doped Nanoscale Zero-Valent Iron (nZVI) in Aqueous Media and Implications for Particle Aging and Reactivity. *Environmental Science & Technology* **2010**, *44*, (11), 4288-4294.
19. McGuire, M.M.; Carlson, D.L.; Vikesland, P.J.; Kohn, T.; Grenier, A.C.; Langley, L.A.; Roberts, A.L.; Fairbrother, D.H., Applications of surface analysis in the environmental sciences: dehalogenation of chlorocarbons with zero-valent iron and iron-containing mineral surfaces. *Analytica Chimica Acta* **2003**, *496*, (1-2), 301-313.
20. Sarathy, V.; Tratnyek, P.G.; Nurmi, J.T.; Baer, D.R.; Amonette, J.E.; Chun, C.L.; Penn, R.L.; Reardon, E.J., Aging of iron nanoparticles in aqueous solution: Effects on structure and reactivity. *Journal of Physical Chemistry C* **2008**, *112*, (7), 2286-2293.
21. Reardon, E.J.; Fagan, R.; Vogan, J.L.; Przepiora, A., Anaerobic corrosion reaction kinetics of nanosized iron. *Environmental Science & Technology* **2008**, *42*, (7), 2420-2425.
22. Hildebrand, H.; Mackenzie, K.; Kopinke, F.-D., Pd/Fe₃O₄ nano-catalysts for selective dehalogenation in wastewater treatment processes-Influence of water constituents. *Applied Catalysis B-Environmental* **2009**, *91*, (1-2), 389-396.
23. Bard, A.J.; Parsons, R.; Jordan, J.; M. Dekker, *Standard Potentials in Aqueous Solution* **1995**, New York.
24. Ponder, S.M.; Darab, J.G.; Mallouk, T.E., Remediation of Cr(VI) and Pb(II) aqueous solutions using supported, nanoscale zero-valent iron. *Environmental Science & Technology* **2000**, *34*, (12), 2564-2569.
25. Yan, W.; Vasic, R.; Frenkel, A.I.; Koel, B.E., Intraparticle Reduction of Arsenite (As(III)) by Nanoscale Zervalent Iron (nZVI) Investigated with In Situ X-ray Absorption Spectroscopy. *Environmental Science & Technology* **2012**, *46*, (13), 7018-7026.
26. Bransfield, S.J.; Cwiertny, D.M.; Livi, K.; Fairbrother, D.H., Influence of transition metal additives and temperature on the rate of organohalide reduction by granular iron: Implications for reaction mechanisms. *Applied Catalysis B-Environmental* **2007**, *76*, (3-4), 348-356.

27. Nurmi, J.T.; Tratnyek, P.G.; Sarathy, V.; Baer, D.R.; Amonette, J.E.; Pecher, K.; Wang, C.M.; Linehan, J.C.; Matson, D.W.; Penn, R.L.; Driessens, M.D., Characterization and properties of metallic iron nanoparticles: Spectroscopy, electrochemistry, and kinetics. *Environmental Science & Technology* **2005**, 39, (5), 1221-1230.
28. Meyer, D.E.; Bhattacharyya, D., Impact of membrane immobilization on particle formation and trichloroethylene dechlorination for bimetallic Fe/Ni nanoparticles in cellulose acetate membranes. *Journal of Physical Chemistry B* **2007**, 111, (25), 7142-7154.
29. Lim, T.T.; Zhu, B.W., Effects of anions on the kinetics and reactivity of nanoscale Pd/Fe in trichlorobenzene dechlorination. *Chemosphere* **2008**, 73, (9), 1471-1477.
30. Kopinke, F.-D.; Angeles-Wedler, D.; Fritsch, D.; Mackenzie, K., Pd-catalyzed hydrodechlorination of chlorinated aromatics in contaminated waters-Effects of surfactants, organic matter and catalyst protection by silicone coating. *Applied Catalysis B-Environmental* **2010**, 96, (3-4), 323-328.
31. Schuth, C.; Kummer, N.A.; Weidenthaler, C.; Schad, H., Field application of a tailored catalyst for hydrodechlorinating chlorinated hydrocarbon contaminants in groundwater. *Applied Catalysis B-Environmental* **2004**, 52, (3), 197-203.
32. Ordonez, S.; Vivas, B.P.; Diez, F.V., Minimization of the deactivation of palladium catalysts in the hydrodechlorination of trichloroethylene in wastewaters. *Applied Catalysis B-Environmental* **2010**, 95, (3-4), 288-296.
33. Schnitzer, M.; Khan, S.U., *Humic Substances in the Environment* **1972**, Marcel Dekker, New York.
34. Artinger, R.; Buckau, G.; Geyer, S.; Fritz, P.; Wolf, M.; Kim, J.I., Characterization of groundwater humic substances: influence of sedimentary organic carbon. *Applied Geochemistry* **2000**, 15, (1), 97-116.
35. Xu, J.; Dozier, A.; Bhattacharyya, D., Synthesis of nanoscale bimetallic particles in polyelectrolyte membrane matrix for reductive transformation of halogenated organic compounds. *Journal of Nanoparticle Research* **2005**, 7, (4-5), 449-467.
36. Grosvenor, A.P.; Biesinger, M.C.; Smart, R.S.; McIntyre, N.S., New interpretations of XPS spectra of nickel metal and oxides. *Surface Science* **2006**, 600, (9), 1771-1779.
37. Biesinger, M.C.; Payne, B.P.; Grosvenor, A.P.; Lau, L.W.M.; Gerson, A.R.; Smart, R.S.C., Resolving surface chemical states in XPS analysis of first row transition metals, oxides and hydroxides: Cr, Mn, Fe, Co and Ni. *Applied Surface Science* **2011**, 257, (7), 2717-2730.
38. Biesinger, M.C.; Payne, B.P.; Lau, L.W.M.; Gerson, A.; Smart, R.S.C., X-ray photoelectron spectroscopic chemical state quantification of mixed nickel metal, oxide and hydroxide systems. *Surface and Interface Analysis* **2009**, 41, (4), 324-332.

39. Li, X.Q.; Zhang, W.X., Iron nanoparticles: the core-shell structure and unique properties for Ni(II) sequestration. *Langmuir* **2006**, 22, (10), 4638-4642.
40. Mackenzie, K.; Frenzel, H.; Kopinke, F.D., Hydrodehalogenation of halogenated hydrocarbons in water with Pd catalysts: Reaction rates and surface competition. *Applied Catalysis B-Environmental* **2006**, 63, (3-4), 161-167.
41. Kim, Y.H.; Carraway, E.R., Dechlorination of chlorinated ethenes and acetylenes by palladized iron. *Environmental Technology* **2003**, 24, (7), 809-819.
42. Martino, M.; Rosal, R.; Sastre, H.; Diez, F.V., Hydrodechlorination of dichloromethane, trichloroethane, trichloroethylene and tetrachloroethylene over a sulfided Ni/Mo-gamma-alumina catalyst. *Applied Catalysis B-Environmental* **1999**, 20, (4), 301-307.
43. Ordonez, S.; Sastre, H.; Diez, F.V., Hydrodechlorination of aliphatic organochlorinated compounds over commercial hydrogenation catalysts. *Applied Catalysis B-Environmental* **2000**, 25, (1), 49-58.
44. Arnold, W.A.; Roberts, A.L., Pathways and kinetics of chlorinated ethylene and chlorinated acetylene reaction with Fe(O) particles. *Environmental Science & Technology* **2000**, 34, (9), 1794-1805.
45. Liu, Y.; Phenrat, T.; Lowry, G.V., Effect of TCE concentration and dissolved groundwater solutes on NUI-Promoted TCE dechlorination and H-2 evolution. *Environmental Science & Technology* **2007**, 41, (22), 7881-7887.
46. Farrell, J.; Kason, M.; Melitas, N.; Li, T., Investigation of the long-term performance of zero-valent iron for reductive dechlorination of trichloroethylene. *Environmental Science & Technology* **2000**, 34, (3).
47. Stumm, W.; Morgan, J.J., *Aquatic Chemistry Chemical Equilibria and Rates in Natural Waters* **1995**, Wiley Interscience.

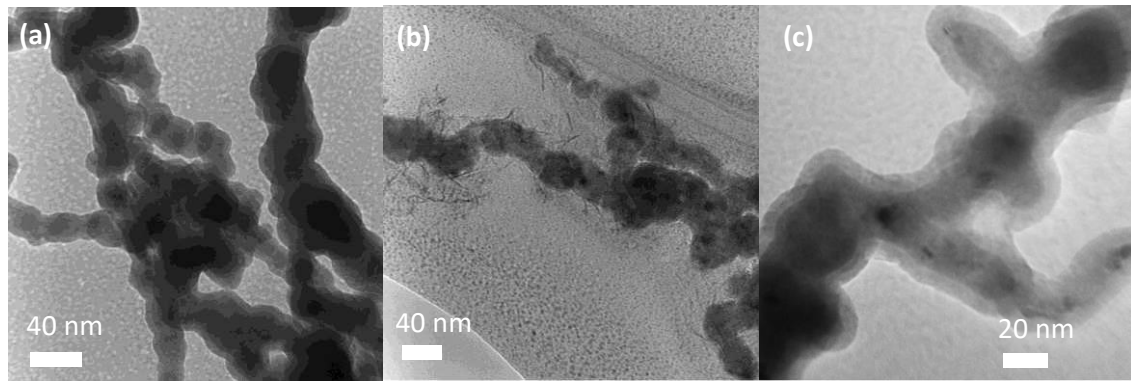


Figure 3.1. TEM micrographs of (a) fresh *CR*-Ni-Fe, (b) fresh *SDP*-Ni-Fe, and (c) *CR*-Ni-Fe aged in 5 mM phosphate solution for 24 h.

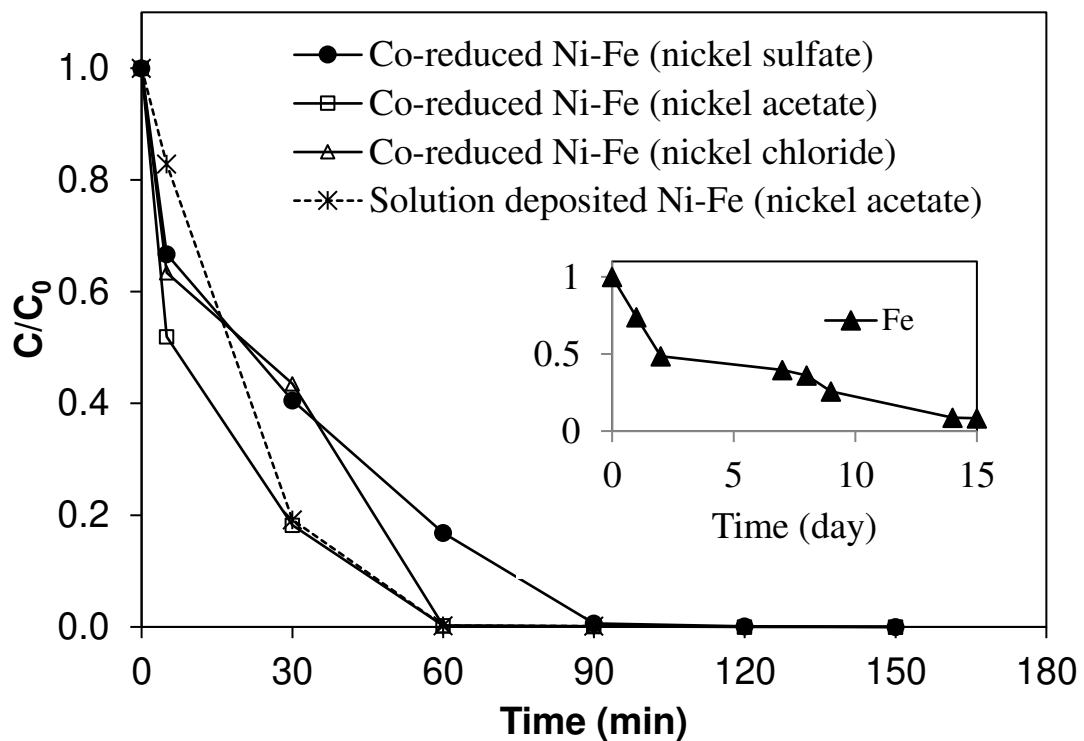


Figure 3.2. TCE degradation by fresh Ni-Fe BNP s prepared from various nickel precursors and synthesis routes. Inset shows TCE degradation by monometallic Fe nanoparticles. Initial TCE concentration was 50 mg/L. Nanoparticle dose was 2 g/L.

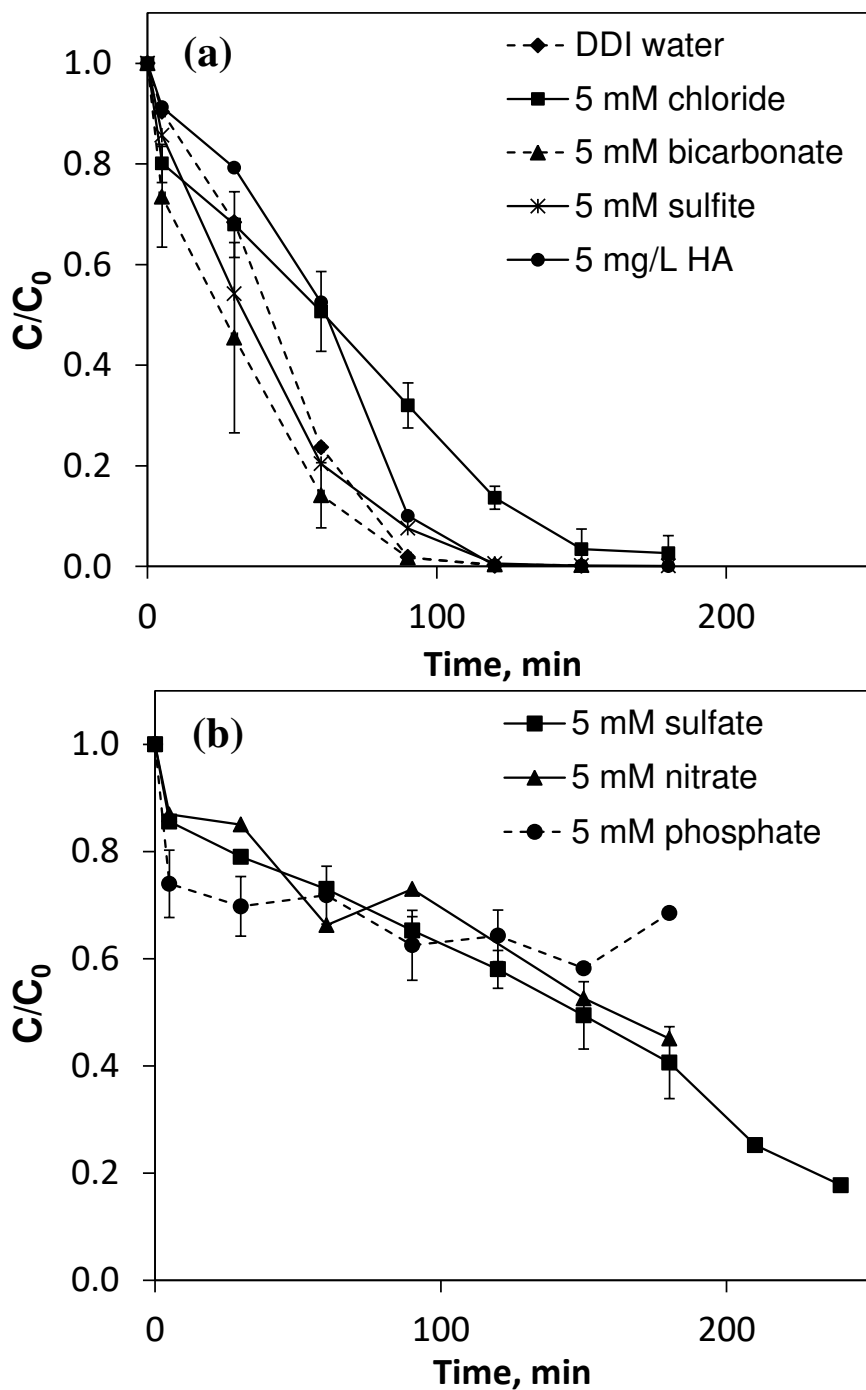


Figure 3.3. Effect of aging of Ni-Fe in solutions with (a) non or mildly-deactivating solutes and (b) strongly deactivating solutes on TCE degradation. Particles were prepared using co-reduction method (i.e., CR-Ni-Fe). Initial TCE concentration was 50 mg/L. Nanoparticle dose was 3.3 g/L. Initial pH was in the range of 8.1 - 8.3.

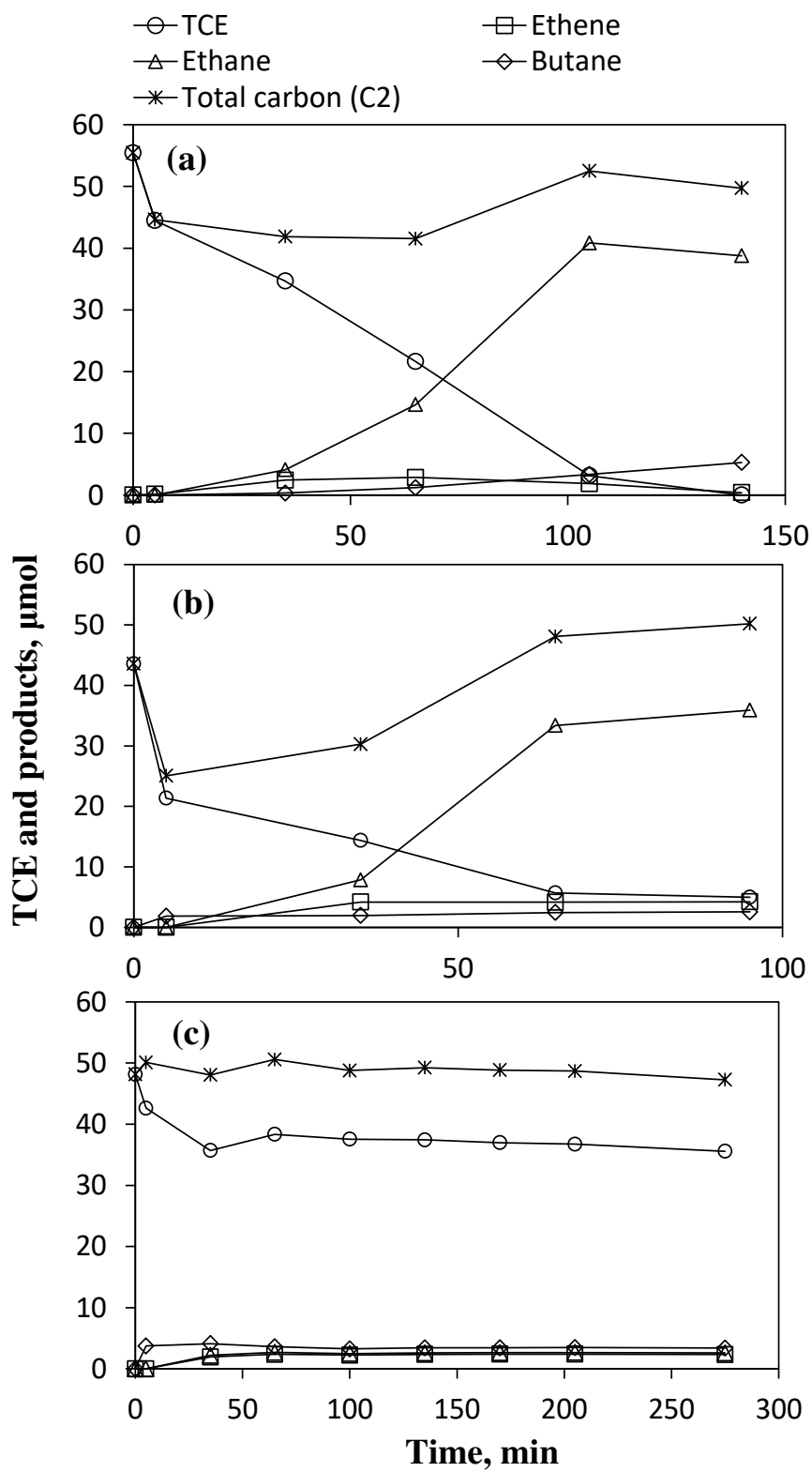


Figure 3.4. Products of TCE degradation by (a) fresh *CR-Ni-Fe*, (b) *CR-Ni-Fe* aged in 5 mM chloride, and (c) *CR-Ni-Fe* aged in 5 mM phosphate solutions. Nanoparticle dose was 2 g/L for (a) and 3.3 g/L for (b) and (c). Initial pH was 8.1 – 8.3.

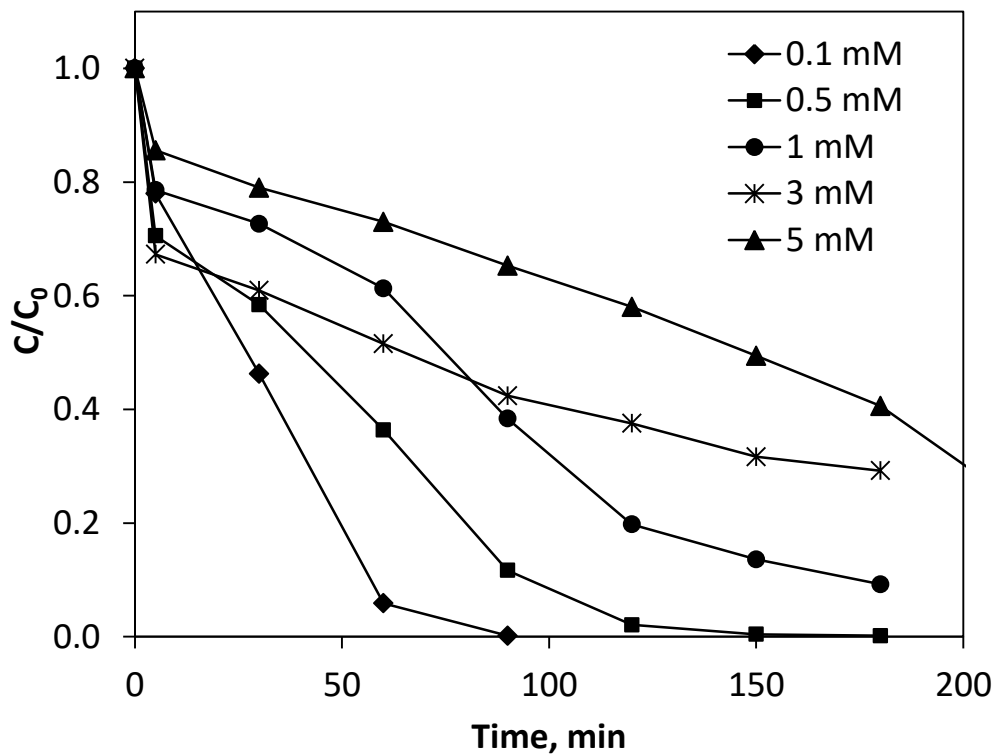


Figure 3.5. Effect of sulfate concentration on TCE dechlorination by aged CR-Ni-Fe BNP s. Initial TCE concentration was 50 mg/L. Nanoparticle dose was 3.3 g/L. Initial pH was in the range of 8.1 -8.3.

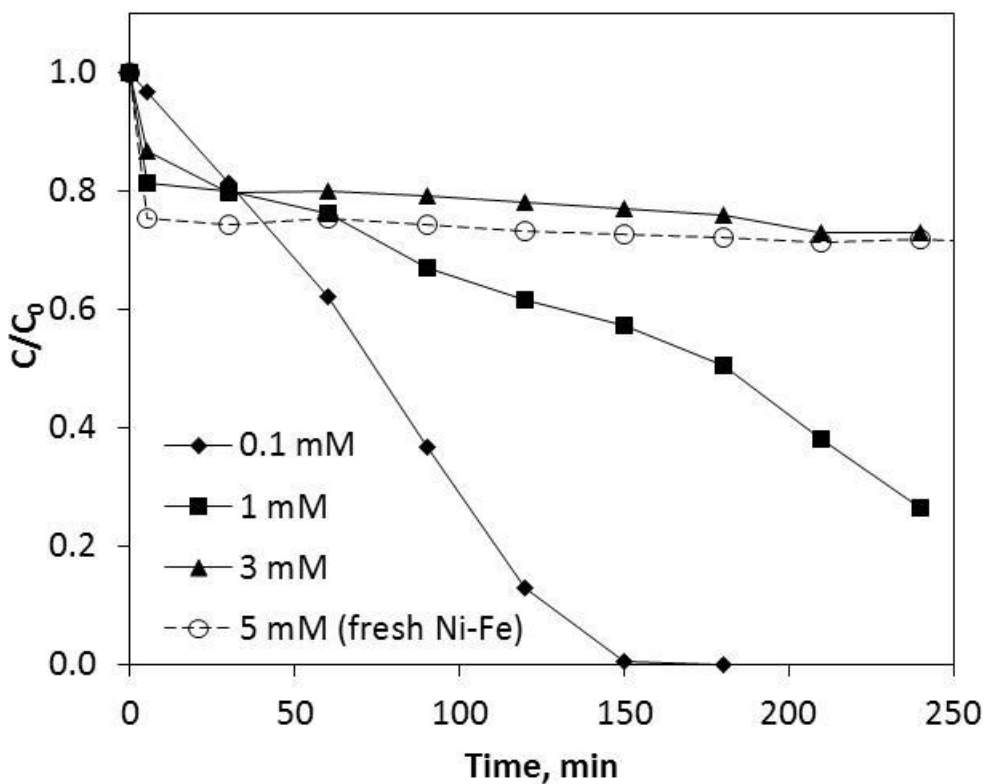


Figure 3.6. Effect of phosphate concentration on TCE dechlorination by CR-Ni-Fe BNPs. Solid lines denote particles that had aged in phosphate solutions prior to reacting with TCE. Dash line represents fresh Ni-Fe particles reacting in a solution containing both phosphate and TCE. Initial TCE concentration was 50 mg/L. Nanoparticle dose was 3.3 g/L. Initial pH was in the range of 8.1 - 8.3.

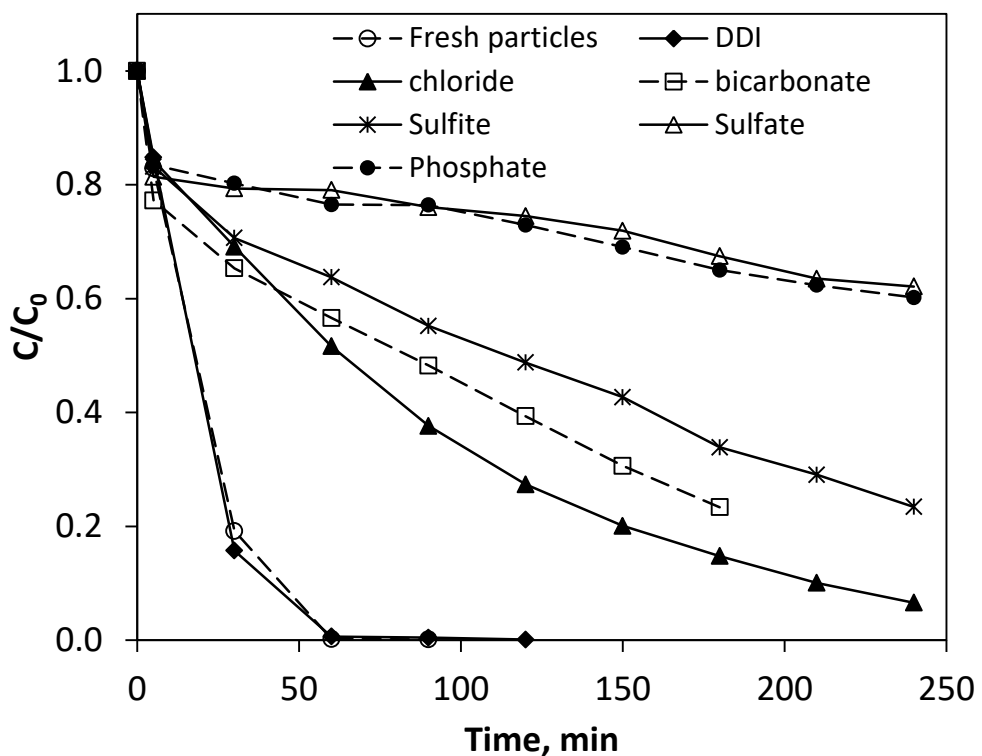


Figure 3.7. TCE degradation by fresh and aged Ni-Fe BNPs prepared via solution deposition method. The concentrations of background anions in the aging media were 5 mM. Initial TCE concentration was 50 mg/L. Nanoparticle dose was 3.3 g/L. Initial pH was in the range of 8.1 - 8.3.

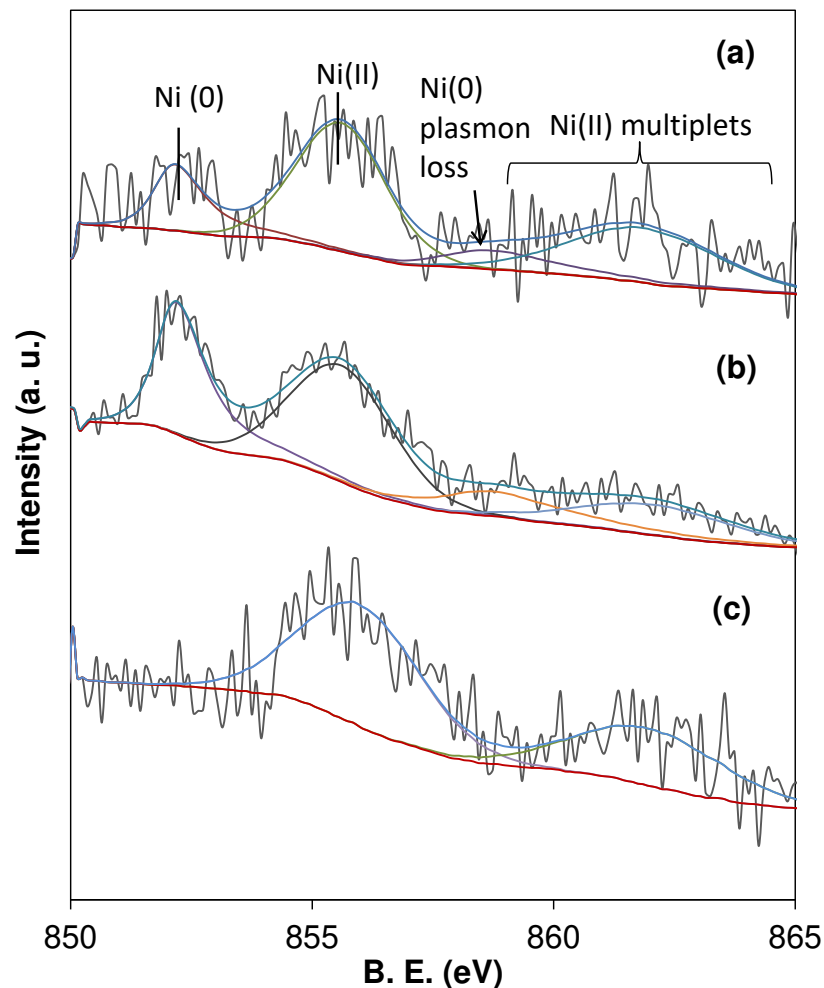


Figure 3.8. XPS Ni 2p_{3/2} spectra of Ni-Fe BNPs prepared via co-reduction method. (a) As-synthesized particles, (b) as-synthesized particles after sputtering in XPS chamber with argon for 2.5 min, and (c) particles aged in DDI for 24 h.

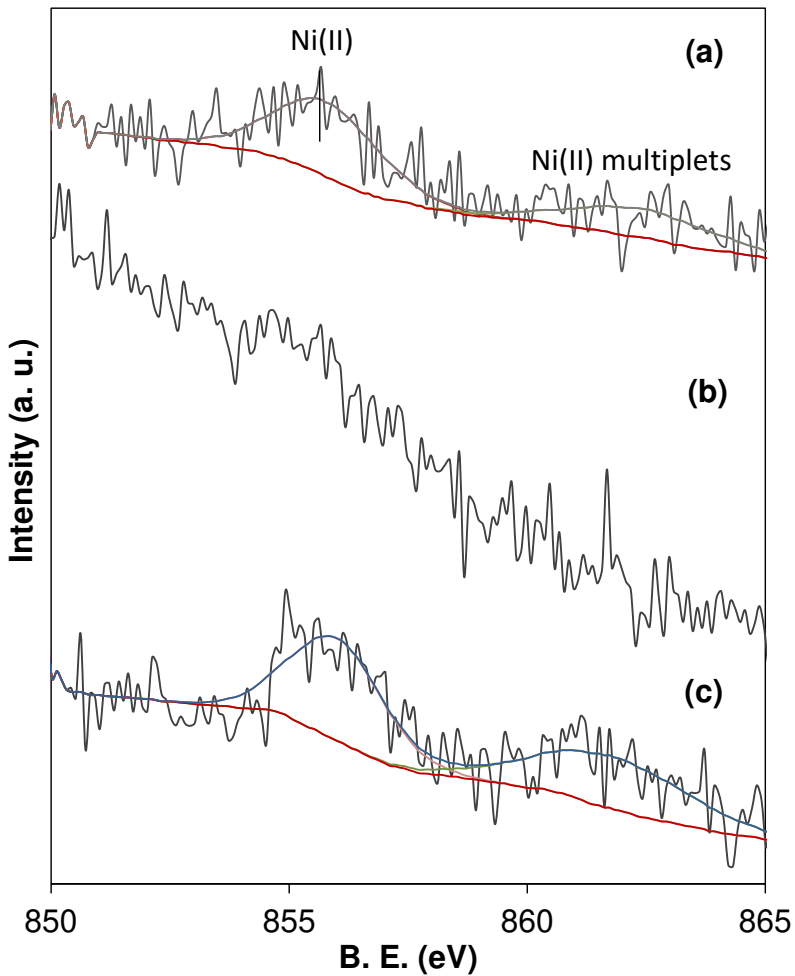


Figure 3.9. XPS Ni 2p_{3/2} spectra of Ni-Fe BNPs prepared via solution-deposition method. (a) As-synthesized particles, (b) as-synthesized particles after sputtering in XPS chamber with argon for 2.5 min, and (c) particles aged in a phosphate solution for 24 h.

Table 3.1. Mass-normalized reaction rate constants (k_m) and product yields of fresh and aged Ni-Fe BNPs

Solution	$k_m (10^{-2} \text{ L g}^{-1} \text{ min}^{-1})$	R^2	Y_{ethane}
As-synthesized nanoparticles (Ni precursor shown in brackets)			
Fe nanoparticles	$(3.22 \pm 1.13) \times 10^{-3}$	0.944	0.09
CR-Ni-Fe (from NiCl_2)	3.05 ± 1.39	0.897	
CR-Ni-Fe (from NiSO_4)	2.80 ± 1.07	0.939	
CR-Ni-Fe (from Ni acetate)	4.16 ± 1.79	0.942	0.81
Solution-aged nanoparticles (aging medium shown in brackets)			
CR-Ni-Fe (DDI)	1.61 ± 0.74	0.915	0.79
CR-Ni-Fe (5 mM Cl^-)	0.62 ± 0.19	0.939	0.69
CR-Ni-Fe (5 mM HCO_3^-)	1.30 ± 0.29	0.974	
CR-Ni-Fe (5 mM NO_3^-)	0.11 ± 0.04	0.926	
CR-Ni-Fe (5 mM SO_4^{2-})	0.16 ± 0.05	0.924	
CR-Ni-Fe (5 mM HPO_4^{2-})	0.05 ± 0.05	0.848	
CR-Ni-Fe (5 mM SO_3^{2-})	1.28 ± 0.29	0.966	
CR-Ni-Fe (5 mg/L humic acid)	1.38 ± 0.52	0.913	0.66
SDP-Ni-Fe (DDI)	1.77 ± 0.61	0.951	
SDP-Ni-Fe (5 mM Cl^-)	0.32 ± 0.02	0.997	
SDP-Ni-Fe (5 mM HCO_3^-)	0.21 ± 0.04	0.976	
SDP-Ni-Fe (5 mM SO_3^{2-})	0.16 ± 0.02	0.986	
SDP-Ni-Fe (5 mM SO_4^{2-})	0.05 ± 0.01	0.848	
SDP-Ni-Fe (5 mM HPO_4^{2-})	0.05 ± 0.01	0.893	

Table 3.2. Surface composition of freshly made and aged Ni-Fe nanoparticles measured by XPS analysis.

Sample	Surface elemental composition, at. %							
	O	C	Fe	Ni	B	N	S	P
<i>CR-Ni-Fe</i>								
As-synthesized	53.5	17.8	9.7	0.2	18.8	-	-	-
Aged in DDI	57.6	23.1	18.9	0.4	-	-	-	-
Aged in nitrate	25.4	73.2	0.9	0.5	-	-	-	-
Aged in sulfate	54.6	22.4	19.1	0.3	-	-	3.6	-
Aged in phosphate	47.2	20.6	13.6	0.5	11.2			6.9
<i>SDP-Ni-Fe</i>								
As-synthesized	51.4	22.4	19.8	0.4	6.0	-	-	-
Aged in phosphate	50.3	19.7	17.9	0.2	7.6	-	-	4.4

3.5. Supporting Information

XPS analysis

High resolution X-ray photoelectron spectroscopy (HR-XPS) analysis was performed on a PHI 5000 Versa Probe system using a monochromated AlK α ($h\nu = 1486.7$ eV) radiation. The instrument was equipped with a 300-mm radius hemispherical analyzer. Samples were mounted on a stainless steel stub using conductive carbon cape. Electron and argon dual-neutralizer system was used for all analyses to compensate for surface charge caused by X-ray microprobe (typical beam size used = 100 μm). The working pressure of the analysis chamber was around 1×10^{-7} Pa. Spectra were obtained using a takeoff angle of 45° with respect to the surface plane of the sample stub. Survey scans of the samples were obtained at 300-eV pass energy, while high-resolution scans of Ni2p_{3/2}, Fe2p, C1s, O1s, B1s, N1s, S2p and P2p transitions were obtained at 150-eV pass energy.

Each spectrum was calibrated against the binding energy (BE) for adventitious carbon detected in the C1s region (284.6 eV BE). Curve-fitting for Ni2p spectra was carried out using the CASA XPS software (Version 2.3.16PR1.6). The procedures summarized in [(Grosvenor et al. 2006),(Biesinger et al. 2011)] were followed here: a Shirley background was used to account for inelastic scattering for all samples. The Ni(0) peaks have a peak shape of LA(1.1,2.2,10) and include a main transition peak at 852.2 eV (FWHM 1.0 eV) and a satellite peak at 6.5 eV higher energy due to surface plasmon loss [(Grosvenor et al. 2006)]. A minor satellite at ~ 3.7 eV higher than Ni(0) main peak was not constructed due to overlapping with the Ni(II) signal and the low signal-to-noise ratios. Ni(II) peaks were fit using a Gaussian/Lorentzian ratio of 70/30. The intensities of the spectra were not sufficient to resolve Ni(II) multiplet contribution with high confidence and were represented by two envelopes at 855.6 eV and ~ 862.0 eV.

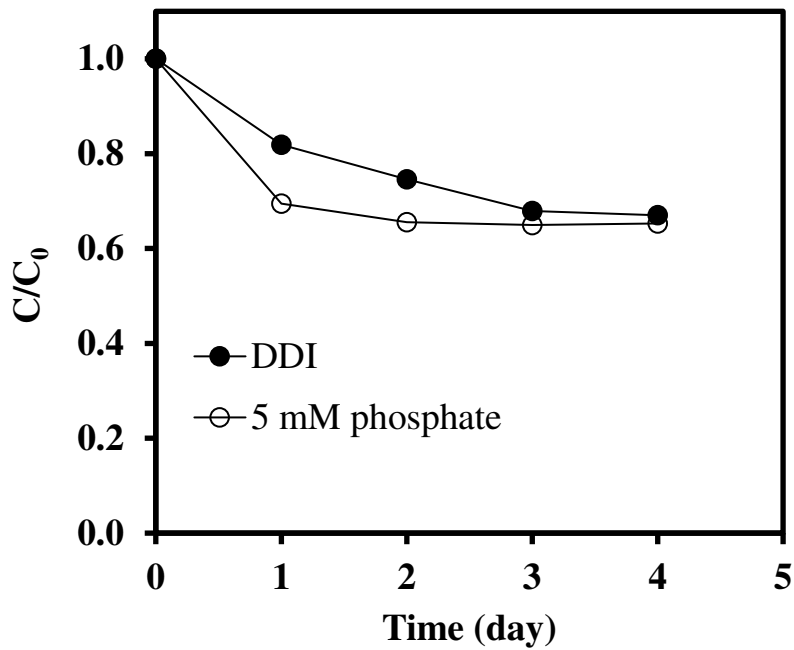


Figure S3.1. Comparison of TCE degradation by monometallic iron nanoparticles in DDI and in 5 mM phosphate solution. Initial TCE concentration was 50 mg/L. Nanoparticle dose was 5 g/L.

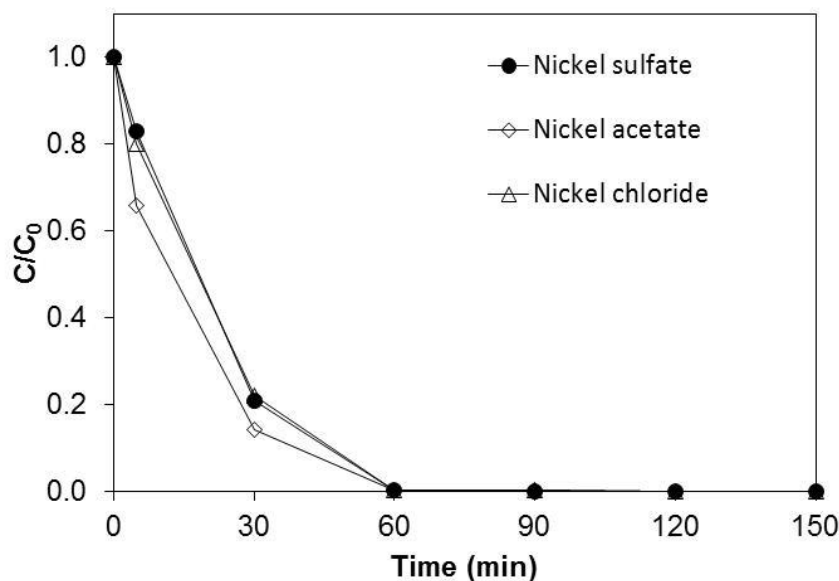


Figure S3.2. TCE degradation by Ni-Fe BNPs prepared from various nickel precursors and aged in 1 mM NaCl solutions for 24 hours. Initial TCE concentration was 50 mg/L. Nanoparticle dose was 3.3 g/L. Initial pH was in the range of 8.1 - 8.3.

Table S3.1. Solution pH before and after TCE dechlorination and loss of nickel and iron due to dissolution into the reaction media

Solution	Solution pH	Loss of Ni (%) ¹	Loss of Fe (%) ²
As-synthesized nanoparticles (Ni precursor shown in brackets)			
Fe nanoparticles	6.74	-	
CR-Ni-Fe (from NiCl ₂)	6.32	0.224	
CR-Ni-Fe (from NiSO ₄)	6.53	0.122	
CR-Ni-Fe (from Ni acetate)	6.12	0.098	
Solution-aged nanoparticles (aging media shown in brackets)			
CR-Ni-Fe (DDI)	8.32	0.357	0.023
CR-Ni-Fe (5 mM Cl ⁻)	8.26	0.634	0.025
CR-Ni-Fe (5 mM HCO ₃ ⁻)	8.36	0.433	0.010
CR-Ni-Fe (5 mM NO ₃ ⁻)	8.41	0.488	0.016
CR-Ni-Fe (5 mM SO ₄ ²⁻)	8.42	0.487	0.034
CR-Ni-Fe (5 mM HPO ₄ ²⁻)	8.38	0.487	0.031
CR-Ni-Fe (5 mM SO ₃ ²⁻)	8.44	0.668	0.022
CR-Ni-Fe (5 mg/L humic acid)	8.4	0.465	0.013
SDP-Ni-Fe (DDI)	8.43	0.641	0.272
SDP-Ni-Fe (5 mM Cl ⁻)	8.15	0.558	0.037
SDP-Ni-Fe (5 mM HCO ₃ ⁻)	8.42	0.054	0.049
SDP-Ni-Fe (5 mM SO ₃ ²⁻)	8.26	0.314	0.025
SDP-Ni-Fe (5 mM SO ₄ ²⁻)	8.35	0.353	0.028
SDP-Ni-Fe (5 mM HPO ₄ ²⁻)	8.42	0.175	0.031

¹ Loss of Ni during TCE reactions, calculated as mass fraction of Ni initially deposited.

² Loss of Fe during various aging treatments, calculated as mass fraction of Fe initially loaded into the aging solutions.

References

1. Biesinger, M.C.; Payne, B.P.; Grosvenor, A.P.; Lau, L.W.M.; Gerson, A.R.; Smart, R.S.C., Resolving surface chemical states in XPS analysis of first row transition metals, oxides and hydroxides: Cr, Mn, Fe, Co and Ni. *Applied Surface Science* **2011**, 257, (7), 2717-2730.
2. Grosvenor, A.P.; Biesinger, M.C.; Smart, R.S.; McIntyre, N.S., New interpretations of XPS spectra of nickel metal and oxides. *Surface Science* **2006**, 600, (9), 1771-1779.

CHAPTER FOUR

Trichloroethene Hydrodechlorination by Ni-Fe Bimetallic Nanoparticles: Reaction Pathways and Catalytic Surface Reaction Mechanisms Analyzed by Carbon Isotope Fractionation³

4.1. Introduction

Release of contaminants into surface water and groundwater due to rapid industrialization has been a global environmental challenge for decades. Many waste streams generated from industrial sources contain toxic and recalcitrant contaminants, and conventional wastewater treatment technologies cannot effectively treat these waste streams. Some contaminants (e.g., chlorinated ethenes) detected in the subsurface environment are also resistant to natural attenuation. Therefore, developing advanced water treatment technologies to remove these industrial contaminants is of great importance to safeguard the quality of potential drinking water sources and to protect the ecosystem. Many heterogeneous catalysts have been applied to transform various industrial contaminants into less harmful chemicals ¹⁻⁷. The advantages of heterogeneous catalytic treatment include rapid reaction rates, formation of benign products, and the catalysts can be easily separated from a reaction mixture for repeated use. Nickel-based catalysts have been widely used as hydrogenation catalysts owing to the ability of nickel to efficiently adsorb and activate hydrogen. In the environmental field, Ni-based catalysts have been employed to catalyze the transformation of a variety of organic contaminants, such as chlorinated ethenes ^{8, 9}, chlorophenols ^{10, 11}, and *p*-chlorobenzoic acid ¹². Ni-Fe bimetallic nanoparticles (BNPs) have shown significant enhanced reactivity for chlorinated ethenes hydrodechlorination ^{8, 9}. In the Ni-Fe BNPs system, the Fe(0) serves as the hydrogen provider by reacting with water, and Ni on the BNPs surface can adsorb the hydrogen, and hydrogen can be transformed into active hydrogen species (atomic hydrogen or hydride) formed from surface-catalyzed dissociation of H₂, and active hydrogen species initiate hydrodechlorination of surface adsorbed chlorinated ethenes. In

³ This chapter is about to submit to Chemosphere, Elsevier Publishing Company.

our previous work, we evaluated the reactivity of Ni-Fe BNPs upon exposure to different groundwater solutes and found that Ni-Fe BNPs were more stable than Pd-Fe BNPs in groundwater media^{13, 14}. However, the detailed surface reaction mechanisms and TCE hydrodechlorination pathways on Ni-Fe BNPs are still unclear.

Compound-specific isotope analysis (CSIA) is a valuable tool for assessing contaminants removal within aquifers¹⁵⁻¹⁸. The kinetic isotope effect (KIE) associated with chemical and biochemical reactions is an important means to monitor the degradation of organic contaminants, which is based on the principle that organic contaminant molecules with heavy isotopes experience slower bond breakage, and therefore the heavy isotopes tend to accumulate in the fraction of molecules that remain when contaminant degradation occurs¹⁹. If the loss of contaminants is associated with nondegradative processes (i.e., volatilization, sorption, diffusion, dilution), isotope fractionation is usually very small and can be neglected^{16, 20}. Liang et al. indicated that the abiotic dechlorination of tetrachloroethylene (PCE) and trichloroethylene (TCE) by ferrous bearing minerals²¹, FeS materials²², and nanoscale iron particles²³ would have more negative carbon isotope enrichment factors than biotic dechlorination. In another work, Liang et al. it showed that the bioremediation of monochlorobenzene (MCB) and 1,2,4-trichlorobenzene (1,2,4-TCB) demonstrates remarkably different isotopic patterns under aerobic and anaerobic dechlorination, respectively²³. CSIA can also serve to explore the reaction mechanisms. Elsner et al. indicated that during the chloroalkane abiotic dechlorination by Zn(0), the carbon isotope fractionation analysis results showed that dechlorination was mostly through β -elimination than hydrogenolysis or α -elimination²⁴. In addition, a detailed study regarding the carbon isotope fractionations during the dechlorination of different chlorinated ethenes by two kinds of nZVI has revealed a common first step shared by the hydrogenolysis and dichloroelimination pathways²⁵. Therefore, CSIA is a promising approach complementary to conventional monitoring methods to validate the occurrence of groundwater remediation, distinguish different types of degradation reactions, and to indicate the reaction mechanisms.

The objective of this research is to understand the effects of common groundwater solutes on TCE dechlorination by Ni-Fe BNPs based on the reaction kinetics and pathways determined through the use of an appropriate kinetic model. The experimental and modeling results as well as carbon isotope fractionation analysis are used to construct the deactivation mechanisms caused by different groundwater solutes. In this study, Ni-Fe BNPs were prepared via co-reduction method and solution deposition method, respectively¹³, and the reactivity of the particles was evaluated by reacting with trichloroethylene (TCE) after immersing the fresh particles in solutions amended with common groundwater anions and/or organic matter for a period of 24 h. Carbon isotope fractionation of TCE and its daughter products were analyzed simultaneously using gas chromatography with a combustion isotope ratio mass-spectrometer (GC-C-IRMS). Quantifying the parent compound degradation and the products formation and their carbon isotope fractionation values allow us to analyze the kinetics and pathways of TCE reactions with Ni-Fe BNPs pre-exposed to different aging conditions. Based on carbon isotope fractionation analyses and C2 carbon mass recovery results during TCE hydrodechlorination, a kinetic model is proposed which can satisfactorily describe TCE degradation and its daughter product formation. The findings of this research suggest that TCE bulk enrichment factors (ε_{bulk}) for TCE hydrodechlorination by Ni-Fe BNPs aged under different conditions can be used to assess whether the Ni catalytic sites on Ni-Fe BNPs surface are functional, which is especially useful for monitoring *in situ* groundwater remediation because it is hard to extract particles back after Ni-Fe BNPs injected into the subsurface.

4.2. Materials and methods

4.2.1. Preparation of Nanoparticles

Two different types of Ni-Fe bimetallic nanoparticles (BNPs) were used in this study. The first type of nanoparticles was Ni-Fe bimetallic nanoparticles (Ni-Fe BNPs) synthesized by reduction of an aqueous solution containing both Fe(III) (from $\text{FeCl}_3 \cdot 6\text{H}_2\text{O}$, Alfa Aesar, USA) and Ni(II) (from nickel acetate, Acros Organics, USA) ions by NaBH_4 (Acros Organics)²⁶. Briefly, 10.8 g of $\text{FeCl}_3 \cdot 6\text{H}_2\text{O}$ (corresponding to 0.08

M Fe³⁺) and an appropriate amount of nickel acetate were dissolved in 500 mL of distilled de-ionized (DDI) water and ethanol mixture (1:1, v/v). 500 mL of NaBH₄ solution (0.4 M) was introduced into the Fe(III) and Ni(II) solution at approximately 17 mL/min with a precision peristaltic pump under intensive mixing. After all NaBH₄ was pumped into the metal solution, the mixture was allowed to stir for approximately 20 min before the particles were collected by vacuum filtration. Particles were rinsed with ethanol to remove chemical residues on the surface and the collected particles were stored in ethanol for further use. The Ni-Fe BNPs synthesized under this method was denoted as *CR*-Ni-Fe BNPs. The second type of Ni-Fe BNPs was prepared using the solution deposit method and is denoted as *SDP*-Ni-Fe BNPs. The synthesis method involved preparation of nZVI first followed the method as described previously. The as-synthesized nZVI was added to a nickel acetate solution and sonicated for 5 min. In this study, the nominal loading of nickel with respect to iron was fixed at a mass fraction of 2%. The dry weight of Ni-Fe BNPs was determined using a halogen-lamp moisture analyzer (OHAUS MB 45). DDI water used in all procedures, including particle synthesis, aging and TCE experiments, was deoxygenated by N₂-purging for 30 min.

4.2.2. Aging Experiments

Aging experiments were conducted in 250-mL glass vials containing 200 mL of deoxygenated solutions amended with a groundwater solute at 0.01 - 5 mM. Stock solutions of chloride, phosphate, sulfate and oxalic were prepared from their sodium salts. Stock solution of humic acid (Sigma-Aldrich, used as received) was prepared at 100 mg/L and was ultrasonicated for 10 min prior to use. The initial pH of the solutions was adjusted with dilute NaOH or HCl to be within the range of 7.8-8.3 to simulate the typical pH values encountered in groundwater. An appropriate amount of freshly made Ni-Fe BNPs was added into each solution at 3.3 g/L (dry weight) and the vial was sealed and agitated on a mechanical shaker for 24 h at room temperature (22 +/- 1 °C). The aged particles were collected by vacuum filtration and were used immediately in TCE degradation experiments.

4.2.3. TCE Experiments

TCE dechlorination experiments were performed to compare the reactivity of fresh and aged Ni-Fe BNPs. All batch experiments were conducted in 250-mL amber serum glass bottles containing 200 mL of aqueous solution and the balance as headspace. Experiments were performed with fresh or aged nanoparticles added at 2 or 3.3 g/L (dry weight), respectively, and an initial concentration of TCE at 50 mg/L. Control experiment without nanoparticles was performed in parallel. Initial pH was adjusted to between 7.8-8.3. The vials were capped with Teflon Mininert valves and placed on a mechanical shaker at 250 rpm at room temperature. Periodically, an aliquot (200 - 500 µL) of headspace gas was withdrawn using a gastight syringe and analyzed for TCE concentrations and reaction intermediates and products using a GC system (Thermo Scientific TRACE GC Ultra) with an Agilent PoraPlot Q column and a flame ionization detector (FID). The amount of TCE in the solution was deduced from its concentration in the headspace using Henry's constant^{27,28}, and products concentrations of ethene, ethane and longer chain hydrocarbons (C₃- C₆) were calibrated using commercial gas standards (1000 ppm olefin or paraffin mixture in helium, Grace).

In this research, product yield was used to characterize the major product distribution during the TCE degradation process. It is defined as the amount of a product formed over the amount of parent compound reacted at a given time, which is expressed as Equation (1)

$$\text{Product Yield} = \frac{P_{i,t}}{\text{TCE}_0 - \text{TCE}_t} \quad (1)$$

where P_{i,t} is the amount of daughter product i at a given time, and TCE₀ and TCE_t are the amounts of TCE in the reactor at the beginning and at a given time, respectively. Carbon recovery was calculated by summing up the amounts of TCE and daughter products detected in the reactor in terms of C₂ equivalents (e.g., 1 mole of butane = 2 mole of C₂ equivalent) as shown in Equation (2):

$$\text{Carbon recovery} = \text{TCE}_t + \sum P_{i,t} \quad (2)$$

4.2.4. Evaluation of Isotope Fractionation

CSIA determines the carbon isotope signatures by measuring two stable isotopes of ^{12}C and ^{13}C via GC-IRMS. This ratio is expressed in Eqation (3):

$$\delta^{13}\text{C} \text{ (unit of ‰)} = \left(\frac{R_{\text{sample}}}{R_{\text{standard}}} - 1 \right) 1000 \quad (3)$$

where R_{sample} is the $^{13}\text{C}/^{12}\text{C}$ ratio in a given sample and R_{standard} is the $^{13}\text{C}/^{12}\text{C}$ ratio in the international standard reference material- Vienna Pee Dee Belemnite (VPDB). For many organic pollutants, the relationship between isotopic fractionation and extent of degradation can be modeled by the Rayleigh model ²⁹. The Rayleigh model assumes constant isotope fractionation during degradation that is represented by the fractionation factor α . α relates the isotopic composition of the substrate at a given time, R , to the initial isotopic composition, R_0 , and to the fraction of substrate remaining, f , through Equation (4):

$$\frac{R}{R_0} = f^{\alpha-1} \quad (4)$$

α value can also be expressed as the bulk enrichment factor, $\varepsilon_{\text{bulk}}$, as in Equation (5) and (6):

$$\ln \frac{R}{R_0} = (\alpha - 1) \ln f \quad (5)$$

$$\varepsilon_{\text{bulk}} = (\alpha - 1) 1000 \quad (6)$$

4.3. Results and Discussion

4.3.1. Carbon Isotope Fractionation during TCE Hydrodechlorination

Figure 4.1 shows TCE hydrodechlorination profiles, major products formation, and carbon isotope fractionation results as a function of time by fresh Ni-Fe BNPs and Ni-Fe BNPs aged in different groundwater solutes. The results indicated that CR-Ni-Fe BNPs aged in DDI water, 5 mM Cl⁻, 5 mM C₂O₄²⁻, and 20 mg/L humic acid had negligible deactivation effects on TCE degradation rate, which is consistent with our previous research finding ¹³. CR-Ni-Fe BNPs aged in 5 mM SO₄²⁻ showed moderate deactivation effects on particles reactivity for TCE dechlorination, which is different

from our previous findings. This discrepancy might be owing to the experimental uncertainty.

Figure 4.1 shows that ethane was the predominant product by fresh Ni-Fe BNPs as well as CR-Ni-Fe BNPs aged in different groundwater solutes. Table 4.1 lists the carbon recovery and ethane yield that were calculated at the last sampling point. The carbon mass balance results suggested satisfactory (> 90%) carbon recovery for most experiments. Ethane yield indicates that ethane was the predominant product formed during TCE hydrodechlorination for fresh and aged Ni-Fe BNPs, which can also be seen in Figure 4.1. Compared to a previous study that only observed ethane as the predominant product during the TCE degradation by Ni-Fe BNPs⁹, ethene was another important product observed during the TCE dechlorination, the concentration of which accumulated at the initial reaction stage then declined as the reaction proceeded. Heavier hydrocarbons (i.e., C₃-C₆ species) were also observed during the TCE dechlorination experiments but only accounted for a minor fraction (< 2%) of the total products formed. Partially dechlorinated species reported in previous studies during abiotic dechlorination^{25, 30}, including dichloroethene isomers (DCE) and vinyl chloride (VC), were not detected. Compared to unamended nZVI, the doping of nickel on the nZVI enhanced TCE degradation rate by approximately three orders of magnitude¹³. The existence of nickel could significantly accelerate TCE dechlorination and hydrogenation of reaction intermediates, resulting in ethane as the predominant product, whereas in the case of nZVI, ethene was the predominant product of TCE dechlorination¹⁴. These results all support the concept that nickel behaves as a catalyst in the TCE hydrodechlorination process. Also, as indicated in our previous study¹³, the prevalent form of nickel deposited on the particles surface was nickel(II), and the existence of Ni(II) decreased the galvanic effect between Fe(0) and Ni catalytic sites, which decreases the electrochemical driving force for Fe(0) oxidation and renders Ni-Fe BNPs to be more stable when exposed to the common groundwater solutes. This point is attested by the evidence that Ni-Fe BNPs after aging in these groundwater solutes (DDI water, Cl⁻, SO₄²⁻, C₂O₄²⁻ and humic acid) still retained a high reactivity compared to Pd-Fe BNPs subject to similar aging treatments .

Compared to particles aged in other media, TCE hydrodechlorination by Ni-Fe BNPs aged in 5 mM phosphate was characteristically slow, consistent with what was observed previously¹⁴. Nonetheless, given sufficient time (2 days), near complete conversion of TCE was observed with ethane as the predominant product. Compared to other groundwater solutes, phosphate ion severely slows down the activity of the nickel sites, but does not completely deactivate the catalyst for the hydrodechlorination process. Previously, we attributed that active nickel sites form strong complexes with phosphate ion, which inhibited the nickel sites to activate hydrogen to initiate TCE dechlorination¹³. However, the observation of TCE degradation by Ni-Fe BNPs aged in 5 mM phosphate over a prolonged time frame suggests that a limited number of active nickel sites were still available after aging in phosphate solutions.

Table 4.1 summarizes the bulk enrichment factors (ε_{bulk}) measured for each TCE dechlorination batch obtained by a linear regression of the data according to the Rayleigh equation (Eq. (5)). Good fits (i.e., $r^2 > 0.9$) to the Rayleigh equation were obtained for all the experiments (Figure 4.2). Strong carbon isotope fractionation during TCE dechlorination by nZVI and different types of Ni-Fe BNPs was observed. The results imply significant enrichment of ¹³C in the remaining reactant during the TCE dechlorination, due to the fact that the rate of reaction of bonds containing ¹²C was expected to be greater than that of bonds containing ¹³C. This finding is consistent with the fact that bonds containing heavier isotopes are more stable and have higher dissociation energies than those containing light isotopes^{21, 23, 31, 32}.

The carbon isotope fractionation of TCE degradation by nZVI had an enrichment factor (ε_{bulk}) of $-15.3 \pm 0.8\text{‰}$ ¹⁴. Compared with ε_{bulk} values of other types of iron particles summarized in Table 4.2, this value is within the typical range of ε_{bulk} reported in the literature for abiotic TCE degradation. The values of ε_{bulk} ($-9.2 \pm 0.8\text{‰}$ for CR-Ni-Fe BNPs and $-9.8 \pm 1.5\text{‰}$ for SDP-Ni-Fe BNPs) were significantly less negative than that of fresh nZVI ($\varepsilon_{bulk} = -15.3 \pm 0.8\text{‰}$). The possibility that mass transport was the rate-limiting process for TCE degradation on Ni-Fe BNPs could be ruled out due to the adequate mixing condition. Accordingly, the less negative ε_{bulk} value of catalysts might

be owing to (i) the catalytic function of Ni ¹⁴, which can decrease the transition state energy and increase the bond cleavage rates and thus causes an overall decrease in the kinetic isotope effect, or (ii) a kinetic masking effect due to the fact that the rapid reaction on Ni sites may cause the preceding steps (e.g., adsorption of reactants to surface sites) to be more rate-limiting ¹⁹. Kinetic solvents experiments was conducted by reacting Ni-Fe BNPs in deuterium oxide (D₂O). Compared to TCE hydrodechlorination by Ni-Fe BNPs in water under the same experimental conditions, a remarkable abatement of TCE degradation rate was observed when Ni-Fe BNPs were in D₂O, which is shown in Figure 4.3. This large H/D isotope effect for TCE degradation by Ni-Fe BNPs is consistent with previous study ⁸, suggesting that C-H bond formation is the rate-limiting step in Ni-Fe BNPs heterogeneous system. The negligible H/D isotope effect for TCE reduction by nZVI suggested that the rate-limiting step was different from that by Ni-Fe BNPs, while no further efforts were made to identify the corresponding rate-limiting step. The H/D isotope results also proved that the diminished carbon isotope effect of TCE degradation by Ni-Fe BNPs was owing to the nature of Ni as the hydrogenation catalyst on the Ni-Fe BNPs surface. TCE degradation by CR-Ni-Fe BNPs aged in DDI water, Cl⁻, SO₄²⁻, C₂O₄²⁻ and 20 mg/L humic acid showed ε_{bulk} values close to that of the fresh Ni-Fe BNPs (Table 4.1). Taken together, this observation and the distribution of products suggested that DDI water, Cl⁻, SO₄²⁻, C₂O₄²⁻ and 20 mg/L humic acid caused mild, non-specific deactivation effects on Ni-Fe BNPs reactivity, and the catalytic function of Ni was not undermined. The ε_{bulk} value of Ni-Fe BNPs aged in phosphate was close to the value of fresh Ni-Fe BNPs, yet the significant decrease in TCE degradation rate compared to other types of Ni-Fe BNPs suggested there was a limited number of active nickel sites available after aging in phosphate solutions.

CSIA has been employed to identify and distinguish abiotic and biotic degradation of chlorinated ethenes in both laboratory and field studies of groundwater remediation ^{16, 31, 33-35}. We showed that ε_{bulk} values could be used to diagnose the catalytic function, so monitoring carbon isotope fractionation could serve as an alternative approach to evaluate the longevity of Ni-Fe BNPs. Measuring carbon isotope fractionation of TCE degradation by Ni-Fe BNPs can be particularly useful to evaluate

Ni-Fe BNPs reactivity and longevity when Ni-Fe BNPs are used in *in situ* groundwater remediation. It is hard to retrieve Ni-Fe BNPs to conduct surface analysis to evaluate the extent of catalyst deactivation after the particles have been injected into an aquifer, but the chemical state of the catalysts can be readily deduced based on measurement of carbon isotope fractionation of field samples.

4.2. Kinetic Modeling Results

Based on the distribution of products during TCE hydrodechlorination (Figure 4.1), ethene shows typical intermediate behavior, the formation of which accumulated at the initial reaction stage and was gradually consumed as the precursor of ethane for both fresh and aged Ni-Fe BNPs. The isotope trends of TCE and its daughter products also attested to this sequential reaction pathway. Figure 4.1 shows the carbon isotope trends of TCE and its daughter products. It was consistently observed among different aged Ni-Fe BNPs that ethene was more depleted of ^{13}C compared to TCE owing to carbon flux of from TCE to ethene, and gradual enrichment of ^{13}C in ethene was observed due to the subsequent hydrogenation, which accords with the behavior of ethene as an intermediate that is simultaneously formed and consumed. It was noted that the $\delta^{13}\text{C}$ value of ethane at the last sampling point was equal to the initial $\delta^{13}\text{C}$ value of TCE, suggesting that TCE was completely transformed into ethane. The isotope profiles of TCE and its daughter products reacted with Ni-Fe BNPs aged in 5 mM Cl^- appear different from the other batch experiments, but it might be due to analysis error. Several previous studies have examined carbon isotope fractionation trends during biological degradation of chlorinated ethenes (e.g., PCE and TCE), which followed hydrogenolysis pathway with step-wise loss of chlorine^{33, 34, 36-38}. Compared to these results, we observed the similar carbon isotope signatures of chlorinated ethenes and their daughter products. Therefore, a sequential pathway of TCE hydrodechlorination was proposed to model the kinetics of TCE degradation and its daughter product formation, which is shown as follows:

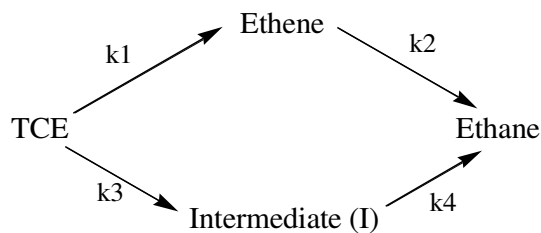


The kinetic modeling software package, Scientist 3.0 for Windows (Micromath, St Louis, MO, USA), was used to evaluate parameters assuming the reaction follows pseudo-first-order reaction. Parameter k_1 was determined by fitting to the decay of TCE concentration. k_2 represents the ethene hydrogenation rate constant, and it was determined experimentally through separate ethene hydrogenation experiments, in which ethene was used as a starting compound to react with various Ni-Fe BNPs. The experimentally recorded rate of ethene conversion to ethane determines the value of k_2 .

We selected two modeling results as representative examples to show the validity of this pathway model (Figure 4.4). While the modeling results could reasonably well describe TCE degradation and ethane formation, excessive overestimation of ethene formation was observed for all TCE hydrodechlorination experiments by different types of Ni-Fe BNPs. Possible explanation for the ethene overestimation could be that not all TCE transformed into ethane via ethene, and a second pathway might exist, in which TCE transformed into ethane via another pathway. This second pathway might occur simultaneously with the pathway of sequential transformation of TCE into ethane via ethene. It is generally acknowledged that heterogeneous catalytic reactions usually involve three steps: (1) adsorption of contaminant on the catalyst surface, (2) catalytic reaction on the surface, and (3) desorption of reaction products from the surface. Scrutinizing the C₂ mass balance results of all experiments shown in Figure 4.1 leads to the inference that a significant fraction of carbon was not accounted for during the initial reaction phase, and the carbon mass balance was gradually restored when TCE degradation approached completion.

The initial loss of carbon indicates the presence of surface-bound intermediates. Our attempt to insert a surface-adsorbed intermediate prior to the formation of ethene led to poor fitting. This suggests the surface-adsorbed intermediate is involved in a parallel way besides the sequential transformation of TCE into ethane via ethene. The gradual decrease in the carbon mass deficiency as reaction progressed to completion implies that this surface intermediate was converted to ethane as the final product. This kinetic model is illustrated below and is denoted as the “dual pathways” model. Reactions of the second

pathway occurred on the Ni-Fe BNPs surface could be complicated, but no specific efforts have been made to identify the detailed reactions on the solids surface before ethane formation, owing to the fact that reactions are fast on heterogeneous catalyst making it hard to identify the possible intermediates. In the absence of detailed knowledge about the nature of the surface-adsorbed intermediate, we simplified the second reaction pathway by assuming that TCE transforms into an intermediate denoted as “I,” which remains on the catalysts surface. As intermediate “I” transformed into ethane, the carbon mass balance could be restored gradually and ethane became the final product. Therefore the “dual pathways” model for TCE hydrodechlorination is proposed as follows



The amount of “I” formed can be calculated based on the carbon mass balance as in Eq.(6)

$$I_t = TCE_o - TCE_t - Ethene_t - Ethane_t - Longer\ Hydrocarbons_t \quad \text{Eq.(6)}$$

where TCE_o is the initial TCE concentration, TCE_t , $Ethene_t$, and $Ethane_t$ are the aqueous concentrations of these three species measured at a given time. $Longer\ Hydrocarbons_t$ is the sum of C_3 , C_4 , C_5 and C_6 species detected in the reactor at a given time. I_o is considered zero as the initial condition.

Attempts to model TCE degradation and its daughter formations based on pseudo-first-order kinetic reaction following the “dual pathways” model yield good fitting for the experimental data, which are illustrated in Figure 4.5. The pseudo-first-order rate constants of k_3 and k_4 estimated by modeling software are listed in Table 4.1. The modeling results indicate that values of k_3 were much greater than those of k_1 , suggesting that the formation of intermediate “I” is much faster than the formation of ethene. As we assumed the formation of “I” happens on the Ni-Fe BNPs surface, the modeling results with higher value of k_3 than that of k_1 supports the experimental observation, because

only if the formation of the intermediate on the surface is faster than that of ethene, the initial deficiency of mass balance can be observed. k_4 values depend on carbon mass recovery rates. If the initial carbon deficiency can be quickly recovered, k_4 takes a greater value than that of k_3 ; otherwise, k_4 is smaller than k_3 .

To glean mechanistic insights into deactivation of Ni-Fe due to aqueous aging, the ‘dual pathways’ model was applied to Ni-Fe BNPs aged in two types of aging media, namely humic acid and phosphate solutions at varying concentrations. Humic acid within the concentration range of 0.5 – 20 mg/L caused a negligible deactivation effect on Ni-Fe BNPs dechlorination reactivity, and TCE degradation by Ni-Fe BNPs aged in humic acid solutions all followed pseudo-first-order kinetics (Figure 4.6). Ni-Fe BNPs exposed to different phosphate concentrations, however, showed a severe deactivation effect at an elevated phosphate concentration. For Ni-Fe BNPs aged in 0.01 mM, 0.1 mM and 0.3 mM phosphate, TCE degradation followed the pseudo-first-order decay, for which the “dual pathways” model yields a good fit with the experimental data (Figure 4.7). However, as phosphate concentration increased to 1 mM, significant inhibition of TCE degradation was observed. Interestingly, we also observed the change of kinetic pattern from first-order to zero-order when phosphate concentration increased to 1 mM and above (Figure 4.8). No efforts has been made to model the TCE hydrodechlorination by Ni-Fe BNPs aged in 1 mM and 5 mM because the transition of kinetic pattern.

4.4. Conclusion

Values of bulk enrichment factor (ε_{bulk}) for TCE hydrodechlorination by Ni-Fe BNPs under different aging conditions were less negative than that of nZVI, suggesting that the catalytic role of Ni on the Ni-Fe BNPs surface resulted in a diminished carbon fractionation effect for TCE hydrodechlorination. As ε_{bulk} of TCE hydrodechlorination by Ni-Fe differs significantly from that of pure nZVI, ε_{bulk} values could be used to infer the activity and availability of Ni sites for TCE degradation under in situ remediation conditions. Together with kinetic and product distribution analyses, carbon isotope measurements could serve as an alternative way to assess the extent of deactivation for Ni-Fe BNPs during TCE hydrodechlorination. The analyses of carbon isotope

fractionation of TCE, ethene, and ethane suggest that TCE completely transformed into ethane via ethene as the intermediate. Furthermore, kinetic modeling results proved that TCE hydrodechlorination involves a surface-mediated pathway leading to ethane formation. A “dual pathways” kinetic model was proposed, in which a fraction of TCE transforms into ethane via ethene, while the rest of TCE is converted to a surface-bound intermediate and the intermediate further reacts to form ethane. The proposed “dual pathways” model was successful at describing TCE hydrodechlorination by fresh and various aged Ni-Fe BNPs. Systematic changes in kinetic parameters for Ni-Fe BNPs exposed to humic acid and phosphate solutions reveal dissimilar aging effects induced by the two types of groundwater constituents.

References

1. Hamoudi, S.; Larachi, F.; Sayari, A., Wet oxidation of phenolic solutions over heterogeneous catalysts: degradation profile and catalyst behavior. *Journal of Catalysis* **1998**, *177*, (2), 247-258.
2. Houas, A.; Lachheb, H.; Ksibi, M.; Elaloui, E.; Guillard, C.; Herrmann, J.-M., Photocatalytic degradation pathway of methylene blue in water. *Applied Catalysis B: Environmental* **2001**, *31*, (2), 145-157.
3. Beltrán, F. J.; Rivas, J.; Alvarez, P.; Montero-de-Espinosa, R., Kinetics of heterogeneous catalytic ozone decomposition in water on an activated carbon. *Ozone: science & engineering* **2002**, *24*, (4), 227-237.
4. Ollis, D. F.; Hsiao, C.-Y.; Budiman, L.; Lee, C.-L., Heterogeneous photoassisted catalysis: conversions of perchloroethylene, dichloroethane, chloroacetic acids, and chlorobenzenes. *Journal of catalysis* **1984**, *88*, (1), 89-96.
5. Kanel, S. R.; Neppolian, B.; Choi, H.; Yang, J.-W., Heterogeneous catalytic oxidation of phenanthrene by hydrogen peroxide in soil slurry: Kinetics, mechanism, and implication. *Soil and Sediment Contamination* **2003**, *12*, (1), 101-117.
6. Lücking, F.; Köser, H.; Jank, M.; Ritter, A., Iron powder, graphite and activated carbon as catalysts for the oxidation of 4-chlorophenol with hydrogen peroxide in aqueous solution. *Water Research* **1998**, *32*, (9), 2607-2614.
7. Kim, K.-H.; Ihm, S.-K., Heterogeneous catalytic wet air oxidation of refractory organic pollutants in industrial wastewaters: A review. *Journal of Hazardous Materials* **2011**, *186*, (1), 16-34.
8. Schrick, B.; Blough, J. L.; Jones, A. D.; Mallouk, T. E., Hydrodechlorination of trichloroethylene to hydrocarbons using bimetallic nickel-iron nanoparticles. *Chemistry of Materials* **2002**, *14*, (12), 5140-5147.

9. Tee, Y.-H.; Grulke, E.; Bhattacharyya, D., Role of Ni/Fe nanoparticle composition on the degradation of trichloroethylene from water. *Industrial & engineering chemistry research* **2005**, *44*, (18), 7062-7070.
10. Alejandre, A.; Medina, F.; Salagre, P.; Fabregat, A.; Sueiras, J. E., Characterization and activity of copper and nickel catalysts for the oxidation of phenol aqueous solutions. *Applied Catalysis B: Environmental* **1998**, *18*, (3), 307-315.
11. Shin, E.-J.; Keane, M. A., Gas phase catalytic hydrodechlorination of chlorophenols using a supported nickel catalyst. *Applied Catalysis B: Environmental* **1998**, *18*, (3), 241-250.
12. Li, X.; Zhang, Q.; Tang, L.; Lu, P.; Sun, F.; Li, L., Catalytic ozonation of p-chlorobenzoic acid by activated carbon and nickel supported activated carbon prepared from petroleum coke. *Journal of Hazardous Materials* **2009**, *163*, (1), 115-120.
13. Han, Y.; Yan, W., Bimetallic nickel–iron nanoparticles for groundwater decontamination: Effect of groundwater constituents on surface deactivation. *Water Research* **2014**, *66*, (0), 149-159.
14. Han, Y.; Liu, C.; Horita, J.; Yan, W., Trichloroethene hydrodechlorination by Pd-Fe bimetallic nanoparticles: Solute-induced catalyst deactivation analyzed by carbon isotope fractionation. *Applied Catalysis B: Environmental* **2016**, *188*, 77-86.
15. Aeppli, C.; Hofstetter, T. B.; Amaral, H. I. F.; Kipfer, R.; Schwarzenbach, R. P.; Berg, M., Quantifying In Situ Transformation Rates of Chlorinated Ethenes by Combining Compound-Specific Stable Isotope Analysis, Groundwater Dating, And Carbon Isotope Mass Balances. *Environmental Science & Technology* **2010**, *44*, (10), 3705-3711.
16. Bouchard, D.; Hunkeler, D.; Gaganis, P.; Aravena, R.; Hohener, P.; Broholm, M. M.; Kjeldsen, P., Carbon isotope fractionation during diffusion and biodegradation of petroleum hydrocarbons in the unsaturated zone: Field experiment at Værlose airbase, Denmark, and modeling. *Environmental Science & Technology* **2008**, *42*, (2), 596-601.
17. Meckenstock, R. U.; Morasch, B.; Griebler, C.; Richnow, H. H., Stable isotope fractionation analysis as a tool to monitor biodegradation in contaminated aquifers. *Journal of Contaminant Hydrology* **2004**, *75*, (3-4), 215-255.
18. Kopinke, F. D.; Georgi, A.; Voskamp, M.; Richnow, H. H., Carbon isotope fractionation of organic contaminants due to retardation on humic substances: Implications for natural attenuation studies in aquifers. *Environmental Science & Technology* **2005**, *39*, (16), 6052-6062.
19. Elsner, M.; Zwank, L.; Hunkeler, D.; Schwarzenbach, R. P., A new concept linking observable stable isotope fractionation to transformation pathways of organic pollutants. *Environmental Science & Technology* **2005**, *39*, (18), 6896-6916.
20. Kuder, T.; Philp, P.; Allen, J., Effects of Volatilization on Carbon and Hydrogen Isotope Ratios of MTBE. *Environmental Science & Technology* **2009**, *43*, (6), 1763-1768.

21. Liang, X.; Philp, R. P.; Butler, E. C., Kinetic and isotope analyses of tetrachloroethylene and trichloroethylene degradation by model Fe(II)-bearing minerals. *Chemosphere* **2009**, 75, (1), 63-69.
22. Zwank, L.; Elsner, M.; Aeberhard, A.; Schwarzenbach, R. P.; Haderlein, S. B., Carbon isotope fractionation in the reductive dehalogenation of carbon tetrachloride at iron (hydr)oxide and iron sulfide minerals. *Environmental Science & Technology* **2005**, 39, (15), 5634-5641.
23. Liang, X.; Dong, Y.; Kuder, T.; Krumholz, L. R.; Philp, R. P.; Butler, E. C., Distinguishing abiotic and biotic transformation of tetrachloroethylene and trichloroethylene by stable carbon isotope fractionation. *Environmental Science & Technology* **2007**, 41, (20), 7094-7100.
24. Vanstone, N.; Elsner, M.; Lacrampe-Couloume, G.; Mabury, S.; Lollar, B. S., Potential for identifying abiotic chloroalkane degradation mechanisms using carbon isotopic fractionation. *Environmental Science & Technology* **2008**, 42, (1), 126-132.
25. Elsner, M.; Chartrand, M.; Vanstone, N.; Couloume, G. L.; Lollar, B. S., Identifying abiotic chlorinated ethene degradation: Characteristic isotope patterns in reaction products with nanoscale zero-valent iron. *Environmental Science & Technology* **2008**, 42, (16), 5963-5970.
26. Chun, C. L.; Baer, D. R.; Matson, D. W.; Amonette, J. E.; Penn, R. L., Characterization and Reactivity of Iron Nanoparticles prepared with added Cu, Pd, and Ni. *Environmental Science & Technology* **2010**, 44, (13), 5079-5085.
27. Yaws, C. L., Yaws' Handbook of Thermodynamic and Physical Properties of Chemical Compounds. In Knovel.
28. Williams, M. L., CRC Handbook of Chemistry and Physics, 76th edition. *Occupational and Environmental Medicine* **1996**, 53, (7), 504-504.
29. Scott, K. M.; Lu, X.; Cavanaugh, C. M.; Liu, J. S., Optimal methods for estimating kinetic isotope effects from different forms of the Rayleigh distillation equation 1. *Geochimica et Cosmochimica Acta* **2004**, 68, (3), 433-442.
30. Liu, Y. Q.; Majetich, S. A.; Tilton, R. D.; Sholl, D. S.; Lowry, G. V., TCE dechlorination rates, pathways, and efficiency of nanoscale iron particles with different properties. *Environmental Science & Technology* **2005**, 39, (5), 1338-1345.
31. Elsner, M.; Haderlein, S. B.; Kellerhals, T.; Luzi, S.; Zwank, L.; Angst, W.; Schwarzenbach, R. P., Mechanisms and products of surface-mediated reductive dehalogenation of carbon tetrachloride by Fe(II) on goethite. *Environmental Science & Technology* **2004**, 38, (7), 2058-2066.
32. Elsner, M.; Cwiertny, D. M.; Roberts, A. L.; Sherwood Lollar, B., 1,1,2,2-tetrachloroethane reactions with OH-, Cr(II), granular iron, and a copper-iron bimetal: Insights from product formation and associated carbon isotope fractionation. *Environmental Science & Technology* **2007**, 41, (11), 4111-4117.

33. Bloom, Y.; Aravena, R.; Hunkeler, D.; Edwards, E.; Frape, S. K., Carbon Isotope Fractionation during Microbial Dechlorination of Trichloroethene, *cis*-1,2-Dichloroethene, and Vinyl Chloride: Implications for Assessment of Natural Attenuation. *Environmental Science & Technology* **2000**, *34*, (13), 2768-2772.
34. Hunkeler, D.; Aravena, R.; Butler, B. J., Monitoring Microbial Dechlorination of Tetrachloroethene (PCE) in Groundwater Using Compound-Specific Stable Carbon Isotope Ratios: Microcosm and Field Studies. *Environmental Science & Technology* **1999**, *33*, (16), 2733-2738.
35. Slater, G. F.; Lollar, B. S.; King, R. A.; O'Hannesin, S., Isotopic fractionation during reductive dechlorination of trichloroethene by zero-valent iron: influence of surface treatment. *Chemosphere* **2002**, *49*, (6), 587-596.
36. Morrill, P. L.; Lacrampe-Couloume, G.; Slater, G. F.; Sleep, B. E.; Edwards, E. A.; McMaster, M. L.; Major, D. W.; Sherwood Lollar, B., Quantifying chlorinated ethene degradation during reductive dechlorination at Kelly AFB using stable carbon isotopes. *Journal of Contaminant Hydrology* **2005**, *76*, (3-4), 279-293.
37. Morrill, P. L.; Sleep, B. E.; Seepersad, D. J.; McMaster, M. L.; Hood, E. D.; LeBron, C.; Major, D. W.; Edwards, E. A.; Sherwood Lollar, B., Variations in expression of carbon isotope fractionation of chlorinated ethenes during biologically enhanced PCE dissolution close to a source zone. *Journal of Contaminant Hydrology* **2009**, *110*, (1-2), 60-71.
38. Slater, G. F.; Sherwood Lollar, B.; Sleep, B. E.; Edwards, E. A., Variability in Carbon Isotopic Fractionation during Biodegradation of Chlorinated Ethenes: Implications for Field Applications. *Environmental Science & Technology* **2001**, *35*, (5), 901-907.
39. VanStone, N. A.; Focht, R. M.; Mabury, S. A.; Lollar, B. S., Effect of iron type on kinetics and carbon isotopic enrichment of chlorinated ethylenes during abiotic reduction on Fe(0). *Ground Water* **2004**, *42*, (2), 268-276.
40. Audi-Miro, C.; Cretnik, S.; Otero, N.; Palau, J.; Shouakar-Stash, O.; Soler, A.; Elsner, M., Cl and C isotope analysis to assess the effectiveness of chlorinated ethene degradation by zero-valent iron: Evidence from dual element and product isotope values. *Applied Geochemistry* **2013**, *32*, 175-183.
41. Schuth, C.; Bill, M.; Barth, J. A. C.; Slater, G. F.; Kalin, R. A., Carbon isotope fractionation during reductive dechlorination of TCE in batch experiments with iron samples from reactive barriers. *Journal of Contaminant Hydrology* **2003**, *66*, (1-2), 25-37.

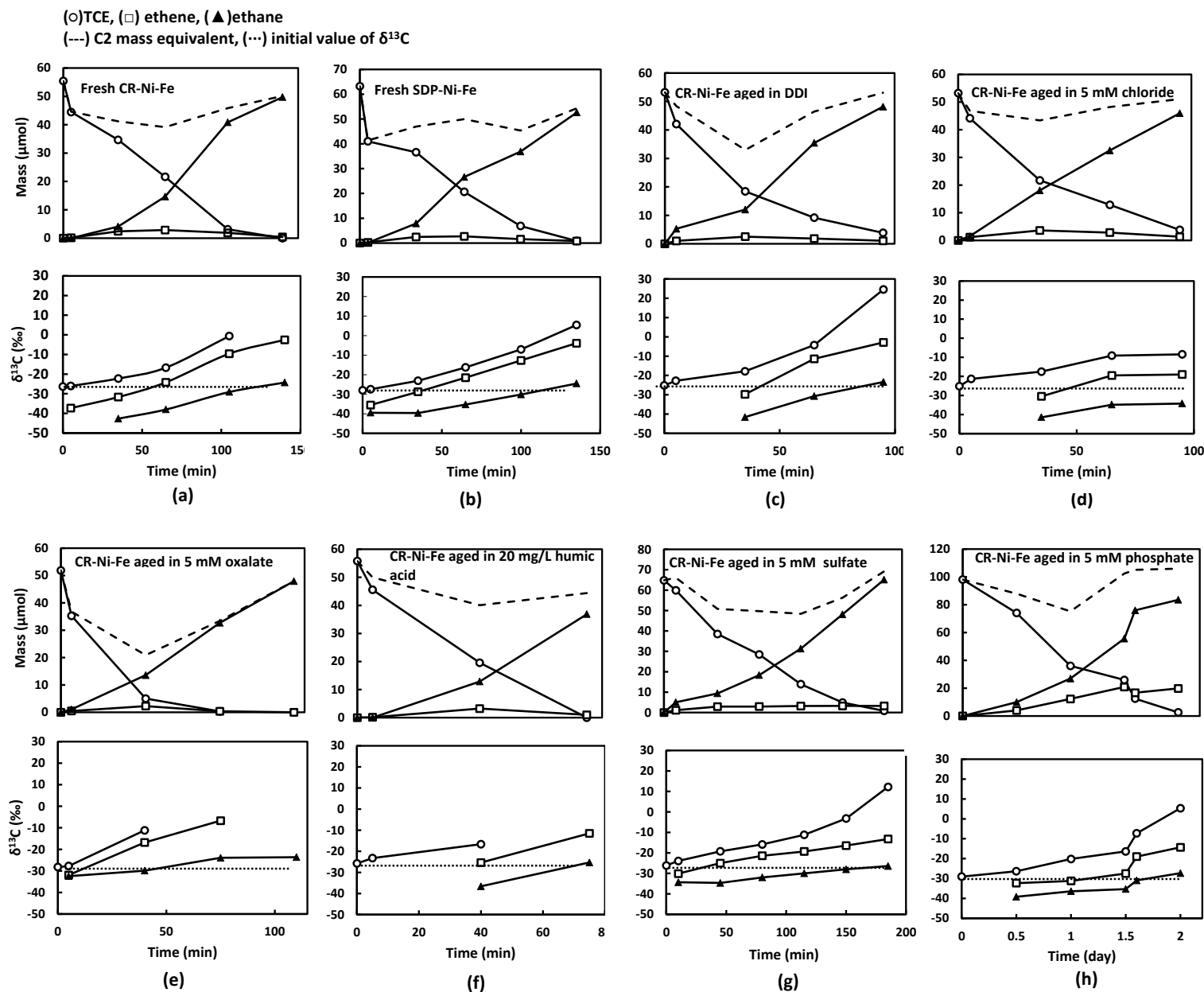


Figure 4.1. TCE dechlorination by fresh Ni-Fe BNPs ((a)-(b)) and those aged in different groundwater solutions for 24 h ((c)-(h)) and carbon isotope fractionation during TCE degradation. The dose of fresh CR-Ni-Fe BNPs and fresh SDP-Ni-Fe BNPs was 2 g/L. CR-Ni-Fe BNPs were used in all aqueous aging experiments. The dose of aged Ni-Fe BNPs was 3.3 g/L. The initial pH values of aging experiments and TCE dechlorination experiments were between 7.8-8.1.

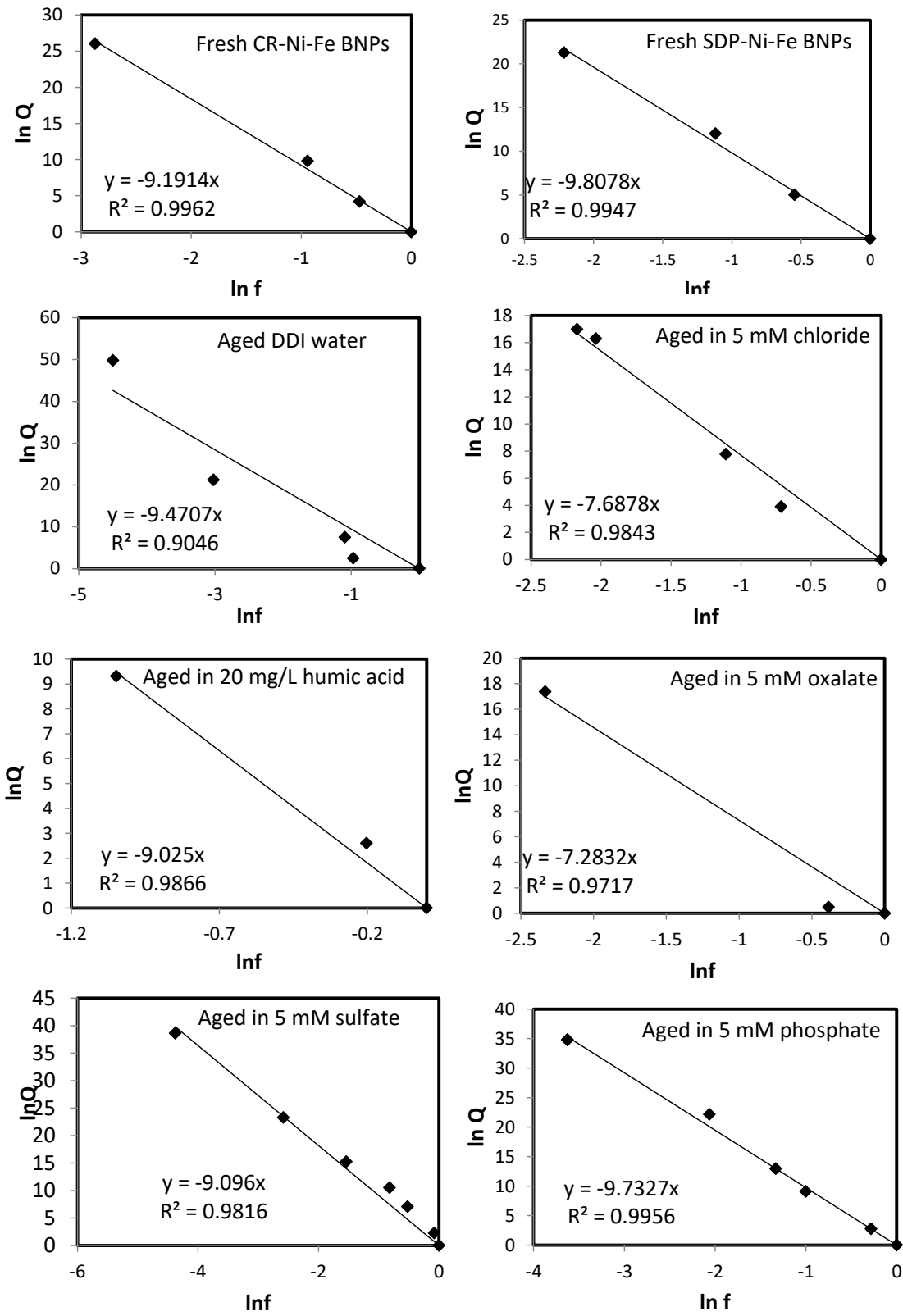


Figure 4.2. Rayleigh plot of different types of Ni-Fe BNPs. Experimental conditions were the same as those described in Figure 4.1. $f = [TCE]/TCE_0$ and $Q=R/R_0$ refer to Rayleigh model equation

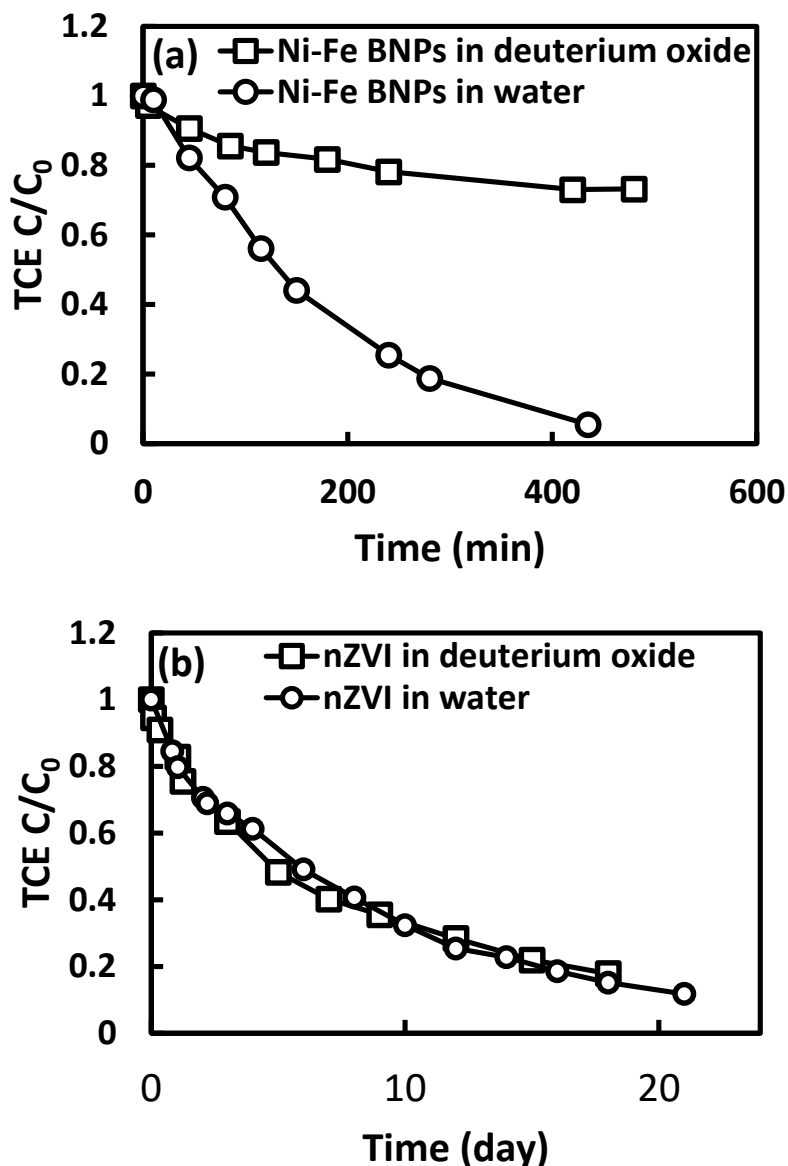


Figure 4.3. TCE degradation by (a) fresh CR-Ni-Fe BNPs in D₂O or in H₂O, and by (b) nZVI in D₂O or in H₂O. Dose of Ni-Fe BNPs was 1 g/L, and dose of nZVI was 5 g/L. Initial pH was between 7.8-8.3 for each reactor batch.

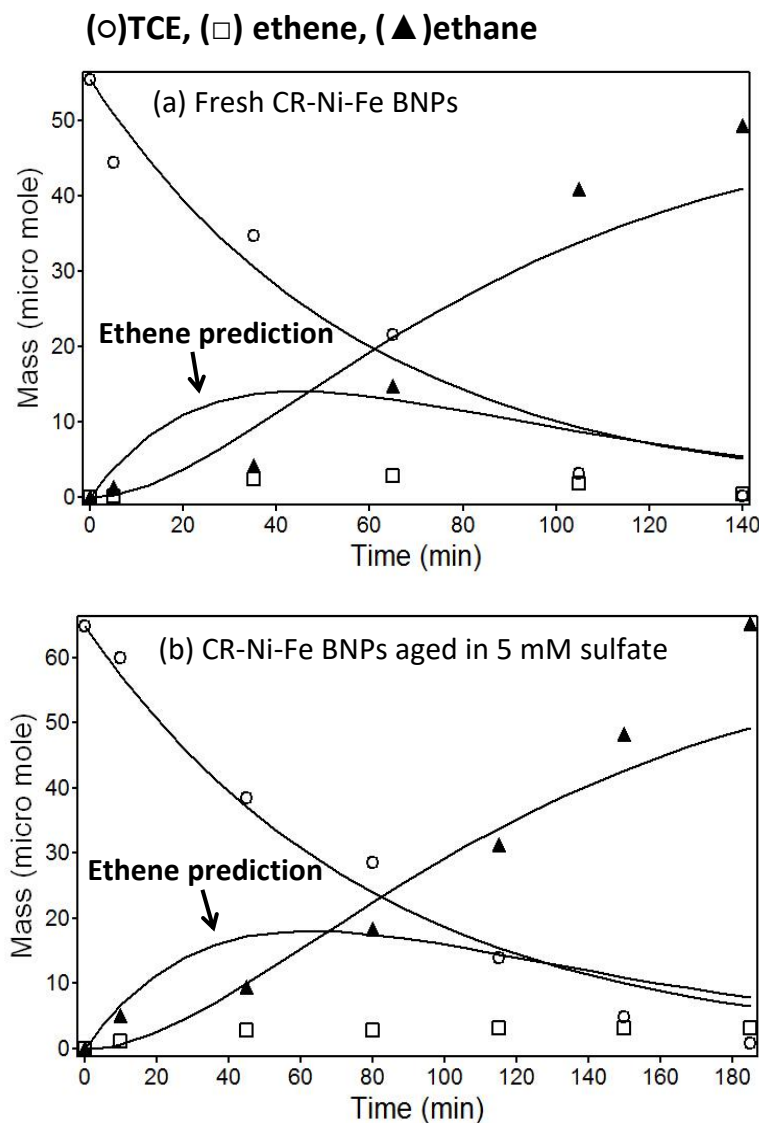


Figure 4.4. Fitting results of TCE dechlorination by Ni-Fe BNPs based on the kinetic model that TCE completely transforms to ethane via ethene as the only intermediate.

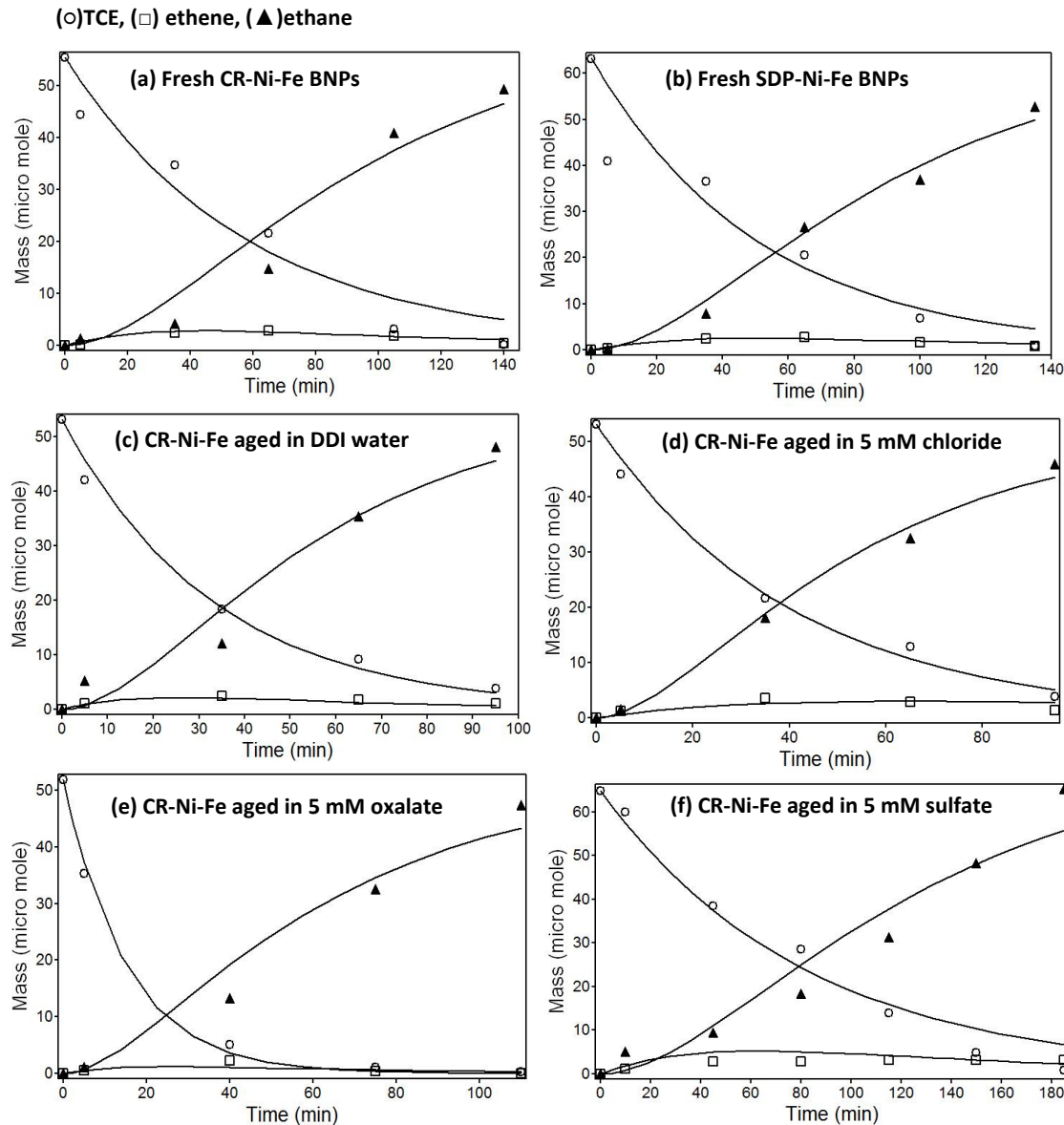


Figure 4.5. Fitting results of TCE dechlorination by Ni-Fe BNPs based on the “dual pathways” model.

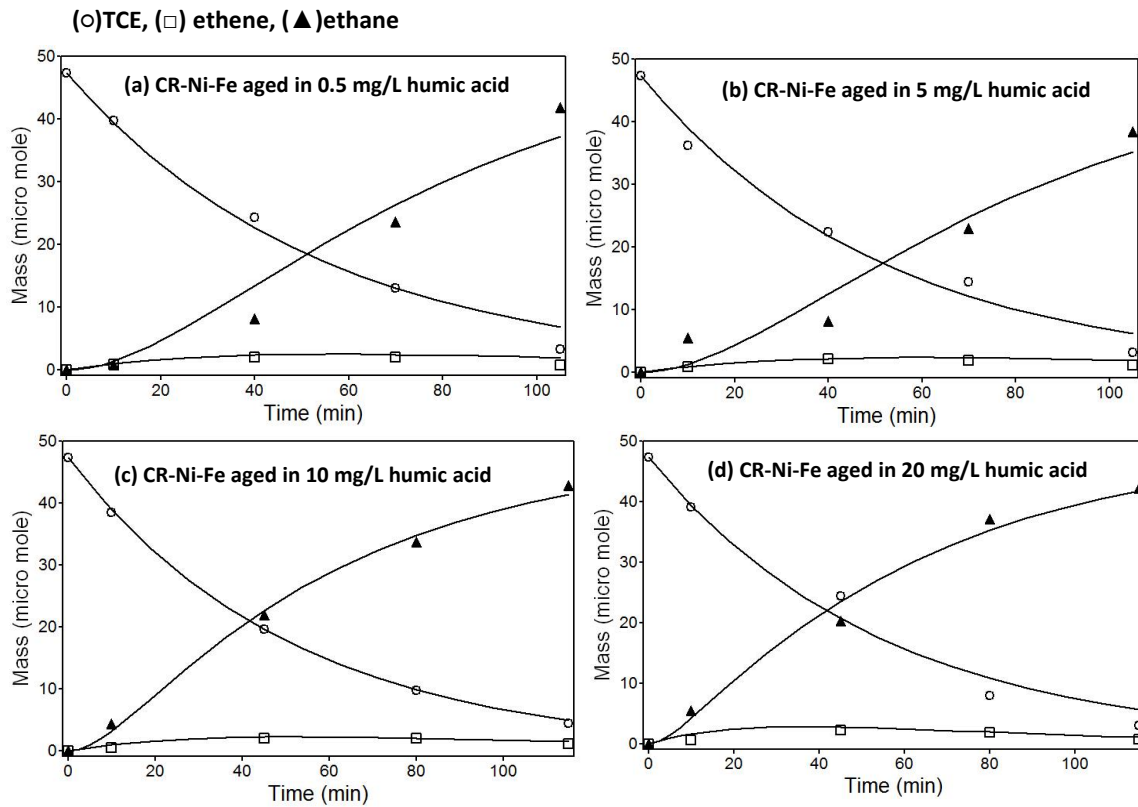


Figure 4.6. TCE dechlorination by Ni-Fe BNPs aged in solutions with different concentrations of humic acid. The particle dose was 3.3 g/L. Initial pH was between 7.8-8.1.

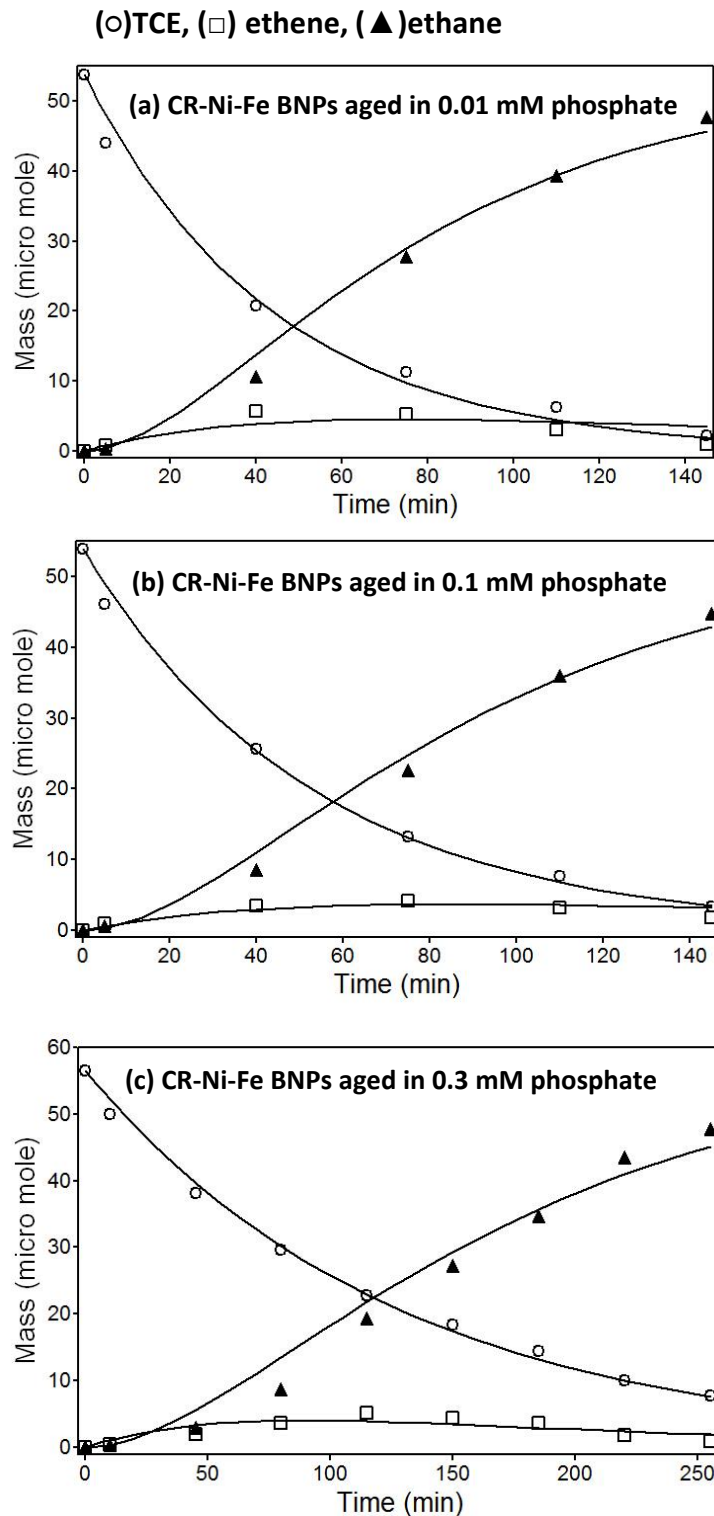


Figure 4.7. TCE dechlorination by Ni-Fe BNPs aged in dilute phosphate solutions (0.01-0.3 mM).

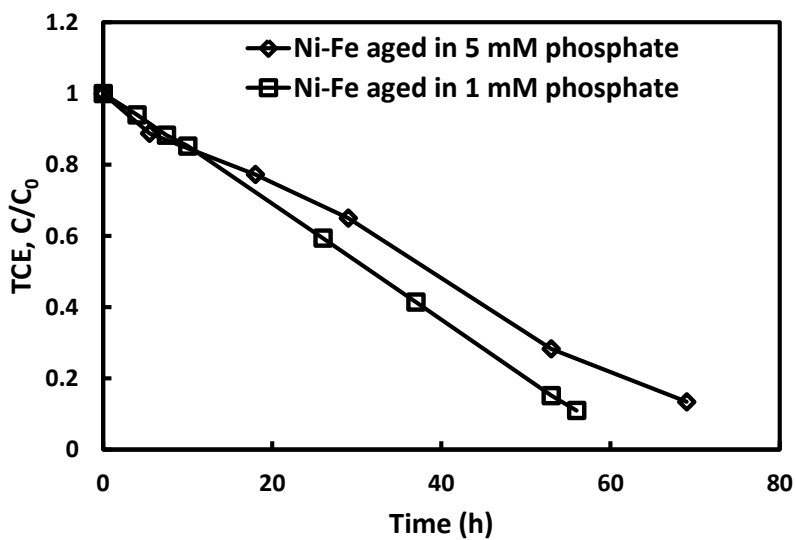


Figure 4.8. TCE dechlorination by aged Ni-Fe BNPs aged in 1 mM and 5 mM phosphate solutions. Initial concentration of TCE was 50 mg/L. The particle dose was 3.3 g/L. Initial pH was between 7.8-8.1.

Table 4.1. Reaction rate constants obtained from model fitting, carbon mass recovery, production distribution, and bulk enrichment factor of TCE dechlorination reactions with fresh and aged Ni-Fe BNPs.

Materials	k_1 (min^{-1}) ^a	k_2 (min^{-1}) ^a	k_3 (min^{-1}) ^a	k_4 (min^{-1}) ^a	C2 mass balance recovery ^b	Ethane yield ^c	Bulk enrichment factor (ε_{bulk}) ^d
Fresh CR-Ni-Fe BNPs	0.0032	0.0290	0.0156	0.0022	0.90	0.99	-15.3 ± 2.0
Fresh SDP-Ni-Fe BNPs	0.0022	0.0200	0.0178	0.0228	0.86	0.92	-8.6 ± 0.8
CR-Ni-Fe BNPs aged in DDI	0.0041	0.0460	0.0268	0.0381	0.99	0.98	-9.8 ± 1.5
CR-Ni-Fe BNPs aged in 5 mM Cl ⁻	0.0025	0.0090	0.0230	0.0614	0.96	0.97	-9.8 ± 0.5
CR-Ni-Fe BNPs aged in 5 mM C ₂ O ₄ ²⁻	0.0027	0.0206	0.0656	0.0180	0.93	1.00	-7.3 ± 1.1
CR-Ni-Fe BNPs aged in 5 mM SO ₄ ²⁻	0.0035	0.0200	0.0102	0.0189	1.07	0.95	-9.1 ± 0.4
CR-Ni-Fe BNPs aged in 0.5 mg/L humic acid	0.0026	0.0170	0.0179	0.0361	0.97	0.98	N.A.
CR-Ni-Fe BNPs aged in 5 mg/L humic acid	0.0022	0.0140	0.0183	0.0328	0.91	0.97	N.A.
CR-Ni-Fe BNPs aged in 10 mg/L humic acid	0.0025	0.0190	0.0177	0.1080	1.02	0.98	N.A.
CR-Ni-Fe BNPs aged in 20 mg/L humic acid	0.0047	0.0400	0.0144	0.2290	0.97	0.98	-9.0 ± 0.8
CR-Ni-Fe BNPs aged in 0.01 mM phosphate	0.0044	0.0074	0.0191	0.0301	1.03	0.89	N.A.
CR-Ni-Fe BNPs aged in 0.1 mM phosphate	0.0029	0.0067	0.0168	0.0245	0.91	0.98	N.A.
CR-Ni-Fe BNPs aged in 0.3 mM phosphate	0.0022	0.0150	0.0061	0.0175	0.98	0.98	N.A.
CR-Ni-Fe BNPs aged in 1 mM phosphate	N.A.	N.A.	N.A.	N.A.	0.75	0.91	N.A.
CR-Ni-Fe BNPs aged in 5 mM phosphate	N.A.	N.A.	N.A.	N.A.	1.00	0.81	-9.7 ± 1.1

a. Estimated by modeling software based on pseudo-first-order kinetic reaction assumption.

b. Mass recovery calculated at last sampling point.

c. Estimated from ethane formation production divided by total TCE removal at last sampling point.

d. Estimated based on Rayleigh equation, uncertainties represents 95% intervals for calculation.

Table 4.2. Bulk ^{13}C enrichment factor (ε_{bulk}) reported in the literature for TCE dechlorination by different types of iron.

Compound	Reagent	ε_{bulk} (%)
TCE	Peerless Iron	-13.9 ~ -13.0 ³⁹
TCE	Connelly Iron	-7.5 ~ -10.5 ³⁹
TCE	Electrolytic (Acid cleaned)	-20.3~ -24.8 ³⁵
TCE	Electrolytic (Autoclaved)	-17.2~ -18.7 ³⁵
TCE	Peerless (Acid cleaned)	-17.1 ³⁵
TCE	Peerless (Autoclaved)	-16.1 ³⁵
TCE	Cast iron	-14.9 ⁴⁰
TCE	Iron filings	-8.8~ -11.7 ⁴¹
TCE	Nanoscale nZVI (Toda Kogyo)	-20.9 ²⁵
TCE	Nanoscale nZVI (from NaBH ₄)	-23.5 ²⁵

CHAPTER FIVE

Trichloroethene Hydrodechlorination by Pd-Fe Bimetallic Nanoparticles: Solute-Induced Catalyst Deactivation Analyzed by Carbon Isotope Fractionation⁴

5.1. Introduction

Catalytic hydrodechlorination (HDC) is an efficient and sustainable approach for the treatment of industrial wastewater or groundwater contaminated with chlorinated contaminants. Among many catalysts evaluated for this application, palladium is considered one of the most active metal for HDC reactions^{1, 2}. The prominent role of Pd stems from its ability in activating molecular hydrogen (H_2) to form reactive hydrogen species (*e.g.*, atomic hydrogen or hydride)^{1, 3} and efficient dissociation of carbon-chlorine bonds^{4, 5}. An important class of materials exemplifying Pd-catalyzed HDC is palladium-iron (Pd-Fe) bimetallic particles, in which a small amount of Pd is deposited onto zero-valent iron particles through a facile aqueous replacement reaction⁶⁻⁸. When colloidal or nanoscale iron is used, the resultant bimetallic nanoparticles (BNPs) can be directly injected into underground environment for *in situ* remediation of aquifers contaminated with chlorinated hydrocarbons^{9, 10}.

Among many groundwater contaminants amenable to dehalogenation with Pd catalysts, chlorinated ethenes including trichloroethene (TCE) and tetrachloroethene (PCE) have received great attention because of their widespread occurrence at many U.S. superfund sites and their rapid transformation in the presence of Pd to completely dechlorinated products^{2, 11}. In contrast to chlorinated methanes or ethanes which undergo reduction via direct electron transfer, TCE or PCE reduction on metal surfaces involves an indirect reduction mechanism via reactive hydrogen species^{12, 13}. To enable *in situ* degradation of subsurface contaminants, a local source of H_2 is needed in the vicinity of Pd. As corrosion of iron in anoxic water produces hydrogen, a favorable synergy is

⁴ This chapter is published as: Yanlai Han, Changjie Liu, Juske Horita, Weile Yan. Trichloroethene hydrodechlorination by Pd-Fe bimetallic nanoparticles: solute-induced catalyst deactivation analyzed by carbon isotope fractionation. Applied Catalysis B: Environmental, 2016. Elsevier Publishing Company.

developed with Pd-Fe bimetallic material, where iron serves as the hydrogen source and catalyst support, and Pd acts as a catalyst for both hydrogen activation and HDC reactions. Indeed, rapid decomposition of chlorinated ethenes at rates thousand times that of the uncatalyzed iron have been documented in many laboratory investigations without forming the harmful less-chlorinated intermediates (*e.g.*, dichloroethenes or vinyl chloride) that are commonly observed in biological dehalogenation systems¹⁴⁻¹⁶.

As with other metal catalysts, a serious impediment associated with the use of Pd is catalyst deactivation in the reaction media. Deactivation is particularly relevant to *in situ* groundwater remediation, as the aqueous phase typically contains substantial amounts of background electrolytes as well as dissolved organic carbon originated from natural decay processes. Typical inorganic solutes include chloride (Cl⁻), sulfate (SO₄²⁻), bicarbonate (HCO₃⁻), nitrate (NO₃⁻), and sulfide (HS⁻), and their concentrations vary considerably with the site location, depth, and biogeochemical conditions. Among them, many are known to be potent deactivators of Fe^{17, 18} or Pd¹⁹⁻²¹. Not surprisingly, the Pd-Fe bimetallic nanoparticles have shown large susceptibility to solute-induced loss of reactivity^{22, 23}. In previous studies, particle deactivation was assessed by the rates of TCE degradation in batch experiments. Although bulk reaction rate is a useful indicator of the apparent effect of aqueous aging on particle reactivity, it offers limited insights into deactivation mechanisms caused by different groundwater solutes and the resultant impact on TCE degradation pathways.

Compound-specific isotope analysis (CSIA) is a valuable tool for assessing contaminant degradation in natural and laboratory environments²⁴⁻²⁷. The kinetic isotope effect (KIE) is built upon the principle that organic molecules with heavier isotopes generally experience slower bond breakage and thus, the heavier isotope tends to accumulate in the parent compound during the course of a degradation process. Consequently, an important application of CSIA is to assess the extent of contaminant transformation in an open system, since non-destructive loss of contaminants at a field site due to processes such as volatilization, sorption, diffusion, or dilution would contribute little to the isotope fractionation^{25, 28}. When applied in a controlled

environment, isotope fractionation is useful to diagnose contaminant reaction pathways. It has been reported that abiotic dechlorination of PCE and TCE mediated by Fe(II)-containing minerals (*e.g.*, green rust, magnetite, or pyrite)²⁹ or zerovalent iron^{15, 30, 31} is associated with more negative carbon isotope enrichment factors than biotic dechlorination processes¹⁶. Liang *et al.* attributed the suppressed isotope fractionation in biotic degradation to an increasing control of the degradation rates by mass transfer or complexation processes¹⁶, which is analogous to the masking effect encountered in abiotic catalytic conversion reactions³². Elsner *et al.* observed that during abiotic dechlorination of dichloroethanes on Zn(0), the carbon isotope fractionation associated with β-dichloroelimination was much greater than the fractionation incurred during hydrogenolysis or α-elimination³³, thus the isotope data can be used to identify plausible mechanisms of the rate-limiting reactions. In a bimetallic system, iron and palladium need to work cooperatively in order to attain optimal HDC efficiency, thus the cause of particles deactivation is potentially more complex than monometallic iron. It is expected that CSIA combined with bulk kinetic and product speciation analyses would enable us to delineate the different causes of catalyst deactivation in different groundwater matrices.

The objective of this study is to investigate the effects of common groundwater anions or natural organic matter on the reactivity of Pd-BNPs in TCE dechlorination reaction and to identify major factors contributing to the loss of reactivity or change in reaction pathways. Specifically, freshly made and various aged Pd-Fe BNPs (*i.e.*, particles pre-exposed to solutions containing different groundwater anions or natural organic carbon) will be evaluated in batch TCE hydrodechlorination experiments. The carbon isotope fractionations of TCE and daughter products were analyzed simultaneously using gas chromatography with a combustion isotope ratio mass-spectrometer (GC-C-IRMS) to quantify the TCE bulk enrichment factor (ε_{bulk}) and product-specific isotope fractionation values. Interpreting isotope effects together with kinetic data and product distribution allows insights to be gained into specific processes responsible for the declines in catalyst activity in different aqueous environment. This

knowledge would serve to better predict and improve the performance of bimetallic material under environmentally relevant conditions.

5.2. Materials and Methods

5.2.1. Preparation of Nanoparticles

Nanoscale zero-valent iron (nZVI) particles were synthesized via borohydride reduction of an aqueous solution of ferric ions. Briefly, 10.8 g of $\text{FeCl}_3 \cdot 6\text{H}_2\text{O}$ (Fisher) were dissolved in a 500-mL solution mixture of distilled de-ionized (DDI) water and ethanol (1:1, v/v). 500 mL of 0.4 M NaBH_4 solution (Acros Organics) was introduced to the ferric solution at approximately 17 mL/min under an vigorous mixing condition, during which the ferric solution turned black due to the formation of colloidal-sized iron particles. The particles formed were collected by vacuum filtration and were stored in ethanol for further use. Pd-Fe bimetallic nanoparticles (denoted as Pd-Fe BNPs) were prepared by immersing the freshly prepared nZVI with an ethanol/water (1:1, v/v) solution of palladium chloride (Acros Organics) and ultrasonicationg the mixture for 5 min²³. The mass loading of Pd with respect to iron was fixed at 1.5 % for all Pd-Fe BNPs. DDI water used in all procedures, including particle synthesis, aging and TCE experiments, was deoxygenated by purging with N_2 for 30 min.

5.2.2. Aging Experiments

Aging experiments were conducted in 250-mL amber glass vials containing 200 mL of deoxygenated solutions amended with a common groundwater solute at 1-5 mM. Stock solutions of chloride, bicarbonate, nitrate, phosphate, sulfate and sulfite were prepared from their sodium salts, respectively. Stock solution of humic acid (Sigma-Aldrich, used as received) was prepared at 100 mg/L and was ultrasonicated for 10 min prior to use. The initial pH of the solutions was adjusted with dilute NaOH or HCl to between 7.4-8.2 to simulate the typical pH values encountered in groundwater. An appropriate amount of freshly made Pd-Fe BNPs was added into each solution at 2 g/L (dry weight) and the vial was sealed and agitated on a mechanical shaker for 24 h at room

temperature (22 +/- 1 °C). The aged particles were collected by vacuum filtration and were used immediately in TCE degradation experiments.

5.2.3. TCE Experiments and Analytical Method

TCE dechlorination experiments were performed to compare the reactivity of fresh and aged Pd-Fe BNPs. All batch experiments were conducted in 250-mL amber glass vials containing 200 mL of aqueous solution and the balance as headspace. Experiments were performed with fresh or aged nanoparticles added at 1 - 4 g/L (dry weight). The vials were capped with Teflon Mininert valves, spiked with a small aliquot of TCE stock solution (in methanol and amended with 2-propanol as an internal standard), and placed on a wrist-action shaker at 250 rpm at room temperature. To monitor the concentrations and carbon isotope ratios of TCE and the reaction products, headspace samples (200 - 500 µL) were manually withdrawn and injected to a gas chromatograph-combustion-isotope ratio mass spectrometer (GC-C-IRMS) system periodically using a gastight syringe. The system comprised of TRACE GC Ultra (Thermo Scientific) installed with a PoraPlot Q capillary column (Varian, #CP7551) and GC Isolink (Thermo Scientific) coupled with ConFlo IV (Thermo Scientific) and Delta V IRMS (Thermo Scientific). The GC temperature program ramped the oven from 35 °C to 220°C in 26 min, with a 4 min hold at 35 °C. The flow rate of He carrier gas was set at 1.2 ml/min with split ratio of 8. TCE and the reaction products were separated by the GC column, and then oxidized into CO₂ by GC Isolink at 1030°C. The CO₂ produced by each analyte was introduced to IRMS for carbon isotope ratio analysis. Based on IRMS signal intensities, the concentrations of TCE and reaction products in the headspace samples were determined using calibration curves constructed with the corresponding commercial standards. Their concentrations in the solution phase were deduced from their concentrations in the headspace using Henry's Law constants ³⁴. Carbon isotope ratios are reported as δ ¹³C following Equation (1):

$$\delta^{13}C(\text{‰}) = \left(\frac{R_{\text{sample}}}{R_{\text{standard}}} - 1 \right) 1000 \quad (1)$$

where R_{sample} is the $^{13}\text{C}/^{12}\text{C}$ ratio of a given sample and R_{standard} is the $^{13}\text{C}/^{12}\text{C}$ ratio of the international standard reference material, V-PDB^{35, 15}. TCE and the reaction products were analyzed for $\delta^{13}\text{C}$ values relative to a reference CO₂ gas, and then normalized to the V-PDB scale against NG2 standard³⁶.

5.2.4. Evaluation of Isotope Fractionation

Isotope fractionation associated with a chemical reaction is usually represented by an isotope fractionation factor (α), which is defined as in Equation (2),

$$\alpha = \frac{k^h}{k^l} \quad (2)$$

where k^h and k^l are the rate constants of a chemical reaction involving a substrate containing the heavier and lighter isotope (in this case, ^{13}C and ^{12}C), respectively. Applying Equation (2) into a relevant kinetic expression and integrating over the extent of the reaction yield the Rayleigh equation (Eq. (3)), where R_0 and R stand for the isotope ratio of a substrate at the beginning of a reaction and at a given time, respectively. f is the fraction of the substrate remain at the specified time.

$$\frac{R}{R_0} = f^{\alpha-1} \quad (3)$$

The isotope fractionation factor is related to the apparent enrichment factor, $\varepsilon_{\text{bulk}}$, as in Equation (4) and (5).

$$\ln \frac{R}{R_0} = (\alpha - 1) \ln f \quad (4)$$

$$\varepsilon_{\text{bulk}} = (\alpha - 1) 1000 \quad (5)$$

Note that in deriving the Rayleigh equation, one assumes that the reaction itself is rate-limiting. This is not necessarily the case in catalytic reactions, where previous steps such as mass diffusion and adsorption of a substrate to reactive sites may proceed irreversibly or be rate-controlling. Since these preceding steps carry no or a minor isotope fractionation effect, $\varepsilon_{\text{bulk}}$ may exhibit a small value that does not correlate with the intrinsic isotope effect of the reaction. In such case, the isotope effect of a reaction can be estimated from the change in $\delta^{13}\text{C}$ of the substrate and product at the initial stage of the

experiments, when accumulation of product is considered negligible¹⁵. If multiple products are formed simultaneously or a product undergoes rapid further transformation steps, an average isotope value weighted by the molar ratio of the respective products may be used. In the case of TCE, the calculation of $\varepsilon_{TCE\ HDC}$ is described in Equation (5), where $\delta^{13}C_{product\ ave,0}$ and $\delta^{13}C_{TCE,0}$ represent the average isotope composition of the products (predominantly, ethene and ethane) and the substrate at the initial stage of an experiment:

$$\varepsilon_{TCE\ HDC} = \delta^{13}C_{product\ ave,0} - \delta^{13}C_{TCE,0} \quad (5)$$

ε_{bulk} and $\varepsilon_{TCE\ HDC}$ differ in the sense that ε_{bulk} reflects the isotope fractionation of the rate-limiting step, whereas $\varepsilon_{TCE\ HDC}$ accounts for the fractionation of all steps involved in converting TCE to the major products. Since mass transport and adsorption steps have considerably smaller isotope effects than chemical conversion, $\varepsilon_{TCE\ HDC}$ is a good indicator of the intrinsic KIE of a reaction and it is not affected by the kinetic masking effect often encountered in catalytic reactions³⁵.

Lastly, possible isotopic fractionation due to the transfer of TCE between the aqueous and gaseous phases is a valid concern during headspace analysis. In this study, the carbon isotope ratios of TCE in a water free vial and TCE in the headspace of the controls were identical within analytical error ($\pm 0.47\text{\textperthousand}$).

5.3. Results

5.3.1. TCE Dechlorination by Fresh Fe and Pd-Fe NPs

The reactivity of various Pd-Fe BNPs was evaluated using TCE batch experiments. Fresh Pd-Fe BNPs exhibited excellent reactivity with greater than 85% of TCE ($C_0 = 50\text{ mg/L}$) degraded within 125 min (Figure 5.1a). Chlorinated intermediates known to form during biological attenuation of TCE (e.g., DCEs and VC) were not detected in the headspace samples, in agreement with previous studies that abiotic reduction of TCE on zero-valent metal surface favors the formation of completely dechlorinated hydrocarbons^{15, 37, 38}. Ethane and ethene are the major products, accounting for 90% and 7.2%, respectively, of the total products formed at the last sampling point.

The ratio of ethane to ethene increased with reaction time, indicating that the fresh Pd-Fe is capable of hydrogenating ethene. Ethene reduction is a distinct capability of the bimetallic particles since additional experiments showed that monometallic Fe nanoparticles were unable to convert ethene to ethane under similar conditions. A small amount of C₄ products (butane and butene isomers) was detected. Their combined concentration accounts for less than 4% of the total carbon, and trace levels of C₅ – C₆ alkanes and alkenes were also detected but not quantified. These minor products suggest hydrocarbon coupling reactions had occurred to a small extent on Pd-Fe BNPs.

TCE reduction by monometallic Fe NPs (Figure 5.2a) was considerably slower, requiring more than 10 days to degrade the equivalent amount of TCE converted by Pd-Fe in 2 hours. Adding up TCE and product concentrations did not give a good carbon balance and this was attributed to sampling loss due to build-up of overpressure in the reaction vessel over a long monitoring period (23 days). Product analysis identified ethene and C₄ hydrocarbons to be the major products. C₄ products were formed primarily at the initial stage of the experiment. Ethane, in comparison, constitutes only 8.5% of the total products formed. Compared to Pd-Fe, monometallic Fe possesses significantly lower activity for hydrodechlorination (of TCE) and hydrogenation (of ethene) but a higher propensity to promote chain growth reactions. The latter property is in line with the prevalent use of iron as hydrocarbon synthesis or reforming catalysts (*e.g.*, in Fischer-Tropsch synthesis)^{39, 40}.

Figures 5.1b and 5.2b illustrate the isotopic composition of TCE and its daughter products with reaction time. Fitting the experimental data to the Raleigh model yields satisfactory fits (Figure 5.9), thus we may consider that a constant isotope fractionation prevails during the experiment periods. Comparing the data of the Pd-Fe and Fe systems, several differences can be discerned. With Pd-Fe (Figure 5.1b), TCE experienced little isotope fractionation during its rapid transformation, whereas TCE degradation by Fe NPs led to a strong enrichment of ¹³C in the remaining TCE. The bulk enrichment factor, ε_{bulk} , of the two materials was evaluated according to the Rayleigh equation (Eq. 3) to be -1.4±0.1‰ and -15.6±2.3‰, respectively (Figure 5.7). In prior studies, ε_{bulk} of TCE

dechlorination was reported in a range of -10.1‰ to -24.8‰ for various commercial or research-grade zero-valent iron materials under laboratory or field conditions^{41, 30, 42}. For nanoscale iron, ε_{bulk} was reported at approximately -20.9‰¹⁵, which is higher than the value obtained in this study (-15.6±2.3‰), but within the range mentioned above for a wide variety of iron materials. The discrepancy in ε_{bulk} may stem from difference in the surface properties of iron used in different studies as well as possible transport limitation in some column experiments. Compared to monometallic Fe, bulk enrichment factor of TCE degradation by Pd-Fe is characteristically small. The greatly diminished isotope effect is often interpreted as due to a kinetic masking effect, in which accelerated surface reactions in the presence of a catalyst cause the preceding less-fractionating steps (*i.e.*, transport of reactant from the bulk solution to the surface and adsorption to reactive sites) to be more rate-limiting³⁵. Another explanation is that smaller TCE fractionation on Pd-Fe BNPs is resulted from a decrease in the kinetic isotope effect (KIE) of TCE reduction due to facilitated bond-breaking on the catalyst surface. Using Eq.(5), $\varepsilon_{TCE\;HDC}$ is estimated to be -2.5‰ and -13.7‰, respectively, for Pd-Fe and the monometallic Fe. The results imply that TCE transformation on the bimetallic surface incurs a much smaller intrinsic kinetic isotope effect than its reaction on Fe particles. It was postulated in previous studies that abiotic reduction of unsaturated chlorinated compounds on metal surface is preceded by the formation of a strong precursor complex^{2, 43, 44}. Spectroscopic investigations suggest the C-Cl bonds of chlorinated ethenes were significantly weakened upon adsorption of the reactant on the Pd surface^{5, 45}. This thus explains the substantially reduced kinetic isotope effect during TCE conversion on fresh Pd-Fe nanoparticles. Lastly, the isotope discrimination between ethene and ethane are relatively small in both Fe and Pd-Fe systems, a result as expected since hydrogenation of carbon double bonds should invoke a minor isotope effect on the participating carbon atoms³¹.

5.3.2. TCE Dechlorination by Aged Pd-Fe NPs

Figure 5.3 shows TCE dechlorination by Pd-Fe nanoparticles that had been pre-exposed to different solution environment for 24 h prior to TCE experiments. On the basis of TCE removal rate, the aged Pd-Fe BNPs exhibit two types of deactivation

behavior. As shown in Figure 5.3(a), particles aged in 5 mM of sulfite, sulfate, and phosphate and humic acid (at 20 mg/L) suffered moderate degrees of reactivity loss compared to the fresh Pd-Fe BNPs. Their apparent mass-normalized pseudo first-order rate constants (k_m) were approximately one order of magnitude lower than that of the fresh Pd-Fe BNPs (Table 5.1). In comparison, particles aged in DDI or 5 mM of chloride (Cl^-), bicarbonate (HCO_3^-), and nitrate (NO_3^-) show signs of severe deactivation. In several cases, there was an initial reduction in TCE concentration in 2 h, however, TCE conversion beyond the initial phase was virtually negligible. Continuous monitoring for up to 2 days suggests these particles were essentially unreactive. We attribute the initial rapid disappearance of TCE to its reaction with a limited amount of active H species accumulated on the catalyst during the aging process. This is supported by the observation that sonicating the aged particles in clean water for several minutes to release the surface bound hydrogen species followed by collecting the particles and placing them in TCE solutions resulted in negligible degradation of TCE even during the initial phase (Figure 5.8).

Product distribution and carbon isotope analysis are used here to further investigate the deactivation mechanisms. Results of BNPs aged in four moderately deactivating solutions are shown in Figure 5.4. Pertinent parameters, including k_m , $\varepsilon_{\text{bulk}}$, and $\varepsilon_{\text{TCE HDC}}$ are summarized in Table 4.1. The table also lists ethane selectivity, which is defined as the amount of ethane produced over the total product formation at approximately 90% TCE conversion or, in the case of incomplete conversion due to strong deactivation, at the last sampling point. In spite of similar TCE degradation rates (Figure 5.3a), values of $\varepsilon_{\text{TCE HDC}}$ and ethane selectivity are remarkably different in these reaction systems. Specifically, Pd-Fe aged in humic acid exhibits a relatively small $\varepsilon_{\text{TCE HDC}}$ and the highest ethane selectivity among the aged Pd-Fe particles (Figure 5.4a). On the other hand, a large isotope depletion was observed in the case of sulfite-aged particles along with a small ethane selectivity (Figure 5.4b), implying that the deactivation effect of sulfite ions is specific to the Pd surface. The BNPs aged in phosphate and sulfate solution demonstrate intermediate shifts in $\varepsilon_{\text{TCE HDC}}$ and ethane

selectivity. However, unlike particles aged in sulfite or humic acid in which ethene and ethane experienced similar extents of isotope enrichment, $\delta^{13}\text{C}$ of the two hydrocarbon products formed in the presence of sulfate or phosphate-aged particles differ considerably (Figures 5.4c and 5.4d). Based on this data, it can be reasoned that ethene is not a precursor of ethane. Rather, independent pathways are involved in the formation of ethene and ethane at possibly different reactive sites on the particles aged in sulfate or phosphate solutions. With phosphate-aged BNPs, ethane undergoes negligible isotope fractionation during its formation, and its isotope ratio is similar to that of the original TCE. In comparison, there is a large isotope depletion during TCE conversion to ethene. These characteristics infer that ethane formation involves predominantly Pd surface while the production of ethene was associated with Fe sites. The conversion of ethene to ethane, a facile process by fresh Pd-Fe BNPs, is severely blocked on particles aged in phosphate and sulfate solutions.

Figure 5.5 shows the isotope fractionation and product formation during TCE degradation by particles aged in four strongly deactivating solutions, namely DDI, chloride, bicarbonate, and nitrate. With BNPs aged in DDI (Figure 5.5a), 40% of TCE was removed in the first 5 min, however, the loss was not accompanied by quantitative formation of dechlorination products, suggesting the initial loss of TCE is due to non-reactive sorption to the solid phase⁴⁶. Of the limited amount of TCE transformed, the isotope discrimination between TCE and dechlorination products is characteristically small ($\varepsilon_{TCE\ HDC} = -2.8\text{\textperthousand}$). On the contrary, particles aged in the chloride solution undergo substantial fractionation during TCE reduction (Figure 5.5b). The highly negative $\varepsilon_{TCE\ HDC}$ value of $-14.0\text{\textperthousand}$, comparable to the value of monometallic iron (-13.7%), points to severe impairment of Pd activity by chloride ions. This observation is also supported by ethene being the predominant product in the chloride-aged BNP system. Due to limited conversion of TCE by Pd-Fe aged in 5 mM nitrate and bicarbonate solutions, we conducted isotope experiments using particles aged in 1 mM of each solute. The results, in Figures 5.5c and 5.5d, show that, the reactions of TCE on bicarbonate- and nitrate-aged BNPs resulted in very small fractionations during both ethene and ethane

production. Hence, the decline in reactivity cannot be attributed to deactivation of Pd sites.

5.4. Discussion

5.4.1. Solute-induced Deactivation Mechanisms

Pd catalysts have been extensively studied for catalytic decomposition of halogenated contaminants. Treatment of industrial wastewater or *ex situ* remediation of contaminated groundwater typically employ the catalyst with H₂ in continuous flow-through reactors. To apply Pd catalysts to *in situ* subsurface remediation, a sustained source of H₂ is required close to the contaminant reaction zone. One strategy to achieve this is to incorporate Pd onto zero-valent iron, where iron oxidation by water provides a continuous supply of H₂ that is subsequently activated by Pd surface ^{9, 47}. Among the common solutes found in the subsurface environment, reduced sulfur species (*e.g.*, sulfite and sulfide ions) ^{2, 19, 48, 49} and natural organic matter (NOM) ^{49, 50} are known to exert strong deactivation effects on Pd reactivity. These observations agree on a large part with findings in the current study. A self-inhibitory effect has also been noted in the past, which is caused by the inhibition of Pd activity by the halogen ions produced during hydrodehalogenation reactions (*i.e.*, Cl⁻ or Br⁻), and such effect is more severe in gas or solvent phase HDC reactions at elevated contaminant concentrations ^{20, 51, 52}. Results in this study demonstrate that chloride ions as a natural constituent in groundwater can induce a serious impairment of Pd activity when present at a significant level. No adverse effect was reported in solute-free water for other bimetallic particles (*e.g.*, iron-supported nickel) ³⁴ or Pd/H₂ systems ¹¹, yet severe deactivation of Pd-Fe results upon immersion in deionized water. Prior surface and electron microscopic characterizations attributed this to the galvanic effect between the nanosized Pd deposits and the underlying Fe phase, leading to excessive iron corrosion in a short period of time (24 h) and the enclosure of Pd deposits by iron oxidation products ^{23, 53}. Other common solutes such as bicarbonate, nitrate, and phosphate do not appreciably affect Pd activity in Pd/H₂ reactors ¹⁹, however, the current study shows that these anions slow down the reactivity of Pd-Fe BNPs to appreciable degrees.

Figure 5.6a shows a conceptual model of TCE transformation on fresh Pd-Fe BNPs. It has been established previously that reductive dechlorination on zero-valent iron or in a Pd-catalyzed system are surface-mediated^{54, 55}. The reaction is initiated by the production of H₂ from Fe(0) corrosion and the adsorption of H₂ on the Pd surface to form dissociated hydrogen species. Subsequently, TCE reduction may occur via three pathways. The first involves the adsorption of TCE at Pd sites followed by multiple surface reactions to form predominantly ethane, as was reported in previous studies⁵⁵. In the second pathway, Fe itself is able to activate H₂ and mediate TCE degradation. This process is however characteristically slow (Figure 5.2), and therefore does not contribute significantly to the observed TCE degradation within the time frame of investigation (< 24 h). In the third pathway, we postulate migration of activated hydrogen from Pd to Fe sites, and TCE was degraded on the Fe surface. Spillover of atomic hydrogen from hydrogen dissociation catalysts such as palladium or platinum to support surface is well documented in heterogeneous catalytic reactions^{56, 57}. This process is considered kinetically facile at ambient temperature and has been proposed as an important pathway of Pd-catalyzed hydrodechlorination in the aqueous environment^{1, 58}. In this instance, Pd serves as an indirect catalyst by facilitating the accumulation active hydrogen species on the Fe surface. It is difficult to differentiate pathway 1 and 3 unambiguously with kinetic data alone, however, the distinct isotope signatures of Pd and Fe-mediated TCE reactions provide powerful insights into the reaction (and deactivation) mechanisms. For freshly prepared Pd-Fe particles, the small isotope fractionation between TCE and daughter products suggests Pd is the dominant site for TCE hydrodechlorination. Upon immersion in aqueous media with different solutes, several outcomes can be postulated. In heterogeneous catalytic systems, two modes of catalyst deactivation often arise: i) physical passivation of the particles due to deposition of carbonaceous or mineral precipitates, thereby blocking access to surface reactive sites, and ii) catalyst poisoning via specific binding of solute molecules to the catalytic sites rendering partial or complete loss of reactivity to the target reagents. In the case of Pd-Fe BNPs, additional factors can contribute to the decline in TCE degradation rate. For one, since Fe serves as an electron source for hydrogen evolution, anions interacting strongly with the Fe surface can slow

down TCE conversion by limiting H₂ production. On the other hand, alteration of the surface chemistry during aging may disable TCE dechlorination sites on Pd, but the catalyst may still be active for hydrogen activation. In this case, obstructing one type of reactive sites may not completely shut down the degradation process, but likely results in a change in reactive sites that can be detected through shifts in the product distribution as well as the isotope composition of the reactants and products.

Based on the observed deactivation behavior and the perceived roles of Pd and Fe in the bimetallic structure, we attribute various solute-induced deactivations to the following scenarios (Figure 5.6b). Type I deactivation involves nonselective blockage of reactive sites by surface deposits. Such process should not affect the isotope fractionation of TCE dechlorination as well as the product distribution. We reason that Pd-Fe particles aged in deionized water manifest Type I deactivation on the basis that the $\varepsilon_{TCE\ HDC}$ is close to that of the fresh Pd-Fe and prior microscopic characterizations reported extensive accumulation of corrosion products as a result of accelerated corrosion^{53, 59}. Alternatively, if Pd poisoning is the dominant deactivation mechanism (Type II deactivation), $\varepsilon_{TCE\ HDC}$ will deviate from that of the fresh Pd-Fe and the value is expected to be more negative due to the increasing role of the Fe-mediated TCE decomposition. Aging in Cl⁻ and SO₃²⁻ solutions falls in this category due to the large $\varepsilon_{TCE\ HDC}$ values and the low selectivity for ethane in the product mixture. Although Cl⁻ and SO₃²⁻ are known potent poisons of Pd metal^{19, 20, 51}, the reaction rate constants (k_m) of BNPs aged in the two solutions are more than one order of magnitude higher than that of the uncatalyzed Fe. This suggests that, while both solutes may hamper the direct reaction of TCE on Pd sites, the catalyst remains (at least partially) active for hydrogen activation and contributes indirectly to the enhanced TCE degradation rates. Humic acid appears to exhibit a mixed effect of surface passivation and catalyst poisoning. This is not unexpected since the humic acid macromolecules can impose a steric blockage of access to the finely dispersed Pd deposits, and natural organic carbon has abundant organothiol groups that can form strong complexes with Pd sites²¹.

Deactivation induced by immersing in HCO_3^- and NO_3^- solutions has not been carefully examined for Pd-Fe BNPs in prior studies. The particles were virtually unreactive upon aging in 5 mM of each solution for 24 h. Reducing the solute concentration to 1 mM renders the particles to be partially reactive and the isotope data suggests that the reactions involve a very small isotope fractionation effect (Figure 5.5c and 5.5d). Additional experiments placing the aged particles in H_2 -saturated TCE solutions recorded exceedingly rapid TCE conversion (> 90% removal in 40 min), hence, HCO_3^- and NO_3^- do not act by direct inactivation of Pd sites. Instead, the two solutes likely behave as corrosion inhibitors thereby impeding the formation of H_2 as the precursor of reactive hydrogen species. This anodic passivation effect is referred to as Type III deactivation in Figure 5.6b.

As an additional line of evidence, we prepared Al_2O_3 -supported Pd materials. The particles were subject to the same aging treatments as those of Pd-Fe BNPs and were subsequently used in TCE dechlorination experiments in the presence of 2.5 g/L of fresh iron nanoparticles as a H_2 source (Figure 5.10). The results indicate that Pd aged in sulfite and chloride solutions suffered the greatest loss of activity. Although immersion in DDI, bicarbonate, and nitrate solutions have caused severe impairment of the reactivity of Pd-Fe BNPs, these solutions only cast a moderate impact on Al_2O_3 -supported Pd. These observations are in line with the proposed mechanisms that sulfite and chloride act specifically on Pd sites, whereas nitrate, chloride and DDI solutions affect Pd-Fe via modulating Fe corrosion and H_2 production rates.

The actions of phosphate and sulfate are interesting as both solutes are hard Lewis bases and would more preferably interact with the oxide skin of the $\text{Fe}(0)$ core than with the Pd surface. Inspection of the isotope trends of ethane and ethene (Figures 5.4c and 5.4d) suggest the existence of separate pathways to ethene and ethane formation, respectively, and ethene conversion to ethane is exceedingly slow in these systems. Previous investigations of supported Pd catalysts indicate that the active sites of ethene hydrogenation are located at the Pd-support interface, where ethene adsorbs onto the support sites receiving hydrogen spilled over from the Pd sites^{60,61}. With these

considerations, we surmise that sulfate and phosphate impair the particle reactivity by diverting away activated hydrogen on the Pd surface and interfering with ethene hydrogenation, both could be resulted from altering the oxide surface close to Pd deposits (Type IV deactivation).

5.5. Environmental Significance

With carbon isotope analysis of TCE and its degradation products, the chemical or physical effects leading to the deterioration of TCE conversion rates were identified for Pd-Fe BNPs aged in different solution environment. This insight is of value for improved design, handling, deployment, and regeneration of BNPs for remediation of site impacted by chlorinated contaminants. For instance, aggravated corrosion of Pd-Fe in solutions of low ionic strength suggests Pd-Fe should not be synthesized and stored in an aqueous environment. Many of the common groundwater solutes as well as dissolved organic matter have been shown to cast a negative influence on the particle HDC activity. The modes of deactivation are not limited to catalyst poisoning and Fe(0) exhaustion as stipulated in previous studies^{59, 62, 13}. As such, conventional regeneration methods (*e.g.*, acid-washing or Fe(0) regeneration with reductants) may offer limited recovery of particle reactivity. Furthermore, the bimetallic design, although elegant in theory, poses practical constraints as it requires both the Fe and Pd phases to be reactive to attain efficient hydrodechlorination performance. In reality, since Fe and Pd are sensitive to different solute environments, the bimetallic material is susceptible to deactivation in a broad range of water matrices. It should be pointed out that in the present study the dose of Pd on Fe nanoparticles is relatively high compared to typical loading in field projects (< 0.5 wt%)^{9, 10}. Increased Pd content in the BNPs beyond an optimal range is known to exacerbate iron corrosion and decrease TCE dechlorination rates¹⁴. While our choice of catalyst loading is to be consistent with earlier studies to permit a fair evaluation of different bimetallic systems⁶³, the results may overestimate the aging effects in field conditions where a much lower Pd content is used.

References

1. Cheng, I. F.; Fernando, Q.; Korte, N., Electrochemical dechlorination of 4-chlorophenol to phenol. *Environmental Science & Technology* **1997**, *31*, (4), 1074-1078.
2. Chaplin, B. P.; Reinhard, M.; Schneider, W. F.; Schuth, C.; Shapley, J. R.; Strathmann, T. J.; Werth, C. J., Critical Review of Pd-Based Catalytic Treatment of Priority Contaminants in Water. *Environmental Science & Technology* **2012**, *46*, (7), 3655-3670.
3. Wong, M. S.; Alvarez, P. J. J.; Fang, Y. I.; Akcin, N.; Nutt, M. O.; Miller, J. T.; Heck, K. N., Cleaner water using bimetallic nanoparticle catalysts. *Journal of Chemical Technology and Biotechnology* **2009**, *84*, (2), 158-166.
4. Alonso, F.; Beletskaya, I. P.; Yus, M., Metal-mediated reductive hydrodehalogenation of organic halides. *Chemical Reviews* **2002**, *102*, (11), 4009-4091.
5. Park, K. T.; Klier, K.; Wang, C. B.; Zhang, W. X., Interaction of tetrachloroethylene with Pd(100) studied by high-resolution X-ray photoemission spectroscopy. *Journal of Physical Chemistry B* **1997**, *101*, (27), 5420-5428.
6. Hoke, J. B.; Gramicci, G. A.; Balko, E. N., Catalytic hydrodechlorination of chlorophenols *Applied Catalysis B-Environmental* **1992**, *1*, (4), 285-296.
7. Wang, C. B.; Zhang, W. X., Synthesizing nanoscale iron particles for rapid and complete dechlorination of TCE and PCBs. *Environmental Science & Technology* **1997**, *31*, (7), 2154-2156.
8. Fennelly, J. P.; Roberts, A. L., Reaction of 1,1,1-trichloroethane with zero-valent metals and bimetallic reductants. *Environmental Science & Technology* **1998**, *32*, (13), 1980-1988.
9. Elliott, D. W.; Zhang, W. X., Field assessment of nanoscale biometallic particles for groundwater treatment. *Environmental Science & Technology* **2001**, *35*, (24), 4922-4926.
10. He, F.; Zhao, D. Y.; Paul, C., Field assessment of carboxymethyl cellulose stabilized iron nanoparticles for in situ destruction of chlorinated solvents in source zones. *Water Research* **2010**, *44*, (7), 2360-2370.
11. Lowry, G. V.; Reinhard, M., Pd-catalyzed TCE dechlorination in groundwater: Solute effects, biological control, and oxidative catalyst regeneration. *Environmental Science & Technology* **2000**, *34*, (15), 3217-3223.
12. Li, T.; Farrell, J., Reductive dechlorination of trichloroethene and carbon tetrachloride using iron and palladized-iron cathodes. *Environmental Science & Technology* **2000**, *34*, (1), 173-179.
13. Xie, Y.; Cwiertny, D. M., Chlorinated Solvent Transformation by Palladized Zerovalent Iron: Mechanistic Insights from Reductant Loading Studies and Solvent Kinetic Isotope Effects. *Environmental Science & Technology* **2013**, *47*, (14), 7940-7948.

14. Kim, Y. H.; Carraway, E. R., Dechlorination of chlorinated ethenes and acetylenes by palladized iron. *Environmental Technology* **2003**, *24*, (7), 809-819.
15. Elsner, M.; Chartrand, M.; Vanstone, N.; Couloume, G. L.; Lollar, B. S., Identifying abiotic chlorinated ethene degradation: Characteristic isotope patterns in reaction products with nanoscale zero-valent iron. *Environmental Science & Technology* **2008**, *42*, (16), 5963-5970.
16. Liang, X.; Dong, Y.; Kuder, T.; Krumholz, L. R.; Philp, R. P.; Butler, E. C., Distinguishing abiotic and biotic transformation of tetrachloroethylene and trichloroethylene by stable carbon isotope fractionation. *Environmental Science & Technology* **2007**, *41*, (20), 7094-7100.
17. Liu, Y.; Phenrat, T.; Lowry, G. V., Effect of TCE concentration and dissolved groundwater solutes on NUI-Promoted TCE dechlorination and H-2 evolution. *Environmental Science & Technology* **2007**, *41*, (22), 7881-7887.
18. Farrell, J.; Kason, M.; Melitas, N.; Li, T., Investigation of the long-term performance of zero-valent iron for reductive dechlorination of trichloroethylene. *Environmental Science & Technology* **2000**, *34*, (3).
19. Hildebrand, H.; Mackenzie, K.; Kopinke, F.-D., Pd/Fe₃O₄ nano-catalysts for selective dehalogenation in wastewater treatment processes-Influence of water constituents. *Applied Catalysis B-Environmental* **2009**, *91*, (1-2), 389-396.
20. Ordonez, S.; Vivas, B. P.; Diez, F. V., Minimization of the deactivation of palladium catalysts in the hydrodechlorination of trichloroethylene in wastewaters. *Applied Catalysis B-Environmental* **2010**, *95*, (3-4), 288-296.
21. Kopinke, F.-D.; Angeles-Wedler, D.; Fritsch, D.; Mackenzie, K., Pd-catalyzed hydrodechlorination of chlorinated aromatics in contaminated waters-Effects of surfactants, organic matter and catalyst protection by silicone coating. *Applied Catalysis B-Environmental* **2010**, *96*, (3-4), 323-328.
22. Zhu, B. W.; Lim, T. T., Catalytic reduction of Chlorobenzenes with Pd/Fe nanoparticles: reactive sites, catalyst stability, particle aging, and regeneration. *Environmental Science & Technology* **2007**, *41*, (21), 7523-7529.
23. Yan, W.; Herzing, A. A.; Li, X.-Q.; Kiely, C. J.; Zhang, W.-X., Structural Evolution of Pd-Doped Nanoscale Zero-Valent Iron (nZVI) in Aqueous Media and Implications for Particle Aging and Reactivity. *Environmental Science & Technology* **2010**, *44*, (11), 4288-4294.
24. Aeppli, C.; Hofstetter, T. B.; Amaral, H. I. F.; Kipfer, R.; Schwarzenbach, R. P.; Berg, M., Quantifying In Situ Transformation Rates of Chlorinated Ethenes by Combining Compound-Specific Stable Isotope Analysis, Groundwater Dating, And Carbon Isotope Mass Balances. *Environmental Science & Technology* **2010**, *44*, (10), 3705-3711.
25. Bouchard, D.; Hunkeler, D.; Gaganis, P.; Aravena, R.; Hohener, P.; Broholm, M.; Kjeldsen, P., Carbon isotope fractionation during diffusion and biodegradation of

- petroleum hydrocarbons in the unsaturated zone: Field experiment at Vaerlose airbase, Denmark, and modeling. *Environmental Science & Technology* **2008**, *42*, (2), 596-601.
26. Meckenstock, R. U.; Morasch, B.; Griebler, C.; Richnow, H. H., Stable isotope fractionation analysis as a tool to monitor biodegradation in contaminated aquifers. *Journal of Contaminant Hydrology* **2004**, *75*, (3-4), 215-255.
27. Kopinke, F. D.; Georgi, A.; Voskamp, M.; Richnow, H. H., Carbon isotope fractionation of organic contaminants due to retardation on humic substances: Implications for natural attenuation studies in aquifers. *Environmental Science & Technology* **2005**, *39*, (16), 6052-6062.
28. Kuder, T.; Philp, P.; Allen, J., Effects of Volatilization on Carbon and Hydrogen Isotope Ratios of MTBE. *Environmental Science & Technology* **2009**, *43*, (6), 1763-1768.
29. Liang, X.; Philp, R. P.; Butler, E. C., Kinetic and isotope analyses of tetrachloroethylene and trichloroethylene degradation by model Fe(II)-bearing minerals. *Chemosphere* **2009**, *75*, (1), 63-69.
30. Slater, G. F.; Lollar, B. S.; King, R. A.; O'Hannesin, S., Isotopic fractionation during reductive dechlorination of trichloroethene by zero-valent iron: influence of surface treatment. *Chemosphere* **2002**, *49*, (6), 587-596.
31. Bill, M.; Schuth, C.; Barth, J. A. C.; Kalin, R. M., Carbon isotope fractionation during abiotic reductive dehalogenation of trichloroethene (TCE). *Chemosphere* **2001**, *44*, (5), 1281-1286.
32. Elsner, M., Stable isotope fractionation to investigate natural transformation mechanisms of organic contaminants: principles, prospects and limitations. *Journal of Environmental Monitoring* **2010**, *12*, (11), 2005-2031.
33. Vanstone, N.; Elsner, M.; Lacrampe-Couloume, G.; Mabury, S.; Lollar, B. S., Potential for identifying abiotic chloroalkane degradation mechanisms using carbon isotopic fractionation. *Environmental Science & Technology* **2008**, *42*, (1), 126-132.
34. Han, Y.; Yan, W., Bimetallic Nickel-Iron Nanoparticles for Groundwater Decontamination: Effect of Groundwater Constituents on Surface Deactivation. *Water Research* **2014**, *under review*.
35. Elsner, M.; Zwank, L.; Hunkeler, D.; Schwarzenbach, R. P., A new concept linking observable stable isotope fractionation to transformation pathways of organic pollutants. *Environmental Science & Technology* **2005**, *39*, (18), 6896-6916.
36. Dai, J.; Xia, X.; Li, Z.; Coleman, D. D.; Dias, R. F.; Gao, L.; Li, J.; Deev, A.; Li, J.; Dessort, D.; Duclerc, D.; Li, L.; Liu, J.; Schloemer, S.; Zhang, W.; Ni, Y.; Hu, G.; Wang, X.; Tang, Y., Inter-laboratory calibration of natural gas round robins for delta H-2 and delta C-13 using off-line and on-line techniques. *Chemical Geology* **2012**, *310*, 49-55.
37. Liu, Y. Q.; Majetich, S. A.; Tilton, R. D.; Sholl, D. S.; Lowry, G. V., TCE dechlorination rates, pathways, and efficiency of nanoscale iron particles with different properties. *Environmental Science & Technology* **2005**, *39*, (5), 1338-1345.

38. Song, H.; Carraway, E. R., Catalytic hydrodechlorination of chlorinated ethenes by nanoscale zero-valent iron. *Applied Catalysis B-Environmental* **2008**, *78*, (1-2), 53-60.
39. Lancet, H. S.; Anders, E., Carbon isotope fractionation in the Fischer-Tropsch synthesis of methane. *Science* **1970**, *170*, 980 - 982.
40. Deng, B. L.; Campbell, T. J.; Burris, D. R., Hydrocarbon formation in metallic iron/water systems. *Environmental Science & Technology* **1997**, *31*, (4), 1185-1190.
41. Schuth, C.; Bill, M.; Barth, J. A. C.; Slater, G. F.; Kalin, R. A., Carbon isotope fractionation during reductive dechlorination of TCE in batch experiments with iron samples from reactive barriers. *Journal of Contaminant Hydrology* **2003**, *66*, (1-2), 25-37.
42. VanStone, N. A.; Focht, R. M.; Mabury, S. A.; Lollar, B. S., Effect of iron type on kinetics and carbon isotopic enrichment of chlorinated ethylenes during abiotic reduction on Fe(0). *Ground Water* **2004**, *42*, (2), 268-276.
43. Arnold, W. A.; Roberts, A. L., Pathways and kinetics of chlorinated ethylene and chlorinated acetylene reaction with Fe(O) particles. *Environmental Science & Technology* **2000**, *34*, (9), 1794-1805.
44. Zhang, N.; Luo, J.; Blowers, P.; Farrell, J., Understanding trichloroethylene chemisorption to iron surfaces using density functional theory. *Environmental Science & Technology* **2008**, *42*, (6), 2015-2020.
45. Heck, K. N.; Janesko, B. G.; Scuseria, G. E.; Halas, N. J.; Wong, M. S., Observing Metal-Catalyzed Chemical Reactions in Situ Using Surface-Enhanced Raman Spectroscopy on Pd-Au Nanoshells. *Journal of the American Chemical Society* **2008**, *130*, (49), 16592-16600.
46. LaBolle, E. M.; Fogg, G. E.; Eweis, J. B.; Gravner, J.; Leaist, D. G., Isotopic fractionation by diffusion in groundwater. *Water Resources Research* **2008**, *44*, (7).
47. Zhu, B.-W.; Lim, T.-T.; Feng, J., Reductive dechlorination of 1,2,4-trichlorobenzene with palladized nanoscale Fe-0 particles supported on chitosan and silica. *Chemosphere* **2006**, *65*, (7), 1137-1145
48. Chaplin, B. P.; Reinhard, M.; Schneider, W. F.; Schueth, C.; Shapley, J. R.; Strathmann, T. J.; Werth, C. J., Critical Review of Pd-Based Catalytic Treatment of Priority Contaminants in Water. *Environmental Science & Technology* **2012**, *46*, (7), 3655-3670.
49. Chaplin, B. P.; Roundy, E.; Guy, K. A.; Shapley, J. R.; Werth, C. J., Effects of natural water ions and humic acid on catalytic nitrate reduction kinetics using an alumina supported Pd-Cu catalyst. *Environmental Science & Technology* **2006**, *40*, (9), 3075-3081.
50. Kopinke, F.-D.; Angeles-Wedler, D.; Fritsch, D.; Mackenzie, K., Pd-catalyzed hydrodechlorination of chlorinated aromatics in contaminated waters—Effects of surfactants, organic matter and catalyst protection by silicone coating. *Applied Catalysis B: Environmental* **2010**, *96*, (3-4), 323-328.

51. de Pedro, Z. M.; Diaz, E.; Mohedano, A. F.; Casas, J. A.; Rodriguez, J. J., Compared activity and stability of Pd/Al₂O₃ and Pd/AC catalysts in 4-chlorophenol hydrodechlorination in different pH media. *Applied Catalysis B: Environmental* **2011**, *103*, (1–2), 128-135.
52. Yuan, G.; Keane, M. A., Catalyst deactivation during the liquid phase hydrodechlorination of 2,4-dichlorophenol over supported Pd: influence of the support. *Catalysis Today* **2003**, *88*, (1–2), 27-36.
53. Muftikian, R.; Nebesny, K.; Fernando, Q.; Korte, N., X-ray photoelectron spectra of the palladium-iron bimetallic surface used for the rapid dechlorination of chlorinated organic environmental contaminants. *Environmental Science & Technology* **1996**, *30*, (12), 3593-3596.
54. Matheson, L. J.; Tratnyek, P. G., Reductive Dehalogenation of Chlorinated Methanes by Iron Metal. *Environmental Science & Technology* **1994**, *28*, (12), 2045-2053.
55. Lowry, G. V.; Reinhard, M., Hydrodehalogenation of 1-to 3-carbon halogenated organic compounds in water using a palladium catalyst and hydrogen gas. *Environmental Science & Technology* **1999**, *33*, (11), 1905-1910.
56. Teichner, S. J., Recent studies on hydrogen and oxygen spillover and their impact on catalysis. *Applied Catalysis* **1990**, *62*, (1), 1-10.
57. Conner, W. C.; Falconer, J. L., Spillover in heterogeneous catalysis *Chemical Reviews* **1995**, *95*, (3), 759-788.
58. Kovenklioglu, S.; Cao, Z. H.; Shah, D.; Farrauto, R. J.; Balko, E. N., Direct catalytic hydrodechlorination of toxic organics in waste-water. *Aiche Journal* **1992**, *38*, (7), 1003-1012.
59. Yan, W. L.; Herzing, A. A.; Li, X. Q.; Kiely, C. J.; Zhang, W. X., Structural Evolution of Pd-Doped Nanoscale Zero-Valent Iron (nZVI) in Aqueous Media and Implications for Particle Aging and Reactivity. *Environmental Science & Technology* **2010**, *44*, (11), 4288-4294.
60. Sarkany, A.; Guczi, L.; Weiss, A. H., On the aging phenomenon in Pd catalyzed acetylene hydrogenation. *Applied Catalysis* **1984**, *10*, (3), 369-388.
61. Leviness, S.; Nair, V.; Weiss, A. H.; Schay, Z.; Guczi, L., Acetylene hydrogenation selectivity control on PdCu/Al₂O₃ catalysts. *Journal of Molecular Catalysis* **1984**, *25*, (1-3), 131-140.
62. Lim, T. T.; Zhu, B. W., Effects of anions on the kinetics and reactivity of nanoscale Pd/Fe in trichlorobenzene dechlorination. *Chemosphere* **2008**, *73*, (9), 1471-1477.
63. Han, Y.; Yan, W., Bimetallic nickel–iron nanoparticles for groundwater decontamination: Effect of groundwater constituents on surface deactivation. *Water Research* **2014**, *66*, (0), 149-159.

Table 5.1. Pertinent kinetic, isotopic, and production distribution parameters of TCE hydrodechlorination reactions with fresh and aged Pd-Fe BNPs

Solution	$k_m (10^{-2} \text{ L g}^{-1} \text{ min}^{-1})^a$	ϵ_{bulk}	ϵ_{TCEHDC}	Ethane Selectivity ^d
Fe nanoparticles	$(2.15 \pm 0.64) \times 10^{-3}$	-15.8 ± 2.6	-13.7	0.08
Fresh Pd-Fe	1.37 ± 0.68	-1.6 ± 0.2	-2.5	0.88
Pd-Fe aged in DDI	N.D. ^b	-4.6 ± 0.7	-2.8	0.54
Pd-Fe aged in 20 mg/L HA	0.37 ± 0.08	-4.9 ± 1.2	-6.0	0.70
Pd-Fe aged in 5 mM Cl ⁻	N.D. ^b	-10.8 ± 2.5	-14.0	0.12
Pd-Fe aged in 5 mM SO ₃ ²⁻	0.24 ± 0.03	-12.6 ± 0.1	-14.3	0.23
Pd-Fe aged in 5 mM SO ₄ ²⁻	0.12 ± 0.03	-6.5 ± 1.6	-15.0	0.29
Pd-Fe aged in 5 mM HPO ₄ ²⁻	0.55 ± 0.04	-6.8 ± 1.5	-10.0	0.29
Pd-Fe aged in 1 mM HCO ₃ ⁻	N.D. ^b	N.D. ^c	-0.5	0.57
Pd-Fe aged in 1 mM NO ₃ ⁻	N.D. ^b	N.D. ^c	-2.3	0.58

^a Estimated by fitting experimental data ($t > 35$ min) to pseudo-first-order kinetic model.^b Not determined (N.D.) due to severe deviation from pseudo-first-order kinetics.^c Not determined (N.D.) due to limited TCE conversion and poor fits to the Raleigh equation (Fig. 5.9).^d Estimated from ethane produced over total product formation at ~ 90% conversion of TCE or the last sampling point for strongly deactivated particles.

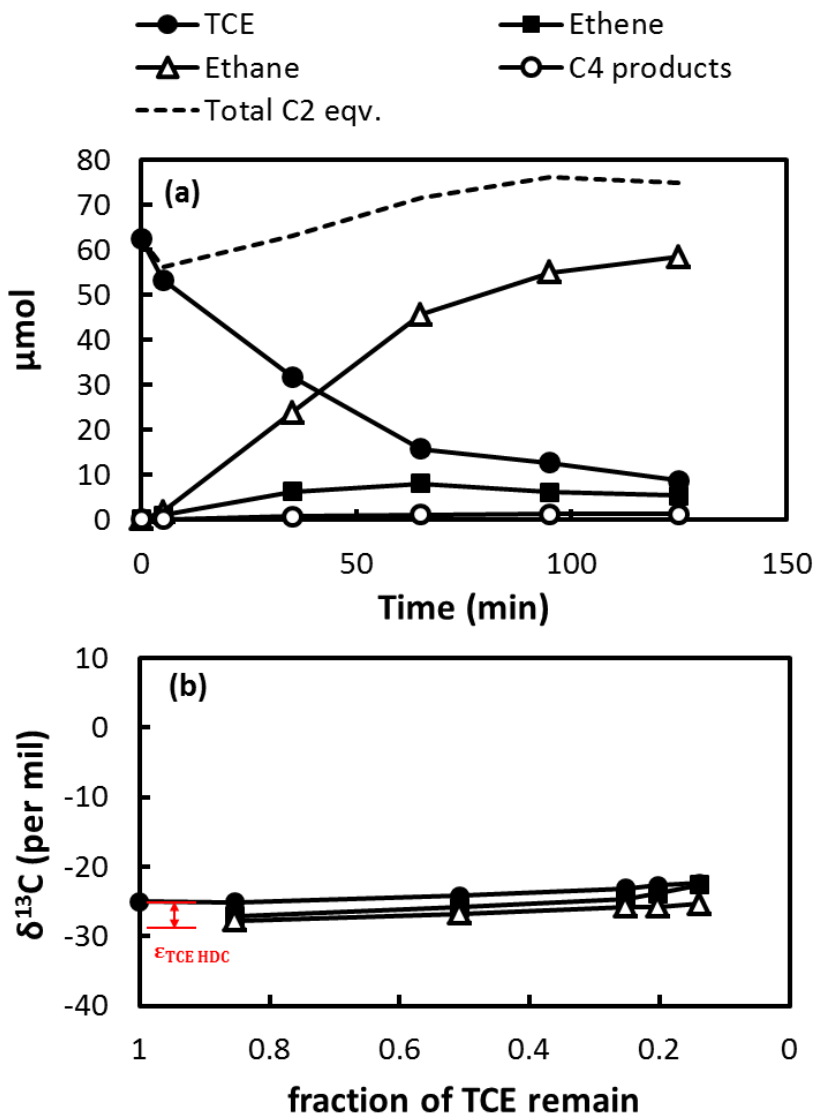


Figure 5.1. (a) Reductive dechlorination of TCE by fresh Pd-Fe nanoparticles and (b) changes in $\delta^{13}\text{C}$ values of TCE and reaction products during the experiment. Nanoparticle dose was 1 g/L.

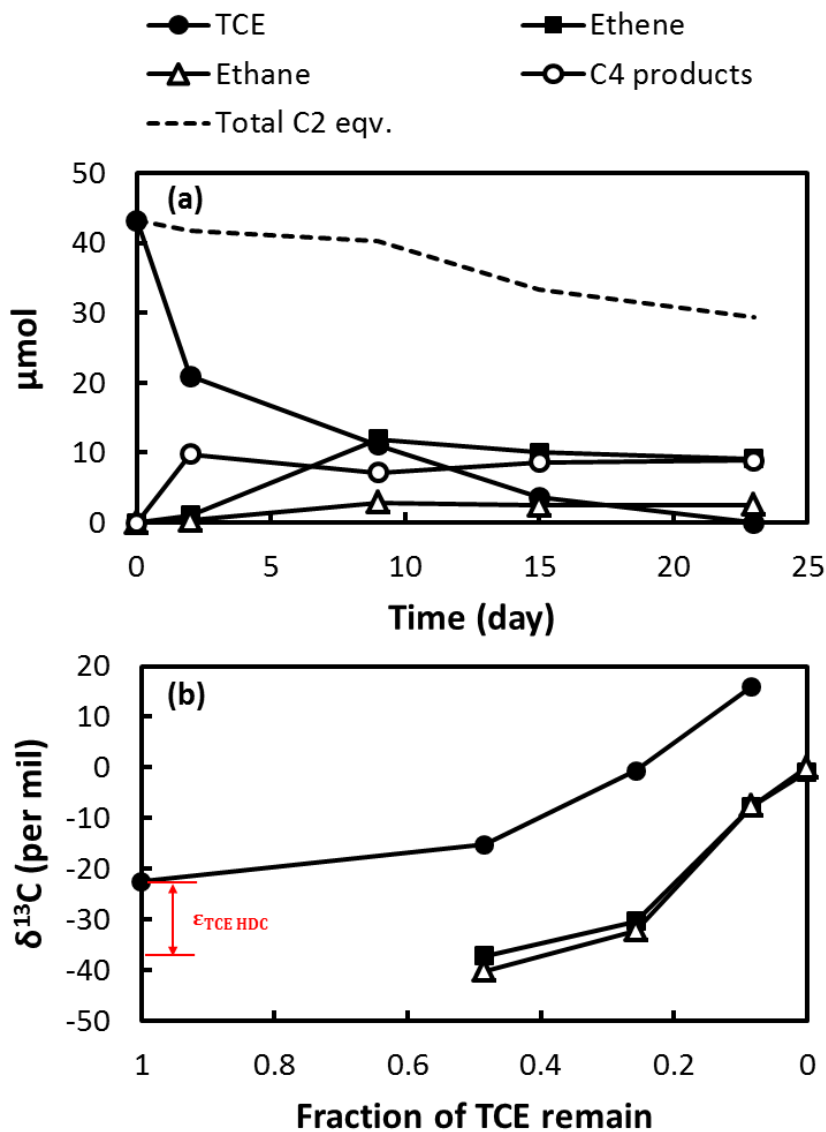


Figure 5.2. (a) Reductive dechlorination of TCE by fresh Fe nanoparticles and (b) changes in $\delta^{13}\text{C}$ values of TCE and reaction products during the experiment. Nanoparticle dose was 4 g/L.

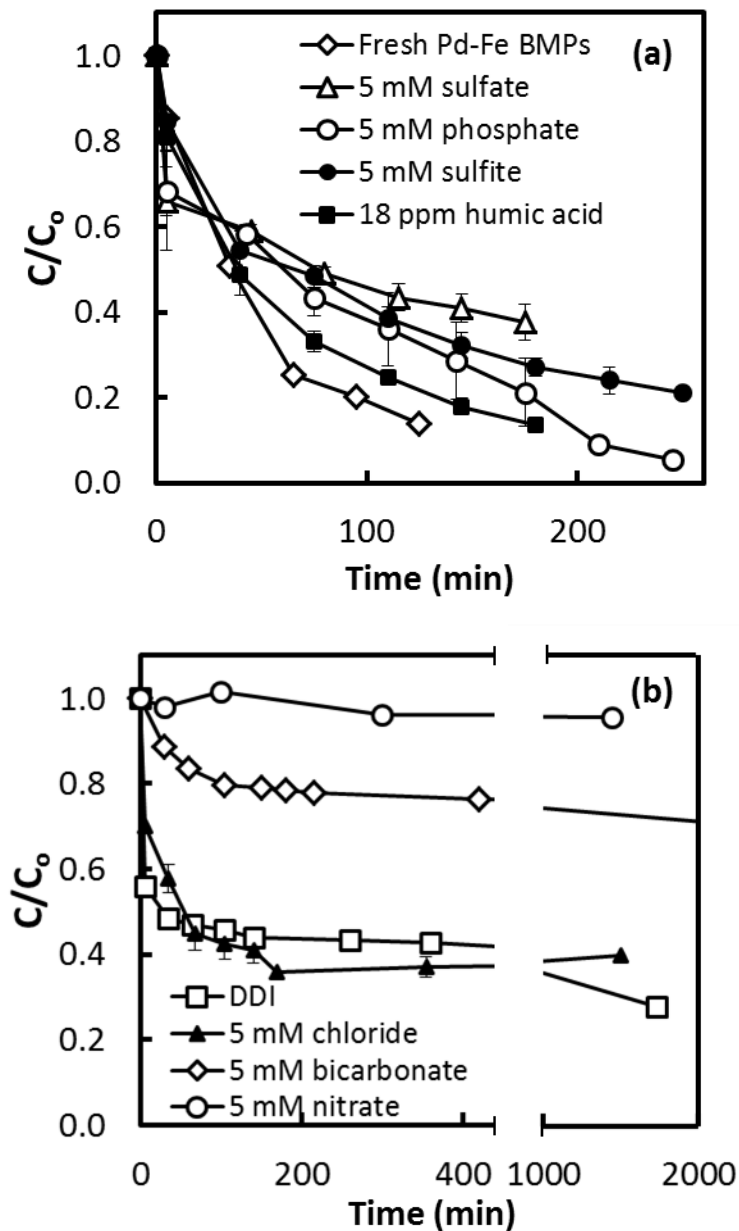


Figure 5.3. TCE degradation by (a) fresh and moderately deactivated and (b) severely deactivated Pd-Fe nanoparticles. Aging was conducted by immersing freshly made Pd-Fe in various aqueous solutions for 24 h prior to TCE experiments. Initial TCE concentration was 50 mg/L. Dose of Pd-Fe was 1 g/L and 2 g/L for fresh and aged particles, respectively.

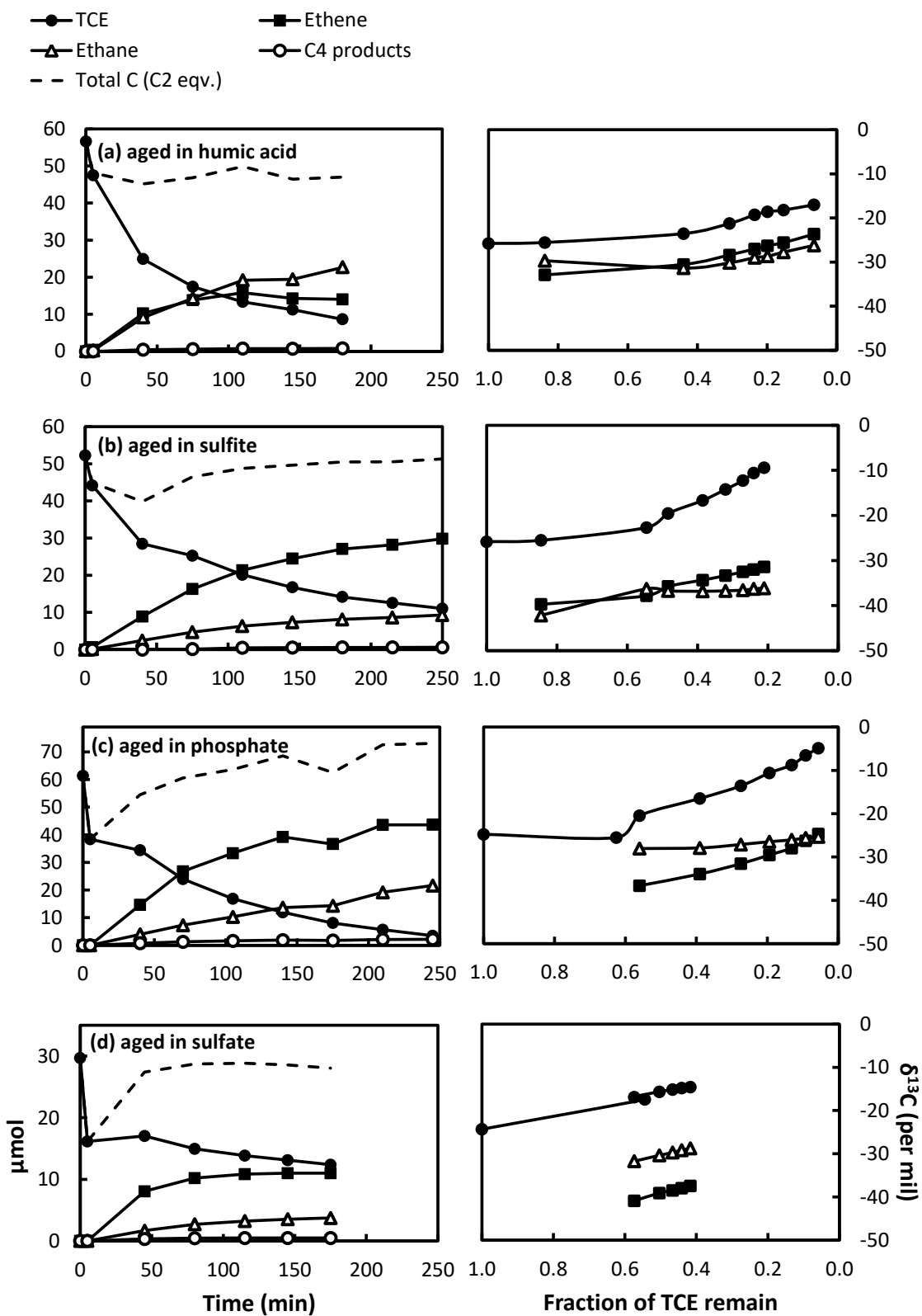


Figure 5.4. Product distribution and carbon isotope fractionation during TCE degradation by Pd-Fe aged in the presence of (a) 20 mg/L humic acid, (b) 5 mM sulfite, (c) 5 mM phosphate, and (d) 5 mM sulfate. The initial pH of the aging solutions was in the range of 7.4 - 8.2.

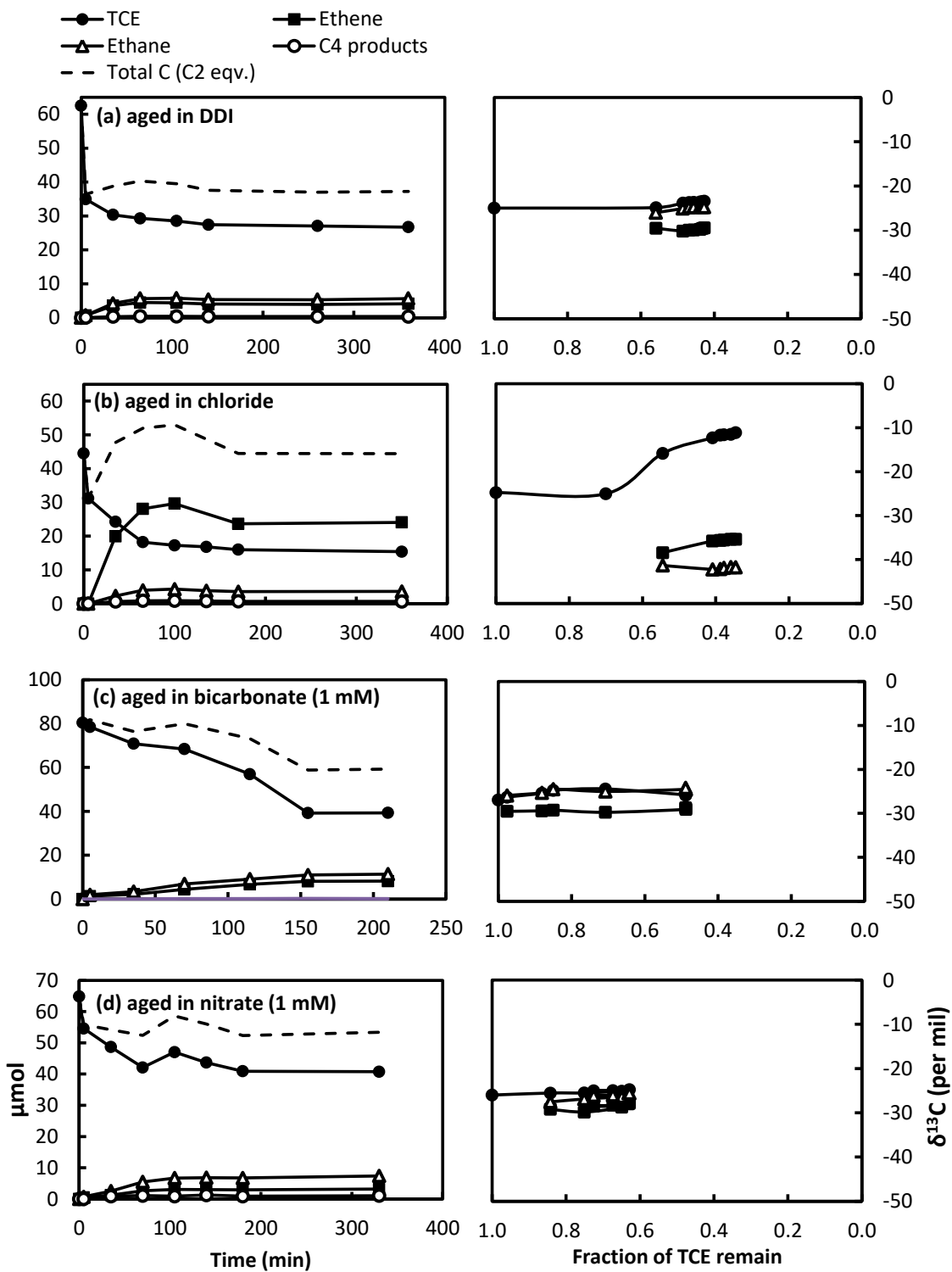


Figure 5.5. Product distribution and carbon isotope fractionation during TCE degradation by Pd-Fe aged in the presence of (a) distilled deionized water (DDI), (b) 5 mM chloride,

(c) 1 mM carbonate, and (d) 1 mM nitrate. The initial pH of the aging solutions was in the range of 7.4 - 8.2.

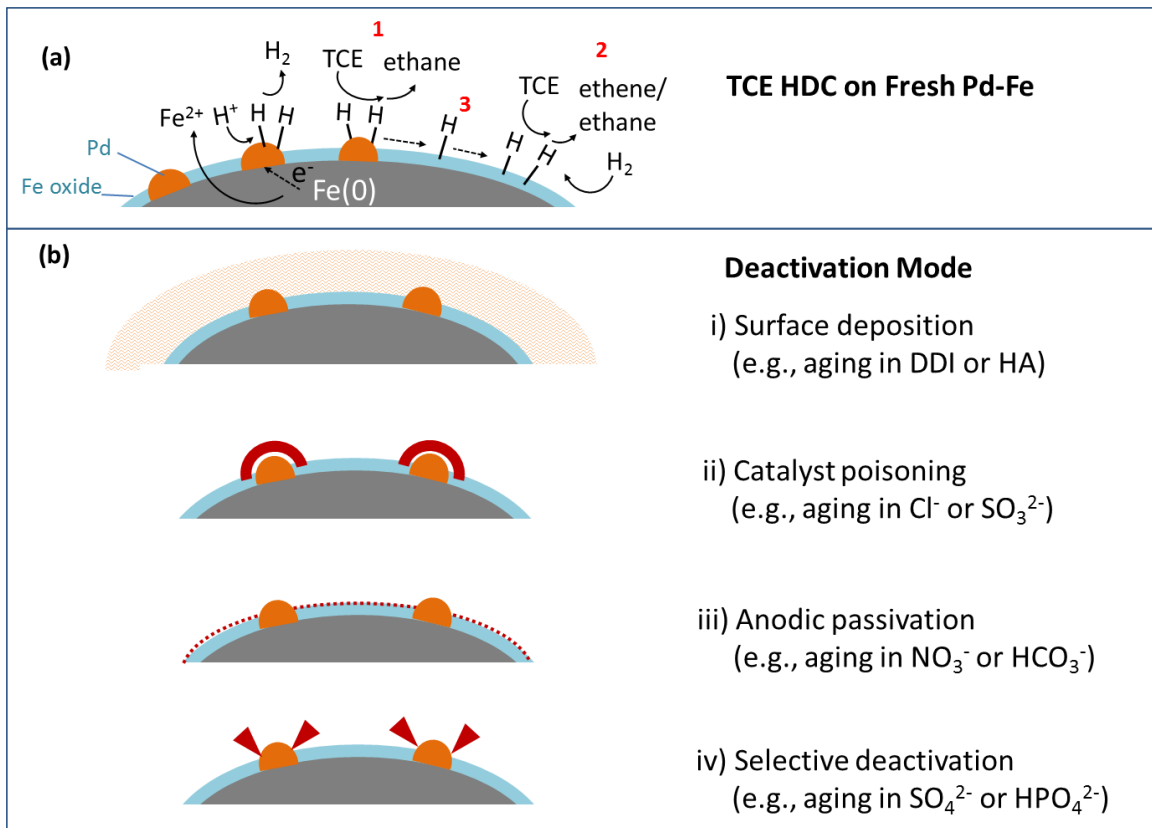


Figure 5.6. Proposed mechanisms for Pd-Fe BNP deactivation in different groundwater media. (i) Surface accumulation of iron oxidation products, (ii) direct poisoning of Pd catalyst, (iii) interaction of Fe surface with passivating anions inhibiting Fe corrosion and H_2 production; and (iv) selective deactivation of hydrogenation sites.

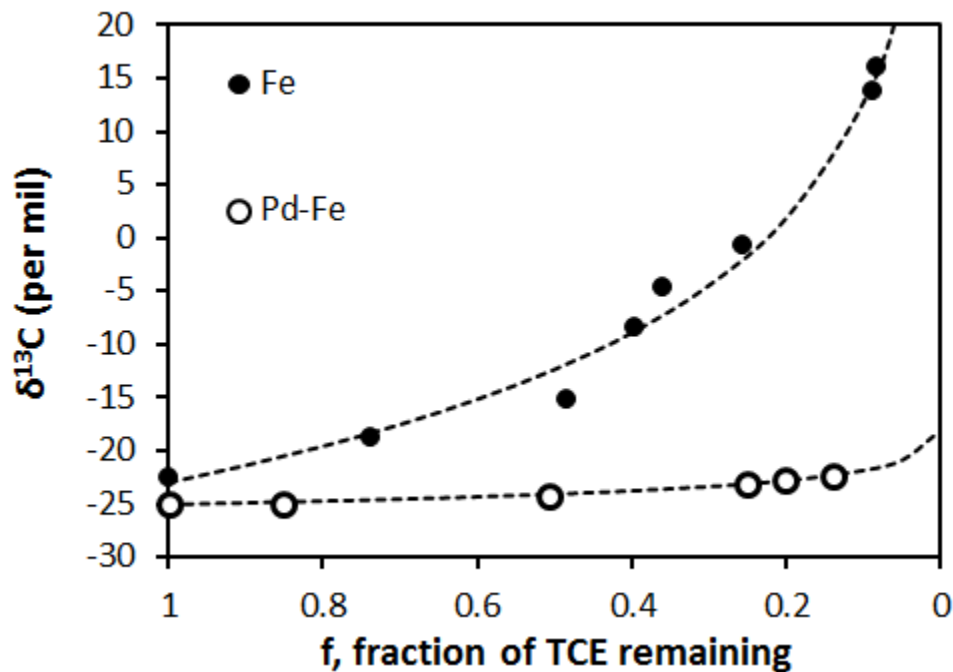


Figure 5.7. Isotope fractionation during TCE hydrodechlorination by freshly made monometallic Fe and Pd-Fe nanoparticles and fitting of the experiment data to the Raleigh model.

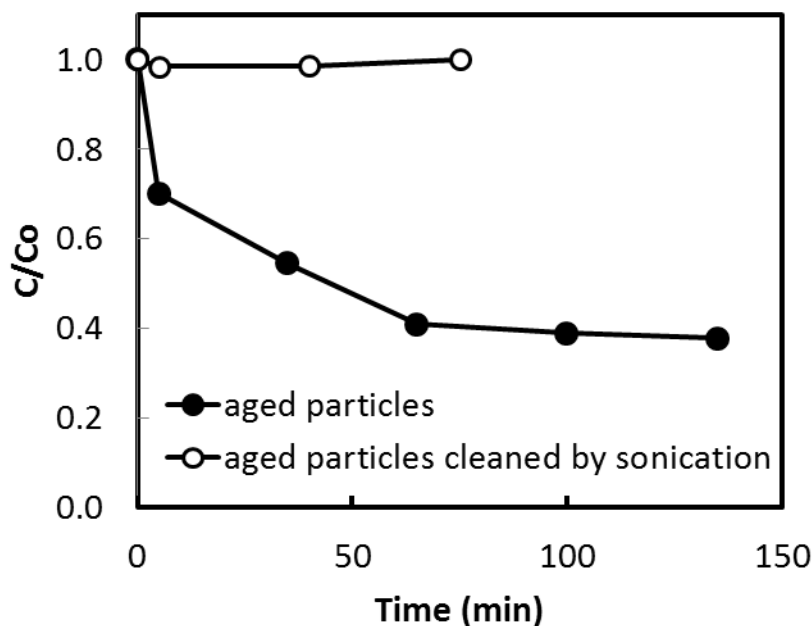


Figure 5.8. TCE degradation by Pd-Fe bimetallic nanoparticles aged in 5 mM Cl⁻ solutions for 24 hours. Solid symbol: aged Pd-Fe without surface cleaning. Hollow symbol: aged Pd-Fe cleaned by sonicating in deionized water for 3 minutes before collection by vacuum filtration and subsequent use in TCE hydrodechlorination experiments. The results suggest that the initial degradation of TCE by the aged Pd-Fe without the ultrasound cleaning procedure was due to a limited amount of reactive hydrogen species accumulated on the Pd-Fe surface during aqueous aging. Removing the reactive hydrogen species by sonication renders the particles to be completely unreactive towards TCE.

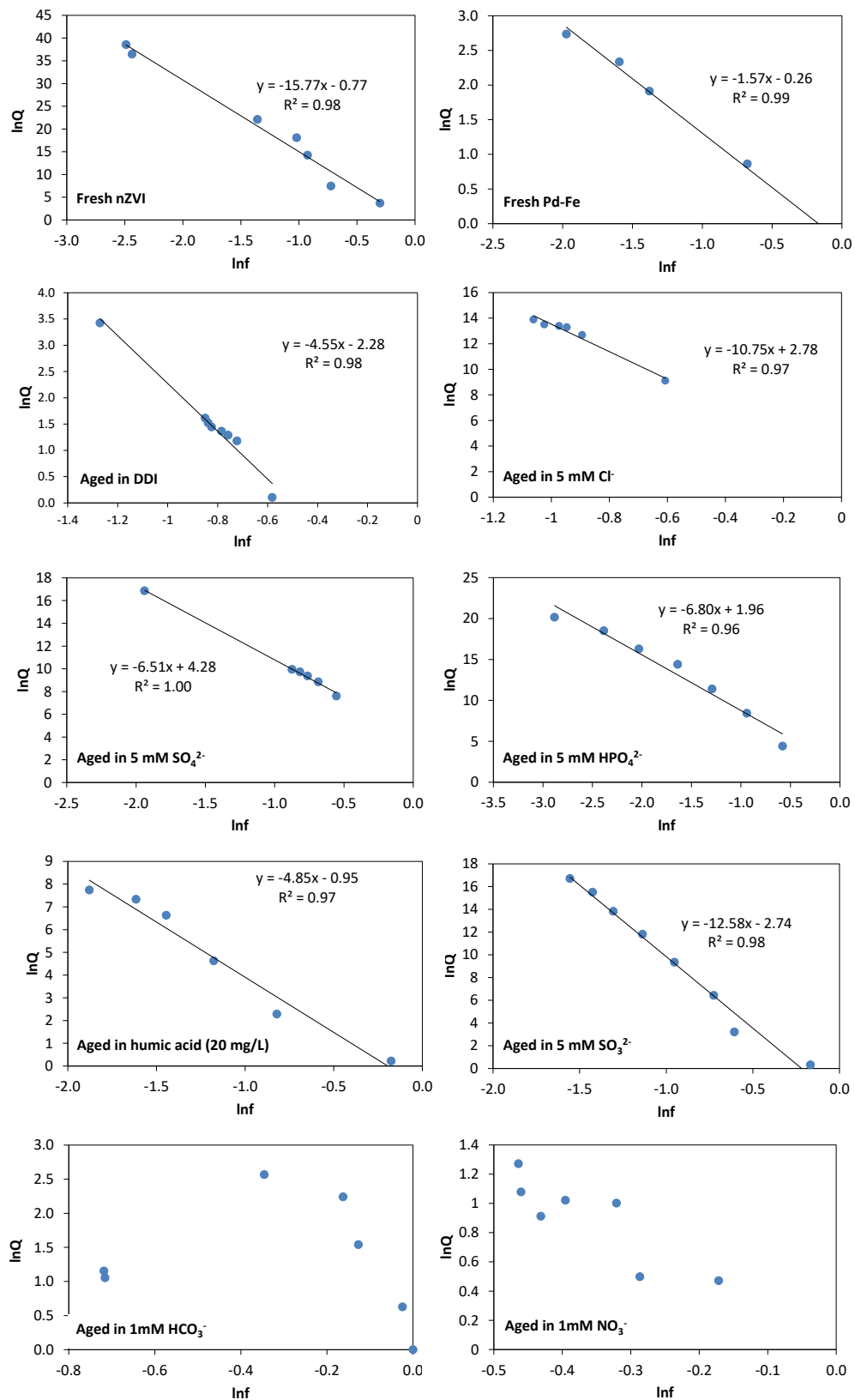


Figure 5.9. Raleigh plots of isotope fractionation during TCE degradation by fresh and aged Fe or Pd-Fe bimetallic nanoparticles. To account for TCE adsorption to the solid phase, the first data point was not included and the fitted line was not forced to pass through zero. $f = [TCE]/[TCE_0]$, and $Q = R/R_0$

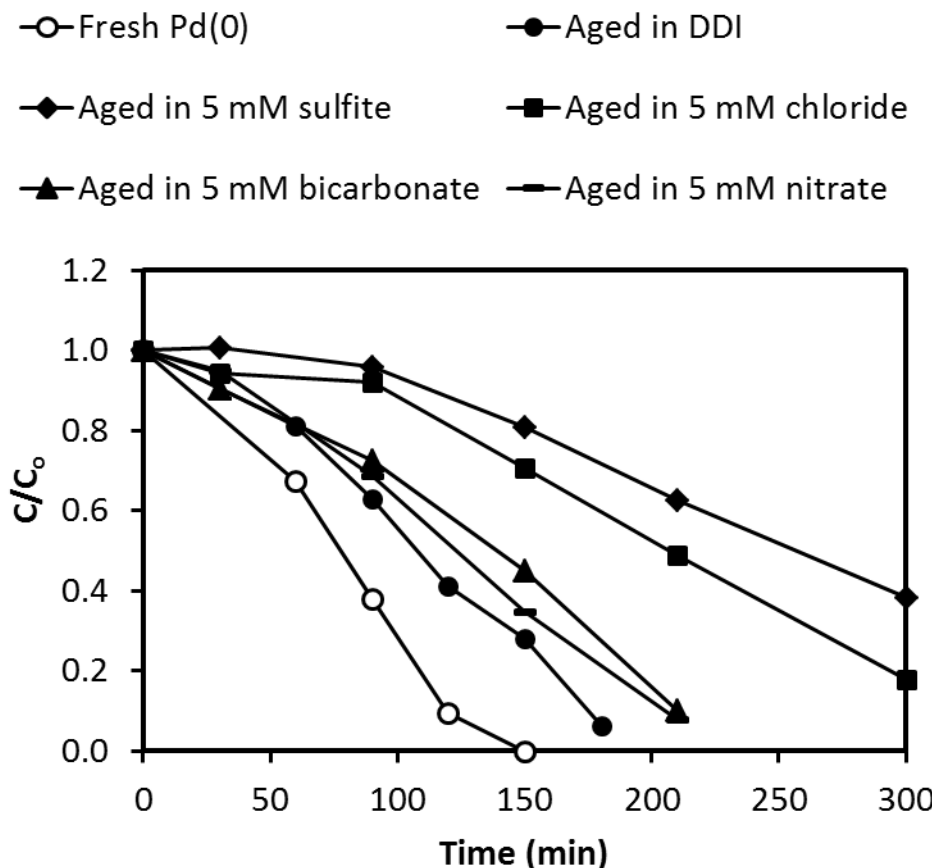


Figure 5.10. TCE degradation by Al_2O_3 -supported Pd. The particles were prepared by mixing a palladium acetate solution with $\alpha\text{-Al}_2\text{O}_3$ particles for 30 min followed by H_2 purging for 30 min. Particles were immersed in various solutions for 24 h and were collected by filtration after aging. TCE experiment was performed by adding aged particles (dose of Pd at 14 mg/L) into a TCE solution ($C_0 = 50 \text{ mg/L}$) amended with 2.5 g/L fresh iron nanoparticles as a hydrogen source.

CHAPTER SIX

Surface Sulfided Nanoscale Zero-Valent Iron (nZVI) for Reductive Dechlorination of Trichloroethene

6.1. Introduction

Chlorinated ethenes (*e.g.*, trichloroethene (TCE) and perchloroethene (PCE)) have had widespread uses as solvents, metal cleaning and degreasing agents, and intermediates in chemical manufacturing for decades ^{1, 2}. Because of their limited aqueous solubility and high density, TCE and PCE are the major chemicals contributing to dense non-aqueous phase liquid (DNAPL) contamination in groundwater at the U.S. superfund sites ³. Extensive research has been conducted to develop cleanup methods to remove chlorinated ethenes from the aquifers. *In situ* bioremediation of chlorinated ethenes has been extensively studied, yet biological degradation often leads to incomplete dechlorination and as a result, the accumulation of chlorinated intermediates, such as *cis*-dichloroethene (c-DCE) and vinyl chloride (VC) ⁴⁻⁶, that are more toxic and volatile than their parent compounds. Compared to biotic dechlorination, abiotic dechlorination can promote complete dechlorination as well as have relatively high dechlorination rates. A widely used material for abiotic dechlorination of TCE and PCE is zero-valent iron ⁷⁻¹⁶, which has been intensively studied for *in situ* decontamination of groundwater impacted by chlorinated ethenes and other contaminants.

Iron sulfide minerals draw attention as a reducing agent for chlorinated ethenes, and extensive studies have been conducted. Abiotic transformation of TCE and PCE by iron sulfides has been evaluated using pyrite (FeS₂) ¹⁷⁻²¹ and mackinawite (FeS) ²¹⁻²⁴. These iron sulfide materials were able to degrade TCE at higher rates than other Fe(II) bearing minerals (*e.g.* magnetite and green rust), but their rates are still considerably slower than ZVI materials and they exhibit limited reductive capacities causing gradual declines in reaction rates even in dilute TCE ²²⁻²⁶. More recently, a biphasic “Fe/FeS” nanocomposite showed great reactivity for TCE dechlorination compared to unamend Fe nanoparticles (nZVI). Kim et al ²⁷ proposed a method of preparing the “Fe/FeS”

nanoparticles by introducing sodium dithionite, a reducing agent used widely in research and industrial applications²⁸, into the synthesis mixture of nZVI and systematically investigated the structure of these “Fe/FeS” nanoparticles. It was hypothesized that the enhanced TCE reductive dechlorination performance of “Fe/FeS” nanoparticles was attributable to a good electron conductive property of the FeS phase compared to the oxide passivation layer of unamend nZVI. This argument is consistent with the fact that iron sulfide is a good semi-conductor material²⁹⁻³³, which might facilitate electron transfer if the iron sulfide was deposited on the surface of the metallic iron phase. A recent study showed that sodium sulfide could also be used to prepare highly reactive sulfided nZVI with enhanced TCE dechlorination reactivity³⁴, and the authors proposed that iron sulfides have a higher binding capacity for TCE than iron oxide on the nZVI surface, and an iron sulfide overlayer is more effective at conducting electrons from the Fe(0) core to TCE than an oxide layer. However, none of these studies have systematically examined the effect of various sulfidation conditions on the reactivity of the resultant materials, the applicability of sulfidation to other forms of ZVI (e.g. conventional Fe granules or powder), and the specific role of sulfide species in the iron matrix in reductive dechlorination reactions.

This research employed different sulfidation conditions to synthesize sulfided nZVI of varying properties. The structure, mineral composition, and surface chemistry of the sulfided nZVI were characterized by transmission electron microscopy (TEM), X-ray powder diffraction (XRD) and high-resolution X-ray photoelectron spectroscopy (HR-XPS). TCE was used as a model chloroethene to evaluate the reactivity of the sulfided nZVI. In addition, a facile sulfidation treatment was applied to commercial iron filings to investigate whether surface sulfidation represents a general approach to enhance the performance of ZVI materials for TCE dechlorination. More importantly, by examining the reaction rates, pathways, and product distribution, we offered mechanistic insights into enhanced dechlorination ability of sulfided iron particles.

6.2. Materials and Methods

6.2.1 Chemicals

TCE (99.5%), *trans*-dichloroethene (*trans*-DCE, 98%), *cis*- dichloroethene (*cis*-DCE, 97%), and *1,1*- dichloroethene (*1,1*-DCE, 99%) were purchased from Aldrich. Vinyl chloride (VC, 1000 µg/mL in methanol) was purchased from AccuStandard. Iron (III) chloride hexahydrate ($\text{FeCl}_3 \cdot 6\text{H}_2\text{O}$, 97.0%-102.0%) and sodium sulfide nonahydrate ($\text{Na}_2\text{S} \cdot 9\text{H}_2\text{O}$, 98%) were from Alfa Aesar. Sodium thiosulfate anhydrous ($\text{Na}_2\text{S}_2\text{O}_3$, 99.6%), sodium dithionite ($\text{Na}_2\text{S}_2\text{O}_4$, 99%) and ethanol (95%) were obtained from Fisher Scientific. Paraffin mixture (1000 ppm of methane, ethane, propane, butane, pentane, and hexane in helium) and olefin mixture (*ca.* 1000 ppm of ethene, propylene, 1-butene, 1-pentene, and 1-hexene in helium) were obtained from Matheson Tri-Gas and were used as calibration standards. PeerlessTM Iron filings (PMP Iron 50D) were provided by Peerless Metal Powders & Abrasive (Detroit, MI, USA). Amorphous iron sulfide (FeS) was synthesized in the lab following the method by Butler and Hayes²⁵. Deoxygenated deionized-distilled water (DDI), prepared by purging DDI with N₂ for 30 min, was used in all procedures including particle synthesis and TCE dechlorination experiments.

6.2.2 Preparation of Sulfided nZVI (S-nZVI)

nZVI was synthesized using the borohydride reduction method. Briefly, 10.8 g of $\text{FeCl}_3 \cdot 6\text{H}_2\text{O}$ were dissolved in a 500-mL solution mixture of distilled de-ionized (DDI) water and ethanol (1:1, v/v). 500 mL of 0.4 M NaBH₄ solution was introduced to the ferric solution at approximately 17 mL/min under intensive mixing. Sulfided nZVI particles (denoted as S-nZVI) were prepared using two approaches. The first approach follows that of Kim et al²⁷, in which an appropriate amount of a sulfidation reagent was introduced into the borohydride solution and the mixture was pumped into the Fe(III) solution. As the sulfidation reagent was applied before the onset of nZVI synthesis, we refer to this as the “initial sulfidation” method. Three common sulfur compounds were evaluated as sulfidation reagents in this study, namely, sodium sulfide (Na_2S), and sodium dithionite ($\text{Na}_2\text{S}_2\text{O}_4$), and sodium thiosulfate ($\text{Na}_2\text{S}_2\text{O}_3$). In the second approach (referred to as “post-synthesis sulfidation” method), a sulfidation reagent was dosed into

the synthesis mixture at 10 min and 20 min after the borohydride solution was introduced into the Fe(III) solution. The dose of the sulfur compound was varied such that the mole ratio of sulfur compound to ferric salt in the synthesis mixture (denoted as S/Fe mole ratio) was the range of 1.25×10^{-3} to 0.75.

6.2.3 Commercial Iron Sulfidation Treatment

PeerlessTM iron filings were used to investigate whether the surface sulfidation treatment could increase the iron filings reactivity on TCE dechlorination. The sulfidation treatment process on PeerlessTM iron filings (with the resultant particles denoted as S-PeerlessTM Fe) involved immersing PeerlessTM Fe in dilute HCl to remove the surface passivation film. The acid-washed particles were collected using vacuum filtration and the solids were mixed with sulfur precursor solution. S/Fe mole ratio was fixed at 0.05 for all batches of S-Peerless iron. Sodium thiosulfate was used as the sulfur precursor for all commercial iron.

6.2.4. TCE Dechlorination Experiments

Batch TCE dechlorination experiments were performed to compare the reactivity of sulfided iron prepared under different synthesis conditions. All batch experiments were conducted in 45-mL EPA vials containing 30 mL of aqueous solution and the balance as headspace. The initial pH of all solutions was adjusted to between 7.8-8.2 using dilute NaOH or HCl to simulate the typical pH in groundwater. The solutions were amended with 5 g/L of S-nZVI or 10 g/L of S-PeerlessTM Fe, respectively (doses as dry weights). The vials were capped with PTFE-lined mininert valves. Experiments were started by injecting a small volume of TCE (in methanol) stock solution to reach an initial TCE concentration of 25 mg/L. The reactors were placed on a wrist-action shaker rotating at 250 rpm at 22 ± 1 °C. Control experiments without iron materials were performed in parallel.

6.2.5. Analytical Methods

Periodically, an aliquot (25 - 50 µL) of headspace gas was withdrawn using a gastight syringe. The samples were directly injected into a GC-FID system (Agilent 6890)

equipped with an Agilent PoraPlot Q column (25 m x 0.32 mm) to analyze for the concentrations of TCE, chlorinated intermediates (not detected in this study), acetylene, ethene, ethane, and longer chain hydrocarbons (up to C₆). The injection port was maintained at 250°C, and the oven temperature profile followed the sequence of 35°C for 5 min, ramp at 12°C/min to 220°C, and hold at 220°C for 5 min. The method provides adequate separation between TCE and the daughter products. TCE calibration line was constructed by headspace analysis of TCE aqueous standard solutions prepared in the same vials as experimental reactors. Calibrations for C₂-C₆ hydrocarbons were performed using the commercial gas standards. The results were used to compute their total concentrations in the reaction vials after accounting for partition between headspace and aqueous phases using the respective Henry's Law constants ^{35, 36}.

In this research, the product yield was used to characterize the major product formation during TCE dechlorination. It is defined as the amount of a product formed over the amount of parent compound reacted at a given time, which is expressed as

$$\text{Product Yield} = \frac{P_{i,t}}{\text{TCE}_0 - \text{TCE}_t} \quad (1)$$

where P_{i,t} is the amount of daughter product i at a given time, and TCE₀ and TCE_t are the amounts of TCE in the reactor at the beginning and at a given time, respectively. Carbon recovery was calculated by summing up the amounts of TCE and daughter products detected in the reactor in terms of C₂ equivalents (e.g., 1 mole of butane = 2 mole of C₂ equivalent)

6.2.6. Material Characterization

Particles were dried immediately after synthesis or aging treatments in a glove-box purged with high purity N₂ for up to 48 h. The dried solids were stored in N2-filled gastight vials prior to analysis. Morphology of the particles was characterized with a transmission electron microscope (TEM) (JOEL 1200 EX) using the conventional bright-field imaging mode at an electron acceleration voltage of 175 kV. All TEM samples were prepared by depositing 1-2 drops of dilute ethanol suspension of the respective

solids on a TEM sample grid followed by air-drying at room temperature. An electron acceleration voltage of 180 kV was applied to obtain the TEM images.

High resolution X-ray photoelectron spectroscopy (HR-XPS) analysis was performed on a PHI 5000 Versa Probe system using a monochromated AlK_α radiation. Sample preparation follows the procedure we described previously in Chapter 3.5. High-resolution scans were acquired at a 45° takeoff angle and 23.5 eV pass energy. The software package CasaXPS (Version 2.3.16PR1.6) was used for HR-XPS spectral analysis. The binding energy was referenced to the C1s peak of adventitious carbon at 284.6 eV.

6.3. Results and Discussion

6.3.1. Effect of Different Sulfur Precursors

Three different sulfur precursors, namely sodium dithionite, sodium sulfide and sodium thiosulfate, were used to synthesize S-nZVI particles. S-nZVI was prepared using the “post-synthesis sulfidation” method, and the sulfur salts were added to the synthesis solution at 20 min after the onset of the borohydride reduction step. The mole ratio of S/Fe was fixed at 0.05 for three different sulfur precursors. Sodium dithionite^{27,37} and sodium sulfide³⁴ have been used to prepare Fe/FeS nanoparticles and sulfided nZVI in previous studies. Other commonly available sulfur compounds such as sodium thiosulfate have not been evaluated as sulfur precursors. Figure 6.1 shows TCE dechlorination by S-nZVI prepared with different sulfur precursors. In general, S-nZVI prepared with the three sulfur precursors showed similar TCE dechlorination rates, therefore, sulfur precursor has a relatively small impact on the reactivity of S-nZVI. Compared to unamended nZVI, which took approximately 24 days to achieve 90% TCE removal (Figure 6.1), reactions with S-nZVI achieved an equivalent TCE removal in 7 hours, representing an increase in TCE dechlorination rate constant by a factor of 60 (Table 6.1).

Pseudo-first-order rate constants, yields of major products, and carbon mass recovery results of TCE dechlorination by various S-nZVI are shown in Table 6.1. The

product distribution observed for nZVI in this study is consistent with that reported in the previous studies^{15, 16, 38}: ethene and ethane emerge as the primary products (yielding for 17.2% and 6.5%, respectively, of the total carbon in the system). Unless otherwise noted, product yields in this study were measured when 90% of TCE was consumed. Longer-chain hydrocarbons (C₃-C₆ species) contribute to 5.7% of the total carbon. DCE isomers and VC, which are the intermediates of TCE hydrogenolysis reactions, were not detected during the entire experiment period, indicating that TCE dechlorination followed predominantly the β -elimination pathway.

Comparison of product speciation and distribution during TCE reductive dechlorination by S-nZVI and the unamended nZVI suggests significant differences between the two systems. In addition to ethene and ethane, a noticeable amount of acetylene was formed during TCE reductive dechlorination by S-nZVI. Acetylene exhibits a typical reaction intermediate behavior, the concentration of which accumulated at initial stage of TCE dechlorination and then decreased with time. One noticeable aspect is that the yields of ethene and ethane by S-nZVI were notably higher than those by nZVI. Table 6.1 shows that the yields of ethene and ethane were 43.5% and 10.3%, respectively, when S-nZVI prepared with sodium thiosulfate was used. The values are much higher than those by nZVI. Similar observations can be made for S-nZVI derived from sulfide and dithionite precursors. Considering that acetylene was not completely consumed at the last sampling point where product yields were quantified, the final yields of ethene and ethane could be even higher when acetylene is completely converted to ethene and ethane. Separate ethene hydrogenation experiments by nZVI and S-nZVI prepared using the “20 min post-synthesis sulfidation” method were conducted. Continuous monitoring of the reaction mixture for 2 months showed that only 3% of ethene was hydrogenated to ethane by S-nZVI, while no ethane formation was observed by nZVI. Heavier hydrocarbons were not detected for both S-nZVI and nZVI during the ethene hydrogenation experiments over the 2-month period (Data not shown). Moreover, continuous monitoring of product distribution after TCE was completely dechlorinated by S-nZVI for up to 2 months indicates the ratio of ethene over ethane was nearly constant (data not shown). These two sets of experiments confirmed that ethene was not a

precursor of ethane and longer hydrocarbons. Instead, ethene and ethane were formed in parallel from acetylene as an intermediate. Based on the analysis, a kinetic model is proposed here, in which TCE undergoes β -elimination reaction to form chloroacetylene, which rapidly decomposes in water to give rise to acetylene. Further, acetylene hydrogenation leads to concurrent formation of ethene and ethane (Figure 6.2). Modeling software package, Scientist v 3.0 (Micromath, St. Louis, MO, USA) was used to model the TCE degradation and its daughter products formation and it results in good fit of the experimental data (Figure 6.3), confirming the validity of the model (Kinetic model equations are in Supporting Information).

6.3.2 Effect of Sulfidation Procedure: Initial Sulfidation vs. Post-synthesis Sulfidation

As sulfur precursor was found to pose a minor effect on the particle reactivity, thiosulfate was consistently used as the sulfur precursor in all subsequent investigations. Two sulfidation methods were adopted, namely the “initial sulfidation” method and “post-synthesis sulfidation” method (refer to Section 6.2.2). For the post-synthesis sulfidation method, thiosulfate was added at either 10 min or 20 min, respectively. The mole ratio of S/Fe was fixed at 0.05. Figure 6.4 shows TCE dechlorination and daughter products formation as a function of time by S-nZVI prepared by the “initial sulfidation method” and “10-min post-synthesis sulfidation” method, respectively. In general, acetylene formation was observed in both reactors, and the rates of TCE degradation were similar among the different types of S-nZVI. Product distribution data in Table 6.1 indicates that the time point at which the sulfur salt was introduced into the synthesis broth exerts negligible effects on the particles dechlorination reactivity and TCE dechlorination pathway.

In spite of comparable reactivity behavior, the morphology and structure of S-nZVI generated by the “initial-sulfidation” method and “post-synthesis sulfidation” method were drastically different based on the TEM images presented in Figure 6.5. The S-nZVI synthesized by “20-min post-synthesis sulfidation” method comprises of spherical particles with the average size of approximately 20 nm. The structure of this type of S-nZVI resembles the classical nZVI structure, with a core-shell structure and

chain-like particle aggregation as described in previous studies^{9, 39, 40}. In contrast, S-nZVI synthesized by the “initial sulfidation” method displays particles of heterogeneous morphology and a large variation in size from 10 nm to 100 nm. Further, the typical core-shell structure of nZVI was not observed, and some dense particles were surrounded by “branch-like” structures of lower contrast, and the observation of this structure was similar to those noted in the previous works^{27, 41}.

Figure 6.6 shows the S 2p_{3/2} HR-XPS spectra of S-nZVI produced using the “initial sulfidation” method and “20-min post sulfidation” method. The peak at 160.7 eV is assigned to monosulfide, S²⁻, the peak at 162.1 eV is assigned to disulfide, S₂²⁻, the peak from 163.4 eV to 165 eV is assigned to elemental and polysulfide species, S_n²⁻ and S₈⁰, and the peaks at 166 eV and 169 eV are from SO₃²⁻ and SO₄²⁻, respectively. Figure 6.6a shows that the surface of S-nZVI prepared using the “initial sulfidation” method was mainly composed of S₂²⁻ and S²⁻. No evident peaks of S_n²⁻, SO₃²⁻ and SO₄²⁻ were detected, which is different from a previous study using a similar synthesis process⁴¹. Figure 6.6b shows the surface of “post-synthesis sulfidation” particles consists of S₂²⁻, S²⁻, S_n²⁻ and SO₄²⁻. X-ray diffraction (XRD) analysis was also conducted on these two types of S-nZVI and the corresponding XRD patterns were provided in Figure S6.1 (Supporting Information). The diffraction patterns indicate the presence of *bbc* Fe and magnetite, but no iron sulfide phase could be identified, suggesting that the iron sulfide coating formed on the S-nZVI is amorphous in nature. Considering that the particles generated using the “20-min post-synthesis sulfidation” have the most uniform and consistent morphology, all S-nZVI used in the subsequent investigations was prepared using this method.

6.3.3 The Effect of S/Fe Mole Ratio

The effect of S/Fe ratio on TCE dechlorination rate was investigated. The mole ratio of S/Fe ranged from 0.00125 to 0.75, and the influence of S/Fe mole ratio on TCE dechlorination rate constants is shown in Figure 6.7. It can be seen that the reaction rate increased dramatically as S/Fe mole ratio increased from 0.00125 to 0.0125. Further increasing the S/Fe ratio, however, did not result in appreciable increase in the TCE dechlorination rate.

Yields of major products, shown in Figure 6.8, also feature distinctive trends with S/Fe mole ratio. When S/Fe mole ratio was in the range of 0.00125 to 0.0125, no acetylene formation can be observed, and the distribution of products is similar to that of nZVI (Table 6.1). Interestingly, even though S-nZVI with lower S/Fe mole ratio exhibits a similar product distribution pattern as the unamended nZVI, the dechlorination rates of these lightly sulfided S-nZVI are substantially higher than that of the unamended nZVI. When S/Fe mole ratio increased beyond 0.0125, substantial acetylene formation was observed.

The total yields of C₂ products (i.e., sum of ethene, ethane and acetylene yields) when 90% of TCE removal was achieved are shown in Figure 6.9. S-nZVI in general delivers a higher yield of C₂ products than nZVI. The increase in total yields of C₂ products was more evident when S/Fe mole ratio is greater than 0.0125, suggesting sulfidation treatment favors the production of ethene and ethane over longer-chain hydrocarbons.

To summarize this section, S/Fe mole ratio has a critical impact on the reactivity of S-nZVI particles. S/Fe mole ratio values can be divided into two regions. Within the range 0.00125 to 0.0125, increasing S/Fe ratio could dramatically increase the particles reactivity for TCE dechlorination, whereas within the range between 0.025 to 0.75, increasing S/Fe mole ratio does not significantly increase the TCE dechlorination rate, but results in a noticeable shift in reaction pathway that favors the production of two-carbon products.

6.3.4 Sulfidation Treatment Process for Peerless™ Iron Filings

Surface sulfidation treatment for Peerless™ iron filings (denoted as S-Peerless™ Fe) was conducted. TCE pseudo-first-order dechlorination rate constants by Peerless™ iron filings and S-Peerless™ Fe, and major products yields of different types of commercial iron are listed in Table 6.2.

It was observed that the surface of as-received Peerless™ iron filings was severely oxidized. TCE dechlorination experiment conducted using the as-received

Peerless™ iron filings took approximately 75 days to achieve more than 90% degradation of TCE at an iron dose of 10 g/L. Ethene and ethane were the predominant products.

Peerless™ iron after acid washing process increased TCE dechlorination rate significantly, shortening the time required for TCE dechlorinaiton to approximately 19 days with 93% TCE removal (Figure S6.2a, Supporting Information).

However, Peerless™ iron after an acid pretreatment followed by surface sulfidation treatment process can dramatically enhance TCE dechlorination rate, in which TCE degradation could be completed within 2 days. The products distribution results during TCE dechlorination by Peerless™ iron filings and S-Peerless™ Fe presented similar results as facile sulfidation treatment process on nZVI (Table 6.2). For the Peerless™ iron filings without sulfidation process, no acetylene formation was observed during the TCE dechlorination by Peerless™ iron filings as received and Peerless™ iron filings pre-washed by diluted HCl, and ethene and ethane were dominant species formed, yielding for approximately 50% and 10%, respectively. It can be seen clearly that if Peerless™ iron filings treated with sulfidation process, the products distribution analysis identified that acetylene was the predominant product accounting for at least more than 55% yield when 10% of TCE left. We kept monitoring the products transformation (S-Peerless™ iron batch No.6) for 20 days, and found that the completion of acetylene hydrogenation took around 18 days (Figure S6.3, Supporting Information), indicating acetylene hydrogenation is not as fast as that of S-nZVI. Higher yield of C3-C6 species formation by Peerless™ iron and S- Peerless™ were observed compared to nZVI and S-nZVI, which might be attributed to the impurities of Peerless iron filings.

6.4. Discussion

6.4.1 S-nZVI

Previous studies examined the effects of different S/Fe mole ratio on S-nZVI reactivity with respect to TCE dechlorination, yet no detailed studies has been conducted from products distribution point of view³⁴. Considering TCE reaction rate and product distribution, one may categorize S-nZVI particles into two groups based on the S/Fe mole ratio used during S-nZVI synthesis: (1) S-nZVI prepared at an S/Fe mole ratio between

0.025 to 0.75 is referred to as S-nZVI prepared under “normal sulfur loading condition,” and (2) S-nZVI prepared at an S/Fe mole ratio between 0.00125 to 0.0125 is defined as S-nZVI with “low sulfur loading condition.”

Recent studies attributed the enhanced TCE dechlorination by S-nZVI to that iron sulfides could facilitate electron transfer and enhance surface binding with TCE compared to the unmanned nZVI^{27, 34}. However, if the facilitation of electron transfer or enhanced binding of TCE on S-nZVI surface are responsible for the enhancement in TCE dechlorination, one would expect the product formation and distribution should be same as those by nZVI. TCE dechlorination by S-nZVI with “normal sulfur loading condition” clearly showed substantial acetylene formation in this research. Therefore, the sulfide species in the iron matrix should affect the chemistry of TCE dechlorination than merely enhancing the rate of electron transfer. On the other hand, TCE adsorption experiments did not support more TCE binding with iron sulfide minerals than with nZVI, thus the hypothesis that an FeS surface layer enhances TCE adsorption cannot be substantiated. Several previous studies presented that TCE reductive dechlorination by iron sulfide materials (*e.g.*, mackinawite (FeS) and pyrite (FeS₂)) resulted in acetylene being the predominant daughter product, yet no further hydrogenation products (*e.g.*, ethene and ethane) were observed in these studies^{18, 22, 23, 26, 42}. It is notable that TCE dechlorination rate by iron sulfide was extremely slow. Summarizing previous studies, TCE reduction by iron sulfides leads to the accumulation of acetylene during the slow TCE reductive dechlorination process. We also conducted acetylene hydrogenation experiment by iron sulfide alone, and no acetylene hydrogenation happened over 2 weeks (data not shown), suggesting that even though iron sulfide could reductively dechlorinate TCE to form acetylene, it was not able to enable acetylene hydrogenation. On the other hand, it is reported that accumulation of acetylene was rarely observed during TCE reductive dechlorination by ZVI particles, mainly because acetylene was highly reactive and could undergo coupling reactions on the metal surface^{38, 43, 44}. As a result, as soon as acetylene was formed on iron particles, it was rapidly consumed. Therefore, the accumulation of acetylene during TCE dechlorination by S-nZVI in this case was not possibly associated with Fe(0) but more with deposition of iron sulfides species on S-nZVI. Given the

features of TCE dechlorination by iron sulfides and nZVI, we proposed a strong synergistic effect occurred to TCE reductive dechlorination by S-nZVI with “normal sulfur loading condition.” The iron sulfide component on the S-nZVI accounts for the quick formation and accumulation of acetylene, and the rapid acetylene hydrogenation is mediated by the Fe(0) phase of the S-nZVI. We also conducted a separate TCE dechlorination experiments by a physical mixture of amorphous iron sulfide and nZVI (Figure S6.4). Compared TCE dechlorinated rate and distribution of products to S-nZVI and unamended nZVI, TCE dechlorination rate increased significantly compared to nZVI but still much was slower than that by S-nZVI, yet the acetylene hydrogenation was exceedingly slow compared to that by S-nZVI. Accordingly, rapid TCE dechlorination by S-nZVI with “normal sulfur loading” condition is owing a strong synergistic effect of this biphasic structure.

For S-nZVI prepared under a “low sulfur loading condition,” TCE dechlorination pathway was different compared to S-nZVI with “normal sulfur loading condition.” Based on daughter product formation and distribution analysis, S-nZVI with “low sulfur loading condition” exhibits a reaction pathway similar to that of nZVI, however, TCE dechlorination rate was evidently enhanced compared to the unamend nZVI. The distribution of products of TCE degradation by S-nZVI under the “low sulfur loading condition” suggests that TCE degradation process mainly mediated by Fe(0) phase. Therefore, the TCE dechlorination was still mediated by Fe(0) phase, while the enhanced dechlorination rate is owing the iron sulfides species on the S-nZVI particles surface. The rate-limiting step for TCE degradation by different ZVI materials was different. One popular argument attributes the transfer of dissociative electron transfer is the rate-limiting stpe, while the formation of surface-bounded intermediate is another prevailing hypothesis. In this research, no more effort have been made to identify which one is the rate-limiting step, but the iron sulfides species on S-nZVI synthesized under this condition could contribute to overcome the rate-limiting step.

Acetylene hydrogenation was conducted using nZVI and S-nZVI prepared at different S/Fe mole ratios, and the results are shown in Figure 6.10. The results illustrated

that acetylene was rapidly consumed, and acetylene hydrogenation rate by nZVI and S-nZVI at an S/Fe mole ratio of 0.00125 was even faster than S-nZVI prepared at a higher S/Fe mole ratios of 0.05 and 0.25. It is widely acknowledged that TCE reductive dechlorination by iron particles or iron sulfides mainly follows the β -elimination pathway^{22, 38}, and acetylene was the precursor of ethene and ethane. Given the fact that acetylene could be rapidly consumed by different types of S-nZVI and nZVI, the S-nZVI under “normal sulfur loading condition” could rapidly complete the β -elimination step and therefore enhance the whole TCE dechlorination rate compared to TCE degradation by S-nZVI under the “low sulfur loading condition” or by nZVI.

6.4.2 S-PeerlessTM Filings

Previous studies indicate that dithionite could be used as an effective reductant to restore the reactivity of passivated nZVI by reducing Fe(III) to Fe(II), or even reducing Fe(II) to Fe(0) under alkaline conditions^{21, 45, 46}. Xie et al³⁷ conducted detailed research about the effect of dithionite reducing effects on passivated nZVI covered with different iron oxides and indicated that dithionite cannot reduce oxide phases such as lepidocrocite to restore the reactivity of nZVI, however, dithionite could restore nZVI reactivity if the surface passivation layer was mainly comprised of magnetite. However, our data suggests that the enhancement of TCE reductive dechlorination was not due to the reduction of Fe(III) to Fe(II) but mainly to the formation of iron sulfide at the interface between Fe(0) and water which can speed up the initial (i.e., β -elimination) step of TCE dechlorination.

6.5. Conclusions

In this study, TCE dechlorination by S-nZVI prepared under different sulfidation conditions were studied. Among the key parameters involved in the sulfidation process, S/Fe mole ratio has significant effects on the rate and pathway of TCE dechlorination by S-nZVI. If S/Fe mole ratio is higher than 0.025, TCE dechlorination rate can be significantly enhanced owing to the increase in the rate of the β -elimination step. If the S/Fe mole ratio is between 0.00125 and 0.0125, enhanced TCE dechlorination is possibly owing to the facilitation of electron transfer or owing to the enhanced binding capacity of TCE on S-nZVI. Sulfidation treatment can tremendously enhance TCE dechlorination

performance of Peerless™ iron filings. This enhanced TCE dechlorination effect is due to the formation of FeS on the surface Fe(0), which brings about a strong chemical synergy for rapid TCE conversion that is not attainable with FeS or Fe(0) alone.

Reference

1. Doherty, R. E., A History of the Production and Use of Carbon Tetrachloride, Tetrachloroethylene, Trichloroethylene and 1,1,1-Trichloroethane in the United States: Part 1--Historical Background; Carbon Tetrachloride and Tetrachloroethylene. *Environmental Forensics* **2000**, 1, (2), 69-81.
2. Doherty, R. E., A History of the Production and Use of Carbon Tetrachloride, Tetrachloroethylene, Trichloroethylene and 1,1,1-Trichloroethane in the United States: Part 2--Trichloroethylene and 1,1,1-Trichloroethane. *Environmental Forensics* **2000**, 1, (2), 83-93.
3. McCarty, P. L., GROUNDWATER CONTAMINATION BY CHLORINATED SOLVENTS: HISTORY, REMEDIATION TECHNOLOGIES AND STRATEGIES. *In Situ Remediation of Chlorinated Solvent Plumes* **2010**, 1-28.
4. Chan, C. C. H.; Mundel, S. O. C.; Eckert, T.; Liang, X.; Tang, S.; Lacrampe-Couloume, G.; Edwards, E. A.; Lollar, B. S., Large Carbon Isotope Fractionation during Biodegradation of Chloroform by Dehalobacter Cultures. *Environmental Science & Technology* **2012**, 46, (18), 10154-10160.
5. Cretnik, S.; Thoreson, K. A.; Bernstein, A.; Ebert, K.; Buchner, D.; Laskov, C.; Haderlein, S.; Shouakar-Stash, O.; Kriegman, S.; McNeill, K.; Elsner, M., Reductive Dechlorination of TCE by Chemical Model Systems in Comparison to Dehalogenating Bacteria: Insights from Dual Element Isotope Analysis (C-13/C-12, Cl-37/Cl-35). *Environmental Science & Technology* **2013**, 47, (13), 6855-6863.
6. Lojkasek-Lima, P.; Aravena, R.; Shouakar-Stash, O.; Frape, S. K.; Marchesi, M.; Fiorenza, S.; Vogan, J., Evaluating TCE Abiotic and Biotic Degradation Pathways in a Permeable Reactive Barrier Using Compound Specific Isotope Analysis. *Ground Water Monitoring and Remediation* **2012**, 32, (4), 53-62.
7. Liu, Y.; Lowry, G. V., Effect of particle age (Fe-o content) and solution pH on NZVI reactivity: H-2 evolution and TCE dechlorination. *Environmental Science & Technology* **2006**, 40, (19), 6085-6090.
8. Liu, Y.; Phenrat, T.; Lowry, G. V., Effect of TCE concentration and dissolved groundwater solutes on NZVI-Promoted TCE dechlorination and H-2 evolution. *Environmental Science & Technology* **2007**, 41, (22), 7881-7887.
9. Li, X.-q.; Elliott, D. W.; Zhang, W.-x., Zero-valent iron nanoparticles for abatement of environmental pollutants: Materials and engineering aspects. *Critical Reviews in Solid State and Materials Sciences* **2006**, 31, (4), 111-122.

10. Cipollone, M. G.; Wolfe, N. L.; Anderson, J. L., Long-term kinetic column studies on the use of iron & iron-pyrite for remediating TCE in water. *Abstracts of Papers of the American Chemical Society* **1997**, 213, 172-ENVR.
11. Gillham, R. W.; Ohannesin, S. F., ENHANCED DEGRADATION OF HALOGENATED ALIPHATICS BY ZERO-VALENT IRON. *Ground Water* **1994**, 32, (6), 958-967.
12. Su, C. M.; Puls, R. W., Kinetics of trichloroethene reduction by zerovalent iron and tin: Pretreatment effect, apparent activation energy, and intermediate products. *Environmental Science & Technology* **1999**, 33, (1), 163-168.
13. Zhang, X.; Lin, Y.-M.; Chen, Z.-I., 2,4,6-Trinitrotoluene reduction kinetics in aqueous solution using nanoscale zero-valent iron. *Journal of Hazardous Materials* **2009**, 165, (1-3), 923-927.
14. Crane, R. A.; Scott, T. B., Nanoscale zero-valent iron: Future prospects for an emerging water treatment technology. *Journal of Hazardous Materials* **2012**, 211, 112-125.
15. Liu, Y. Q.; Majetich, S. A.; Tilton, R. D.; Sholl, D. S.; Lowry, G. V., TCE dechlorination rates, pathways, and efficiency of nanoscale iron particles with different properties. *Environmental Science & Technology* **2005**, 39, (5), 1338-1345.
16. Song, H.; Carraway, E. R., Catalytic hydrodechlorination of chlorinated ethenes by nanoscale zero-valent iron. *Applied Catalysis B-Environmental* **2008**, 78, (1-2), 53-60.
17. Cipollone, M. G.; Wolfe, N. L.; Anderson, J. L., Long-term kinetic column studies on the iron and iron-pyrite for remediating TCE in water. *Abstracts of Papers American Chemical Society* **1997**, 213, (1-3), 172-ENVR 172.
18. Lee, W.; Batchelor, B., Abiotic reductive dechlorination of chlorinated ethylenes by iron-bearing soil minerals. 1. Pyrite and magnetite. *Environmental Science & Technology* **2002**, 36, (23), 5147-5154.
19. Pham, H. T.; Kitsuneduka, M.; Hara, J.; Suto, K.; Inoue, C., Trichloroethylene transformation by natural mineral pyrite: The deciding role of oxygen. *Environmental Science & Technology* **2008**, 42, (19), 7470-7475.
20. Weerasooriya, R.; Dharmasena, B., Pyrite-assisted degradation of trichloroethene (TCE). *Chemosphere* **2001**, 42, (4), 389-396.
21. Elsner, M.; Schwarzenbach, R. P.; Haderlein, S. B., Reactivity of Fe(II)-bearing minerals toward reductive transformation of organic contaminants. *Environmental Science & Technology* **2004**, 38, (3), 799-807.
22. Butler, E. C.; Hayes, K. F., Kinetics of the transformation of trichloroethylene and tetrachloroethylene by iron sulfide. *Environmental Science & Technology* **1999**, 33, (12), 2021-2027.

23. Butler, E. C.; Hayes, K. F., Factors influencing rates and products in the transformation of trichloroethylene by iron sulfide and iron metal. *Environmental Science & Technology* **2001**, *35*, (19), 3884-3891.
24. Kyung, D.; Amir, A.; Choi, K.; Lee, W., Reductive Transformation of Tetrachloroethene Catalyzed by Sulfide–Cobalamin in Nano-Mackinawite Suspension. *Industrial & Engineering Chemistry Research* **2015**, *54*, (5), 1439-1446.
25. Butler, E. C.; Hayes, K. F., Effects of Solution Composition and pH on the Reductive Dechlorination of Hexachloroethane by Iron Sulfide. *Environmental Science & Technology* **1998**, *32*, (9), 1276-1284.
26. Jeong, H. Y.; Kim, H.; Hayes, K. F., Reductive dechlorination pathways of tetrachloroethylene and trichloroethylene and subsequent transformation of their dechlorination products by mackinawite (FeS) in the presence of metals. *Environmental Science & Technology* **2007**, *41*, (22), 7736-7743.
27. Kim, E.-J.; Kim, J.-H.; Azad, A.-M.; Chang, Y.-S., Facile Synthesis and Characterization of Fe/FeS Nanoparticles for Environmental Applications. *Acs Applied Materials & Interfaces* **2011**, *3*, (5), 1457-1462.
28. Sun, Q.; Feitz, A. J.; Guan, J.; Waite, T. D., COMPARISON OF THE REACTIVITY OF NANOSIZED ZERO-VALENT IRON (nZVI) PARTICLES PRODUCED BY BOROHYDRIDE AND DITHIONITE REDUCTION OF IRON SALTS. *Nano* **2008**, *3*, (5), 341-349.
29. Karguppikar, A. M.; Vedeshwar, A. G., ELECTRICAL AND OPTICAL-PROPERTIES OF NATURAL IRON PYRITE (FES₂). *Physica Status Solidi a-Applied Research* **1988**, *109*, (2), 549-558.
30. Tributsch, H.; Rojas-Chapana, J. A., Metal sulfide semiconductor electrochemical mechanisms induced by bacterial activity. *Electrochimica Acta* **2000**, *45*, (28), 4705-4716.
31. Puthussery, J.; Seefeld, S.; Berry, N.; Gibbs, M.; Law, M., Colloidal Iron Pyrite (FeS₂) Nanocrystal Inks for Thin-Film Photovoltaics. *Journal of the American Chemical Society* **2011**, *133*, (4), 716-719.
32. Caban-Acevedo, M.; Faber, M. S.; Tan, Y.; Hamers, R. J.; Jin, S., Synthesis and Properties of Semiconducting Iron Pyrite (FeS₂) Nanowires. *Nano Letters* **2012**, *12*, (4), 1977-1982.
33. Lai, C.-H.; Lu, M.-Y.; Chen, L.-J., Metal sulfide nanostructures: synthesis, properties and applications in energy conversion and storage. *Journal of Materials Chemistry* **2012**, *22*, (1), 19-30.
34. Rajajayavel, S. R. C.; Ghoshal, S., Enhanced reductive dechlorination of trichloroethylene by sulfidated nanoscale zerovalent iron. *Water Research* **2015**, *78*, 144-153.
35. Yaws, C. L., Yaws' Handbook of Thermodynamic and Physical Properties of Chemical Compounds. In Knovel.

36. Williams, M. L., CRC Handbook of Chemistry and Physics, 76th edition. *Occupational and Environmental Medicine* **1996**, *53*, (7), 504-504.
37. Xie, Y.; Cwiertny, D. M., Use of Dithionite to Extend the Reactive Lifetime of Nanoscale Zero-Valent Iron Treatment Systems. *Environmental Science & Technology* **2010**, *44*, (22), 8649-8655.
38. Arnold, W. A.; Roberts, A. L., Pathways and kinetics of chlorinated ethylene and chlorinated acetylene reaction with Fe(O) particles. *Environmental Science & Technology* **2000**, *34*, (9), 1794-1805.
39. Yan, W.; Vasic, R.; Frenkel, A. I.; Koel, B. E., Intraparticle Reduction of Arsenite (As(III)) by Nanoscale Zerovalent Iron (nZVI) Investigated with In Situ X-ray Absorption Spectroscopy. *Environmental Science & Technology* **2012**, *46*, (13), 7018-7026.
40. Martin, J. E.; Herzing, A. A.; Yan, W.; Li, X.-q.; Koel, B. E.; Kiely, C. J.; Zhang, W.-x., Determination of the oxide layer thickness in core-shell zerovalent iron nanoparticles. *Langmuir* **2008**, *24*, (8), 4329-4334.
41. Su, Y.; Adeleye, A. S.; Keller, A. A.; Huang, Y.; Dai, C.; Zhou, X.; Zhang, Y., Magnetic sulfide-modified nanoscale zerovalent iron (S-nZVI) for dissolved metal ion removal. *Water Research* **2015**, *74*, 47-57.
42. Lee, W.; Batchelor, B., Abiotic reductive dechlorination of chlorinated ethylenes by iron-bearing soil minerals. 2. Green rust. *Environmental Science & Technology* **2002**, *36*, (24), 5348-5354.
43. Roberts, A. L.; Totten, L. A.; Arnold, W. A.; Burris, D. R.; Campbell, T. J., Reductive elimination of chlorinated ethylenes by zero valent metals. *Environmental Science & Technology* **1996**, *30*, (8), 2654-2659.
44. Ponec, V.; Bond, G. C., Studies in Surface Science and Catalysis. In *Catalysis by Metals and Alloys*, Elsevier Science BV Amsterdam: 1995.
45. Ludwig, R. D.; Su, C.; Lee, T. R.; Wilkin, R. T.; Acree, S. D.; Ross, R. R.; Keeley, A., In situ chemical reduction of Cr(VI) in groundwater using a combination of ferrous sulfate and sodium dithionite: A field investigation. *Environmental Science & Technology* **2007**, *41*, (15), 5299-5305.
46. Szecsody, J. E.; Fruchter, J. S.; Williams, M. D.; Vermeul, V. R.; Sklarew, D., In situ chemical reduction of aquifer sediments: Enhancement of reactive iron phases and TCE dechlorination. *Environmental Science & Technology* **2004**, *38*, (17), 4656-4663.

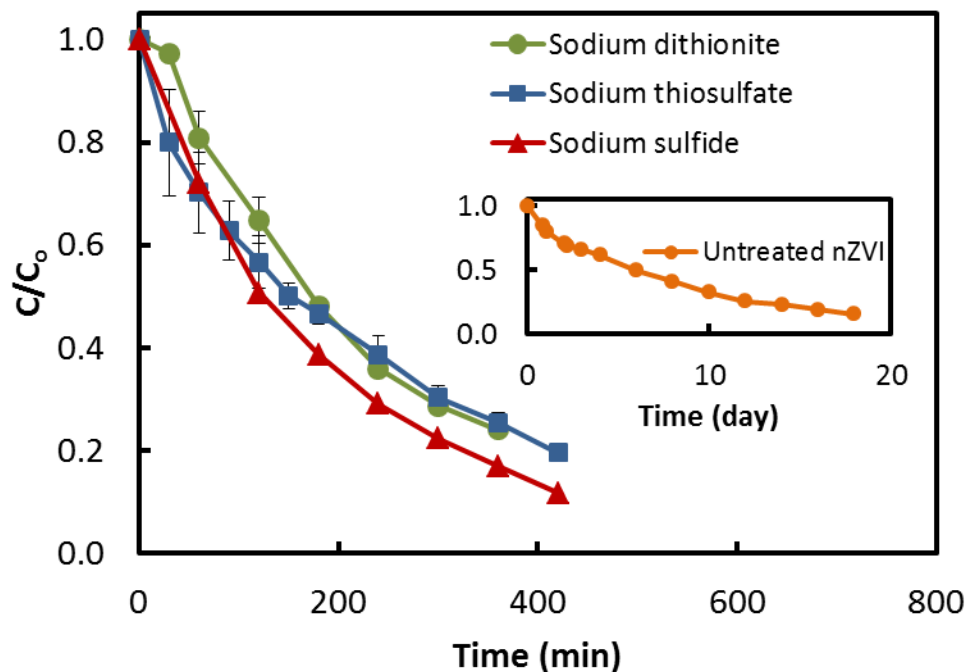


Figure 6.1. TCE dechlorination by sulfided nZVI (s-nZVI) prepared using different sulfur precursors. All particles were prepared using the “20-min post-synthesis sulfidation” method. The mole ratio of sulfur precursor to iron (S/Fe mole ratio) was fixed at 0.05. Initial TCE concentration was approximately 25 mg/L. Solid dose was at 5 g/L. Initial pH was between 7.8-8.1.

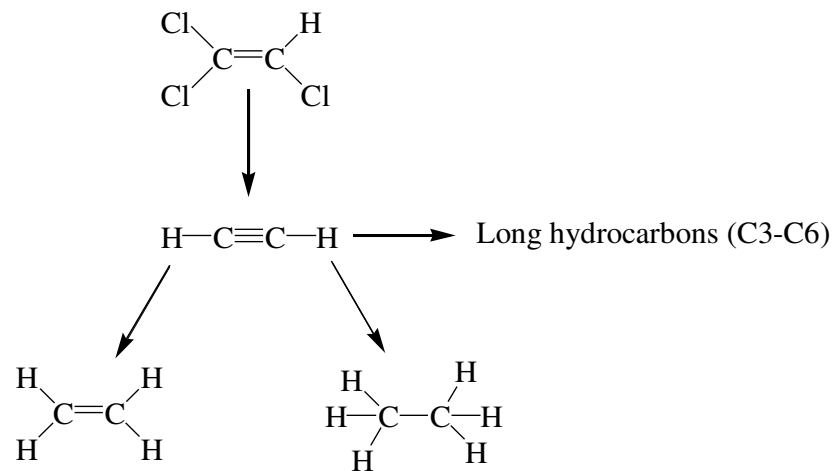


Figure 6.2. Pathways for TCE reductive dechlorination by nZVI and S-nZVI.

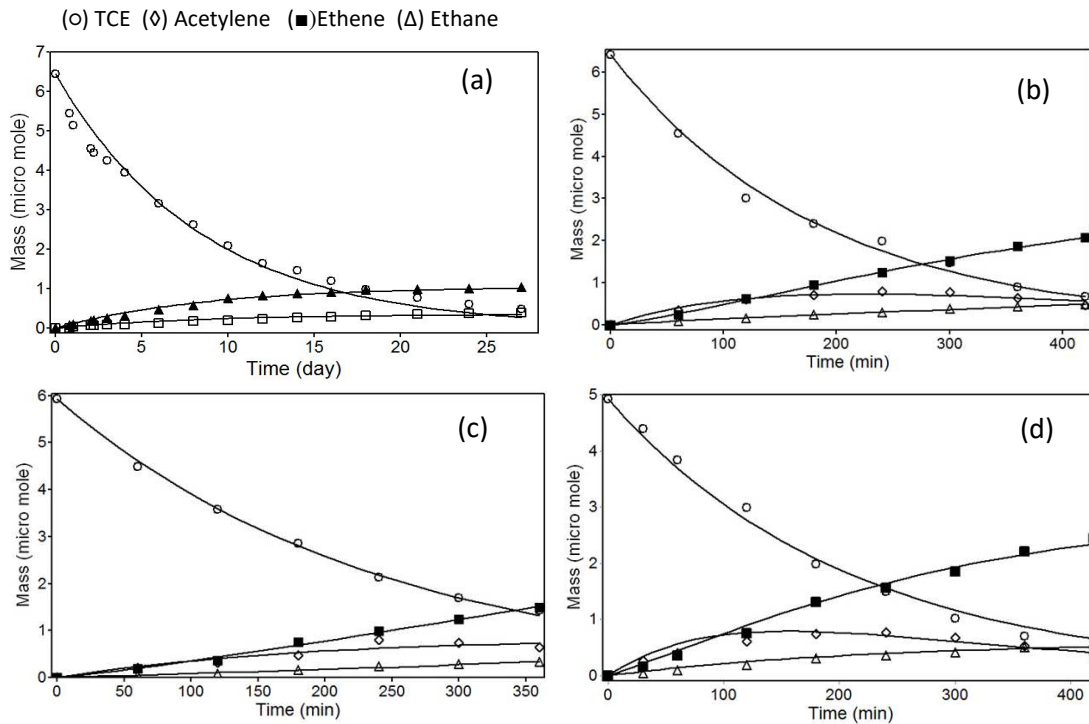


Figure 6.3. TCE dechlorination by (a) nZVI, (b) S-nZVI prepared with sodium sulfide, (c) sodium dithionite, and (d) sodium thiosulfate, respectively. The “20-min post-synthesis sulfidation” method was used for (b) – (d). S/Fe mole ratio was fixed at 0.05. Initial TCE concentration was approximately 25 mg/L. Nanoparticles dose was at 5 g/L. Initial pH was between 7.8–8.1.

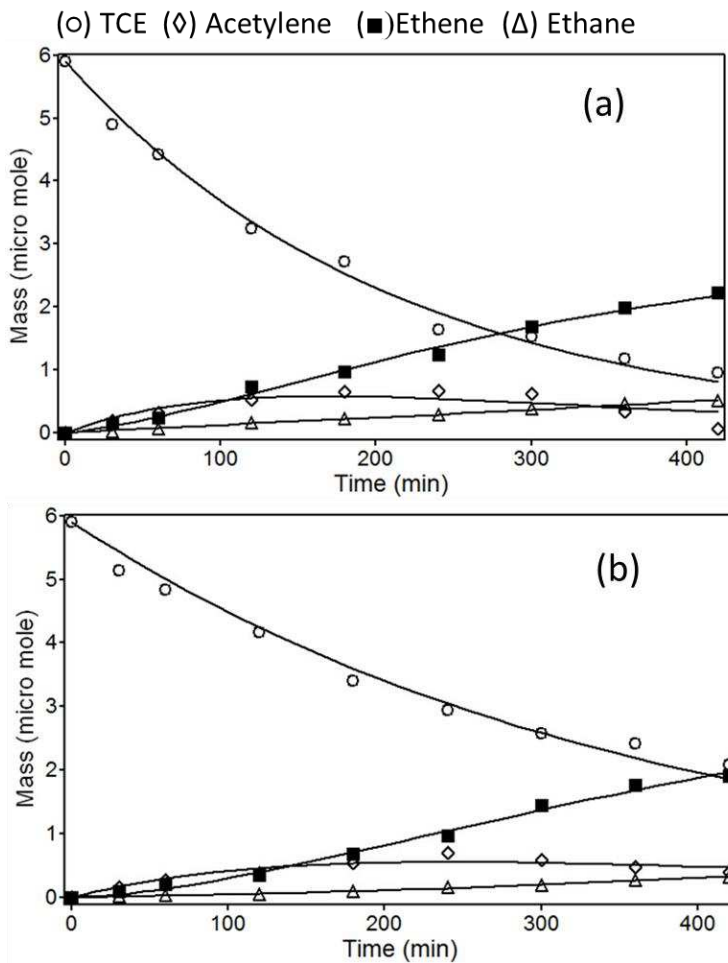


Figure 6.4. Product formation during TCE dechlorination by S-nZVI prepared using the (a) “initial sulfidation” method (b) and “10-min post-synthesis sulfidation” method, respectively. All particles used sodium thiosulfate as the sulfur precursor. S/Fe mole ratio was fixed at 0.05. Nanoparticles dose was at 5 g/L. Initial pH was between 7.8-8.1.

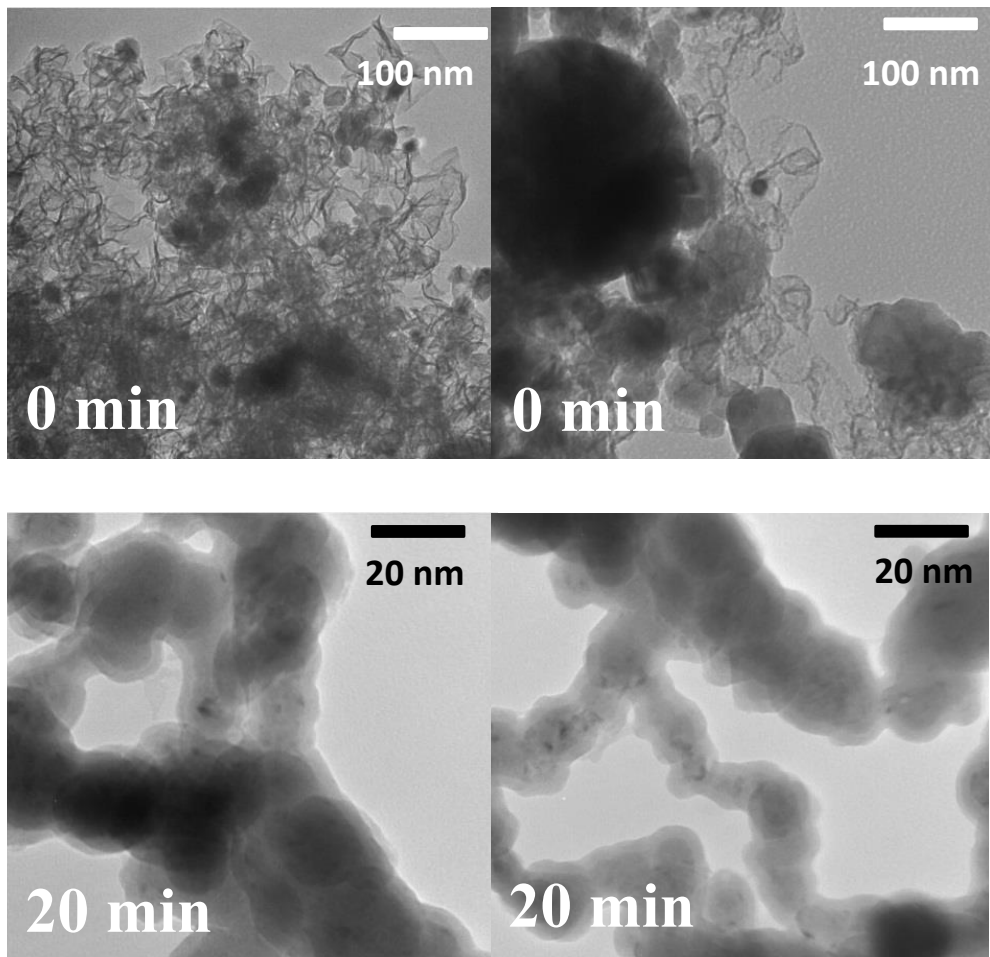


Figure 6.5. TEM micrographs of S-nZVI prepared using the “initial sulfidation” method (labeled with “0 min”) and “20-min post-synthesis sulfidation” method (labeled with “20 min”), respectively. S/Fe mole ratio was at 0.05.

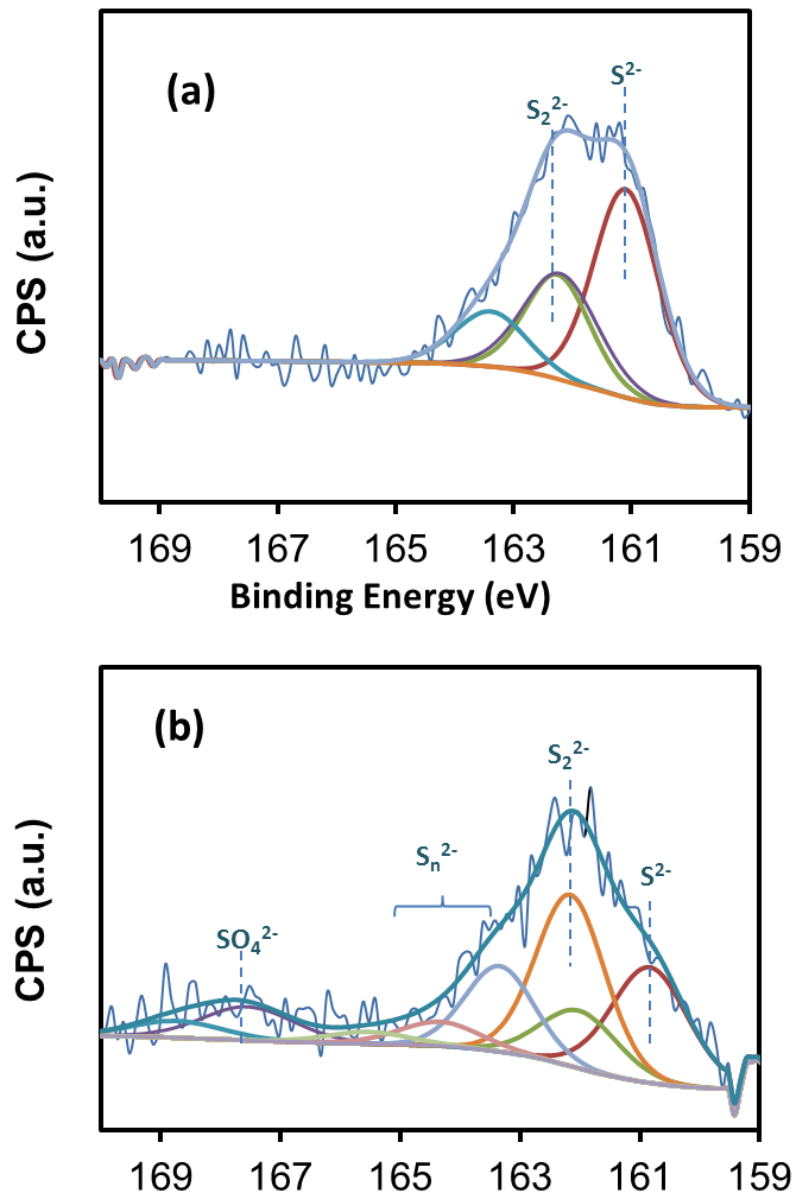


Figure 6.6. XPS S 2p_{3/2} spectra of S-nZVI prepared using (a) the “initial sulfidation” method and (b) “20-min post-synthesis sulfidation” method. Sodium thiosulfate was used as sulfur precursor, and S/Fe mole ratio was at 0.05

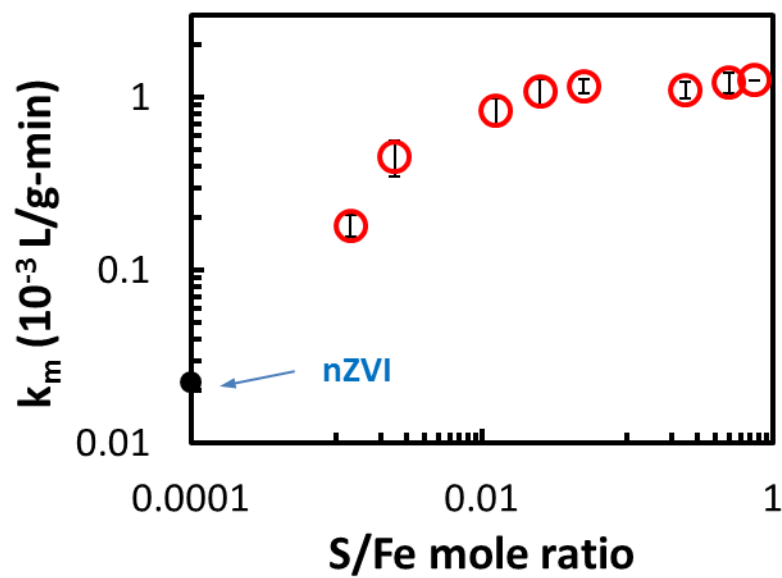


Figure 6.7. Impact of varying S/Fe mole ratio on TCE pseudo-first-order dechlorination rate constants. Nanoparticles were prepared using the “20-min post-synthesis sulfidation” method. Nanoparticles dose was at 5 g/L. Initial pH was between 7.8-8.1.

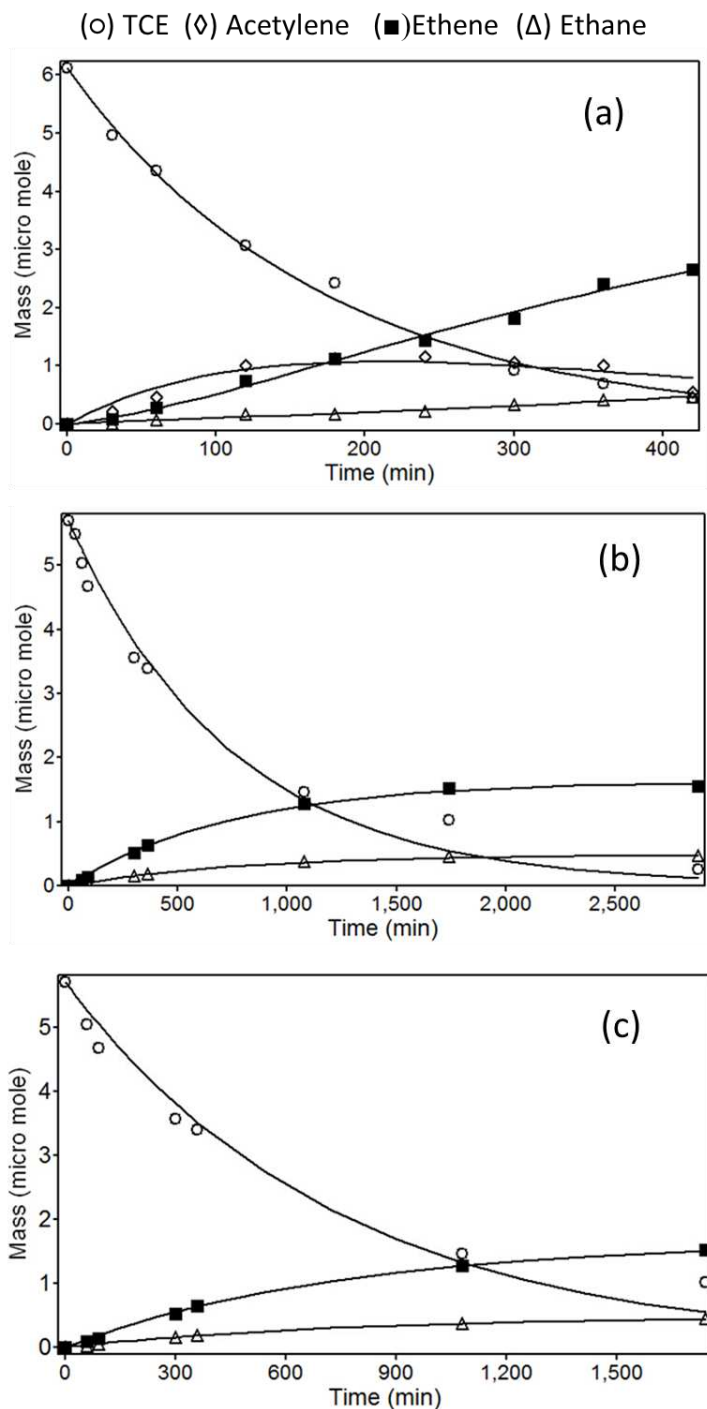


Figure 6.8. Product formation during TCE dechlorination by S-nZVI prepared at an S/Fe mole ratio of (a) 0.5, (b) 0.0025, and (c) 0.00125, respectively. Nanoparticles dose was at 5 g/L. Initial pH was between 7.8-8.1.

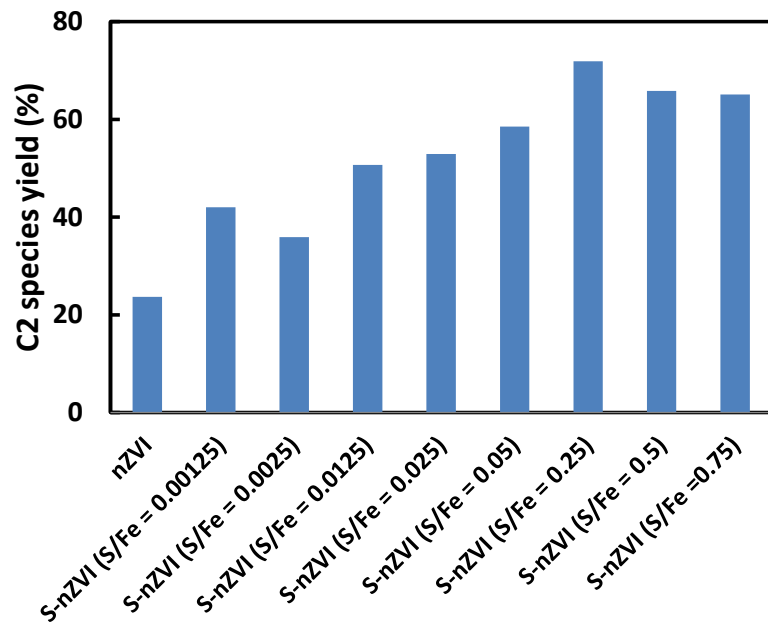


Figure 6.9. Total yield of C₂ products (i.e., acetylene, ethene, and ethane) by S-nZVI prepared at different S/Fe mole ratios. Product yield was measured when approximately 90% of TCE was degraded. Nanoparticles dose was at 5 g/L. Initial pH was between 7.8-8.1.

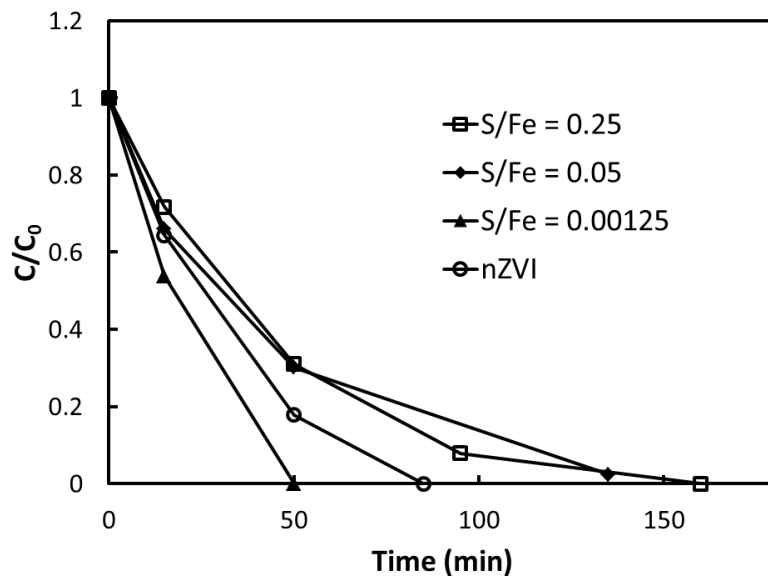


Figure 6.10. Acetylene hydrogenation by S-nZVI prepared at different S/Fe mole ratios. Initial acetylene concentration was 13 μM . Nanoparticles dose was at 5 g/L. Initial pH was between 7.8-8.1.

Table 6.1. Pseudo-first-order rate constants, product yields, and carbon mass recovery for TCE dechlorination by nZVI and S-nZVI synthesized under different conditions

Particles type and synthesis conditions	Products	Yield ^a	C2 Mass recovery (%) ^b	$k_{\text{obs}} (10^{-3} \text{ L g}^{-1} \text{ min}^{-1})^c$
nZVI (Sampled at 24 day when 10% of TCE left)	Ethene	17.2	36.0	0.0141 ± 0.0008
	Ethane	6.5		
	Acetylene	0.0		
	C3-C6	5.7		
S-nZVI (20 min), sodium thiosulfate was used as precursor, and S/Fe mole ratio was at 0.05 (Sampled at 7 h)	Ethene	43.5	68.0	0.800 ± 0.046
	Ethane	10.3		
	Acetylene	4.5		
	C3-C6	7.2		
S-nZVI (20 min), sodium dithionite was used as precursor, S/Fe mole ratio was at 0.05 (Sampled at 7 h)	Ethene	32.6	68.0	0.780 ± 0.210
	Ethane	8.2		
	Acetylene	10.3		
	C3-C6	9.6		
S-nZVI (20 min), sodium sulfide was used as precursor, S/Fe mole ratio was at 0.05 (Sampled at 7 h)	Ethene	39.0	67.4	1.040 ± 0.126
	Ethane	9.4		
	Acetylene	7.2		
	C3-C6	7.5		
S-nZVI (0 min), sodium thiosulfate was used as precursor, S/Fe mole ratio was at 0.05 (Sampled at 7 h)	Ethene	44.9	70.4	0.900 ± 0.084
	Ethane	10.3		
	Acetylene	1.3		
	C3-C6	8.1		
S-nZVI (10 min), sodium thiosulfate was used as precursor, S/Fe mole ratio was at 0.05 (Sampled at 7 h)	Ethene	50.1	86.8	0.520 ± 0.078
	Ethane	8.5		
	Acetylene	10.3		
	C3-C6	10.8		
S-nZVI (20 min), sodium thiosulfate was used as precursor, and S/Fe mole ratio was at 0.0025 (Sampled at 26 h when 10% of TCE left)	Ethene	27.1	52.3	0.420 ± 0.007
	Ethane	8.8		
	Acetylene	0.0		
	C3-C6	10.4		
S-nZVI (20 min), sodium thiosulfate was used as precursor, and S/Fe mole ratio was at 0.00125 (Sampled at 47.5 h when 10% of TCE left)	Ethene	29.0	57.0	0.190 ± 0.059
	Ethane	13.0		
	Acetylene	0.0		
	C3-C6	10.3		

^aProduct yield refers the product formation in terms of C2 over the TCE removal. ^bC2 mass recovery refers the sum of remaining TCE and sum of daughter products in terms of C2 (*i.e.*, 1.5 mol of TCE = 1 mole C_3H_8 , 2 mol of TCE = 1 mole C_4H_{10}). ^cPseudo first-order rate constant, uncertainties represent 95% confidence intervals.

Table 6.2. Effects of sulfidation conditions on pseudo-first-order rate constants, product yields, and carbon mass recovery for TCE dechlorination by different S-Peerless™ iron filings

Preparation conditions	Products	Yield (%) ^a	$k_{\text{obs}} (10^{-4} \text{ L g}^{-1} \text{ min}^{-1})$ ^b
Peerless iron filings as received, without any treatment	Ethene	49.3	N.A.
	Ethane	9.1	
	Acetylene	0.0	
	C3-C6	32.9	
Peerless iron filings followed acid pretreatment	Ethene	47.3	0.099 ± 0.007
	Ethane	13.9	
	Acetylene	0.0	
	C3-C6	32.9	
Peerless iron filings underwent acid pretreatment first, and then followed sulfidation treatment	Ethene	5.5	1.164 ± 0.402
	Ethane	1.3	
	Acetylene	57.1	
	C3-C6	18.5	

^aProduct yield was calculated when 90% of TCE removal was achieved, and product was calculated in terms of C2 mass (i.e., 1.5 mol of TCE = 1 mole C₃H₈, 2 mol of TCE = 1 mole C₄H₁₀). ^bPseudo first-order rate constant, uncertainties represents 95% confidence intervals.

6.5. Support Information

Kinetic model equations in differential equation format used in data fitting

- TCE degradation by nZVI or S-nZVI without the acetylene formation

$$\frac{d[TCE]}{dt} = -k [TCE]$$

$$\frac{d[Ethene]}{dt} = -k_1 [Ethene]$$

$$\frac{d[Ethane]}{dt} = -k_2 [Ethane]$$

- TCE degradation by S-nZVI with the acetylene formation

$$\frac{d[TCE]}{dt} = -k [TCE]$$

$$\frac{d[Acetylene]}{dt} = k_1 [TCE] - k_2 [Acetylene]$$

$$\frac{d[Ethene]}{dt} = -k_3 [Acetylene]$$

$$\frac{d[Ethane]}{dt} = -k_4 [Acetylene]$$

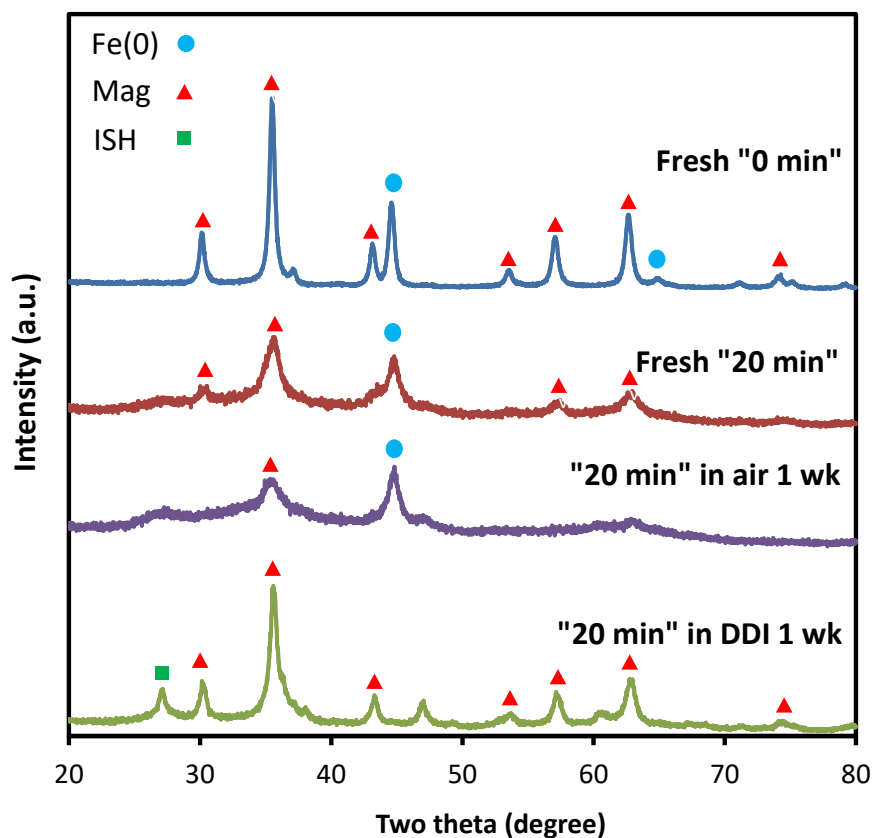


Figure S6.1. X-ray diffraction patterns of S-nZVI (0 min), S-nZVI (20 min), S-nZVI (20 min) exposed to air for 1 week, and S-nZVI (20 min) aged in DDI water for 1 week. Sodium thiosulfate was used as sulfur precursor. S/Fe mole ratio was at 0.05. “Mag” refers to magnetite, and “ISH” refers to hydrous iron sulfate.

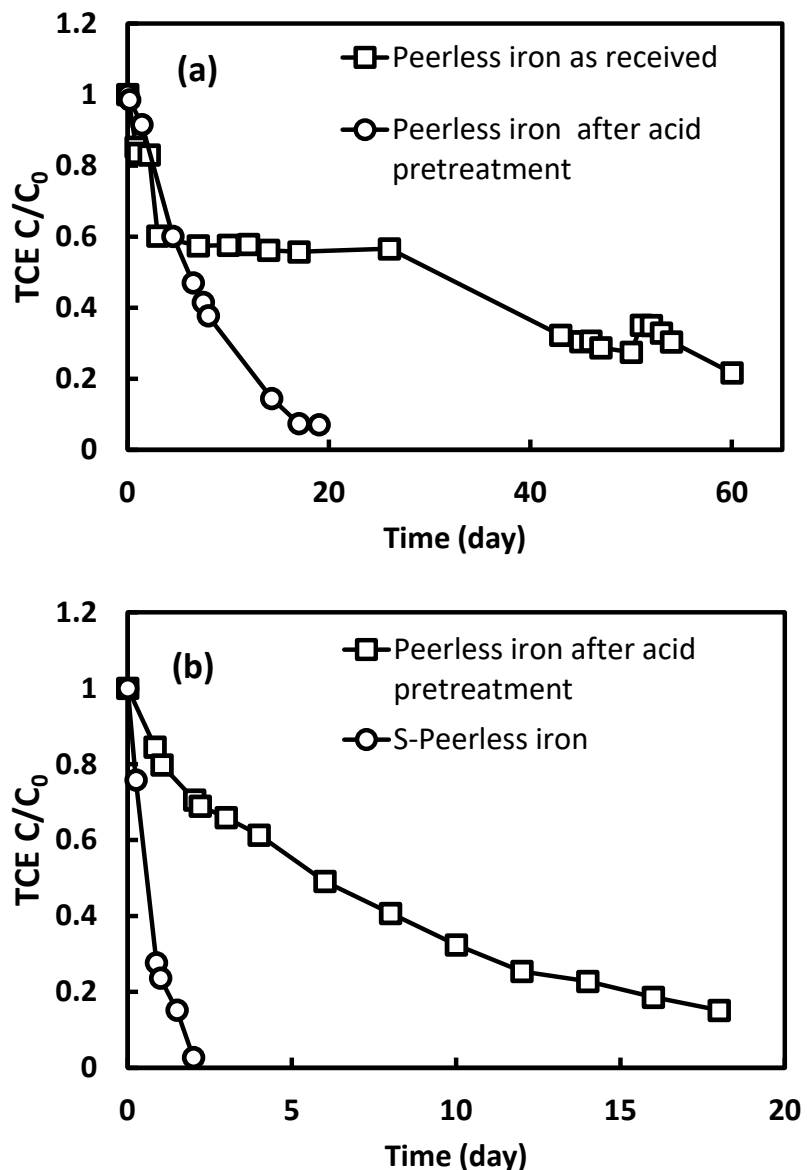


Figure S6.2. TCE dechlorination by PeerlessTM iron filings prepared under different sulfidation conditions. TCE concentration was 25 mg/L. Particles dose was 10 g/L. Initial pH was between 7.8-8.1.

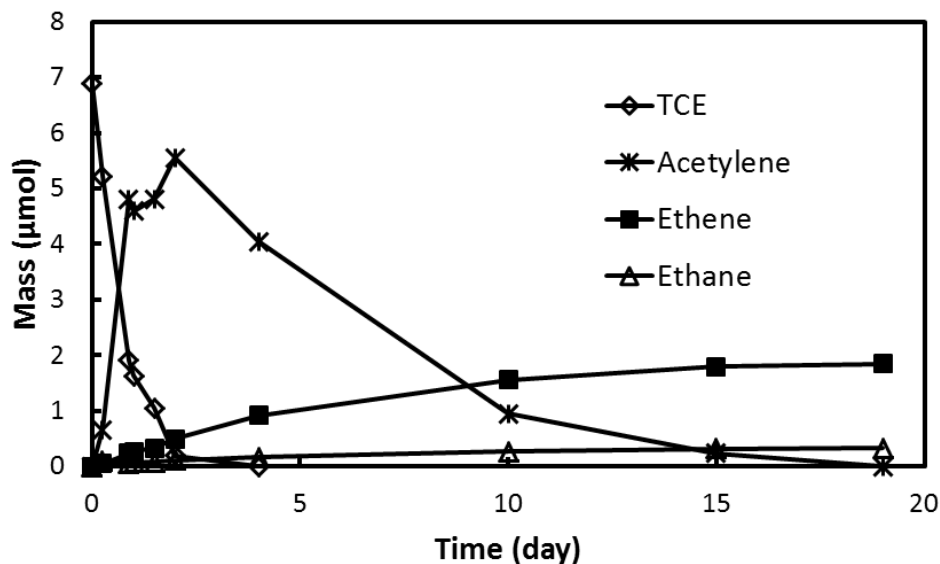


Figure S6.3. TCE dechlorination and major daughter product formation by S-PeerlessTM iron filings. TCE concentration was 25 mg/L. Particles dose was 10 g/L. Initial pH was between 7.8-8.1.

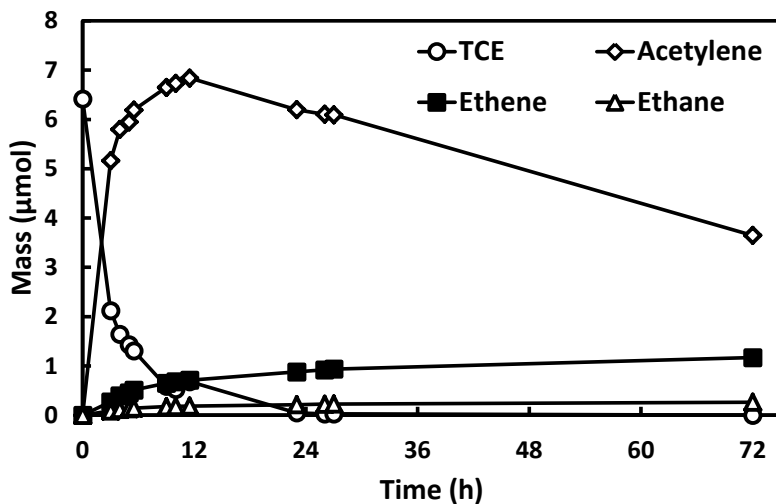


Figure S6.4. TCE dechlorination and major daughter product formation by a physical mixture of amorphous iron sulfide and nZVI. TCE concentration was 25 mg/L. Dose of amorphous iron sulfide was 1 g/L, and dose of nZVI was 5 g/L. Initial pH was between 7.8-8.1.

CHAPTER SEVEN

Reductive Dechlorination of Chlorinated Ethenes by Sulfided Zero-Valent Iron Materials: Kinetic, Pathways, Aqueous Stability and Reaction Mechanism

7.1. Introduction

Chlorinated ethenes, such as tetrachloroethene (PCE) and trichloroethene (TCE), are widespread groundwater and soil contaminants in US superfund sites as the dense non-aqueous liquid (DNAPL) due to their extensive use as the industrial solvents for extraction, spraying, cleaning and degreasing¹⁻³. PCE and TCE are reported to be toxic, carcinogenic and mutagenic to human being and animals⁴, and they are also very recalcitrant to the nature attenuation degradation⁵, therefore, removing PCE and TCE from subsurface has been a primary environmental challenge for decades. Besides PCE and TCE, *trans*- dichloroethene (*trans*-DCE), *cis*-dichloroethene (*cis*-DCE), 1,1-dichloroethene (1,1-DCE) and vinyl chloride (VC) are chlorinated contaminants detected in the subsurface environment⁵⁻⁷, and the accumulation of DCE isomers and VC are usually owing to the incomplete of bioremediation^{8,9} or are produced as the intermediate during the abiotic degradation^{10,11}. Furthermore, *cis*-DCE, 1,1-DCE and VC are even more toxic and difficult to remove^{6,12} compared to PCE and TCE. Therefore, the development of effective remediation technologies to remove chlorinated ethenes from subsurface has been an active research field for decades.

Zero-valent iron (ZVI) materials have been extensively applied for the remediation of chlorinated ethenes in subsurface for 20 years¹³⁻¹⁷. The first field application of ZVI filled in permeable reactive barrier (ZVI-PBR) technology was reported at the Canadian Force Base, Ontario in 1991 to clean the aquifer contaminated with PCE and TCE¹⁸. In 2002, ZVI-PBR was designated as a standard remediation technology by USEPA for plume treatment^{19,20}. Wang and Zhang first reported that nZVI could degrade trichloroethene (TCE) and polychlorinated biphenyls (PCBs) with remarkable higher degradation rates than conventional ZVI²¹. Nanoscale zero-valent iron (nZVI) is one of most prevalently used engineering nanoparticles for subsurface

remediation^{13, 14, 16, 22}. nZVI has been proved to be able to transform chlorinated ethenes into non-toxic end products^{23, 24}, can be directly delivered to subsurface contamination source²⁵⁻²⁷, and has the relatively higher dechlorination reactivity on chlorinated ethenes²⁸ due to the relatively higher surface areas compared to commercial ZVI. These specific advantages of nZVI render it a good flexible treatment technology for contaminants source remediation and an alternative to PRB-ZVI technology. However, one serious drawback about ZVI technology is that ZVI has low reactivity since the material is covered with an intrinsic passivation layer generated during its manufacturing and handling process²⁹, caused by the corrosion products during the reactions with contaminants when ZVI is in the aqueous environment³⁰, or generated during the interactions with groundwater common solutes^{31, 32}. Bimetallic nanoscale zero-valent iron (BNPs), by doping a small amount of catalyst (e.g., Ni or Pd) can significantly enhance the dechlorination rates towards PCE and TCE³³⁻³⁵. However, several concerns are aroused over the application of BNPs for subsurface remediation. Even though BNPs can rapid dechlorinate chlorinated ethenes, the particles undergone rapid deactivation when the particles exposed in complex groundwater media, which limits the application of BNPs for field application³⁶⁻³⁹. Also, because iron-based BNPs contain heavy metals as the heavy metals, so the dissolution of heavy metals into the environment is another serious issue for BNPs application⁴⁰.

The nZVI after surface facile sulfidation treatment process using sodium dithionite as the sulfur precursor showed great reactivity on TCE dechlorination compared to unamend nZVI⁴¹⁻⁴⁴. In our previous research, we have demonstrated that an enhanced β -elimination route could occur to enhance TCE degradation owing to this “iron sulfides/iron” biphasic structure when S/Fe mole ratios were over 0.0125. When S-nZVI was prepared when S/Fe mole ratios were within 0.00125 to 0.0125, TCE degradation rate could be increased yet the enhancement effect occurred to a smaller extent compared to that by S-nZVI synthesized with S/Fe mole ratio in a relative higher range. Also, we have also proved that a common type of commercial iron, Peerless iron, after sulfidation process could significantly enhance the TCE dechlorination compared to the iron without sulfidation process.

In this study, we chose three types of iron materials, one is laboratory synthesized nZVI followed by the borohydride reduction method, and the others are two typical types of commercial iron, Peerless iron filings and BASF carbonyl iron which are commonly used for subsurface remediation. Surface sulfidation treatment was conducted on these three iron materials, and sodium thiosulfate was used as the only sulfur precursor to prepare the sulfided iron materials. We systematically investigated sulfided iron materials reactivity on five typical types of chlorinated ethenes, namely tetrachloroethene (PCE), trichloroethene (TCE), *cis*-dichloroethene (*cis*-DCE), *trans*-dichloroethene (*trans*-DCE) and 1,1- dichloroethene (1,1-DCE). High resolution X-ray photoelectron spectroscopy (HR-XPS) was used to examine the surface compositions before and after sulfidation treatment process. Products formed during chlorinated ethenes dechlorination process were identified by gas chromatography- flame ionization detector (GC-FID). Sulfidation effects on dechlorination rates, pathways, and mechanisms of reductive dechlorination on chlorinated ethenes were proposed based on the product distribution analysis. We also assessed the chemical stability of sulfided ZVI materials through solution or air-exposing aging experiments.

7.2. Materials and Methods

7.2.1 Chemicals

TCE (99.5%), *trans*-dichloroethene (*trans*-DCE, 98%), *cis*- dichloroethene (*cis*-DCE, 97%), and 1,1- dichloroethene (1,1-DCE, 99%) were purchased from Aldrich. Vinyl chloride (VC, 1000 µg/mL in methanol) was purchased from AccuStandard. Iron (III) chloride hexahydrate ($\text{FeCl}_3 \cdot 6\text{H}_2\text{O}$, 97.0%-102.0%) and sodium sulfide nonahydrate ($\text{Na}_2\text{S} \cdot 9\text{H}_2\text{O}$, 98%) were from Alfa Aesar. Sodium thiosulfate anhydrous ($\text{Na}_2\text{S}_2\text{O}_3$, 99.6%), sodium dithionite ($\text{Na}_2\text{S}_2\text{O}_4$, 99%) and ethanol (95%) were obtained from Fisher Scientific. Paraffin mixture (1000 ppm of methane, ethane, propane, butane, pentane, and hexane in helium) and olefin mixture (*ca.* 1000 ppm of ethene, propylene, 1-butene, 1-pentene, and 1-hexene in helium) were obtained from Matheson Tri-Gas and were used as calibration standards. PeerlessTM Iron filings (PMP Iron 50D) were provided by Peerless Metal Powders & Abrasive (Detroit, MI, USA). BASF carbonyl iron powder

was obtained from BASF Company (Ludwigshafen, Germany). Deoxygenated deionized-distilled water (DDI), prepared by purging DDI with N₂ for 30 min, was used in all procedures including particle synthesis and TCE dechlorination experiments.

7.2.2 Sulfided nZVI Preparation Method

The synthesis of sulfided nZVI (denoted as S-nZVI) involved the reduction of aqueous solution of Fe(III) and sulfur precursor by sodium borohydride, and sodium thiosulfate was used as the sulfur precursor. Briefly, 10.812 g of FeCl₃•6H₂O (0.08 M) were dissolved in 500 mL of distilled de-ionized (DDI) water and ethanol mixture (1:1, v/v). 500 mL of NaBH₄ (0.4 M) was introduced into the ferric solution at approximately 17 mL/min under intensive mixing. Appropriate amount of sodium thiosulfate was added into ferric solution after 20 min when NaBH₄ began to pump into ferric solution. The mole ratio between sulfur salt and ferric salt (Denoted as S/Fe mole ratio) was investigated. The S/Fe mole ratio is calculated as mole of sulfur salt divided by mole of ferric chloride used for S-nZVI synthesis, and the S/Fe mole ratio ranged from 0.00125 to 0.50. In this research, the S-nZVI synthesized with S/Fe mole ratio at 0.05 was considered as the default procedure to prepare S-nZVI. The dry weight of particles was determined by using a halogen-lamp moisture analyzer (OHAUS MB45).

7.2.3 Commercial Iron Sulfidation Treatment

Two common types of commercial iron, PeerlessTM iron filings and BASFTM carbonyl iron powder, were used to investigate whether the surface sulfidation treatment could increase the iron filings dechlorination reactivity on chlorinated ethenes. The sulfidation treatment process for commercial iron involved initial acid-wash and subsequent sulfidation treatment. Two type of commercial iron after sulfidation process were denoted as S-PeerlessTM Fe and S-BASFTM Fe, respectively. The S/Fe mole ratio is calculated as mole of sulfur salt divided by mole of iron, and the mole of iron is calculated that the weight of iron particles is divided by iron molecular weight. The S/Fe mole ratio was fixed at 0.05 for the commercial iron sulfidation treatment.

7.2.4. Reduction of Chlorinated Ethenes Experiments

Reductive dechlorination of chlorinated ethenes experiments were performed to compare the reactivity of sulfided iron materials on chlorinated ethenes dechlorination. All batch experiments were conducted in 45-mL EPA vials containing 30 mL of aqueous solution and the balance as headspace. Experiments were performed with S-nZVI particles added at 5 g/L (dry weight) and an initial mass of chlorinated ethenes was approximated 6 μ mol. For the dechlorination experiments by commercial iron, the particles dose was fixed at 10 g/L with the initial mass of chlorinated ethenes at approximately 6 μ mol. Control experiment without nanoparticles was performed in parallel. The vials were capped with Teflon Mininert valves and placed on a mechanical shaker at 250 rpm at room temperature. The initial pH of TCE solution was adjusted to the range between 7.8-8.2 by diluted NaOH or diluted HCl to simulate typical groundwater pH values.

7.2.5 Aging Experiments

Aging experiments were conducted in 45-mL EPA glass vials containing 30 mL of deoxygenated solutions amended with a groundwater solute at 0.1- 5 mM. Stock solutions of chloride, bicarbonate, nitrate, phosphate, sulfite, and sulfate were prepared from their sodium salts. Stock solution of humic acid (Sigma-Aldrich, used as received) was prepared at 50 mg/L and was ultrasonicated for 10 min prior to use. The initial pH of the solution with groundwater solute was adjusted with dilute NaOH or HCl to between a range of 7.7 - 8.3 to simulate the typical pH values encountered in groundwater. Freshly made S-nZVI (S/Fe mole ratio at 0.05) was added into each solution at 5 g/L (dry weight) and the vial was sealed and agitated on a mechanical shaker for 24 h or 1 months at room temperature (22 +/- 1 °C), respectively. The aged particles were collected by vacuum filtration and were used immediately in TCE degradation experiments. Freshly prepared S-Peerless™ Fe was exposed to air for 6 months to check the material reactivity over long-term air-exposing, and TCE was still used as the model contaminant.

7.2.6. Analytical Methods

Periodically, an aliquot (25 - 50 μL) of headspace gas was withdrawn using a gastight syringe, and a gas chromatography system (Agilent 6890) with an Agilent PoraPlot Q column (25 m \times 0.32 mm) and a flame ionization detector (FID) was used to identify and determine chlorinated ethenes as well as reaction intermediates and products. Samples were injected splitless mode at 250°C. The oven temperature (35°C for 5 min, ramp 12°C/min to 220°C, and at 220°C hold for 5 min) provided adequate separation between chlorinated ethenes and all chlorinated and non-chlorinated reaction products. TCE calibration line was constructed by headspace analysis of TCE aqueous standard solutions prepared in the same vials as experimental reactors. Calibrations for C₂-C₆ hydrocarbons were performed using the commercial gas standards. The results were used to compute their total concentrations in the reaction vials after accounting for partition between headspace and aqueous phases using the respective Henry's Law constants ^{45, 46}.

In this research, the product yield was used to characterize the major product formation during the chlorinated ethenes reduction process. It is defined as the amount of product formation over the parent product removal at a given time, which expresses as

$$\text{Product Yield} = \frac{P_{i,t}}{E_0 - E_t} \quad (1)$$

where $P_{i,t}$ is the amount of daughter product i at a given time, E_0 is the initial concentration of certain chlorinated ethene, and E_t is the concentration of chlorinated ethene at given time. Mass balance was calculated by summing up the amount of chlorinated ethene and daughter products detected in the reactor in terms of C₂ equivalents at a given time (e.g., 1 mole of butane = 2 mole of C₂ equivalent).

7.3. Results and Discussion

7.3.1 Reduction of Chlorinated Ethenes by nZVI and S-nZVI

7.3.1.1 Ethene and Acetylene

Ethene and acetylene hydrogenation experiments by nZVI and S-nZVI (S/Fe mole ratio at 0.05) were conducted in order to identify the possible precursors of ethane and

longer hydrocarbons (C3-C6 species). Several previous published papers assumed ethene is the precursor of ethane by zero-valent iron materials^{23, 47, 48}, however, our hydrogenation results suggest different scenario. For the ethene hydrogenation by nZVI, no ethane formation was observed over two months. Also, the ethene hydrogenation by S-nZVI was also extremely slow, because we found only 3% of ethene was hydrogenated into ethane over two months. No longer hydrocarbon species were detected during the ethene hydrogenation experiments by either nZVI or S-nZVI (Data not shown). It is possible that the ethene hydrogenation can be completed by nZVI or S-nZVI over long-term, however, it should be a remarkable slow process and therefore does not contribute significantly to the observed reduction of chlorinated ethenes within the time frame of this research (Mostly less than three months).

Acetylene was extremely reactive, and its hydrogenation process by nZVI was even faster than that by S-nZVI (Figure 7.1). The kinetic model was proposed based on the assumption that the formation of ethene, ethane, and longer hydrocarbons were produced directly from acetylene as the only precursor (Figure 7.2). Kinetic modeling software package, Windows Scientist 3.0 (Micromath, Saint Louis, Missouri, USA) was used to fit the parent compound degradation and products formation based on the proposed kinetic pathway, and the reaction was assumed as pseudo-first-order kinetic reaction. The kinetic modeling results of acetylene hydrogenation by nZVI and S-nZVI were proved to be successful, which are shown in Figure 7.1. The distribution of products observed during the acetylene hydrogenation by nZVI is basically consistent with previous study²³: when acetylene was completely removed measured at 125 min, the major products were ethene and ethane, with the yield of 11.9% and 3.7%, respectively. Longer coupling hydrocarbons were detected: C4 species yield was 4.1%, which was the highest yield among the longer hydrocarbons. C3, C5 and C6 species were also detected, with the yield of 0.9%, 0.8%, and 1.8%, respectively. However, around 75% C2 carbon mass could not be recovered by nZVI when acetylene was completely removed. Product formation of acetylene hydrogenation by S-nZVI was similar as that by nZVI: major products were still ethene and ethane, the yield of which was 13.9% and 2.9%, respectively. Values of longer hydrocarbon species yields were relatively lower

compared to those by nZVI: C4 species yield was 3.0%, and C3, C5 and C6 yield was 0.5%, 0.3% and 1.1%, respectively, yet C2 mass balance by S-nZVI when acetylene completely removed could be recovered to 40%. Another aspect should be noted is that after acetylene completely hydrogenated mediated by both nZVI and S-nZVI, continuous monitoring of reaction mixture for 2 months showed that no more ethane was formed and the amount of longer hydrocarbon species all kept unchanged over the 2-month period. Therefore, by summarizing the hydrogenation results, ethene is not the precursor of ethane or longer hydrocarbon species, and acetylene is the precursor of ethene, ethane and longer hydrocarbons.

7.3.1.2 Tetrachloroethene (PCE)

Figure 7.3(a) shows the PCE dechlorination and its daughter products formation as function of time. PCE dechlorination was a slow process by nZVI which took approximately 80 days to achieve 90% PCE removal. Kinetic modeling was conducted to assume the production of ethene and ethane via parallel formation pathway produced from acetylene. Acetylene was not detected during the PCE dechlorination mediated by nZVI owing to its extreme reactive property, which is commonly accepted as a reactive intermediate during the β -elimination pathway for chlorinated ethenes reductive dechlorination^{23, 47, 49}. In Section 7.3.1.1, we also proved that acetylene was the precursor of ethene, ethane, and longer hydrocarbon species. The degradation of PCE and formation of ethene and ethane were predicted well followed parallel pathway assumption. Table 7.1 shows the pseudo-first-order dechlorination rate constants, major product yields, and C2 mass recovery of different chlorinated ethenes by different types of nano iron materials when 10% of chlorinated ethenes left in the reactor. Unless otherwise noted, product yields in this study were measured when 90% of chlorinated ethene was consumed. As shown in Table 7.1, ethene and ethane were the major products of PCE dechlorination by nZVI, with the yield of 20.8% and 10.1%, respectively. Minor amount of TCE was formed during the initial reaction phase as the hydrogenolysis product, while TCE disappeared as the reaction proceeded. Longer chain hydrocarbon species (C3-C6 species) were produced during the PCE dechlorination process, with the

yield of 4.9%. DCE isomers and VC were not detected during the PCE dechlorination process. In summary, PCE dechlorination by nZVI primarily followed β -elimination, while because acetylene was extremely reactive, no acetylene was detected which was consumed immediately as it formed.

PCE dechlorination was significantly enhanced by S-nZVI (S/Fe mole ratio at 0.05), in which the pseudo-first-order dechlorinated rate constant was increased by a factor of 9 compared to PCE dechlorination by nZVI. The daughter product formation was mainly composed of ethene, ethane and longer hydrocarbons (C3-C6 species). The parallel pathway was used to model the production of ethene and ethane which was similar as PCE dechlorination by nZVI, and the kinetic model yielded satisfactory results (Figure 7.3(b)). However, the values of yields of ethene and ethane of PCE dechlorination by S-nZVI were notably higher than those by nZVI, which were 55.5% and 20.8%, respectively (Table 7.1). TCE, DCE isomers, and VC were not detected.

Varied S/Fe mole ratios during S-nZVI synthesis process had significant impacts on TCE dechlorination rate and TCE dechlorination pathway, which was proved in our previous study. We also investigated the impact of varied S/Fe mole ratios on the reduction of other chlorinated ethenes by S-nZVI. Three different S/Fe mole ratios were used to synthesize S-nZVI, namely S-nZVI with the S/Fe mole ratios of 0.00125, 0.05 and 0.5, respectively. As can be seen in Figure 7.4, when S/Fe mole ratios were at 0.05 and 0.5, respectively, PCE dechlorination rates were closed, while when S/Fe mole ratio was at 0.00125, remarkable abatement of PCE dechlorination rate was observed in which PCE reduction by S-nZVI with S/Fe mole ratio at 0.00125 took around 50 days to achieve 90% of PCE removal (Figure S7.1). Major products of PCE dechlorination by S-nZVI with the S/Fe mole ratio at 0.05 and 0.00125 were ethene and ethane, modeled following the parallel formation pathway which is shown in Figure S7.1. The yields of major products of PCE degradation by S-nZVI with different S/Fe mole ratios were different (Table 7.2). Figure 7.5(a) shows that the yields of ethene, ethane and longer hydrocarbons of PCE dechlorination by S-nZVI with the S/Fe mole ratio at 0.5 were 55.3%, 14.4% and 5.1%, respectively, and the yields of these three products were closed

to those by S-nZVI with the S/Fe mole ratio at 0.05. However, the yields of these three products were 20.5%, 7.4%, and 5.1% when the dechlorination was mediated by S-nZVI with the S/Fe mole ratio at 0.00125, and these values were closed to those by nZVI. Obviously the results strongly suggested that S/Fe mole ratio could affect yields of the major products as well as the dechlorination rates, which was similar as TCE dechlorination by S-nZVI with varied S/Fe mole ratio.

7.3.1.3 *trans*-dichloroethene (*trans*-DCE)

The reduction of *trans*-DCE by nZVI was the fastest among the selected chlorinated ethenes, which took around 13 days to remove 90% of *trans*-DCE, with the yield of ethene, ethane and longer hydrocarbons as 17.6%, 11.1% and 4.2%, respectively (Table 7.1). *trans*-DCE reduction by S-nZVI showed similar trend as TCE reduction by S-nZVI (S/Fe mole ratio at 0.05): Dechlorination of *trans*-DCE could be rapidly finished, and 90% *trans*-DCE removal could be achieved within 12 h, during which considerable acetylene formation was detected yet rapidly consumed as the reaction proceeded. The kinetic model to assume that acetylene was the precursor of ethene and ethane proved to be successful, which is shown in Figure 7.6 (b). The yields of ethene, ethane, and longer hydrocarbons were 34.6%, 7.3%, and 1.9%, respectively. The impacts of varied S/Fe mole ratios during the S-nZVI synthesis process on *trans*-DCE dechlorination showed similar trend as TCE dechlorination by S-nZVI with varied S/Fe mole ratios, and the *trans*-DCE degradation and products formation profiles as a function of time are shown in Figure S7.2. When S-nZVI with the S/Fe mole ratios of 0.05 or 0.5 was used to mediate the *trans*-DCE reduction, *trans*-DCE dechlorination rates were closed and had similar yields of major products, in which acetylene was produced and rapidly consumed as an intermediate. When S-nZVI with the S/Fe mole ratio at 0.00125 was used, the decrease of *trans*-DCE reduction rate was observed, and no acetylene formed during the dechlorination process. As indicated in our previous study, the formation of acetylene was the clear indication that an “enhanced β-elimination effect” was established, and accordingly the whole dechlorination process was accelerated. Also the yields of ethene and ethane by S-nZVI with S/Fe ratio at 0.5 and 0.05 were higher than those by S-nZVI

with the S/Fe ratio at 0.00125 and those by nZVI (Figure 7.5 (b) and Table 2). The mechanisms of *trans*-DCE dechlorination by S-nZVI were similar as the mechanisms of TCE dechlorination by S-nZVI.

7.3.1.4 *cis*-dichloroethene (*cis*-DCE)

The reduction of *cis*-DCE to 90% removal took approximately 20 days, as shown in Figure 7.7(a). The major products formed were ethene and ethane, with the yield of 43.3% and 8.5%, respectively.

The enhanced effect on *cis*-DCE dechlorination by S-nZVI (S/Fe mole ratio at 0.05) was evident, although the enhancement effect occurred to a smaller extent compared to that on PCE, TCE and *trans*-DCE dechlorination, because the dechlorination rate constant of *cis*-DCE by S-nZVI increased a factor of approximately 3. The kinetic model to assume ethene and ethane formed in the parallel pathway following β -elimination could well predict the parent compound degradation and daughter products formation as shown in Figure 7.7. The yields of major products of *cis*-DCE dechlorination by S-nZVI were closed to those by nZVI, values of which were 46.7%, 9.1%, and 4.3% for ethene, ethane, and longer hydrocarbons, respectively (Figure 7.5(c)). Interestingly, for *cis*-DCE reduction by S-nZVI synthesized with varied S/Fe mole ratios, the dechlorination rates were independent of S/Fe mole ratios because no significant improvement on dechlorination rates were achieved when S/Fe mole ratios increased from 0.00125 to 0.5 as shown in Figure 7.8. Also, the S-nZVI with varied S/Fe mole ratios almost posed negligible impact on the distribution and yields of major products because the yields of major products were basically same no matter which type of S-nZVI was used, which are shown in Figure 7.5(c) and Table 7.2.

7.3.1.5 1,1-dichloroethene (1,1-DCE)

The completion of 1,1-DCE took noticeable longer time compared to the other two kinds of DCE isomers. Interestingly we found that during the 1,1-DCE dechlorination, the yields of major products were extremely low, in which ethene yielded 6.0%, ethane yielded 1.2%, and minor quantity of longer hydrocarbon species was

formed with yield of 1.1%. The remarkable slow 1,1-DCE dechlorination rate by nZVI in this research showed totally different trend compared to previous studies, because previous studies all reported that 1,1-DCE could be rapidly dechlorinated by either common types of commercial iron or titanium^{11, 23, 50, 51}. Arnold and Roberts proposed that the reductive elimination of 1,1-DCE by electrolytic iron underwent through the α -elimination, in which 1,1-DCE dechlorination involved two electron α -reductive elimination with alkylidene carbene as the intermediate and alkylidene carbene was precursor of ethene²³. However, compared to their results which stated that only ethene and ethane were observed and no longer hydrocarbon species were produced, we observed the formation of longer hydrocarbons, mainly composed of C4 and C6 species. Another noticeable difference compared to Arnold and Roberts result which assumed that ethene was the precursor of ethane, kinetic modeling followed the assumption that ethene and ethane produced from the same precursor proved successful in this research. Alkylidene carbene could possibly react with 1,1-DCE to form C4 species, yet it seemed not possible to be the precursor of ethane based on previous study⁵². Accordingly the distribution of products suggested that acetylene was still the precursor for ethene, ethane and longer hydrocarbons. However, it is still hard to infer whether the formation of acetylene was from α -elimination or β -elimination pathway. Acetylene could be produced directly through the β -elimination pathway, or could be possibly produced from alkylidene carbene owing to the rearrangement effect of alkylidene carbene⁵².

The reduction of 1,1-DCE by S-nZVI could be completed within 4 days, achieving around 95% TCE removal (Figure 7.9(b)). Compared to the dechlorination mediated by nZVI, the pseudo-first-order dechlorination rate constant increased by a factor of 15 by S-nZVI. Even though the dechlorination rate was dramatically increased by S-nZVI, the yields of major products of 1,1-DCE dechlorination by S-nZVI were basically consistent with those by nZVI, which was still featured with extremely low yields of major products formation. The results indicated that when 10% of 1,1-DCE left in the reactor, the yields of ethene, ethane and longer hydrocarbons were 9.2%, 2.7%, and 2.6%, respectively (Table 7.1). Figure 7.10 shows the 1,1-DCE dechlorination profiles by S-nZVI with varied S/Fe mole ratios, the results indicated that S-nZVI with different S/Fe

mole ratios could affect the 1,1-DCE dechlorination rates, while the impact of varied S/Fe moles ratio on 1,1-DCE dechlorination rates was not as strong as the cases of PCE, TCE and *cis*-DCE dechlorination by S-nZVI with varied S/Fe mole ratios. The dechlorination rate constant of 1,1-DCE by S-nZVI with the S/Fe mole ratio at 0.5 was merely slightly higher than the other two types of S-nZVI, and no dramatic reactivity abatement was observed when the S/Fe mole ratio dropped to 0.00125. The 1,1-DCE reduction by S-nZVI with S/Fe mole ratio at 0.00125 and 0.5 were featured with low yields of ethene and ethane formation as well, which are shown in Figure 7.5(d) and Table 7.2.

7.3.1.6 Discussion

Reduction of chlorinated ethenes dechlorination by nZVI followed the order as PCE < 1,1-DCE < *cis*-DCE < TCE < *trans*-DCE based on the pseudo-first-order dechlorination rate constants (Table 7.1), and the reaction pathways for chlorinated ethenes by nZVI in this study was summarized in Figure 7.11. Previous research has studied the reduction of chlorinated ethenes by commercial iron and nanoscale iron, while no consistent trend of dechlorination rate with chlorination extent on chlorinated ethenes has been concluded. Johnson, et al¹¹ systematically summarized the reduction of chlorinated ethenes by commercial iron and suggested that dechlorination rate decreased as chlorination decreased (*c*-DCE < 1,1-DCE < TCE < PCE), which indicated that reduction of chlorinated ethenes by microscale nZVI was under thermodynamic control because chlorinated ethene with higher chlorination extent was with higher reduction potential^{23, 53}. Arnold and Roberts suggested the opposite way based on their research results, suggesting the rate-limiting process involved the formation of di- σ -bonded intermediate on the iron surface²³. Song and Carraway used laboratory synthesized nZVI and studied the reduction of chlorinated ethenes, and found that chlorinated ethenes dechlorination increased with decreasing chlorination, yet the mechanism of reduction of chlorinated ethenes was owing to the hydrogenation catalytic effect involving reactive hydrogen species adsorbed in the nZVI surface⁵⁴. The reduction of chlorinated ethenes by nZVI based on in this research seemed to suggest that the dechlorination rate

increased with the decrease of halogenation, which accorded with Arnold and Roberts²³ and Song and Carraway's⁵⁵ observation, expect 1,1-DCE was extremely resistant to the dechlorination mediated by nZVI. However, compared to Song and Carraway's results, we did not observe the catalytic hydrogenation effects on chlorinated ethenes reduction, because ethene was the predominant daughter product for all batches and ethene hydrogenation could not be completed over long term. Accordingly, the reasonable explanation for the rate-limiting step could possibly owing to the formation of bonded surface intermediate on the nZVI in this study. However it is still hard to find the rate-limiting step for 1,1-DCE reduction by nZVI. According to Arnold and Roberts proposition²³, if the formation of di- σ -bonded surface intermediate was the rate-limiting process, the reduction of 1,1-DCE should be a rapid process. Also, the reduction of 1,1-DCE by microscale nZVI was reported to be a rapid reduction process compared to two the reduction of other two DCE isomers, in contrast to our results⁵⁶. The kinetic modeling results suggested that for the reduction of all types of chlorinated ethenes by nZVI, acetylene was the precursor of ethene and ethane. Reduction of PCE, TCE, trans-DCE and cis-DCE, the reduction mainly followed β -elimination (Figure 7.11). 1,1-DCE reduction followed α -elimination, and the acetylene was the precursor of ethene and ethane. We also have confirmed that the acetylene is the precursor of ethene, ethane, and longer hydrocarbons, and ethene was not the precursor of ethane, which is different from Arnold and Roberts suggestion²³.

For reduction of chlorinated ethenes mediated by S-nZVI with the S/Fe ratio at 0.05, the reduction rate order followed *cis*-DCE \approx PCE < 1,1-DCE < *trans*-DCE < TCE. Significant enhanced dechlorination effect on PCE, *trans*-DCE and TCE was achieved. Our previous study has confirmed that the effect of sulfidation is mainly associated with an enhanced enhanced β -elimination step and thus accelerates the overall dechlorination process if the particles have a high sulfur loading (i.e. prepared at a high S/Fe mole ratio). This process is featured with three distinctive characters: (1) significantly enhanced dechlorinate rate, (2) the accumulation of acetylene, and (3) high yield of sum of C2 species (ethene, ethane and acetylene). Obviously, the enhancement on TCE and *trans*-DCE dechlorination was due to the "enhanced β -elimination effect." No acetylene

formation was observed during the PCE dechlorination by S-nZVI, yet the modeling results suggest that acetylene was the precursor of ethene and ethane, meaning that acetylene might rapidly be consumed. Besides no observed acetylene formation, PCE dechlorination process fitted the other two characters. Therefore we still attributed the enhanced dechlorination effect on PCE to the establishment of “enhanced β -elimination effect” owing to the biphasic structure. For the reduction of 1,1-DCE and *cis*-DCE by S-nZVI under this synthesis condition, only dechlorination rate was increased while the distribution and yields of major products kept same compared to that by nZVI, indicating that the reduction of 1,1-DCE or *cis*-DCE by S-nZVI underwent same dechlorination pathway compared to that by nZVI yet the binding capacity of contaminants on the S-nZVI might be enhanced because the formation of surface-bound intermediate could be the possible rate-limiting step for chlorinated ethenes degradation based on degradation order of different chlorinated ethenes by nZVI.

When S-nZVI with the S/Fe ratio at 0.00125 was used as the reducing agent for chlorinated ethenes reduction, the reduction order followed PCE < *cis*-DCE < 1,1-DCE < trans-DCE < TCE (Table 7.2). In our previous study, we found that when S-nZVI synthesized under low S/Fe mole ratio condition, the distribution and yields of major products stayed same compared to those by nZVI, indicating S-nZVI synthesized under this condition could not change the reaction pathways. For the reduction of the other four types of chlorinated ethenes in this research, we found that only the dechlorination rate was increased for each reaction batch yet no change of distribution and yields of major products were observed compared to the dechlorination process mediated by nZVI. Therefore, under this situation, the dechlorination still mediate by Fe(0) phase but the iron sulfide species may enhance the binding capacity of TCE on the S-nZVI.

7.3.2 Reduction of Chlorinated Ethenes by PeerlessTM Fe and S-PeerlessTM Fe

Table 7.3 shows the pseudo-first-order dechlorination rate constants, major product yields, and C2 mass recovery of different chlorinated ethenes by different types of Peerless iron when 10% of chlorinated ethenes was left in the reactor. The pseudo-first-order reduction rate constants of chlorinated ethenes by Peerless iron follows the

order as PCE < TCE < 1,1-DCE < trans-DCE. *cis*-DCE reduction by Peerless iron could be completed within 6 days yet the pseudo-first-order kinetic model failed to yield satisfactory fit (Figure 7.12). Ethene and ethane were still primary products by Peerless iron for each batch, while the yield of longer hydrocarbon species for each reaction batch was much higher than that by nZVI. Interestingly, 1,1-DCE reduction by Peerless iron underwent rapid dechlorination by Peerless iron, yet one similar aspect is that the major products were still with remarkably low yields compared to those by nZVI.

PeerlessTM Fe after sulfidation process rendered interesting results about reduction of chlorinated ethenes compared to S-nZVI. It can be seen that significant enhanced dechlorination effect occurred to TCE dechlorination by S- PeerlessTM Fe compared to PeerlessTM Fe, also evident enhanced dechlorination effect on PCE was achieved by S- PeerlessTM Fe (Figure 7.12(a) and (b)). For *trans*-DCE reduction, the dechlorination profile as a function of time by PeerlessTM Fe with or without sulfidation process was almost same, suggesting that no specific enhancement effect was achieved for *trans*-DCE reduction by S- PeerlessTM Fe. Only difference is that acetylene formation was observed by S- PeerlessTM Fe. Strikingly, remarkable inhibition effect occurred to the *cis*-DCE and 1,1-DCE dechlorination if PeerlessTM Fe after sulfidation treatment, which is shown in Figure 7.12 (c) and (d). XPS analysis results show that iron sulfide (FeS) were formed on the PeerlessTM Fe after surface sulfidation treatment, and results of which were similar as nZVI after sulfidation treatment process. However, small amount of copper (Cu) was also detected on the PeerlessTM Fe surface after the acid-wash process (Figure S7.5). Rapid dechlorination of three DCE isomers by PeerlessTM Fe without sulfidation process could be possibly owing to the existence of Cu on the PeerlessTM Fe, because previous studies have suggested that Cu could perform as the hydrogenation catalyst, which was able to speed up the contaminants degradation rate and yield with saturated products^{35, 57-61}. However, as pointed out by several studies, metal catalysts were particularly sensitive to sulfide, a fouling agent which could rapidly deactivate the catalysts⁶¹⁻⁶⁴. Accordingly, after sulfidation treatment, Cu could be deactivated by sulfide to form CuS, resulting in a decreased rate in *cis*-DCE and 1,1-DCE degradation. Evidence to substantiate this proposition is the distribution of products: The hydrodechlorination of PCE, TCE, and

three DCE isomers could be completed by PeerlessTM Fe, which yielded as the ethane as the predominant product with a yield of more than 95% when chlorinated ethenes were completely removed for each reaction batch. However, the hydrodechlorination of PCE, TCE and DCE isomers could not be finished by S- PeerlessTM Fe based on 1 year monitoring results, in which the ethene was the predominant product and no more ethane formation was observed after chlorinated ethenes were completely dechlorinated. A separate *cis*-DCE dechlorination experiments was conducted by Cu-nZVI and sulfided Cu-nZVI (Denoted as S-Cu-nZVI), and the synthesis method of Cu-nZVI and S-Cu-nZVI was described in Support Information. The dechlorination results by Cu-nZVI and S-Cu-nZVI is shown in Figure S7.6, and indicated that dechlorinated rate by Cu-nZVI was faster than that by S-Cu-nZVI, and the predominant product of *cis*-DCE dechlorination by Cu-nZVI was ethane, while ethene was primary product by S-Cu-nZVI when *cis*-DCE was compared dechlorinated.

7.3.3 Reduction of Chlorinated Ethenes by BASFTM Fe and S- BASFTM Fe

We conducted sulfidation surface treatment process on BASFTM Fe, including initial acid-wash and subsequent sulfidation surface treatment process. PCE, TCE and *cis*-DCE were selected as the model contaminants to assess the iron material reactivity after the sulfidation process. Unlike the Peerless iron contains copper impurity, BASFTM Fe features with highly purity of iron without other metal impurities, and the major contents of BASFTM Fe used in this research are listed in Table S7.1. Similar trend for reduction of chlorinated ethenes by S-BASF iron was observed compared to nZVI with and without sulfidation treatment process. S- BASFTM Fe could enhance the PCE and TCE dechlorination rates, yet no evident enhancement effect was observed during the *cis*-DCE reduction, which are shown in Figure 7.13.

7.3.4 Reactivity of Particles Aged in Groundwater Media and Air

The chemical stability of S-nZVI with S/Fe mole ratio at 0.05 was evaluated by aging the particle in aqueous solutions of groundwater solutes for 24 h and for 1 month. As shown in Figure 7.14(a), no significant reactivity loss was observed for S-nZVI after 1 day aging process. Aging S-nZVI for a longer period of time (1 month) in the same

solutions resulted in a moderate loss of reactivity compared to those aged for 1 day, except in the case of nitrate that caused completely deactivation of particles for TCE degradation. By comparing the TCE degradation reactivity by Pd-Fe bimetallic nanoparticles (Pd-Fe BNPs) aged for 1 day (Figure 7.14(b)), Pd-Fe BNPs underwent rapid deactivation when BNPs aged in the presence of different common groundwater solutes even though the freshly-made Pd-Fe BNPs had remarkable high TCE degradation rate. In contrast, no significant reactivity loss was observed for S-nZVI subject to the same aging conditions.

Fresh-prepared S-PeerlessTM Fe was exposed to air for up to 6 months to assess its stability in atmospheric environment. We found that air exposure for up to 6 months did not affect particle reactivity (Figure S7.7). Several research papers have stated that, in order to preserve the reactivity of ZVI materials, particles need to be stored in an anaerobic environment. The results suggested that the surface sulfidation process could help to preserve the reactivity of commercial ZVI, which would simplify iron storage/handling procedures.

7.4. Implications for Subsurface Remediation

The surface sulfidation treatment process has been conducted on three different types of iron materials, including laboratory synthesized nZVI and another two types of commercial iron. The study suggests that nZVI after sulfidation treatment process possessed enhanced reactivity for all selected chlorinated ethenes compared to unamend nZVI, and commercial iron after sulfidation could enhance TCE and PCE dechlorination yet showed some inconsistent trend to the DCE isomers degradation compared to S-nZVI. However, taken together the dechlorination results of these three types of iron materials, iron materials after surface sulfidation treatment have unique selectivity to enhance TCE and PCE dechlorination. Considering the fact that TCE and PCE are widespread groundwater contaminants and they are the parent compound of DCE isomers, the sulfided iron materials are suitable for treating for DNAPL of chlorinated ethenes source zones. As DNAPL composed of chlorinated ethenes evolves, DCE isomers might be produced as the intermediates owing to the biotic or abiotic degradation. Our results

suggested that S-nZVI could enhance the dechlorination rates of all selected chlorinated ethenes, and this advantage makes that S-nZVI is suitable for treating the chlorinated ethenes DNAPL in different stages.

Besides the finding that surface-sulfided iron possesses remarkably higher reactivity in reductive dechlorination of chlorinated ethenes, sulfided iron materials exhibit improved aqueous/air stability than conventional monometallic or bimetallic iron materials. They represent an alternative form of ZVI materials that can overcome the intrinsic limitations of conventional ZVI including rapid passivation and low reactivity in the absence of catalyst additives. The proposed surface treatment method is simple and involves inexpensive chemical reagents, and the process can be readily scaled up for pilot or large-scale implementations. The study also suggests for the first time that this facile surface treatment protocol can be extended to commercially available ZVI (Peerless iron and BASF iron) to achieve enhanced dechlorination performance. Furthermore, air-exposure experiments suggest that the reactive properties of surface sulfided iron can be preserved in air for a long period of time, saving the use of sophisticated instruments or handling procedures during the production, transfer, and use of these reactive iron materials.

Reference

1. Norris, R. D., *Handbook of bioremediation*. CRC press: 1993.
2. McCarty, P. L., GROUNDWATER CONTAMINATION BY CHLORINATED SOLVENTS: HISTORY, REMEDIATION TECHNOLOGIES AND STRATEGIES. In *Situ Remediation of Chlorinated Solvent Plumes* **2010**, 1-28.
3. Moran, M. J.; Zogorski, J. S.; Squillace, P. J., Chlorinated solvents in groundwater of the United States. *Environmental Science & Technology* **2007**, *41*, (1), 74-81.
4. Hileman, B., Concerns broaden over chlorine and chlorinated hydrocarbons. *Chemical and Engineering News(USA)* **1993**, *71*, (16), 11-20.
5. McCarty, P. L., In situ bioremediation of chlorinated solvents. *Current opinion in biotechnology* **1993**, *4*, (3), 323-330.
6. Kielhorn, J.; Melber, C.; Wahnschaffe, U.; Aitio, A.; Mangelsdorf, I., Vinyl chloride: still a cause for concern. *Environmental Health Perspectives* **2000**, *108*, (7), 579.

7. Chen, K. F.; Kao, C. M.; Sung, W. P.; Lin, C. C.; Yeh, T. Y., Enhanced In Situ Anaerobic Bioremediation of TCE-contaminated Groundwater Using Nanoscale Zero-valent Iron (nZVI). *Frontier of Nanoscience and Technology* **2011**, *694*, 3-7.
8. Kao, C. M.; Chen, Y. L.; Chen, S. C.; Yeh, T. Y.; Wu, W. S., Enhanced PCE dechlorination by biobarrier systems under different redox conditions. *Water research* **2003**, *37*, (20), 4885-4894.
9. Pant, P.; Pant, S., A review: Advances in microbial remediation of trichloroethylene (TCE). *Journal of Environmental Sciences* **2010**, *22*, (1), 116-126.
10. Su, C.; Puls, R. W., Kinetics of Trichloroethene Reduction by Zerovalent Iron and Tin: Pretreatment Effect, Apparent Activation Energy, and Intermediate Products. *Environmental Science & Technology* **1999**, *33*, (1), 163-168.
11. Johnson, T. L.; Scherer, M. M.; Tratnyek, P. G., Kinetics of Halogenated Organic Compound Degradation by Iron Metal. *Environmental Science & Technology* **1996**, *30*, (8), 2634-2640.
12. Weaver, J. W.; Wilson, J. T.; Campbell, D. H. In *Case study of natural attenuation of trichloroethene at St. Joseph, Michigan*, 1997, p 67.
13. Crane, R. A.; Scott, T. B., Nanoscale zero-valent iron: Future prospects for an emerging water treatment technology. *Journal of Hazardous Materials* **2012**, *211*, 112-125.
14. O'Carroll, D.; Sleep, B.; Krol, M.; Boparai, H.; Kocur, C., Nanoscale zero valent iron and bimetallic particles for contaminated site remediation. *Advances in Water Resources* **2013**, *51*, 104-122.
15. Theron, J.; Walker, J. A.; Cloete, T. E., Nanotechnology and water treatment: Applications and emerging opportunities. *Critical Reviews in Microbiology* **2008**, *34*, (1), 43-69.
16. Li, X.-q.; Elliott, D. W.; Zhang, W.-x., Zero-valent iron nanoparticles for abatement of environmental pollutants: Materials and engineering aspects. *Critical Reviews in Solid State and Materials Sciences* **2006**, *31*, (4), 111-122.
17. Mueller, N. C.; Braun, J.; Bruns, J.; Cernik, M.; Rissing, P.; Rickerby, D.; Nowack, B., Application of nanoscale zero valent iron (NZVI) for groundwater remediation in Europe. *Environmental Science and Pollution Research International* **2012**, *19*, (2), 550-558.
18. Gillham, R. W.; Ohannesin, S. F., ENHANCED DEGRADATION OF HALOGENATED ALIPHATICS BY ZERO-VALENT IRON. *Ground Water* **1994**, *32*, (6), 958-967.
19. Gillham, R. W.; Vogan, J.; Gui, L.; Duchene, M.; Son, J., Iron barrier walls for chlorinated solvent remediation. In *In situ remediation of chlorinated solvent plumes*, Springer: 2010; pp 537-571.

20. Wadley, S. L. S.; Gillham, R. W.; Gui, L., Remediation of DNAPL source zones with granular iron: Laboratory and field tests. *Ground Water* **2005**, *43*, (1), 9-18.
21. Wang, C.-B.; Zhang, W.-x., Synthesizing Nanoscale Iron Particles for Rapid and Complete Dechlorination of TCE and PCBs. *Environmental Science & Technology* **1997**, *31*, (7), 2154-2156.
22. Lien, H.-L.; Zhang, W.-x., Nanoscale iron particles for complete reduction of chlorinated ethenes. *Colloids and Surfaces A: Physicochemical and Engineering Aspects* **2001**, *191*, (1-2), 97-105.
23. Arnold, W. A.; Roberts, A. L., Pathways and kinetics of chlorinated ethylene and chlorinated acetylene reaction with Fe(O) particles. *Environmental Science & Technology* **2000**, *34*, (9), 1794-1805.
24. Choe, S.; Lee, S. H.; Chang, Y. Y.; Hwang, K. Y.; Khim, J., Rapid reductive destruction of hazardous organic compounds by nanoscale Fe-0. *Chemosphere* **2001**, *42*, (4), 367-372.
25. Elliott, D. W.; Zhang, W. X., Field assessment of nanoscale biometallic particles for groundwater treatment. *Environmental Science & Technology* **2001**, *35*, (24), 4922-4926.
26. Saleh, N.; Sirk, K.; Liu, Y.; Phenrat, T.; Dufour, B.; Matyjaszewski, K.; Tilton, R. D.; Lowry, G. V., Surface modifications enhance nanoiron transport and NAPL targeting in saturated porous media. *Environmental Engineering Science* **2007**, *24*, (1), 45-57.
27. Quinn, J.; Geiger, C.; Clausen, C.; Brooks, K.; Coon, C.; O'Hara, S.; Krug, T.; Major, D.; Yoon, W. S.; Gavaskar, A.; Holdsworth, T., Field demonstration of DNAPL dehalogenation using emulsified zero-valent iron. *Environmental Science & Technology* **2005**, *39*, (5), 1309-1318.
28. Comba, S.; Di Molfetta, A.; Sethi, R., A Comparison Between Field Applications of Nano-, Micro-, and Millimetric Zero-Valent Iron for the Remediation of Contaminated Aquifers. *Water Air and Soil Pollution* **2011**, *215*, (1-4), 595-607.
29. Martin, J. E.; Herzing, A. A.; Yan, W.; Li, X.-q.; Koel, B. E.; Kiely, C. J.; Zhang, W.-x., Determination of the oxide layer thickness in core-shell zerovalent iron nanoparticles. *Langmuir* **2008**, *24*, (8), 4329-4334.
30. Cornell, R. M.; Schwertmann, U., *The iron oxides: structure, properties, reactions, occurrences and uses*. John Wiley & Sons: 2003.
31. Liu, Y.; Phenrat, T.; Lowry, G. V., Effect of TCE concentration and dissolved groundwater solutes on NZVI-Promoted TCE dechlorination and H-2 evolution. *Environmental Science & Technology* **2007**, *41*, (22), 7881-7887.
32. Farrell, J.; Kason, M.; Melitas, N.; Li, T., Investigation of the long-term performance of zero-valent iron for reductive dechlorination of trichloroethylene. *Environmental Science & Technology* **2000**, *34*, (3), 514-521.

33. Lien, H.-L.; Zhang, W.-X., Nanoscale Pd/Fe bimetallic particles: Catalytic effects of palladium on hydrodechlorination. *Applied Catalysis B-Environmental* **2007**, *77*, (1-2), 110-116.
34. Schrick, B.; Blough, J. L.; Jones, A. D.; Mallouk, T. E., Hydrodechlorination of trichloroethylene to hydrocarbons using bimetallic nickel-iron nanoparticles. *Chemistry of Materials* **2002**, *14*, (12), 5140-5147.
35. Chun, C. L.; Baer, D. R.; Matson, D. W.; Amonette, J. E.; Penn, R. L., Characterization and Reactivity of Iron Nanoparticles prepared with added Cu, Pd, and Ni. *Environmental Science & Technology* **2010**, *44*, (13), 5079-5085.
36. Han, Y.; Yan, W., Bimetallic nickel–iron nanoparticles for groundwater decontamination: Effect of groundwater constituents on surface deactivation. *Water Research* **2014**, *66*, (0), 149-159.
37. Han, Y.; Liu, C.; Horita, J.; Yan, W., Trichloroethene hydrodechlorination by Pd-Fe bimetallic nanoparticles: Solute-induced catalyst deactivation analyzed by carbon isotope fractionation. *Applied Catalysis B: Environmental* **2016**, *188*, 77-86.
38. Chaplin, B. P.; Roundy, E.; Guy, K. A.; Shapley, J. R.; Werth, C. J., Effects of natural water ions and humic acid on catalytic nitrate reduction kinetics using an alumina supported Pd-Cu catalyst. *Environmental Science & Technology* **2006**, *40*, (9), 3075-3081.
39. Lim, T.-T.; Zhu, B.-W., Effects of anions on the kinetics and reactivity of nanoscale Pd/Fe in trichlorobenzene dechlorination. *Chemosphere* **2008**, *73*, (9), 1471-1477.
40. Xu, Y.; Zhang, W. X., Subcolloidal Fe/Ag particles for reductive dehalogenation of chlorinated benzenes. *Industrial & Engineering Chemistry Research* **2000**, *39*, (7), 2238-2244.
41. Kim, E.-J.; Kim, J.-H.; Azad, A.-M.; Chang, Y.-S., Facile Synthesis and Characterization of Fe/FeS Nanoparticles for Environmental Applications. *Acs Applied Materials & Interfaces* **2011**, *3*, (5), 1457-1462.
42. Kim, E.-J.; Murugesan, K.; Kim, J.-H.; Tratnyek, P. G.; Chang, Y.-S., Remediation of Trichloroethylene by FeS-Coated Iron Nanoparticles in Simulated and Real Groundwater: Effects of Water Chemistry. *Industrial & Engineering Chemistry Research* **2013**, *52*, (27), 9343-9350.
43. Kim, E.-J.; Kim, J.-H.; Chang, Y.-S.; Turcio-Ortega, D.; Tratnyek, P. G., Effects of Metal Ions on the Reactivity and Corrosion Electrochemistry of Fe/FeS Nanoparticles. *Environmental Science & Technology* **2014**, *48*, (7), 4002-4011.
44. Rajajayavel, S. R. C.; Ghoshal, S., Enhanced reductive dechlorination of trichloroethylene by sulfided nanoscale zerovalent iron. *Water Research* **2015**, *78*, 144-153.
45. Yaws, C. L., Yaws' Handbook of Thermodynamic and Physical Properties of Chemical Compounds. In Knovel.

46. Williams, M. L., CRC Handbook of Chemistry and Physics, 76th edition. *Occupational and Environmental Medicine* **1996**, *53*, (7), 504-504.
47. Liu, Y. Q.; Majetich, S. A.; Tilton, R. D.; Sholl, D. S.; Lowry, G. V., TCE dechlorination rates, pathways, and efficiency of nanoscale iron particles with different properties. *Environmental Science & Technology* **2005**, *39*, (5), 1338-1345.
48. Elsner, M.; Chartrand, M.; Vanstone, N.; Couloume, G. L.; Lollar, B. S., Identifying abiotic chlorinated ethene degradation: Characteristic isotope patterns in reaction products with nanoscale zero-valent iron. *Environmental Science & Technology* **2008**, *42*, (16), 5963-5970.
49. Arnold, W. A.; Roberts, A. L., Pathways of Chlorinated Ethylene and Chlorinated Acetylene Reaction with Zn(0). *Environmental Science & Technology* **1998**, *32*, (19), 3017-3025.
50. Lesage, S.; Brown, S.; Millar, K., A Different Mechanism for the Reductive Dechlorination of Chlorinated Ethenes: Kinetic and Spectroscopic Evidence. *Environmental Science & Technology* **1998**, *32*, (15), 2264-2272.
51. Glod, G.; Brodmann, U.; Angst, W.; Holliger, C.; Schwarzenbach, R. P., Cobalamin-Mediated Reduction of cis- and trans-Dichloroethene, 1,1-Dichloroethene, and Vinyl Chloride in Homogeneous Aqueous Solution: Reaction Kinetics and Mechanistic Considerations. *Environmental Science & Technology* **1997**, *31*, (11), 3154-3160.
52. Stang, P. J., Unsaturated carbenes. *Chemical Reviews* **1978**, *78*, (4), 383-405.
53. Roberts, A. L.; Totten, L. A.; Arnold, W. A.; Burris, D. R.; Campbell, T. J., Reductive elimination of chlorinated ethylenes by zero valent metals. *Environmental Science & Technology* **1996**, *30*, (8), 2654-2659.
54. Song, H.; Carraway, E. R., Catalytic hydrodechlorination of chlorinated ethenes by nanoscale zero-valent iron. *Applied Catalysis B-Environmental* **2008**, *78*, (1-2), 53-60.
55. Song, H.; Carraway, E. R., Reduction of chlorinated ethanes by nanosized zero-valent iron: kinetics, pathways, and effects of reaction conditions. *Environmental science & technology* **2005**, *39*, (16), 6237-6245.
56. Ebert, M.; Köber, R.; Parbs, A.; Plagertz, V.; Schäfer, D.; Dahmke, A., Assessing Degradation Rates of Chlorinated Ethylenes in Column Experiments with Commercial Iron Materials Used in Permeable Reactive Barriers. *Environmental Science & Technology* **2006**, *40*, (6), 2004-2010.
57. Arena, F.; Barbera, K.; Italiano, G.; Bonura, G.; Spadaro, L.; Frusteri, F., Synthesis, characterization and activity pattern of Cu-ZnO/ZrO₂ catalysts in the hydrogenation of carbon dioxide to methanol. *Journal of Catalysis* **2007**, *249*, (2), 185-194.

58. Zheng, Z.; Yuan, S.; Liu, Y.; Lu, X.; Wan, J.; Wu, X.; Chen, J., Reductive dechlorination of hexachlorobenzene by Cu/Fe bimetal in the presence of nonionic surfactant. *Journal of Hazardous Materials* **2009**, *170*, (2–3), 895-901.
59. Wang, W.; Wang, S.; Ma, X.; Gong, J., Recent advances in catalytic hydrogenation of carbon dioxide. *Chemical Society Reviews* **2011**, *40*, (7), 3703-3727.
60. Alejandre, A.; Medina, F.; Salagre, P.; Fabregat, A.; Sueiras, J. E., Characterization and activity of copper and nickel catalysts for the oxidation of phenol aqueous solutions. *Applied Catalysis B: Environmental* **1998**, *18*, (3), 307-315.
61. Twigg, M. V.; Spencer, M. S., Deactivation of supported copper metal catalysts for hydrogenation reactions. *Applied Catalysis A: General* **2001**, *212*, (1), 161-174.
62. Chaplin, B. P.; Roundy, E.; Guy, K. A.; Shapley, J. R.; Werth, C. J., Effects of Natural Water Ions and Humic Acid on Catalytic Nitrate Reduction Kinetics Using an Alumina Supported Pd–Cu Catalyst. *Environmental Science & Technology* **2006**, *40*, (9), 3075-3081.
63. Chaplin, B. P.; Shapley, J. R.; Werth, C. J., Regeneration of sulfur-fouled bimetallic Pd-based catalysts. *Environmental science & technology* **2007**, *41*, (15), 5491-5497.
64. Chen, H.-Y.; Lo, S.-L.; Ou, H.-H., Catalytic hydrogenation of nitrate on Cu–Pd supported on titanate nanotube and the experiment after aging, sulfide fouling and regeneration procedures. *Applied Catalysis B: Environmental* **2013**, *142*, 65-71.

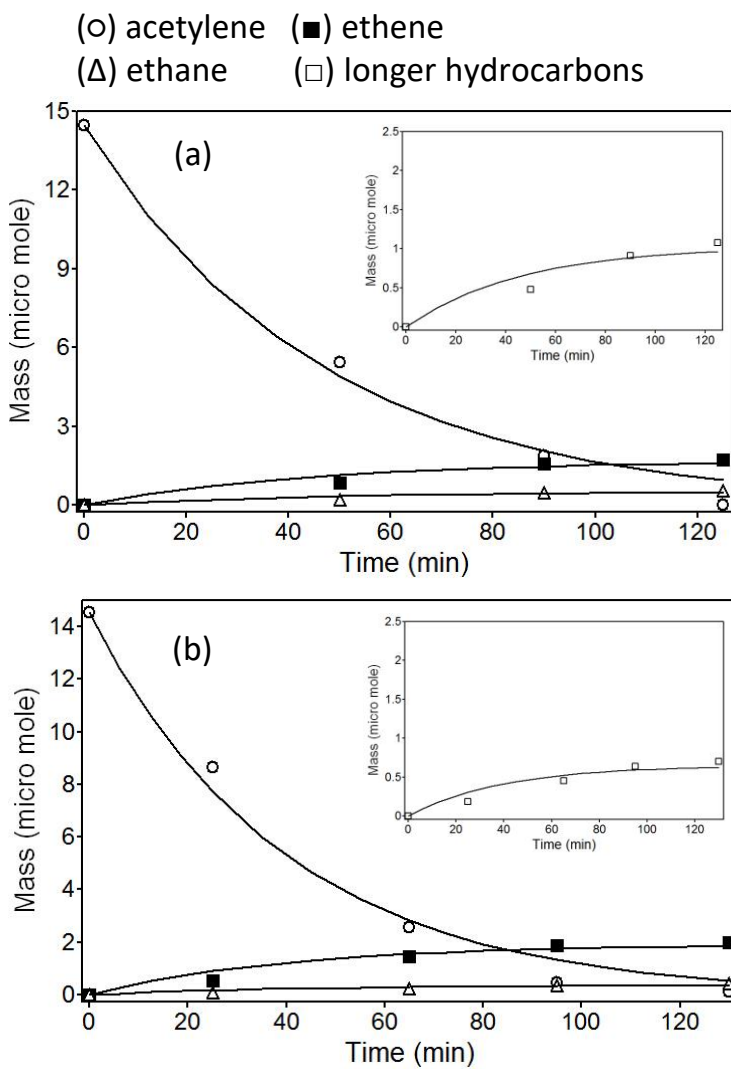


Figure 7.1. Acetylene hydrogenation by (a) nZVI, and (b) S-nZVI. Sulfidation was conducted at an S/Fe mole ratio of 0.05. Inserted shows the formation of longer hydrocarbons (sum of mole of C3, C4, C5 and C6 species detected in the reactor in terms of C2 mass balance). Initial mass of acetylene was 14 μmol . Nanoparticles dose was at 5 g/L for two batches. Initial pH was between 7.8-8.1.

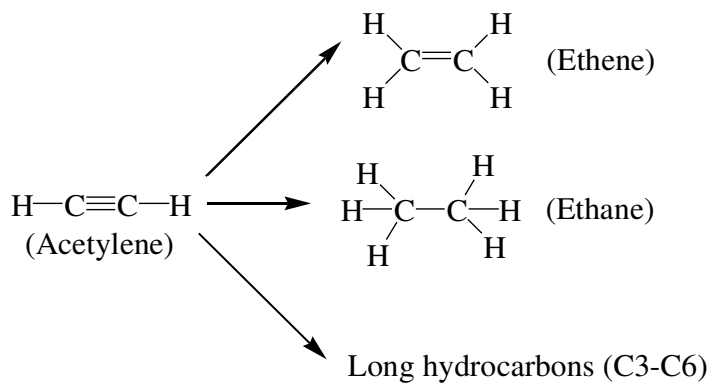


Figure 7.2. Proposed acetylene hydrogenation pathways mediated by nZVI and S-nZVI. Longer hydrocarbons represent the sum of mole of C3, C4, C5 and C6 species detected in the reactor in terms of C2 mass balance.

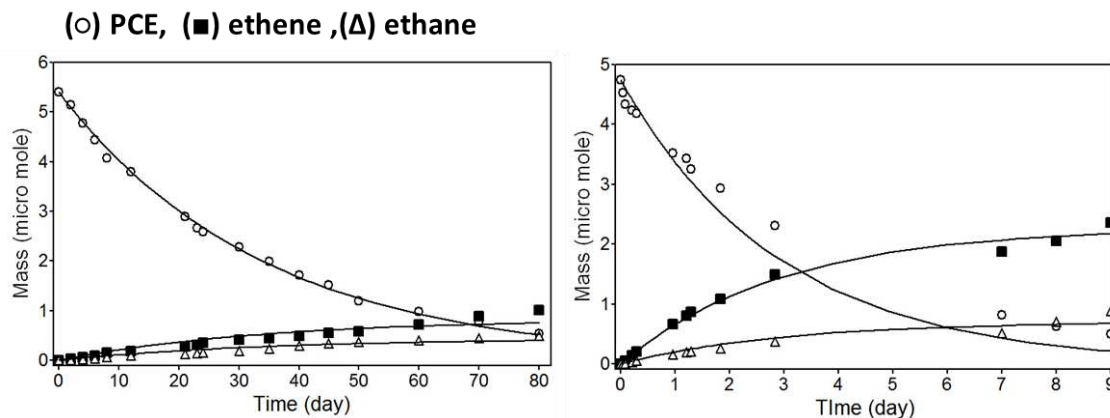


Figure 7.3. PCE dechlorination by (a) nZVI, and (b) S-nZVI (S/Fe mole ratio at 0.05). Nanoparticles dose was at 5 g/L for each reaction batch. Initial pH was between 7.8-8.1.

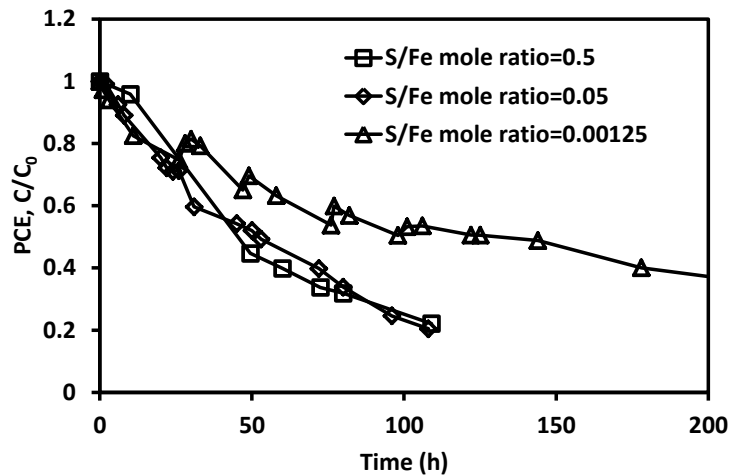


Figure 7.4. PCE dechlorination by S-nZVI synthesized at different S/Fe mole ratios. Initial PCE mass was around 6 μmol for each batch. Nanoparticles dose was at 5 g/L. Initial pH was between 7.8-8.1.

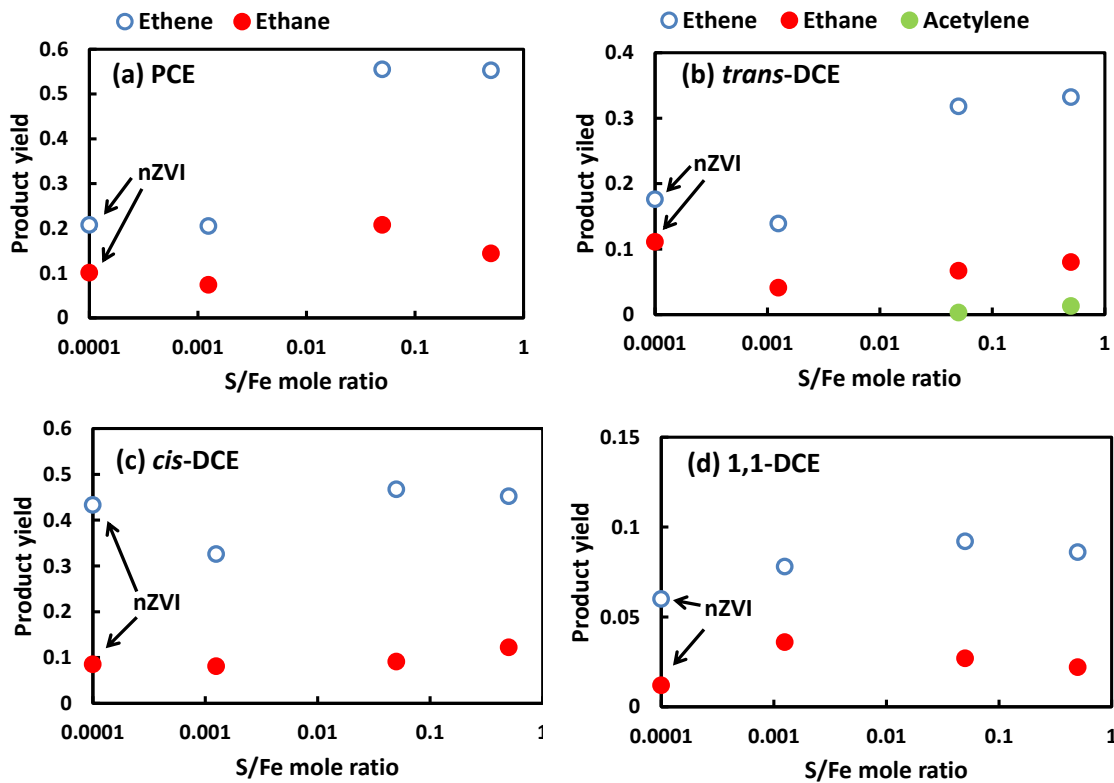


Figure 7.5. Yields of ethene and ethane upon dechlorination of different chlorinated ethenes by S-nZVI prepared at varied S/Fe mole ratios. Products yields were determined when 90% of the parent compounds were consumed in the reaction system. Dose of particles was 5 g/L for each reaction batch. Initial pH was between 7.8-8.1.

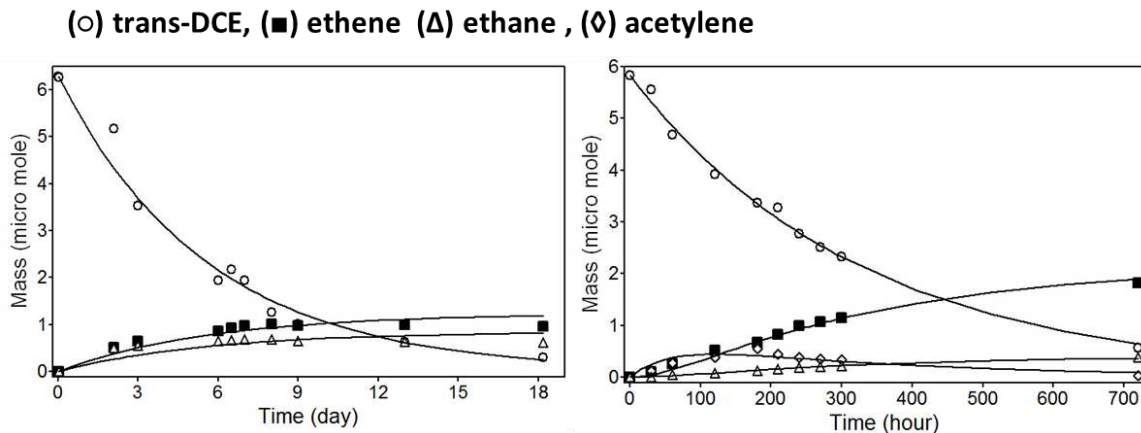


Figure 7.6. *trans*-DCE dechlorination by (a) nZVI, and (b) S-nZVI (S/Fe mole ratio at 0.05). Initial *trans*-DCE mass was 6 μmol . Dose of particles was at 5 g/L. Initial pH was between 7.8-8.1.

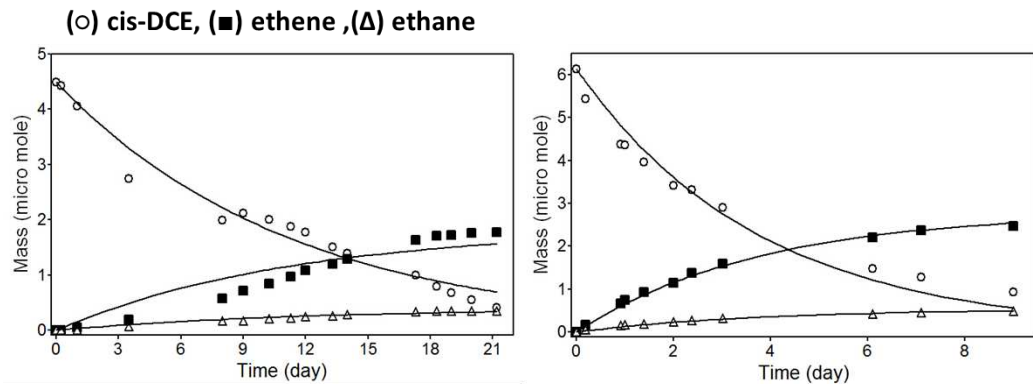


Figure 7.7. *cis*-DCE dechlorination by (a) nZVI and (b) S-nZVI (S/Fe mole ratio at 0.05). Dose of particles was at 5 g/L. Initial pH was between 7.8-8.1.

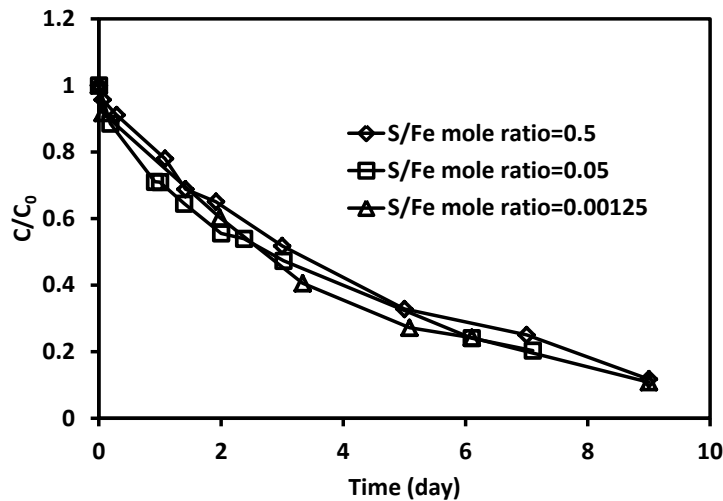


Figure 7.8. Degradation of *cis*-DCE by S-nZVI synthesized at different S/Fe mole ratios. Initial *cis*-DCE mass was 6 μmol . Dose of particles was at 5 g/L. Initial pH was between 7.8-8.1.

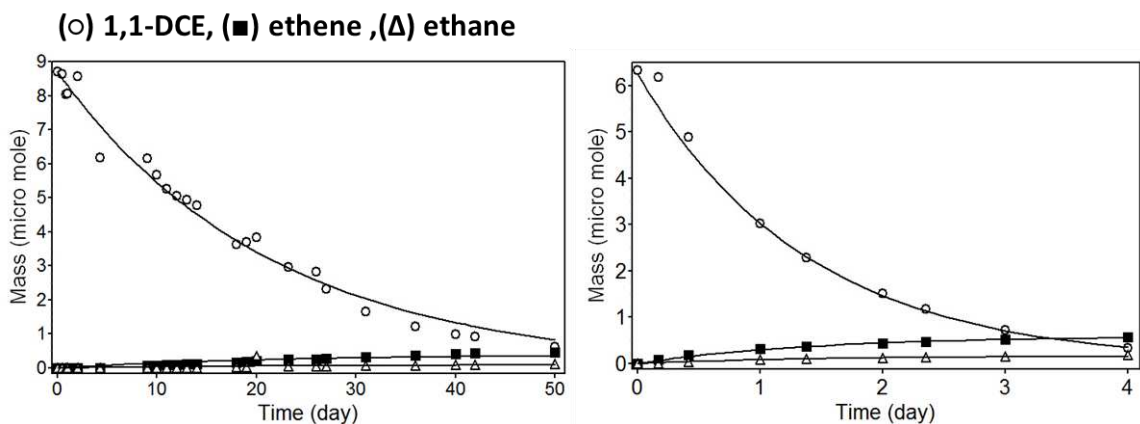


Figure 7.9. 1,1-DCE dechlorination by (a) nZVI and (b) S-nZVI (S/Fe mole ratio at 0.05). Dose of particles was at 5 g/L. Initial pH was between 7.8-8.1.

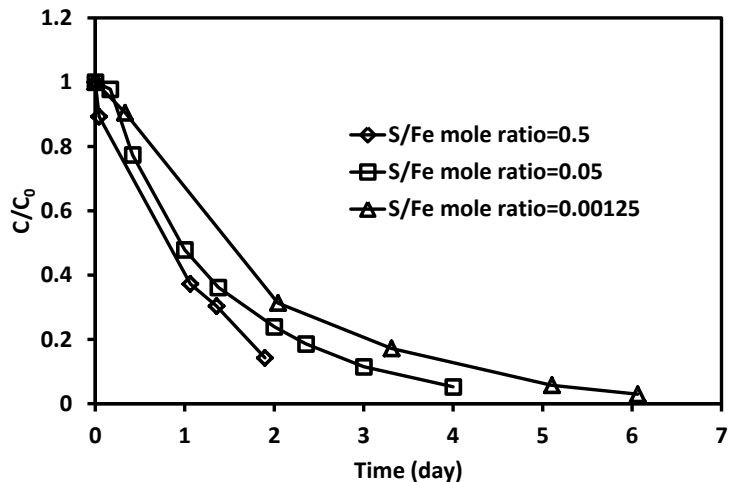


Figure 7.10. 1,1-DCE by S-nZVI synthesized at different S/Fe mole ratios. Dose of particles was at 5 g/L. Initial pH was between 7.8-8.1.

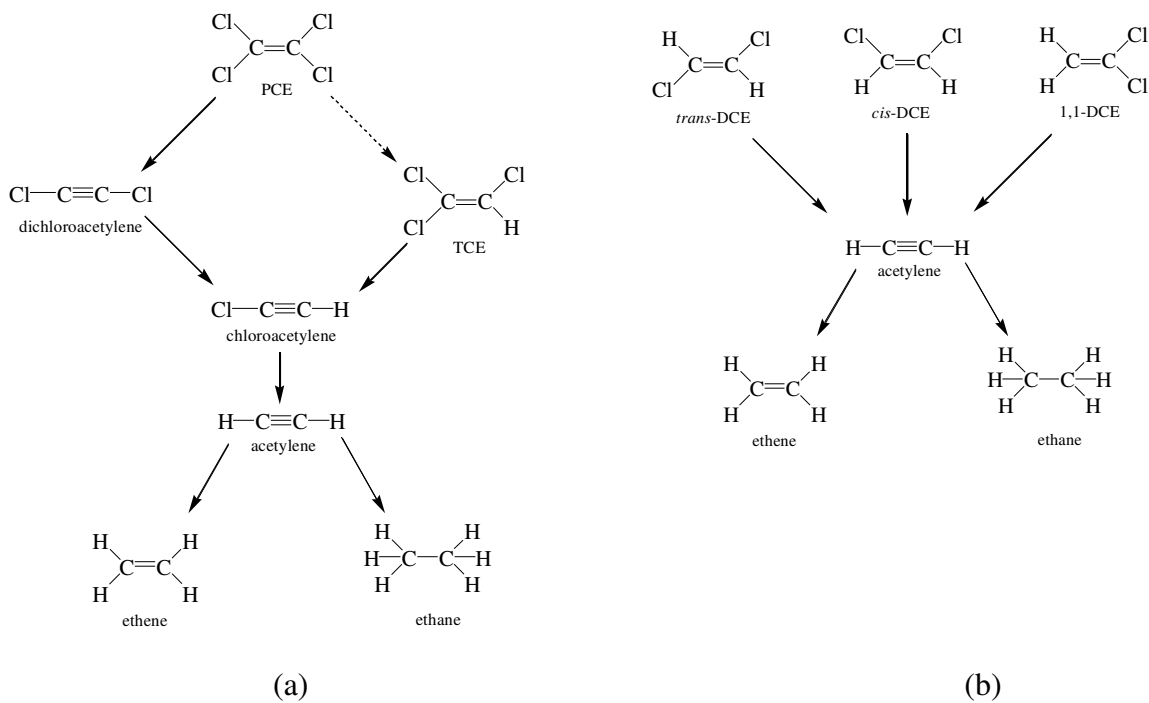


Figure 7.11. Proposed reduction pathways of chlorinated ethene by nZVI and S-nZVI. For PCE reduction, because only minor quantity of TCE was formed, so a dash arrow was used to indicate TCE formation was only a minor pathway.

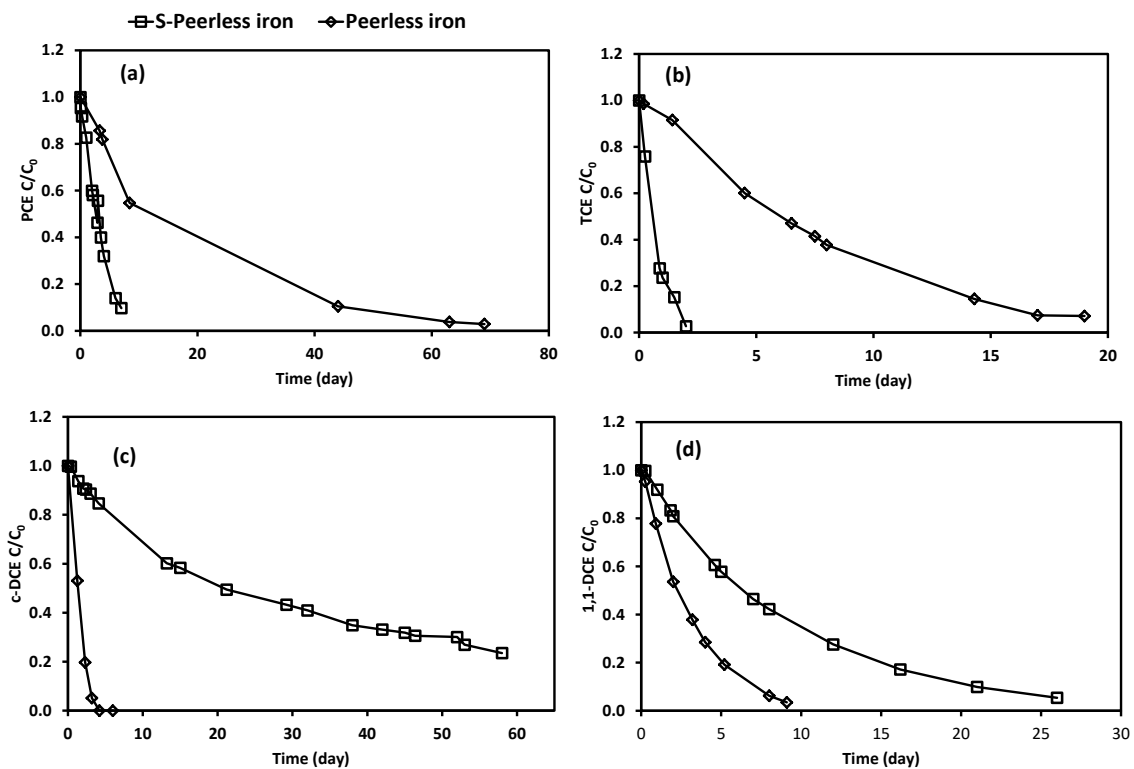


Figure 7.12. Reduction of chlorinated ethenes by S-PeerlessTM iron and PeerlessTM iron after acid-wash treatment. (a) PCE, (b) TCE, (c) cis-DCE and (d) 1,1-DCE. Iron dose was at 10 g/L for all batches. Initial pH was between 7.8-8.1.

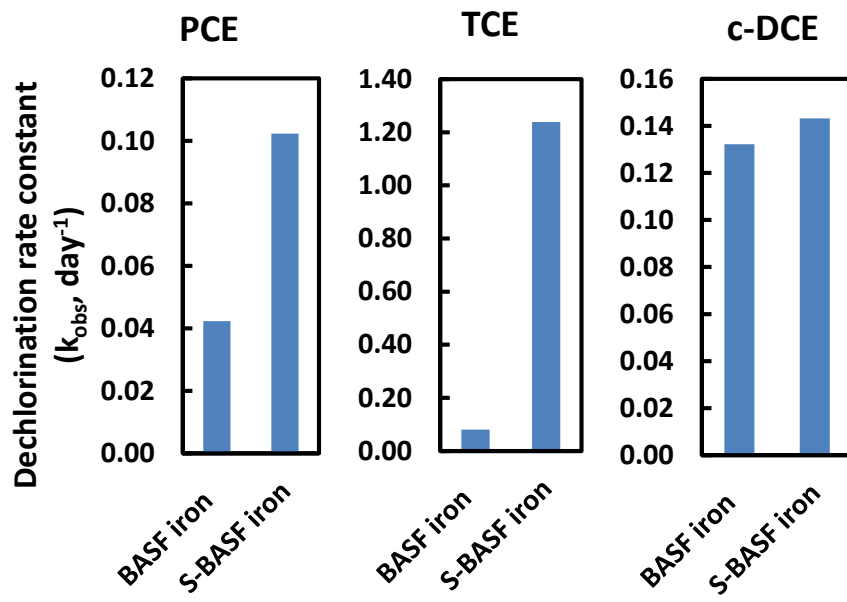


Figure 7.13. Rate constants of PCE, TCE and cis-DCE dechlorination by S-BASFTM iron and BASFTM iron pre-washed by HCl. The rate constant was calculated based on a pseudo-first-order kinetic model. Mass of initial PCE, TCE and cis-DCE were 6 μ mol. Iron dose was 10 g/L. Initial pH was between 7.8-8.1

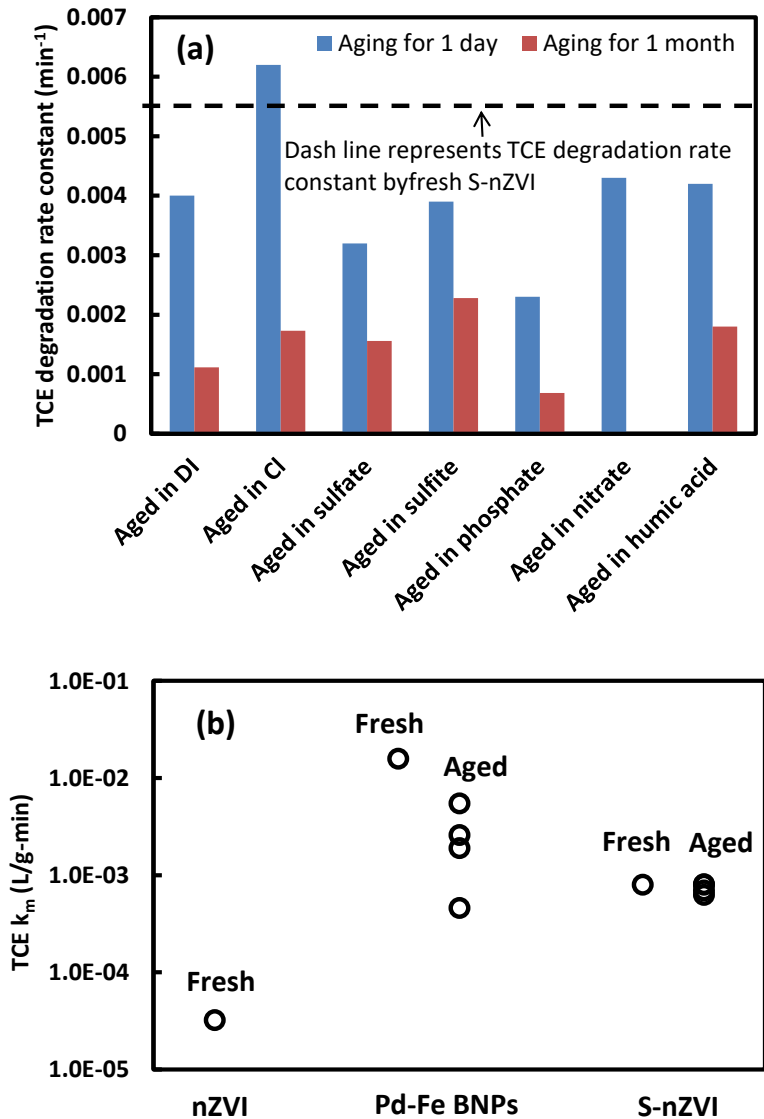


Figure 7.14. (a) TCE dechlorination rate constant by S-nZVI aged for 1 day and 1 month in aqueous solutions containing different groundwater solutes. (b) Comparison of aqueous aging effect on nZVI, S-nZVI, and Pd-Fe BNPs. The pH of aging solution and TCE solution was between 7.8-8.1. nZVI and S-nZVI particles dose was at 5 g/L, whereas Pd-Fe BNPs were used at 2 g/L.

Table 7.1. Pseudo-first-order rate constants, products yield, and C2 mass recoveries for chlorinated ethenes by nZVI and S-nZVI (S/Fe mole ratio at 0.05)

Materials	Contaminants	Products	Yield (%) ^a	C2 Mass recovery (%) ^b	k_{obs} (10^{-3} min $^{-1}$) ^c	R^2 ^d
nZVI	PCE	Ethene	20.8	42.3	0.020	0.9979
		Ethane	10.1			
		Acetylene	0.0			
		C3-C6	4.9			
S-nZVI	PCE	Ethene	55.5	85.2	0.182	0.9525
		Ethane	20.8			
		Acetylene	0.0			
		C3-C6	7.2			
nZVI	TCE	Ethene	17.2	36.0	0.073	0.9848
		Ethane	6.5			
		Acetylene	0.0			
		C3-C6	5.7			
S-nZVI	TCE	Ethene	42.7	68.5	5.400	0.9918
		Ethane	10.1			
		Acetylene	5.7			
		C3-C6	7.0			
nZVI	t-DCE	Ethene	17.6	39.7	0.122	0.9803
		Ethane	11.1			
		Acetylene	0.0			
		C3-C6	4.2			
S-nZVI	t-DCE	Ethene	34.6	49.8	3.000	0.9982
		Ethane	7.3			
		Acetylene	0.4			
		C3-C6	1.9			
nZVI	c-DCE	Ethene	43.3	62.5	0.066	0.9474
		Ethane	8.5			
		Acetylene	0.0			
		C3-C6	6.9			
S-nZVI	c-DCE	Ethene	46.7	64.4	0.173	0.9795
		Ethane	9.1			
		Acetylene	0.0			
		C3-C6	4.3			
nZVI	1,1-DCE	Ethene	6.0	18.0	0.035	0.9812
		Ethane	1.2			
		Acetylene	0.0			
		C3-C6	1.1			
S-nZVI	1,1-DCE	Ethene	9.2	24.3	0.505	0.9981
		Ethane	2.7			
		Acetylene	0.0			
		C3-C6	2.6			

^a Product yield calculated when 10% of chlorinated ethenes left in the reactor. ^b Mass balance in terms of C2 mass (i.e., 1.5 mol of TCE = 1 mole C_3H_8 , 2 mol of TCE = 1 mole C_4H_{10}). ^c Pseudo first-order rate constant. ^d R^2 value of linear relationship based on pseudo-first-order kinetic model

Table 7.2. Pseudo-first-order rate constants, products yields, and C2 mass recoveries for chlorinated ethenes by S-nZVI sulfided at different S/Fe mole ratios

Materials	Contaminants	Products	Yield (%) ^a	C2 Mass recovery (%) ^b	$k_{\text{obs}} (10^{-3} \text{ min}^{-1})^c$	R^2 ^d
S-nZVI (S/Fe mole ratio at 0.5)	PCE	Ethene	55.3	77.2	0.663	0.9926
		Ethane	14.4			
		Acetylene	0.0			
		C3-C6	5.1			
S-nZVI (S/Fe mole ratio at 0.00125)	PCE	Ethene	20.5	38.2	N.A.	N.A.
		Ethane	7.4			
		Acetylene	0.0			
		C3-C6	5.1			
S-nZVI (S/Fe mole ratio at 0.5)	t-DCE	Ethene	40.2	54.2	3.122	0.9818
		Ethane	10.2			
		Acetylene	4.2			
		C3-C6	5.5			
S-nZVI (S/Fe mole ratio at 0.00125)	t-DCE	Ethene	11.3	26.2	2.430	0.9903
		Ethane	3.2			
		Acetylene	0.0			
		C3-C6	4.2			
S-nZVI (S/Fe mole ratio at 0.5)	c-DCE	Ethene	45.2	70.9	0.155	0.9876
		Ethane	12.2			
		Acetylene	0.0			
		C3-C6	9.6			
S-nZVI (S/Fe mole ratio at 0.00125)	c-DCE	Ethene	32.6	51.8	0.171	0.9943
		Ethane	8.1			
		Acetylene	0.0			
		C3-C6	5.2			
S-nZVI (S/Fe mole ratio at 0.5)	1,1-DCE	Ethene	8.6	20.4	0.597	0.9898
		Ethane	2.2			
		Acetylene	0.0			
		C3-C6	1.9			
S-nZVI (S/Fe mole ratio at 0.00125)	1,1-DCE	Ethene	7.8	21.2	0.396	0.9963
		Ethane	3.6			
		Acetylene	0.0			
		C3-C6	1.7			

^a Product yield calculated when 10% of chlorinated ethenes left in the reactor. ^bMass balance in terms of C2 mass (*i.e.*, 1.5 mol of TCE = 1 mole C_3H_8 , 2 mol of TCE = 1 mole C_4H_{10}). ^c Pesudo first-order rate constant. ^d R^2 value of linear relationship based on pesudo-first-order kinetic model. PCE reduction by S-Peerless iron (S/Fe mole ratio at 0.00125) fails to yield satisfactory pesudo-first-order linear fit.

Table 7.3. Pseudo-first-order rate constants, products yield, and C2 mass recoveries for chlorinated ethenes by Peerless™ iron and S-Peerless™ iron

Materials	Contaminants	Products	Yield (%) ^a	C2 Mass recovery (%) ^b	k_{obs} (day ⁻¹) ^c	R^2 ^d
Peerless iron	PCE	Ethene	37.5	90.7	0.0517	0.9979
		Ethane	33.6			
		Acetylene	0.0			
		C3-C6	17.6			
S-Peerless iron	PCE	Ethene	6.4	94.5	0.3054	0.9525
		Ethane	1.7			
		Acetylene	72.1			
		C3-C6	13.7			
Peerless iron	TCE	Ethene	54.9	89.3	0.1267	0.9873
		Ethane	16.2			
		Acetylene	0.0			
		C3-C6	17.3			
S-Peerless iron	TCE	Ethene	5.7	68.5	1.5667	0.9435
		Ethane	1.4			
		Acetylene	82.3			
		C3-C6	10.0			
Peerless iron	t-DCE	Ethene	19.7	53.8	0.3895	0.998
		Ethane	6.7			
		Acetylene	0.0			
		C3-C6	22.0			
S-Peerless iron	t-DCE	Ethene	16.4	66.3	0.3964	0.9986
		Ethane	4.8			
		Acetylene	35.3			
		C3-C6	5.6			
Peerless iron	c-DCE	Ethene	68.3	99.7	N.A.	N.A.
		Ethane	14.3			
		Acetylene	0.0			
		C3-C6	17.1			
S-Peerless iron	c-DCE	Ethene	50.0	72.8	0.0261	0.9819
		Ethane	9.7			
		Acetylene	2.9			
		C3-C6	7.1			
Peerless iron	1,1-DCE	Ethene	11.3	25.8	0.3464	0.9901
		Ethane	3.4			
		Acetylene	0.0			
		C3-C6	5.7			
S-Peerless iron	1,1-DCE	Ethene	9.5	20.0	0.1104	0.9993
		Ethane	0.8			
		Acetylene	0.0			
		C3-C6	0.9			

^a Product yield calculated when 10% of chlorinated ethenes left in the reactor. ^b Mass balance in terms of C2 mass (i.e., 1.5 mol of TCE = 1 mole C_3H_8 , 2 mol of TCE = 1 mole C_4H_{10}). ^c Pseudo first-order rate constant. ^d R^2 value of linear relationship based on pseudo-first-order kinetic model. cis-DCE reduction of Peerless iron fails to yield satisfactory pseudo-first-order linear fit.

7.5 Supporting information

Cu-nZVI synthesis method:

Nanoscale zero-valent iron (nZVI) particles were synthesized via borohydride reduction of an aqueous solution of ferric ions. Briefly, 10.8 g of FeCl₃·6H₂O (Fisher) were dissolved in a 500-mL solution mixture of distilled de-ionized (DDI) water and ethanol (1:1, v/v). 500 mL of 0.4 M NaBH₄ solution (Acros Organics) was introduced to the ferric solution at approximately 17 mL/min under a vigorous mixing condition, during which the ferric solution turned black due to the formation of colloidal-sized iron particles. The particles formed were collected by vacuum filtration and were stored in ethanol for further use. Cu-nZVI particles were prepared by immersing the freshly prepared nZVI with an ethanol/water (1:1, v/v) solution of copper chloride (Acros Organics) and ultrasonication of the mixture for 5 min. The mass loading of Cu with respect to iron was fixed at 2% for all Pd-Fe BNPs. DDI water used in all procedures, including particle synthesis, aging and TCE experiments, was deoxygenated by purging with N₂ for 30 min.

Cu-S-nZVI synthesis method

S-nZVI was first obtained according to the synthesis method described in Section 7.2.2. S-nZVI particles were collected by vacuum filtration and were stored in ethanol for further use. Cu-S-nZVI particles were prepared by immersing the freshly prepared S-nZVI with an ethanol/water (1:1, v/v) solution of copper chloride (Acros Organics) and ultrasonication of the mixture for 5 min. The mass loading of Cu with respect to iron was fixed at 2% for all Pd-Fe BNPs. DDI water used in all procedures, including particle synthesis, aging and TCE experiments, was deoxygenated by purging with N₂ for 30 min.

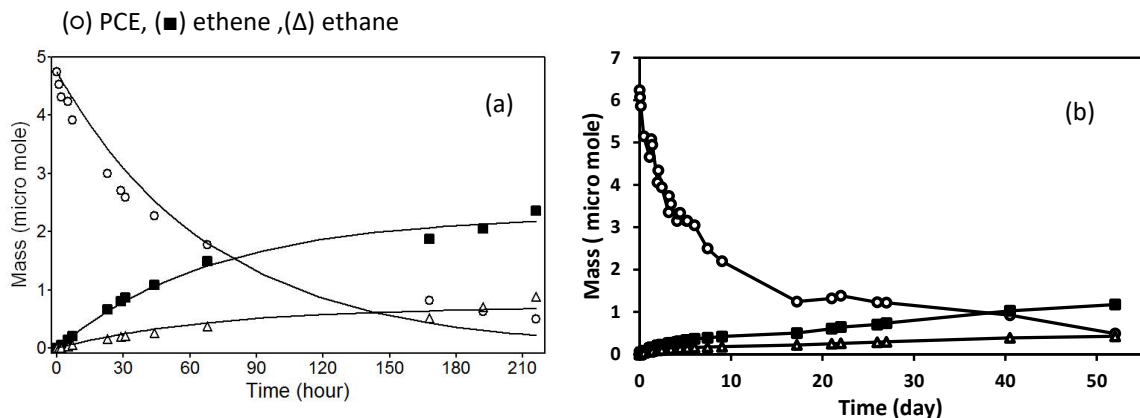


Figure S7.1. PCE dechlorination by S-nZVI prepared at an S/Fe ratio at (a) 0.5, and (b) 0.00125, respectively. Nanoparticle dose was 5 g/L. Initial pH was between 7.8-8.1. For (b), PCE dechlorination and major products formation could not be fitted well with the kinetic model.

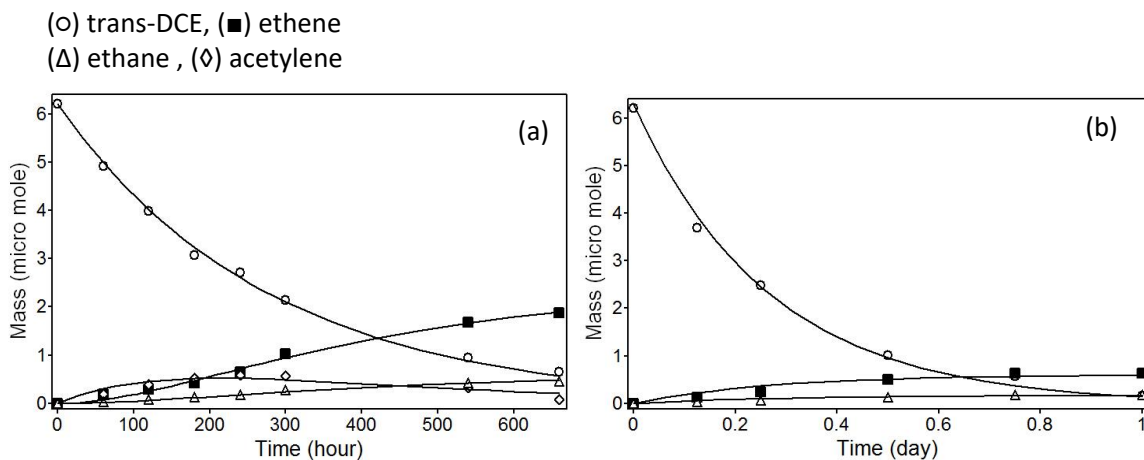


Figure S7.2. *trans*-DCE dechlorination by S-nZVI prepared at an S/Fe ratio at (a) 0.5, and (b) 0.00125, respectively. Nanoparticle dose was 5 g/L. Initial pH was between 7.8-8.1.

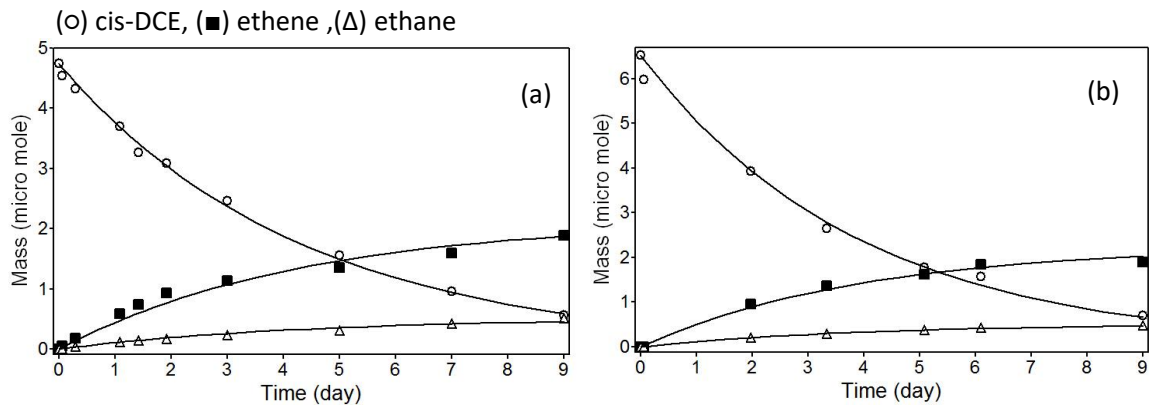


Figure S7.3. *cis*-DCE dechlorination by S-nZVI prepared at an S/Fe ratio at (a) 0.5, and (b) 0.00125, respectively. Nanoparticle dose was 5 g/L. Initial pH was between 7.8-8.1.

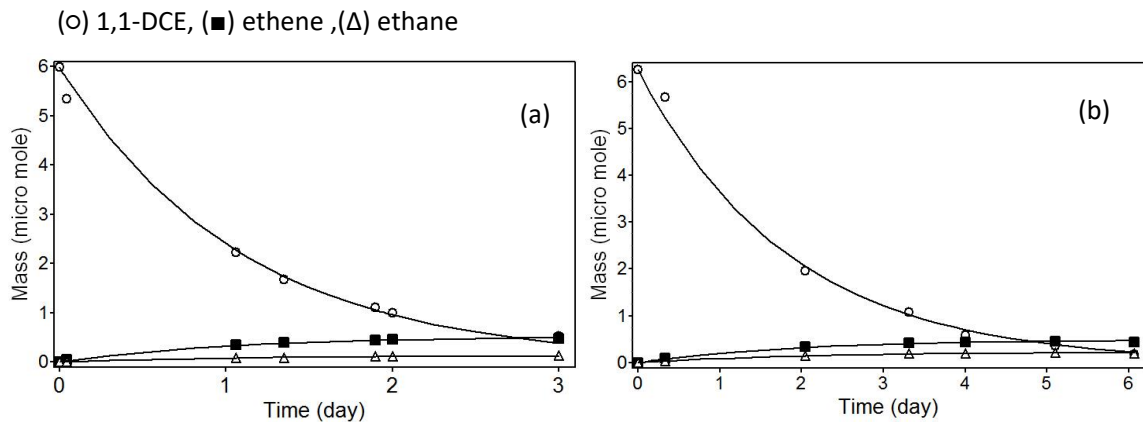


Figure S7.4. 1,1-DCE dechlorination by S-nZVI prepared at an S/Fe ratio at (a) 0.5, and (b) 0.00125, respectively. Nanoparticle dose was 5 g/L. Initial pH was between 7.8-8.1.

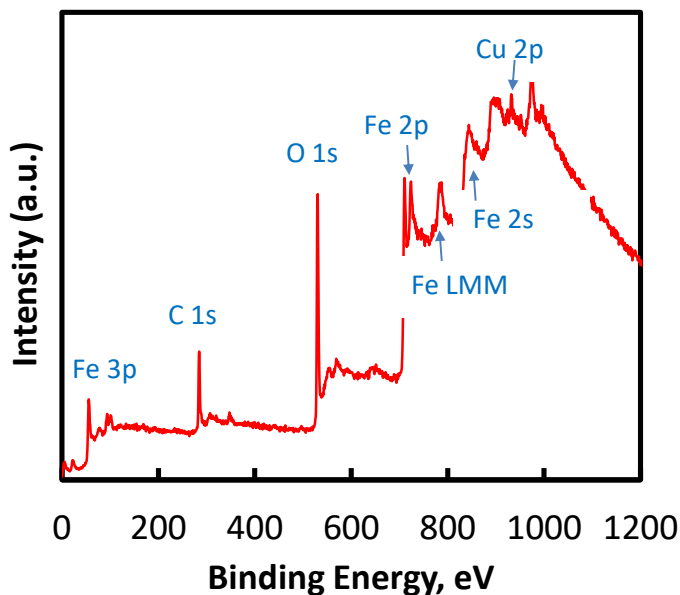


Figure S7.5. XPS survey spectrum of as-received PeerlessTM Fe.

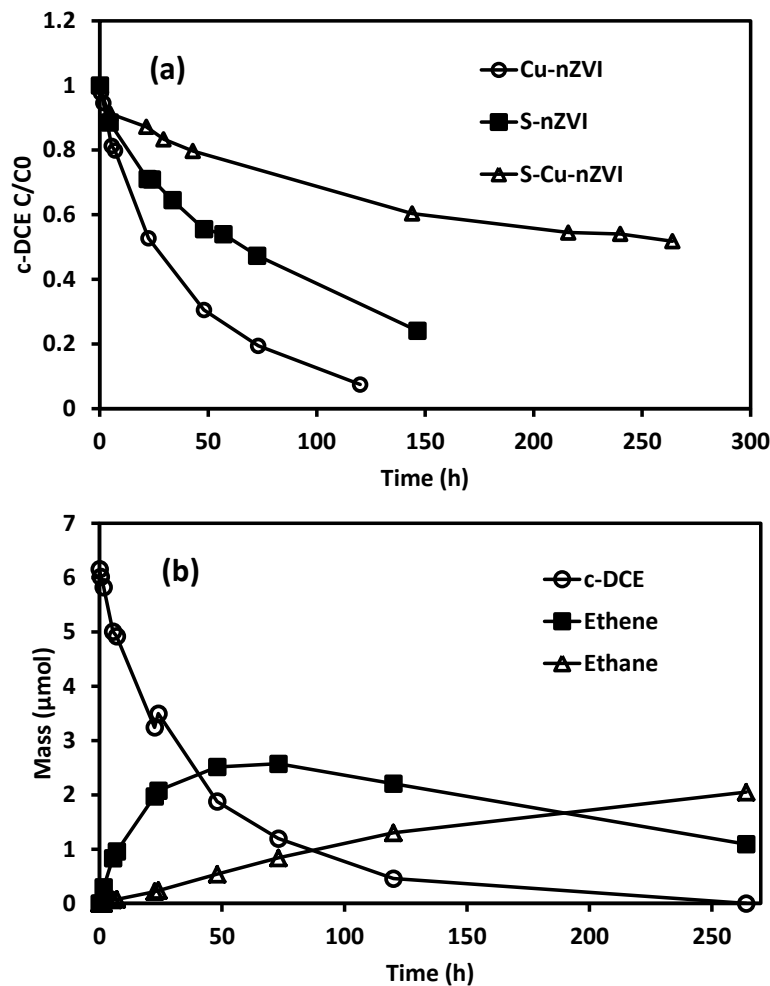


Figure S7.6. (a) Reduction of *cis*-DCE by Cu-nZVI, S-nZVI and S-Cu-nZVI, and (b) products formation during *cis*-DCE dechlorination by Cu-nZVI. Mass of *cis*-DCE was 6 μmol. Nanoparticles dose was at 5 g/L. Initial pH was between 7.8-8.

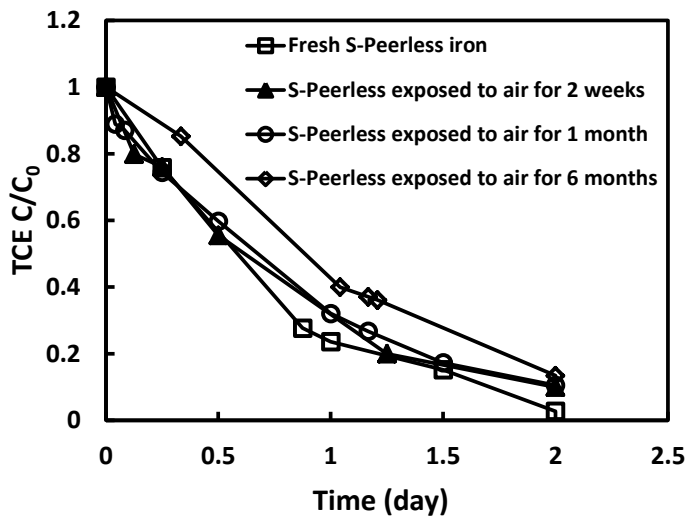


Figure S7.7. TCE dechlorination by S-PeerlessTM iron exposed to air for different amount of time. Particles dose was at 10 g/L. Initial pH was between 7.8-8.1.

Table S7.1. Elemental composition of BASFTM iron powder^a

Composition of BASF CIP CC iron powder	Content (%)
Fe	>97.8
C	<0.75-0.90
N	<0.65-0.90
O	<0.15-0.40

^aValue provided by BASF

Table S7.2. Pseudo-first-order rate constants of TCE degradation rate constant of S-nZVI (S/Fe mole ratio at 0.05) aged in aqueous for 1 day and for 1 month, respectively

Materials	$k_{\text{obs}} (\text{min}^{-1})$ aged for 1 day	$k_{\text{obs}} (\text{min}^{-1})$ aged for 1 month
S-nZVI (S/Fe mole ratio at 0.05) aged in 5 mM Cl ⁻	0.0043	0.0017
S-nZVI (S/Fe mole ratio at 0.05) aged in 5 mM NO ₃ ⁻	0.0043	N.A.
S-nZVI (S/Fe mole ratio at 0.05) aged in 5 mM DDI water	0.0040	0.0011
S-nZVI (S/Fe mole ratio at 0.05) aged in 5 mM SO ₃ ²⁻	0.0039	0.0023
S-nZVI (S/Fe mole ratio at 0.05) aged in 5 mM SO ₄ ²⁻	0.0032	0.0016
S-nZVI (S/Fe mole ratio at 0.05) aged in 5 mM phosphate	0.0023	0.0007
S-nZVI (S/Fe mole ratio at 0.05) aged in 20 mg/L humic acid	0.0042	0.0011

CHAPTER EIGHT

Conclusions and Future Research Recommendations

8.1 Conclusions

The overarching goal of this dissertation was to investigate the deactivation mechanisms of iron-based BNPs in groundwater media and develop reactive and sustainable iron-based materials for the remediation of chlorinated ethenes. The aqueous stability and deactivation of iron-based BNPs mechanisms were studied, and the reactivity and stability of a new type of ZVI material were investigated. The main findings and conclusions obtained are summarized as follows:

First, an optimized nZVI synthesis protocol was developed and two facile but sensitive methods were proposed to evaluate the nZVI reactivity. The established synthesis protocol suggests that, for the experiment setup employed in this lab, the most reactive nZVI could be obtained at a ferric chloride concentration of 0.08 M, a molar ratio of NaBH₄ to FeCl₃ of 5:1, a NaBH₄ feeding rate at 17 mL·min⁻¹ and a stirring speed of 650 rpm. Another important finding was that reduction of Cu(II) and nitrate could be used as probing reactions to evaluate the reactivity of nZVI. It was noted that the nitrate reduction method is effective only at a dilute concentration because a higher nitrate concentration could cause severe passivation of the iron surface.

Subsequently, the research was focused on iron-based bimetallic iron nanoparticles (BNPs) because of their superior reactivity compared to nZVI in simple aqueous systems, but there is limited knowledge on their performance in realistic groundwater matrices. The effects of common groundwater solutes on TCE reduction with Ni-Fe BNPs were investigated. Batch experiments involved pre-exposing the nanoparticles to various groundwater solutions for 24 h followed by reactions with TCE solution. The results suggest that the deactivation behavior of Ni-Fe BNPs differs significantly from that of the well-studied Pd-Fe BNPs. Specifically, Ni-Fe BNPs were chemically stable in pure water. Mild decreases in TCE reaction rates were observed for

Ni–Fe BNPs pre-exposed to chloride (Cl^-), bicarbonate (HCO_3^-), sulfite (SO_3^{2-}) and humic acid solutions. Nitrate (NO_3^-), sulfate (SO_4^{2-}) and phosphate (HPO_4^{2-}) may cause moderate to severe deactivation at elevated concentrations ($>1 \text{ mM}$). Product analysis and surface chemistry investigations using high-resolution X-ray photoelectron spectroscopy (HR-XPS) reveal that NO_3^- decreased particle reactivity mainly due to progressive formation of passivating oxides, whereas SO_4^{2-} and phosphate elicited rapid deactivation as a result of specific poisoning of the surface nickel sites. At similar levels, phosphate is the most potent deactivation agent among the solutes examined in this study. Compared to the Pd–Fe counterpart, Ni–Fe BNPs possess several notable strengths that include improved electrochemical stability in the aqueous environment and good chemical resistance to common solutes in groundwater such as chloride, bicarbonate, and dissolved organic matter. These attractive attributes suggest that Ni–Fe is a more viable material than the palladized iron materials for hydrodechlorination of chlorinated ethenes in groundwater remediation and wastewater decontamination applications.

To understand the mechanistic causes of solute-induced deactivation, carbon isotope fractionation analyses of TCE degradation by different types of Ni–Fe BNPs were conducted, and ε_{bulk} values of TCE degradation were found to be an useful indication of the catalytic activity of Ni sites on Ni–Fe BNPs. The analyses of carbon isotope fractionation of TCE and major daughter products including ethene and ethane suggest that TCE undergoes predominantly a dichloro-elimination pathway on Ni–Fe BNPs and is transformed to ethane via ethene and a surface intermediate. Taken together the carbon mass balance trend during TCE hydrodechlorination, a “dual pathways” kinetic model was proposed, in which a fraction of TCE is transformed into ethane via ethene and the remaining TCE is converted into ethane through surface reactions. Good fittings of experimentally measured TCE degradation and major product formation data to the model were obtained.

The mechanisms of Pd–Fe BNPs deactivation in the presence of different groundwater solutes were investigated based on the TCE degradation rates, the

distribution of daughter products, and stable carbon isotope fractionation measurements. Based on the apparent TCE degradation rates and at a constant solute concentration of 5 mM (except for humic acid, which was dosed at 20 mg/L), Pd-Fe BNPs exposed to SO_4^{2-} , HPO_4^{2-} , and humic acid solutions showed moderate declines in TCE dechlorination rates. Aging the bimetallic particles in Cl^- , SO_3^{2-} , HCO_3^- , and NO_3^- solutions, however, resulted in excessive or complete loss of TCE dechlorination reactivity. Analyses of the isotope fractionation associated with TCE hydrodechlorination ($\varepsilon_{\text{TCE HDC}}$) as well as the yield of ethane over other dechlorination products suggest at least four distinctive causes of deactivation: (i) aging the BNPs in deionized water and humic acid induces surface passivation due to buildup of mineral or organic carbon deposits; (ii) SO_3^{2-} and Cl^- ions interact specifically with Pd sites and disable the catalyst functions; (iii) NO_3^- and HCO_3^- inhibit iron corrosion, thereby limiting the production of H_2 as the precursor of reactive hydrogen species, and (iv) selective deactivation of surface sites involved in ethene hydrogenation was observed for BNPs aged in SO_4^{2-} and HPO_4^{2-} solutions. The findings suggest the Pd-on-Fe configuration of the bimetallic particles is susceptible to deactivation in a broader range of groundwater chemistry than previously expected.

The susceptibility of BNPs to passivation or catalyst poisoning calls for an alternate type of ZVI material that is more resistant to environmental passivation and at the same time, maintains good reactivity towards the target contaminants. In this regard, sulfided nZVI (S-nZVI) showed enhanced dechlorination effects for PCE, TCE and all DCE isomers. Furthermore, surface sulfidation treatment was also applied to two common types of commercial iron, and it was found that sulfidation of BASF iron powders could enhance their TCE and PCE dechlorination rates significantly, but reactivity with *cis*-DCE was not improved to an appreciable extent. Treatment of Peerless iron could enhance TCE and PCE degradation, but interestingly, inhibit *cis*-DCE and 1,1-DCE degradation. The latter observation is owing to the unique surface chemistry of Peerless iron containing a minute amount of cooper as surface impurity and also an adventitious catalyst. Sulfidation of Peerless iron likely results in the poisoning of the

surface Cu species. Importantly, aging experiments indicate that S-nZVI and S-Peerless iron both had good chemical stability in groundwater media and in the atmospheric environment compared to the bimetallic iron materials.

Taken together the above results, surface sulfidation treatment of nanoscale or bulk iron materials is particularly effective for enhancing the reactivity of iron towards TCE and PCE dechlorination. Considering the fact that TCE and PCE are widespread groundwater contaminants and they are the parent compounds of DCE isomers, these sulfided iron materials represent an alternative and effective form of ZVI materials for subsurface remediation of chlorinated contaminants. The proposed surface treatment method is simple and involves inexpensive chemical reagents, and the process can be readily scaled up for pilot or large-scale implementations. Aging experiments involving immersing S-nZVI in solutions containing common groundwater solutes or exposing S-Peerless iron to air clearly show that the iron materials after sulfidation process have remarkable stability to retain the dechlorination reactivity. The study also suggests for the first time that this facile surface treatment protocol can be extended to commercially available ZVI (e.g., Peerless iron and BASF iron) to achieve enhanced dechlorination performance. From a practical point of view, the observed good resistance against aqueous and atmospheric deactivation of various sulfided iron would save the use of sophisticated instruments or handling procedures during the production, transfer, and use of these reactive iron materials.

8.2 Future Research Recommendations

In order to advance the nZVI technology for subsurface remediation, two directions of further studies are proposed.

8.2.1 Interactions of nZVI with Microorganisms in the Subsurface Environment

The interactions of nZVI and iron-based bimetallic nanoparticles (BNPs) with common groundwater constituents (e.g., Cl^- , NO_3^- , and nature organic matters) have been intensively investigated ¹⁻³. Subsurface environments feature a relatively low level of dissolved oxygen (DO) compared to surface water and hosts various microorganisms,

such as denitrifying bacteria, sulfate-reducing bacteria and iron-reducing bacteria. Therefore, the interactions of nZVI with different microorganisms cannot be ignored when nZVI is used for subsurface remediation.

As indicated in the Chapter 6.1, the formation of passivation layer on nZVI is a serious technical limitation for field applications, and many efforts have been conducted to overcome this intrinsic drawback. The use of chemical reducing agent (e.g., dithionite ($S_2O_4^{2-}$)) has been demonstrated to be able to restore the reductive capacity of passivated nZVI, and the principle is that dithionite can reduce Fe(III) to ferrous iron Fe(II). The application of dithionite has been successfully applied to restore passivated iron phase to degrade trichloroethene (TCE) for *in situ* remediation⁴. Based on this principle, iron-reducing bacteria is able to reduce Fe(III) oxides under a reducing environment which might possibly restore the passivated nZVI. The interaction of nZVI in the subsurface with iron-reducing bacteria may help retain the nZVI reactivity and prolong the nZVI longevity.

Besides zero-valent iron materials, iron sulfides have been shown to degrade chlorinated ethenes⁵. Iron sulfides can participate under anaerobic conditions in natural environments and in engineered zero-valent iron systems designed for groundwater remediation in subsurface environment by sulfate-reducing bacteria. This research shows convincingly that an “FeS on Fe(0)” structure could enhance the degradation rates of chlorinated ethenes. In the subsurface and sediment environment, dissimilatory microbial SO_4^{2-} reduction is an active microbial activity with the formation of S^{2-} . S^{2-} can potentially react with Fe(0) and result in the formation of FeS. If FeS can be formed on nZVI surface, it may enhance its reactivity with chlorinated ethenes. Also, this SO_4^{2-} reduction can also potentially restore the reactivity of passivated nZVI as discussed in Chapter 6. In summary, it is of great interest to identify the specific biogeochemical conditions of the subsurface environment where the nZVI is located. Even though the groundwater anions could impair the nZVI longevity, the microbial activity may possibly restore the nZVI reactivity.

8.2.2 Target Delivery Study of S-nZVI

S-nZVI has shown its great reactivity for PCE and TCE degradation compared to the unamend nZVI, and good stability in the groundwater media compared to BNPs. The TEM study indicates that S-nZVI prepared using the “post-synthesis sulfidation” method has a similar structure as nZVI, and the particles tend to agglomerate together. Therefore, it is of interest to study the behavior of S-nZVI coated with polymers, and investigate the corresponding transport behavior of polymer coated S-nZVI through the porous media.

References

1. Liu, Y.; Phenrat, T.; Lowry, G. V., Effect of TCE concentration and dissolved groundwater solutes on NZVI-Promoted TCE dechlorination and H₂ evolution. *Environmental Science & Technology* **2007**, *41*, (22), 7881-7887.
2. Han, Y.; Yan, W., Bimetallic nickel–iron nanoparticles for groundwater decontamination: Effect of groundwater constituents on surface deactivation. *Water Research* **2014**, *66*, (0), 149-159.
3. Han, Y.; Liu, C.; Horita, J.; Yan, W., Trichloroethene hydrodechlorination by Pd-Fe bimetallic nanoparticles: Solute-induced catalyst deactivation analyzed by carbon isotope fractionation. *Applied Catalysis B: Environmental* **2016**, *188*, 77-86.
4. Szecsody, J. E.; Fruchter, J. S.; Williams, M. D.; Vermeul, V. R.; Sklarew, D., In situ chemical reduction of aquifer sediments: Enhancement of reactive iron phases and TCE dechlorination. *Environmental Science & Technology* **2004**, *38*, (17), 4656-4663.
5. Butler, E. C.; Hayes, K. F., Kinetics of the transformation of trichloroethylene and tetrachloroethylene by iron sulfide. *Environmental Science & Technology* **1999**, *33*, (12), 2021-2027.